Regulation of transcriptional responses in T cells and upon SARS-CoV-2 infection

Dissertation

der Fakultät für Biologie
der Ludwig-Maximilians-Universität München

Marie Johanne Tofaute

München, den 01.12.2023

In remembrance of my grandparents,

their belief in me blossoms still, a timeless gift that nurtured my dreams,

endowing me with sails to navigate the winds of possibility.

Diese Dissertation wurde angefertigt

am **Helmholtz Zentrum München**

Deutsches Forschungszentrum für Gesundheit und Umwelt

Molecular Targets and Therapeutics Center

Abteilung Signaling and Translation

unter der Leitung von **Prof. Dr. Daniel Krappmann**

1. Gutachter: Prof. Dr. Daniel Krappmann

2. Gutachter: Prof. Dr. Christof Osman

Tag der Abgabe: 01.12.2023

Tag der mündlichen Prüfung: 26.11.2024

Table of contents

Table of contents ..... **VII**
List of figures ..... **XIII**
Acknowledgements **17**
Summary **19**
Zusammenfassung **21**
1 Introduction **23**
1.1 Transcriptional regulators of immune cells 23
1.1.1 The transcription factor NF-κB 23
1.1.1.1 The canonical and non-canonical pathways of NF-κB activation 25
1.1.2 The transcription factor AP-1 27
1.1.3 The transcription factor NF-AT 29
1.2 Transcriptional response in adaptive immunity 31
1.2.1 The T cell response is regulated by the transcription factors NF-κB, NF-AT and AP1 31
1.2.1.1 Signaling pathways induced by TCR/CD28 co-engagement 31
1.2.1.2 CARD11 – the molecular seed of the CBM complex 34
1.2.1.3 Crosstalk of NF-κB, AP-1 and NF-AT in T lymphocytes 36
1.2.2 The adaptive immune system 37
1.2.2.1 B Lymphocytes 39
1.2.2.2 T Lymphocytes 39
1.2.2.3 Heterogeneous germline mutations in *CARD11* cause BENTA and CADINS diseases 41
1.3 Transcriptional response upon SARS-CoV-2 infection 43
1.3.1 Human immune response against pathogens 43
1.3.1.1 The innate immune system 43
1.3.1.2 Immune response to viral infection 45
1.3.1.3 Diseases caused by human coronaviruses 46
1.3.2 SARS-CoV-2 – the newly emerged human coronavirus 47
1.3.2.1 COVID-19 – the disease caused by SARS-CoV-2 47
1.3.2.2 Pathogenic inflammatory response in severe cases of COVID-19 48
1.3.2.3 SARS-CoV-2 genome and proteome 49
1.3.2.4 SARS-CoV-2 Nsp14 51

1.3.2.5 SARS-CoV-2-human contactome maps viral protein-protein interactions with NF-κB signaling pathway 53
2 Aims of the study 55
3 Results 57
3.1 Transcriptional activation in T cells 57
3.1.1 A novel reporter Jurkat T cell line to study NF-κB, AP1 and NF-AT crosstalk 57
3.1.1.1 Generation of a fluorescence-based triple transcriptional reporter Jurkat T cell line 57
3.1.1.2 Specificity analysis of transcriptional reporters in the TTR Jurkat T cell line 59
3.1.1.3 Determination of optimal stimulation conditions in TTR Jurkat T cells 65
3.1.2 No transcriptional crosstalk induced by patient-derived CARD11 mutations 72
3.1.2.1 Overexpressing mutant CARD11 replicates heterozygous mutations in patients 72
3.1.2.2 CADINS- and BENTA-associated CARD11 mutations only mildly affect AP-1 and NF-AT activity 77
3.2 Transcriptional activation upon SARS-CoV-2 infection 80
3.2.1 SARS-CoV-2 Nsp14 activates the transcription factor NF-κB 80
3.2.1.1 Coronaviral Nsp14 is sufficient for NF-κB activation 80
3.2.1.2 Nsp14 is stabilized by Nsp10 and S-adenosylmethionine 85
3.2.1.3 Nsp14 requires functional MTase domain for NF-κB activation 86
3.2.2 SARS-CoV-2 Nsp14 is inherently unstable 88
3.2.2.1 Nsp14 expression is downregulated upon stable integration in HEK293 cells 88
3.2.2.2 Inducible Nsp14 expression reveals post-translational instability of Nsp14 90
3.2.3 Overexpressed Nsp14 is not sufficient to induce endogenous NF-κB signaling 92
3.2.3.1 Nsp14 does not activate the endogenous NF-κB signaling pathway 92
3.2.3.2 Nsp14 does not efficiently induce transcription of endogenous NF-κB target gene loci 95
3.2.4 Nsp14-induced canonical NF-κB signaling relies on NEMO/IKKγ and NF-κB p65 98
3.2.4.1 Nsp14 does not form stable complexes with putative human binding partners 98
3.2.4.2 Nsp14 induces canonical NF-κB signaling via NEMO and p65, but not c-Rel 101

3.2.4.3 Non-canonical NF-κB signaling is not essential for Nsp14-driven NF-κB activity ... 104
4 Discussion ... 109
4.1 Generation and application of a TTR Jurkat T cell line ... 109
4.1.1 The TTR system displays the activation of major T cell transcription factors ... 109
4.1.2 CADINS- and BENTA-causing *CARD11* mutations are not inducing transcriptional crosstalk in T cells ... 114
4.2 The SARS-CoV-2 Nsp14 stimulates host cell NF-κB activity ... 117
4.2.1 Full length Nsp14 with active MTase domain stimulates NF-κB ... 117
4.2.2 Nsp14 is instable without viral accessory proteins ... 120
4.2.3 Nsp14 induces NF-κB activity via the canonical signaling pathway ... 121
4.3 Conclusion and perspectives ... 125
5 Materials ... 129
5.1 Instruments and equipment ... 129
5.2 Chemicals ... 131
5.2.1 General chemicals ... 131
5.2.2 Cell culture ... 132
5.2.3 Stimulants and inhibitors ... 132
5.3 Buffers and solutions ... 133
5.4 Kits and enzymes ... 133
5.5 Plasmids and Oligonucleotides ... 134
5.5.1 Vectors ... 134
5.5.2 Sequences of used sgRNA ... 136
5.5.3 Primer for RT-PCR ... 136
5.6 *Escherichia coli* (*E. coli*) strains ... 137
5.7 Eukaryotic cell lines ... 137
5.8 Antibodies ... 137
5.8.1 Primary antibodies ... 137
5.8.2 Secondary antibodies ... 138
5.8.3 Stimulatory antibodies ... 139
5.8.4 FACS antibodies ... 139
5.9 Software ... 139
6 Methods ... 141
6.1 Molecular biology methods ... 141
6.1.1 Polymerase chain reaction ... 141

6.1.2 DNA restriction digestion, agarose gel electrophoresis and DNA extraction 142
6.1.3 DNA ligation and transformation of *E.coli* 142
6.1.4 Cultivation of *E.coli* and plasmid preparation 142
6.1.5 DNA sequencing 143
6.1.6 Genomic DNA extraction 143
6.1.7 RNA extraction 143
6.1.8 Reverse transcription into cDNA 143
6.1.9 Real-time PCR 144
6.2 Cell culture methods 144
6.2.1 Storage of cell lines 144
6.2.2 Cultivation of cell lines 145
6.2.3 Lentiviral transduction of Jurkat T cells and Hek293 cells 145
6.2.4 Generation of knock out cell lines 146
6.2.5 Generation of HCT116 and Hek293 cells with tet-on regulated Nsp14 expression 146
6.2.6 Overexpressing proteins in Hek293 cells 147
6.2.7 Stimulation and inhibitor treatment of Jurkat T cells 147
6.2.8 Stimulation and compound treatment of Hek293 cells 148
6.3 Flow cytometry 148
6.3.1 Staining of surface molecules 148
6.3.2 Flow cytometry and cell sorting 148
6.4 Biochemical and immunological methods 149
6.4.1 Preparation of whole cell lysates 149
6.4.2 Protein-protein interaction studies 149
6.4.3 SDS polyacrylamide gel electrophoresis 149
6.4.4 Western Blot 150
6.4.5 NF-κB reporter assay 150
6.5 Statistical analysis 151
7 Abbreviations 153
8 References 159
Appendix 183
Publications 183
Eidesstattliche Erklärung 185
Erklärung 185

List of figures

Figure 1-1: Schematic representation of the NF-κB/Rel protein family and the IκB protein family. 25
Figure 1-2: The canonical and non-canonical NF-κB signaling pathway. 27
Figure 1-3: The AP-1 signaling pathway. 28
Figure 1-4: The NF-AT signaling pathway. 30
Figure 1-5: Proximal T cell receptor signaling and activation of NF-κB, AP-1 and NF-AT. 33
Figure 1-6: Assembly of the CBM complex. 35
Figure 1-7: Schematic representation of the phosphorylation sites in CARD11. 36
Figure 1-8: Schematic of heterozygous germline mutations in CARD11. 42
Figure 1-9: Schematic representation of the SARS-CoV-2 genome. 50
Figure 1-10: Schematic representation of Nsp14. 52
Figure 1-11: SARS-CoV-2 contactome with human interacting proteins. 54
Figure 3-1: Scheme of NF-κB eCFP, AP-1 mCherry and NF-AT eGFP reporter constructs. 57
Figure 3-2: TTR Jurkat T cell line stimulated with anti-CD3/CD28. 58
Figure 3-3: T cell signaling with inhibitors used for specificity analysis of the triple reporter system. 60
Figure 3-4: TTR Jurkat T cells treated with dasatinib and stimulated with anti-CD3/CD28. 61
Figure 3-5: TTR Jurkat T cells treated with FK506 and stimulated with anti-CD3/CD28. 62
Figure 3-6: TTR Jurkat T cells treated with sotrastaurin and stimulated with anti-CD3/CD28. 63
Figure 3-7: TTR Jurkat T cells treated with MLN120B and stimulated with anti-CD3/CD28. 64
Figure 3-8: T cell signaling with stimuli used to characterize transcription factor activation dynamics. 65
Figure 3-9: Anti-CD3/CD28, P/I and TNF-α stimulation of TTR Jurkat T cells for 0, 5 and 24 hours. 68
Figure 3-10: Titration of anti-CD3 for optimal stimulation of TTR Jurkat T cells. 71
Figure 3-11: Titration of anti-CD28 for optimal stimulation of TTR Jurkat T cells. 71
Figure 3-12: TTR Jurkat T cells overexpressing patient-derived CADINS and BENTA *CARD11* mutations. 74
Figure 3-13: NF-κB activity in TTR Jurkat T cells overexpressing patient-derived CADINS *CARD11* mutations. 75
Figure 3-14: NF-κB activity in TTR Jurkat T cells overexpressing patient-derived BENTA *CARD11* mutations. 76
Figure 3-15: AP-1 and NF-AT activity in TTR Jurkat T cells overexpressing patient-derived CADINS *CARD11* mutations. 78

Figure 3-16: AP-1 and NF-AT activity in TTR Jurkat T cells overexpressing patient-derived BENTA *CARD11* mutations....79
Figure 3-17: Nsp14 overexpression induces NF-κB activity in Hek293....82
Figure 3-18: Nsp14 from SARS-CoV-2 variants....83
Figure 3-19: Nsp14 from various coronaviruses....84
Figure 3-20: Nsp14 is stabilized by Nsp10 and SAM....86
Figure 3-21: Nsp14 truncation and catalytically inactive mutants....87
Figure 3-22: Nsp14 treated with MTase inhibitors....88
Figure 3-23: Hek293 stably expressing Nsp14....90
Figure 3-24: Hek293 and HCT116 with inducible Nsp14 expression....91
Figure 3-25: WT Nsp14 protein is instable in Hek293 and HCT116 cells....92
Figure 3-26: The endogenous NF-κB signaling pathway is not activated by Nsp14 overexpression....94
Figure 3-27: Expression of NF-κB target genes upon Nsp14 overexpression....95
Figure 3-28: Expression of NF-κB target genes upon Nsp14 overexpression and TNF-α stimulation....96
Figure 3-29: Expression of NF-κB target genes upon Nsp14 overexpression and Nsp10 co-expression....97
Figure 3-30: Expression of NF-κB target genes upon Nsp14 overexpression and SAM treatment....98
Figure 3-31: Schematic of the canonical and non-canonical NF-κB signaling pathways with putative Nsp14 interactors highlighted....99
Figure 3-32: Nsp14 does not stably bind putative human binding partners....100
Figure 3-33: Nsp14-induced NF-κB signaling is significantly impaired in *IKBKG* (NEMO) KO Hek293....102
Figure 3-34: cRel is not essential for NF-κB activation induced by Nsp14....103
Figure 3-35: Nsp14-induced NF-κB activity is mainly based on p65....104
Figure 3-36: TRAF2 is not required for Nsp14-driven activation of NF-κB....105
Figure 3-37: Nsp14 does not trigger RelB-dependent non-canonical NF-κB signaling....106
Figure 4-1: T cell signaling with crosstalk between NF-κB, AP-1 and NF-AT signaling pathways....112

Acknowledgements

First, I would like to thank my supervisor Prof. Dr. Daniel Krappmann. Thank you for your guidance and advice, your mentorship, for helping me develop an analytical and scientific mindset, your patience and support throughout the years and especially during the pandemic.

I would like to thank my thesis committee members Prof. Dr. Kathrin Schumann and Prof. Dr. Christof Osman for their advice and great support, and I would also like to thank the members of my doctoral defense committee for their time and effort: Prof. Dr. Heinrich Jung, Dr. Serena Schwenkert, Dr. Silke Robatzek, and Prof. Dr. Thomas Nägele.

Special thanks to all my fellows and colleagues, I could not have done this without you! I thank the members of the Krappmann lab and other Helmholtz Munich research groups for their fantastic support, scientific and non-scientific input, and companionship over the years. I would like to thank Kerstin Kutzner, Dr. Carina Graß and Bahareh Nemati Moud for all their time, patience and support inside and outside the lab, as well as Dr. Aurelia Stangl, Dr. Thomas Seeholzer and Dr. Torben Gehring for introducing me to the Helmholtz universe.

Finally, I am deeply grateful to my friends and family who have celebrated the good days with me and supported me through the more challenging ones. Without your love, patience, motivation and encouragement, this thesis would not have been possible.

Thank you!

Summary

Transcription factor activity shapes a wide variety of cellular processes, from directing cell fate during tissue development to modulating responses to environmental stimuli. The transcription factors NF-κB, AP-1, and NF-AT are particularly noteworthy because of their ubiquitous expression and the breadth of processes they regulate. In T lymphocytes, they are essential for both activation and effector functions, tailoring the adaptive immune response through a pathogen-specific gene expression profile. However, T cell stimulation by an antigen not only stimulates isolated signaling pathways culminating in the activation of these transcription factors, but also induces extensive crosstalk within a complex signaling network.

In this study, we engineered a reporter Jurkat T cell line with eCFP, mCherry, and eGFP as fluorescent markers of NF-κB, AP-1, and NF-AT transcriptional activities. Using different inhibitors and stimulation conditions, we demonstrated the accurate and comprehensive quantification of T cell signaling crosstalk, activation kinetics, and responsiveness to stimuli. This novel Jurkat cell line thus serves as a powerful tool to elucidate T lymphocyte signaling and activation mechanisms in physiological and disease contexts.

Using our newly generated reporter Jurkat T cell line, we studied the consequences of congenital gain- or loss-of-function *CARD11* mutations leading to immunological diseases. Overexpression of these patient-derived mutations allowed us to assess their impact on the activation of NF-κB, AP-1 and NF-AT signaling. We could not detect any aberrant AP-1 and NF-AT transcriptional activity induced by mutant CARD11 beyond the previously characterized dysregulation of NF-κB, suggesting that the patients' symptoms may not be linked to transcriptional activity of AP-1 and NF-AT. Nevertheless, the novel reporter Jurkat T cell line has established itself as a versatile biological platform for the concurrent, comprehensive study of key T cell transcription factors, both qualitatively and quantitatively.

In the second part of this study, we demonstrate that SARS-CoV-2 triggers NF-κB-mediated transcriptional responses in host cells. By overexpressing (OE) SARS-CoV-2 proteins identified in a SARS-CoV-2 human contactome study for their binding to human NF-κB pathway components and performing NF-κB reporter assays, we identified Nsp14 as a key inducer of

NF-κB activity, a function observed in several human coronaviruses and SARS-CoV-2 variants. In addition, our studies revealed a dose-dependent relationship between Nsp14 and NF-κB induction that was amplified by Nsp14's cofactors. By evaluating Nsp14 mutants, we linked NF-κB up-regulation to the N7-methyltransferase enzymatic activity of Nsp14. Under stable or inducible Nsp14 expression, the inherent instability of Nsp14 became apparent, and we could not detect Nsp14-induced expression of classical NF-κB target genes beyond a very weak induction of *CXCL8*. Furthermore, although we could not determine stable protein-protein interactions, gene knockout studies implicated Nsp14 in the activation of canonical NF-κB signaling through NEMO and p65, whereas the non-canonical pathway remained unaffected. Overall, we propose that Nsp14 potentiates the transcriptional activity of canonical NF-κB complexes, rather than directly initiating NF-κB activation. This suggests that other SARS-CoV-2 proteins and the host innate immune response may synergistically contribute to primary NF-κB activation, culminating in an escalating cycle of inflammation with excessive cytokine release.

Zusammenfassung

Die Aktivität von Transkriptionsfaktoren beeinflusst eine Vielzahl von zellulären Prozessen, von der Steuerung der Zelldifferenzierung während der Gewebeentwicklung bis zur Modulation von Reaktionen auf Umweltreize. Die Transkriptionsfaktoren NF-κB, AP-1 und NF-AT sind aufgrund ihrer ubiquitären Expression und der Diversität der Prozesse, die sie regulieren, besonders bemerkenswert. In T-Lymphozyten sind sie sowohl für die Aktivierung als auch für die Effektor-Funktionen von wesentlicher Bedeutung und steuern die adaptive Immunantwort durch ein pathogenspezifisches Genexpressionsprofil. Die Stimulierung der T-Zellen durch ein Antigen stimuliert jedoch nicht nur isolierte Signalwege, die in der Aktivierung dieser Transkriptionsfaktoren gipfeln, sondern führt auch zu einem umfangreichen Crosstalk innerhalb eines komplexen Signalnetzwerks.

In dieser Studie haben wir eine Reporter-Jurkat T-Zelllinie mit eCFP, mCherry und eGFP als fluoreszierende Marker für die Transkriptionsaktivitäten von NF-κB, AP-1 und NF-AT entwickelt. Durch den Einsatz verschiedener Inhibitoren und Stimulationsbedingungen konnten wir eine genaue und umfassende Quantifizierung der T-Zell-Signalübertragung, der Aktivierungskinetik und der Reaktion auf Stimuli nachweisen. Diese neuartige Jurkat-Zelllinie dient somit als leistungsfähiges Instrument zur Aufklärung von Signal- und Aktivierungsmechanismen in T-Lymphozyten unter physiologischen und krankheitsbedingten Bedingungen.

Anhand unserer neu entwickelten Reporter-Jurkat T-Zelllinie untersuchten wir die Folgen angeborener *CARD11*-Mutationen mit aktivierendem oder inhibierendem Effekt, die zu immunologischen Erkrankungen führen. Die Überexpression dieser von Patienten stammenden Mutationen ermöglichte es uns, ihre Auswirkungen auf die Aktivierung von NF-κB, AP-1 und NF-AT-Signalen zu bewerten. Wir konnten keine abweichende AP-1- und NF-AT-Transkriptionsaktivität feststellen, die durch die *CARD11*-Mutation über die bereits beschriebene Dysregulation von NF-κB hinaus induziert wurde, was darauf hindeutet, dass die Symptome der Patienten möglicherweise nicht mit der Transkriptionsaktivität von AP-1 und NF-AT zusammenhängen. Nichtsdestotrotz hat sich die neuartige Reporter-Jurkat T-Zelllinie

als vielseitige biologische Plattform für die gleichzeitige, umfassende Untersuchung wichtiger T-Zell-Transkriptionsfaktoren sowohl in qualitativer als auch in quantitativer Hinsicht bewährt.

Im zweiten Teil dieser Studie zeigen wir, dass SARS-CoV-2 NF-κB-vermittelte transkriptionelle Reaktionen in Wirtszellen auslöst. Durch Überexpression von SARS-CoV-2-Proteinen, die in einer Studie zum SARS-CoV-2-Mensch Kontaktom aufgrund ihrer Bindung an Komponenten des menschlichen NF-κB-Signalwegs identifiziert wurden, und durch die Durchführung von NF-κB-Reporter-Assays konnten wir Nsp14 als einen wichtigen Auslöser der NF-κB-Aktivität identifizieren, eine Funktion, die bei mehreren humanen Coronaviren und SARS-CoV-2-Varianten beobachtet wird. Darüber hinaus zeigten unsere Studien eine dosisabhängige Beziehung zwischen Nsp14 und der NF-κB-Induktion, die durch die Nsp14-Kofaktoren verstärkt wurde. Durch die Untersuchung von Nsp14-Mutanten konnten wir die stärkere Aktivierung von NF-κB mit der enzymatischen Aktivität der Nsp14 N7-Methyltransferase in Verbindung bringen. Bei stabiler oder induzierbarer Nsp14-Expression wurde die inhärente Instabilität von Nsp14 deutlich, und wir konnten keine Nsp14-induzierte Expression klassischer NF-κB-Zielgene über eine sehr schwache Induktion von *CXCL8* hinaus feststellen. Darüber hinaus konnten wir zwar keine stabilen Protein-Protein-Bindungen feststellen, aber Gen-Knockout-Studien ergaben, dass Nsp14 an der Aktivierung der kanonischen NF-κB-Signalübertragung durch NEMO und p65 beteiligt ist, während der nicht-kanonische Signalweg unbeeinflusst blieb. Insgesamt schlagen wir vor, dass Nsp14 die Transkriptionsaktivität der kanonischen NF-κB-Komplexe potenziert, anstatt die NF-κB-Aktivierung direkt zu initiieren. Dies deutet darauf hin, dass andere SARS-CoV-2-Proteine und die angeborene Immunreaktion des Wirtes synergistisch zur primären NF-κB-Aktivierung beitragen, die in einem eskalierenden Entzündungszyklus mit übermäßiger Zytokinfreisetzung gipfelt.

1 Introduction

Transcription factors play a pivotal role in the regulation of gene expression and serve as central mediators in a variety of essential cellular processes (1). These range from determining cell fate during development to initiating specific cellular programs in response to external stimuli. Although every cell within an organism shares identical genetic information, it's the differential transcription of genes that allows for the vast biological diversity among cell types. In general, there are general transcription factors that regulate the expression of all genes, and master transcription factors that drive the formation of specific organs by controlling specific sets of genes. Such factors ensure the expression of essential proteins, such as structural proteins. In addition, many genes are regulated by a complex network of specific transcription factors. This interplay results in the formation and regulation of different cell types with unique structures and functions. In other cases, transcription factors play a key role in modifying gene transcription patterns in response to external stimuli, reflecting changing conditions surrounding differentiated cells.

Among the ubiquitously expressed transcription factors, nuclear factor κ-light-chain-enhancer of activated B-cells (NF-κB) stands out as it regulates a wide range of processes from development to homeostasis and disease (2). Within immune cells, NF-κB plays a central role in shaping the pathogen-specific inflammatory response. This function is complemented and sometimes intertwined with other key transcription factors such as nuclear factor of activated T-cells (NF-AT) and activator protein-1 (AP-1) (3, 4).

1.1 Transcriptional regulators of immune cells

1.1.1 The transcription factor NF-κB

The transcription factor nuclear factor κ-light-chain-enhancer of activated B-cells (NF-κB) is ubiquitously expressed and is activated by a variety of stimuli. These include physical and oxidative stress, cellular stress, and the engagement of various immune cell receptors (2, 5). The role of NF-κB is diverse, ranging from the regulation of embryonic development, apoptosis and proliferation to inflammatory responses, cell adhesion, and even tumorigenesis (2, 5-7). In

lymphocytes, it is essential for the activation, expansion, and effector functions during an immune response, as demonstrated in numerous genetic mouse models (8).

NF-κB is assembled from the group of five evolutionarily conserved proteins, the Rel family, which are structurally related (9, 10). All Rel family proteins share the Rel homology domain (RHD), which allows dimerization, nuclear translocation, and DNA binding (Figure 1-1). Three of them, RelA/p65, RelB and c-Rel, contain an additional transcriptional activation domain (TAD), providing transcriptional activity to the dimers. In contrast, NF-κB1 (p50) and NF-κB2 (p52) lack such a transactivation domain and are therefore transcriptionally inactive. NF-κB exists as homo- or heterodimers and in resting cells it is tightly controlled by inhibitor of NF-κB (IκB) family members (2). The IκB proteins, such as IκBα, IκBβ or IκBγ, all contain five to seven ankyrin repeats that bind to the RHD domain of the NF-κB subunits. This interaction masks the nuclear localization signal in the RHD domain and sequesters NF-κB in the cytosol. Comparable ankyrin repeats that function similarly to IκBs are contained in the C-terminal halves of NF-κB1 and NF-κB2, both of which are synthesized as long precursor proteins p105 and p100. Upon stimulation, degradation of the IκB proteins and cleavage of p105 and p100 to p50 and p52, respectively, leads to release of NF-κB, which then translocates to the nucleus. Since each NF-κB subunit has distinct functions and specific preferences for DNA binding sites, the multitude of combinations allows for specific target gene activation and therefore highly specific responses (11-13).

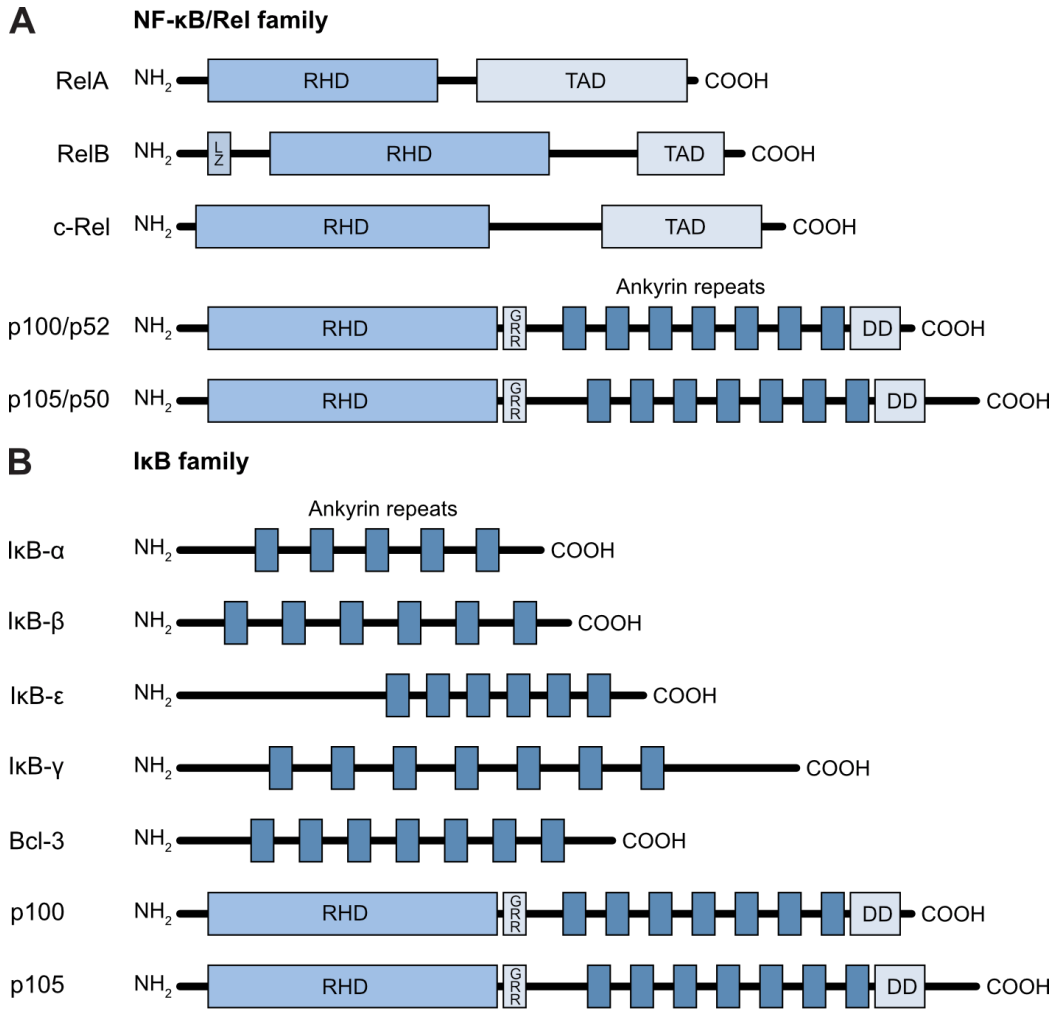

Figure 1-1: Schematic representation of the NF-κB/Rel protein family and the IκB protein family.
(A) Members of the NF-κB protein family are shown. All share a Rel homology domain (RHD), while only RelA, RelB and c-Rel additionally contain a transactivation domain (TAD). RelB contains an additional leucine zipper (LZ) domain, while p100 and p105 contain an additional glycine-rich region (GRR), ankyrin repeats and a death domain (DD). (B) Members of the IκB protein family are shown. All contain a variable number of ankyrin repeats.

1.1.1.1 The canonical and non-canonical pathways of NF-κB activation

The wide range of stimuli induces NF-κB activation by either the canonical or the non-canonical pathway (2, 8). The canonical NF-κB pathway is defined by activation of the IKK complex, leading to degradation of IκB proteins and engagement of heterodimers containing RelA/p65 or c-Rel (Figure 1-2) (14). This pathway is activated by a plethora of stimuli ranging from engagement of immune cell membrane receptors such as T cell receptor (TCR), TNFR1, TLR and IL1-R to DNA damage or oxidative stress, as well as intracellular immune receptors such as NOD-like and RIG-I-like receptors (NLR and RLR). All these triggers initiate signaling cascades involving phosphorylation, ubiquitination, and assembly of protein complexes that

converge on the activation of the IκB kinase (IKK) complex. Consisting of the ubiquitin-binding regulatory subunit IKKγ/NEMO and the catalytic subunits IKKα and IKKβ, the IKK complex integrates inputs from various upstream signaling cascades. Ubiquitination of NEMO and phosphorylation of IKKβ activate the complex, which phosphorylates IκB proteins, induces their proteasomal degradation, and promotes translocation of NF-κB to the nucleus (14, 15).

The non-canonical NF-κB pathway relies exclusively on NF-κB-inducing kinase (NIK)-mediated processing of p100 to p52, which forms heterodimers with RelB (8, 16). This pathway is associated with a subset of the TNFR superfamily, including lymphotoxin-β receptor (LTβR), B-cell activating factor receptor (BAFFR), receptor activator of NF-κB (RANK), and CD40 (17-21). While NIK is proteasomally degraded under basal conditions, receptor ligation mediates the accumulation of NIK (22, 23). Once stabilized, NIK forms a complex with IKKα, inducing its activation and thus IKKα-mediated phosphorylation of p100 (24-26). This induces p100 ubiquitination and selective proteasomal processing to p52 by removing the inhibitory C-terminal domain (24). The released p52 forms transcriptionally active heterodimers with RelB in the nucleus (16).

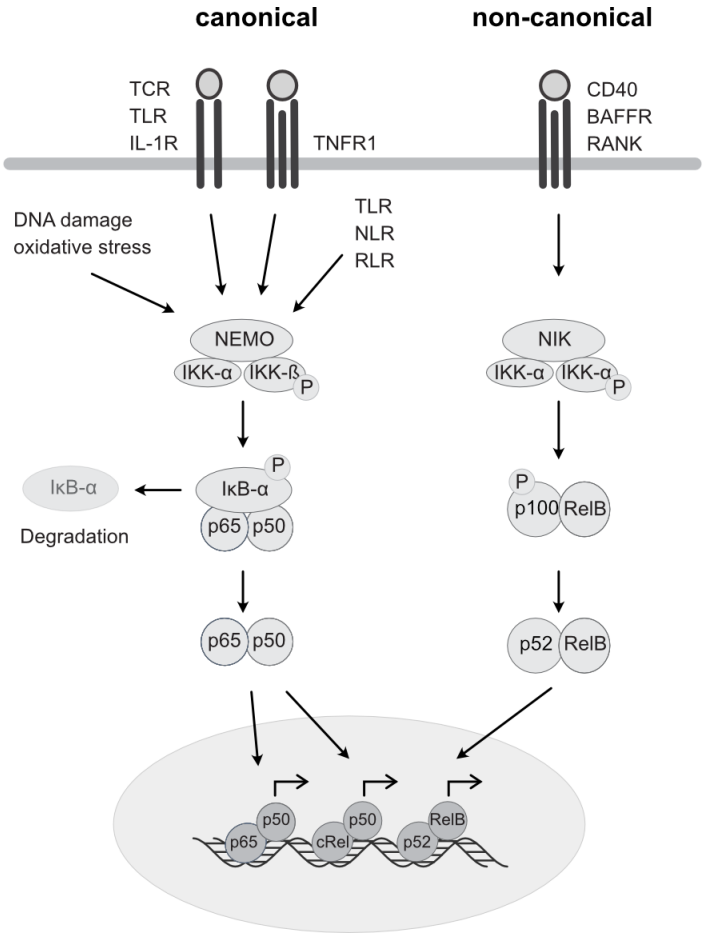

Figure 1-2: The canonical and non-canonical NF-κB signaling pathway.
The canonical NF-κB signaling pathway is activated by receptor stimulation, including TCR, TLR, IL-1R, and TNFR1. This triggers a series of protein modifications and complex formations, culminating in the assembly of the NEMO/IKK complex. Once active, IKK-β phosphorylates IκB-α, leading to its proteasomal degradation, which facilitates the release and subsequent nuclear translocation of NF-κB. Alternatively, the non-canonical pathway is activated by receptors such as CD40, BAFFR, and RANK. In this pathway, the continuous degradation of NIK is inhibited upon stimulation. Stabilized NIK then associates with IKK-α dimers. Activated IKK-α mediates the processing of p100 to p52, thus releasing the p52/RelB dimer, which then translocates to the nucleus.

1.1.2 The transcription factor AP-1

The activator protein-1 (AP-1) is one of the longest known transcription factors and its activity is induced by a variety of stimuli ranging from physical stress to growth factors, hormones, and cytokines (3). While it generally mediates a wide spectrum of effects such as cell survival, proliferation, and death, it specifically has a crucial role for the immune system by regulating T-cell activation, differentiation, effector function and T-cell anergy (27).

AP-1 transcription factors are dimers formed by proteins belonging to the Jun, Fos, Maf and activating transcription factor (ATF) subfamilies and all of them share a basic region-leucine zipper (bZIP) domain that allows their dimerization (28). Among the variety of AP-1 proteins,

c-Jun has the highest transcriptional activation potency and often forms stable heterodimers with Fos proteins, whereas other AP-1 proteins show variance in their ability to dimerize and induce gene expression (3). This combinatorial diversity, coupled with the intricate regulatory mechanisms, results in a plethora of AP-1 target genes and biological effects (28, 29).

However, unlike NF-κB, AP-1 proteins are present at low levels in the basal state and must be expressed upon stimulation before they can act as transcription factors. Stimulatory signals induce a plethora of mitogen-activated protein kinase (MAPK) pathways that lead to AP-1 activity (30, 31). In general, these pathways can be grouped into three distinct cascades that induce activation of the MAPK subgroups extracellular-signal-regulated kinase (ERK) 1/2, c-Jun N-terminal kinases (JNK) 1/2, and p38 (Figure 1-3). Once activated, both ERK and JNK proteins act in the nucleus and promote transcription of the fos gene (32). In addition, JNK proteins directly modify pre-existing c-Jun and ATF2 in the nucleus and enhance their transcriptional activity (33, 34). Finally, p38 activates various transcription factors for Jun expression (35).

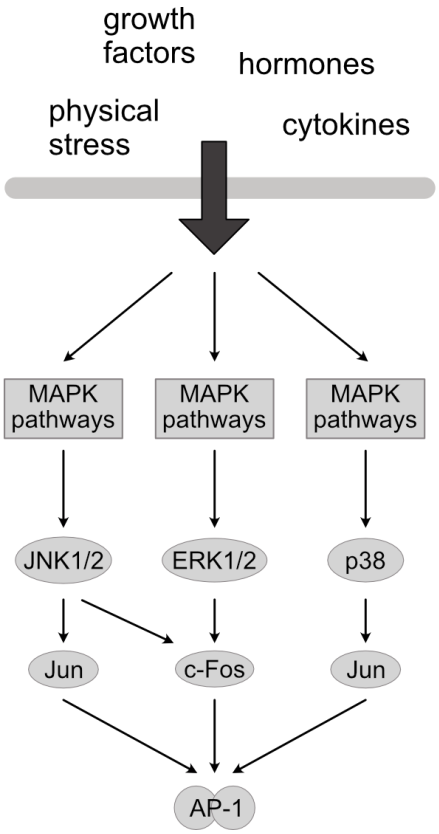

Figure 1-3: The AP-1 signaling pathway.

Stimulatory signals induce a plethora of mitogen-activated protein kinase (MAPK) pathways with three distinct major cascades. They differ in the activation of the ERK1/2, JNK1/2, and p38 MAPK subgroups. Once activated, they promote transcription and activation of AP-1 proteins, thereby stimulating AP-1 transcriptional activity.

1.1.3 The transcription factor NF-AT

As NF-κB, also the transcription factor nuclear factor of activated T-cells (NF-AT) is expressed ubiquitously and implicated in a broad set of functions including developmental processes in various tissues, cell growth, angiogenesis and cancer formation (4, 36, 37). In lymphocytes, NF-AT regulates activation, differentiation, metabolism, cytokine expression and apoptosis and is therefore essential for an effective immune response (38-41). However, it is also associated with T cell anergy and exhaustion (see 1.2.1) (42).

The NF-AT family consists of the four calcineurin-regulated NF-AT1-4 and the calcineurin-independent NF-AT5 (43, 44). While NF-AT5 is associated with osmotic stress, NF-AT1-4 are regulated by cytosolic Ca^{2+} levels (43, 45). All NF-AT proteins share a conserved REL homology domain for DNA binding and dimer formation as well as a less conserved regulatory domain, also called NF-AT homology domain (43). Alternative splicing in combination with different promoters and polyadenylation sites leads to numerous isoforms with each NF-AT protein having distinct as well as redundant functions (38, 41). NF-AT forms transcriptionally active homo- and heterodimers, but more often it functions in high-affinity complexes with other transcription factors, such as AP-1 (see 1.1.2), allowing for different sets of transcribed target genes and thus biological responses driven by NF-AT (4).

The transcriptional activity of NF-AT is tightly regulated by phosphorylation. Under basal conditions, NF-AT is highly phosphorylated and remains in the cytosol (46). Upon stimulation of cell surface receptors, such as receptor tyrosine kinases, GPCRs, or immunoreceptors, the phospholipase catalyzes the formation of IP_3, which activates store-operated Ca^{2+} influx from the ER (4, 47). The subsequent induced Ca^{2+} influx across the plasma membrane contributes to the elevation of intracellular Ca^{2+} levels and Ca^{2+}-activated calmodulin binds to the phosphatase calcineurin. This promotes calcineurin to release its autoinhibition and expose its active site (Figure 1-4) (48-51). Extensive calcineurin-mediated dephosphorylation of NF-AT in its regulatory domain induces conformational changes that unmask nuclear localization signals and induce NF-AT translocation to the nucleus (46, 52-54). In addition,

dephosphorylated NF-AT shows increased affinity for binding DNA (55). In the nucleus, NF-AT is immediately subjected to re-phosphorylation, which promotes its export back to the cytosol (4). Re-phosphorylation is a multi-step mechanism involving nuclear priming and export kinases as well as cytosolic maintenance kinases such as GSK3β or CK1 (4, 56-58). Overall, the Ca^{2+} levels required for efficient activation, inactivation kinetics and post-translational regulation differ between the different NF-AT proteins, suggesting specificity depending on the type and intensity of stimulation (59-62).

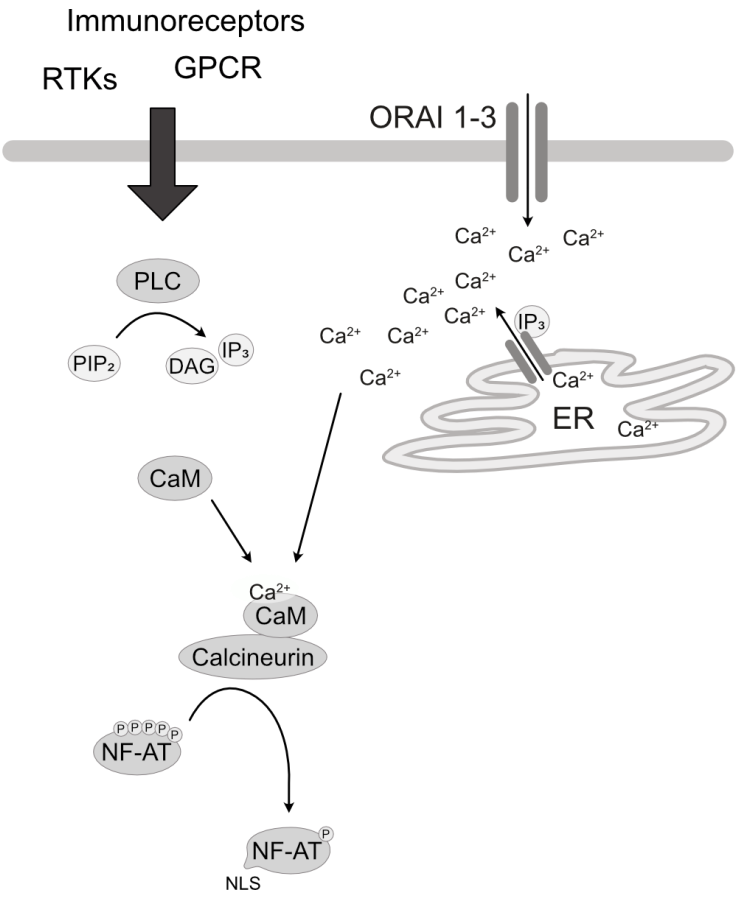

Figure 1-4: The NF-AT signaling pathway.
Stimulatory signals induce the synthesis of IP_3, which leads to calcium efflux from the ER and calcium influx across the plasma membrane. As intracellular Ca^{2+} levels are elevated, Ca^{2+}-activated calmodulin (CaM) binds and activates the phosphatase calcineurin. Calcineurin-mediated dephosphorylation of NF-AT induces conformational changes that unmask the nuclear localization signal (NLS) of NF-AT. As a result, NF-AT translocates to the nucleus and becomes transcriptionally active.

1.2 Transcriptional response in adaptive immunity

Transcription factors are critical for modulating cellular responses to a variety of external stimuli (1). The nature of the stimulus and the associated intracellular signaling pathways determine which transcription factors are activated. While a given stimulus may affect different cell types, each cell type responds differently based on its inherent function. The combined influence of the type of transcription factors activated and the transcription of selected target genes determines the overall response of the cell.

T-lymphocytes, as part of the adaptive immune system, play an important role by recognizing non-self-antigens via their T-cell receptors (see 1.2.2) (1, 63). In response to this recognition, intracellular signaling cascades are initiated, leading to the activation of transcription factors such as NF-κB, NF-AT, and AP1. These factors orchestrate a defense response consisting of specific target gene expression tailored to the particular immune challenge.

1.2.1 The T cell response is regulated by the transcription factors NF-κB, NF-AT and AP1

Stimulation of the TCR activates T cells and induces their differentiation into specific subtypes, proliferation, cytokine production and survival (64). While the different subtypes of T cells allow a targeted response to any type of pathogen (see 1.2.2), their tight regulation is essential for a balanced response and to avoid autoimmune or inflammatory diseases. The molecular signaling induced by TCR stimulation is complemented and intertwined with signaling pathways activated by costimulatory receptors and cytokines. Together, they form a complex signaling network that activates and controls the transcription factors nuclear factor κ-light-chain-enhancer of activated B-cells (NF-κB) (see 1.1.1), AP-1 (see 1.1.2), and nuclear factor of activated T-cells (NF-AT) (see 1.1.3).

1.2.1.1 Signaling pathways induced by TCR/CD28 co-engagement

Upon antigen stimulation, TCR-CD3 complexes form clusters with their co-receptors CD4 / CD8 and CD28 and recruit numerous other signaling proteins (Figure 1-5). They associate with and activate the protein tyrosine kinases Lck and Fyn, which phosphorylate CD3 at its conserved immunoreceptor tyrosine activation motifs (ITAMs) (65, 66). The phosphorylated ITAMs allow binding of zeta-chain-associated protein kinase 70 (ZAP70) through its SH2

domain and activation of ZAP70 by Lck-mediated phosphorylation (66, 67). ZAP70 phosphorylates the transmembrane adaptor molecule linker for activation of T cells (LAT) as well as the cytosolic adaptor molecule lymphocyte cytosolic protein 2 (SLP76) (68-70). Together, they provide the seed for the formation of a multiprotein signaling complex that includes growth factor receptor-bound protein 2 (Grb2), GRB2-related adaptor downstream of Shc (GADS), and phospholipase C gamma (PLCγ) and activates several downstream proteins (68, 71). Activated PLCγ generates the second messengers DAG and IP_3 from membrane-bound PIP_2, which mediate the activation of NF-κB, AP-1, and NF-AT through various downstream signaling pathways (72, 73).

To achieve full and productive T cell activation, CD80 or CD86 presented on APCs is required to stimulate the co-receptor CD28. It recruits and activates the p85 regulatory subunit of PI3K, which in turn synthesizes PIP_2 and PIP_3 (74, 75). These are second messengers that recruit pleckstrin homology domain-containing proteins such as phosphatidylinositol-dependent kinase 1 (PDK1) and Vav (76). While Vav1 is proposed to integrate signals from TCR and CD28, activated PDK1 binds and phosphorylates PKCθ (77-79). Moreover, PKCθ is recruited by DAG to the TCR/CD28 complex, and thus PKCθ integrates signals from both TCR and CD28 and is a central component for antigen-induced activation of NF-κB (80).

The link from upstream TCR signaling to downstream canonical NF-κB and AP1 activation is formed by the high molecular weight complex of caspase recruitment domain (CARD)-containing MAGUK 1 (CARD11), B-cell CLL/lymphoma 10 (BCL10), and mucosa-associated lymphoid tissue protein 1 (MALT1) (CBM) (see below) (78, 81, 82). Upon antigen ligation, the CBM complex is formed and upon polyubiquitination, BCL10 and MALT1 recruit the IKK complex via its ubiquitin-binding subunit NEMO and activate the canonical NF-κB pathway (83, 84).

The second protein recruited to the TCR/CD28 complex by DAG is the Ras guanyl nucleotide exchange factor RAS guanyl releasing protein 1 (RasGRP1) (85). It activates Ras, which in turn initiates the MAPK cascade that ends in the activation of ERK1/2 (85, 86). In contrast, activation of JNK1/2 and p38 in T cells depends mainly on BCL10 and MALT1 activity in the CBM complex (87, 88). Also, IKK-β promotes AP-1 activity by promoting MAPK/ERK1/2 signaling and stabilizing phosphorylation of c-Fos (89, 90).

The second messenger IP_3 generated by PLCγ opens IP_3 receptor channels in the endoplasmic reticulum (ER) and induces an initial Ca^{2+} influx upon TCR stimulation (47). ER membrane-bound calcium sensor proteins then activate Ca^{2+}-release-activated Ca^{2+} (CRAC) channels in the plasma membrane to promote a prolonged increase in cytosolic Ca^{2+} levels (48, 49). This induces the Ca^{2+}/Calcineurin signaling pathway and hence NF-AT activity. In addition, CD28 co-stimulatory signals indirectly prevent NF-AT deactivation and thus increase NF-AT transcriptional activity (91).

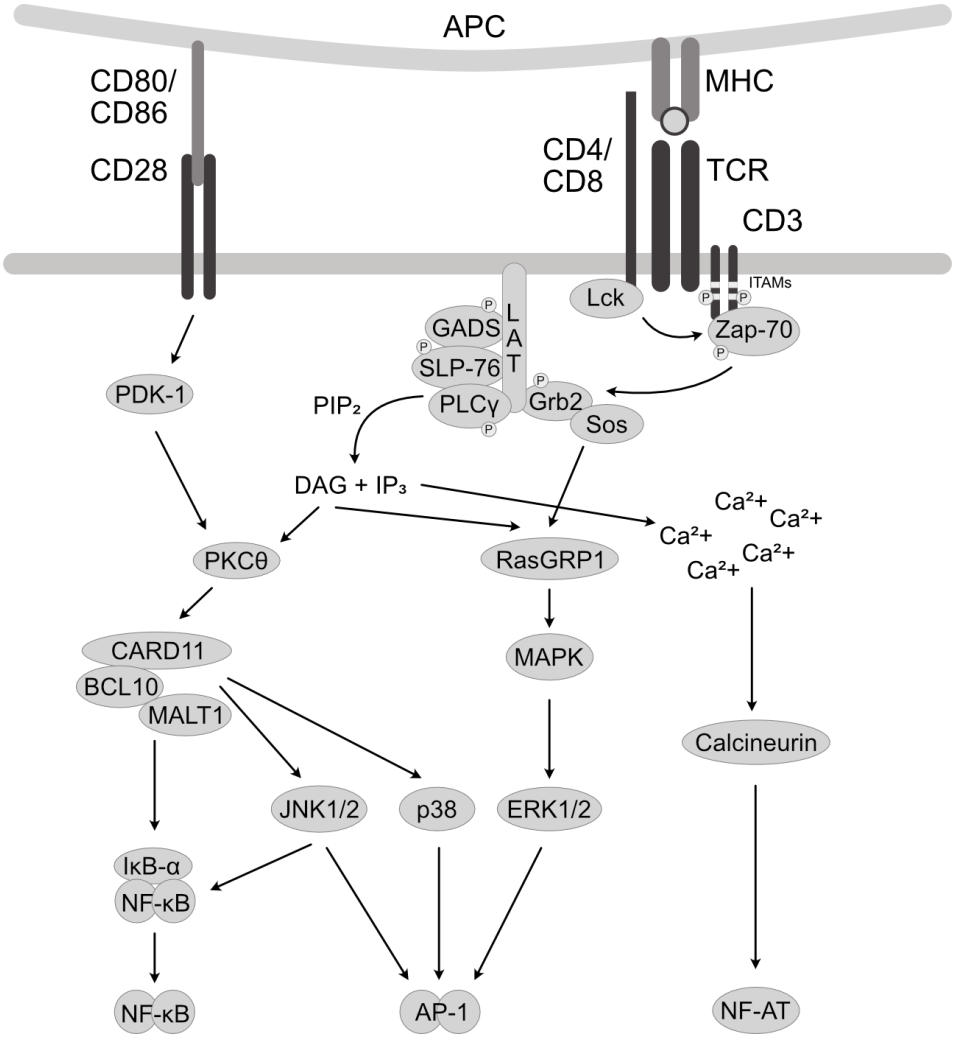

Figure 1-5: Proximal T cell receptor signaling and activation of NF-κB, AP-1 and NF-AT.
Stimulation of the TCR and its co-receptors CD4/CD8 and CD28 induces various intracellular signaling cascades that activate the transcription factors NF-κB, AP-1 and NF-AT. Upon receptor ligation, a multi-protein complex forms at the immunological synapse. Following a cascade of tyrosine phosphorylations, PLCγ generates DAG and IP3. These allow for the activation of the canonical NF-κB, MAPK-AP-1 and calcineurin-NF-AT pathways.

1.2.1.2 CARD11 – the molecular seed of the CBM complex

The CBM complex assembles upon TCR/CD28 stimulation and connects the proximal TCR signaling with the canonical NF-κB and JNK signaling cascades and is therefore not only essential for the activation of transcriptional activity, but also indispensable for all NF-κB and JNK-driven processes such as efficient T cell activation, proliferation and cytokine expression (92, 93). It consists of the proteins CARD11, BCL10 and MALT1.

CARD11 belongs to the MAGUK family of kinases and is expressed only in lymphoid and myeloid cells (94). It can be divided into five domains that provide different functions necessary for effective signaling (Figure 1-6) (94). The C-terminal PDZ, SH3 and GUK domains together form the MAGUK domain, which localizes CARD11 to the plasma membrane and contributes to the formation of CARD11 multimers upon activation (82, 95). Similarly, the coiled-coil domain is involved in CARD11 oligomerization, whereas the N-terminal CARD domain assembles with the CARD domain of BCL10 (96, 97). In addition to its N-terminal CARD domain, BCL10 contains a C-terminal S/T-rich region (92, 93). MALT1 consists of an N-terminal death domain (DD), three immunoglobulin-like (Ig) domains and a paracaspase domain between Ig2 and Ig3. Together, BCL10 and MALT1 constitutively form pre-assembled complexes by interaction of the BCL10 CARD and S/T-rich domain with the MALT1 Ig1, Ig2 and DD domain (98-100).

Upon TCR/CD28 stimulation various kinases, including PKCθ, are activated and promote strong phosphorylation of CARD11, which induces structural rearrangement to an active open CARD11 conformation (Figure 1-6) (101, 102). Active CARD11 then recruits pre-assembled BCL10-MALT1 molecules and large signaling filaments are formed (78, 98, 103). Subsequently, BCL10 and MALT1 recruit additional protein complexes and promote the activation of the canonical NF-κB signaling pathway (92).

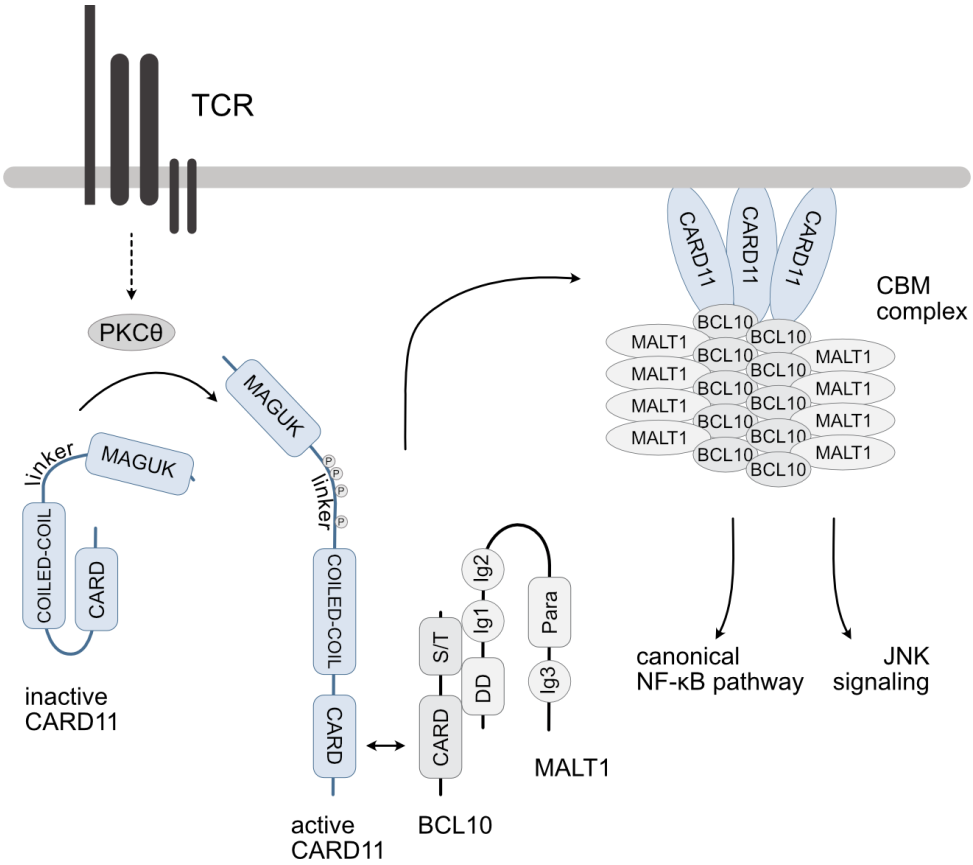

Figure 1-6: Assembly of the CBM complex.
Upon TCR engagement, the closed, inactive conformation of CARD11 is released by phosphorylation to an open, active conformation. CARD11 oligomerizes at the cell membrane, recruits pre-assembled BCL10-MALT1 complexes and initiates the formation of CBM filaments. Abbreviations: immunoglobulin-like (Ig), paracaspase (Para), death domain (DD).

CARD11 has been shown to regulate its activity by modulating its conformational state. The linker region between the coiled-coil and the MAGUK domain is central to this process. At rest, the linker region binds the CARD and the coiled-coil domain intramolecularly and thus keeps CARD11 folded in an inactive closed conformation (Figure 1-6) (104, 105). Upon antigen ligation, the linker region is strongly phosphorylated, which disrupts the intramolecular interactions and induces a conformational change to an active open conformation. The best studied phosphorylation sites for CARD11 activation are S559 and S652, which are targeted by PKCθ/PKCβ (Figure 1-7) (101, 102). In addition, numerous phosphorylation sites have been associated with activating effects, such as S116, S556, S558, and S562, which are modified by CaMKII, HPK1, and IKKβ, respectively (101, 106-108). However, phosphorylation of other sites such as S615, S644 and S893 have an inactivating effect on CARD11 (108-111). In addition, dephosphorylation and proteasomal degradation are also used to counteract CARD11 activity

(112, 113). Overall, CARD11 is regulated by a complex interplay of modifications and interacting proteins, reflecting its importance for lymphocyte function.

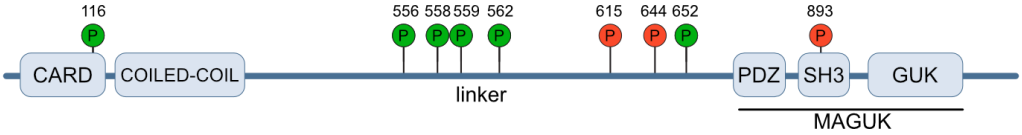

Figure 1-7: Schematic representation of the phosphorylation sites in CARD11.
The open active conformation of CARD11 with its protein domains and major phosphorylation sites are indicated. Phosphorylation events associated with CARD11 activation are shown in green and phosphorylation events associated with CARD11 inactivation are shown in red.

1.2.1.3 Crosstalk of NF-κB, AP-1 and NF-AT in T lymphocytes

In addition to the individual effect of each transcription factor activity, there is also crosstalk between activated transcription factors. This emphasizes that transcriptional regulation is driven by an intertwined, finely tuned signaling network in which small defects can have far-reaching detrimental consequences.

The availability of AP-1 is partially dependent on NF-κB activity, because on the one hand, a major transcription factor that drives the expression of AP-1 family proteins is a target gene of NF-κB (114). On the other hand, a certain subset of AP-1 proteins is also NF-κB target genes and is expressed upon canonical NF-κB activity (115). After their expression, the delayed activity of these AP-1 factors is required for a continued, fully functional secondary transcriptional response. In addition, direct binding of NF-κB p65 to c-Jun and c-Fos induces their DNA binding and activation (116). In turn, c-Jun and c-Fos can promote as well as inhibit the transactivation of p65 (90, 116). Taken together, NF-κB activity facilitates and regulates the expression and activation of AP-1 at multiple levels, but AP-1 also affects NF-κB activity.

NF-AT partners with various transcription factors that determine the induced biological response. In immune effector cells, it often cooperates with AP-1, integrating (co-stimulatory) signals from multiple pathways, which is essential for an effective immune response (43). The concerted action of NF-AT and AP-1 is based on composite DNA regions that contain the respective binding sites in close proximity to each other and allow a stable complex formation between NF-AT, AP-1 and DNA (117).

Without a partner transcription factor, e.g., in the absence of a co-stimulus that induces AP-1 activity, the binding of NF-AT dimers to target genes that drive T-cell activation is particularly weak and leads to weak T-cell activation (43). In the further course the T cells become unresponsive to antigen stimulation, even after re-stimulation with a new, strong stimulus, which characterizes the states of T cell anergy and exhaustion (42). At the molecular level, anergic cells exhibit defective Ras activation and thus impaired AP-1 activity, whereas Ca^{2+}-induced activation of NF-AT is unaffected (118, 119). In fact, pure NF-AT transcription complexes and a specific set of anergy-associated target genes are proposed to drive the anergy program (37). The balance between T cell activation and T cell anergy is controlled by the availability of partner transcription factors for NF-AT: while both gene programs are induced upon T cell activation, NF-AT complexes are more stable once they interact with partner transcription factors and thus deactivate the activity of weak-affinity pure NF-AT complexes (120).

1.2.2 The adaptive immune system

The human body is constantly exposed to pathogenic organisms such as bacteria, viruses, and fungi. Therefore, it has evolved an immune system that prevents pathogens from invading, multiplying, and spreading in the body, but also detects and eliminates them once they have invaded the human host (121). The immune system consists of the lymphoid organs, various cell types (leucocytes) and proteins and can be divided into two main parts, the innate and the adaptive immune system. Both components interact and are tightly regulated, as deregulation can lead to diseases such as serious infections, inflammation, cancer, and autoimmune diseases.

The adaptive immune response is evolutionarily younger than the innate immune system and takes several days to fully develop after infection (63, 121). Instead, it is highly specific in the recognition of various antigens, fights pathogens systemically and specifically, and forms an immunological memory (63, 122). It also includes positive amplification that provides an appropriate level of response as well as self-limiting negative feedback mechanisms that prevent severe tissue damage and disease (63, 123). It consists of a humoral and a cell-mediated part: The humoral response consists of antibodies produced and secreted by B

lymphocytes that target free, extracellular pathogens (see below), while the cell-mediated response is implemented by T lymphocytes that target intracellular pathogens (see below). Both B and T lymphocytes originate from bone marrow lymphoid progenitors (123, 124). However, while B cells undergo their entire development in the bone marrow, early-stage T cells migrate to the thymus as thymocytes to complete their development.

Both B and T cells express antigen receptors that belong to the Ig superfamily (1). The B cell receptor (BCR) consists of two light chains and two heavy chains, with the entire light chains and the N-terminal portions of the heavy chains forming the antigen-binding site (variable region). In contrast, the T cell receptor (TCR) consists of only two transmembrane polypeptides (α and β or δ and γ chains). To be able to respond to the infinite variety of antigens, the BCR and TCR antigen-binding domains must exist with a wide range of affinities. This is achieved by the process of V(D)J recombination, in which gene segments are joined by site-specific genetic recombination. The V, D, and J gene segments are encoded at different loci, each of which contains a large number of gene segment alleles from which to choose. In addition, junctional diversification is added by the loss or insertion of nucleotides at the recombination sites. In this way, combinatorial diversification is ensured, allowing for a reservoir of an estimated 10^7 to 10^9 different receptors early in lymphocyte development, even before the first antigen contact (63). Newly generated antigen receptors are tested for central tolerance, which includes efficient binding in positive selection and lack of self-reactivity in negative selection, and later controlled for peripheral tolerance (1, 121, 123).

Upon pathogenic invasion, antigen-presenting cells (APCs) of the innate immune system (see 1.3.1), such as dendritic cells, internalize the pathogen and present the processed antigen to lymphocytes located in secondary lymphoid organs, including lymph nodes (63, 125). There, T cells with TCRs that bind the presented antigen are activated (see below). In parallel, B cells within the lymph node are activated upon antigen recognition by their BCRs, aided by T helper cell presentation (see below). Following this antigen-specific activation, also known as clonal selection, both T and B cells undergo clonal expansion and subsequently differentiate into effector and memory cells. Soon after responding to the invader, most effector cells die by apoptosis, but the memory cells persist and provide the basis for a potential secondary

response. When the body is challenged by the same antigen again, the memory cells are activated and ensure a faster and stronger secondary response.

1.2.2.1 B Lymphocytes

B lymphocytes are primarily responsible for the production and secretion of antibodies specific to a pathogen (63, 124). They are activated either by binding free antigen with their BCR, which is a membrane-bound antibody, or by pathogen presentation from antigen-binding follicular dendritic cells. Upon co-stimulation by T lymphocytes with affinity for the same antigen, provided by binding the CD40 receptor of the B cell and secreting cytokines (see 2.2.2), the B cells mature into antibody-producing plasma cells. These then migrate to the periphery and secrete large amounts of antibodies with the same antigen binding site as their BCR.

Secreted antibodies circulate in body fluids where they specifically recognize and bind antigens, which can be pathogen-derived proteins as well as polysaccharides, lipids, or small molecules (1, 63). By binding, they neutralize pathogenicity and mark the pathogen for detection by the complement system or phagocytes. There are different classes of antibodies that all share the same antigen binding site but differ in the immune responses they mediate. The initial BCR and first secreted antibodies are class IgM antibodies, which have the most antigen binding sites and efficiently induce the complement system. During maturation, T cell signals induce isotype switching and promote the synthesis of other antibody classes with individual biological functions, such as either IgG, the major antibody in secondary immune responses, or IgD, IgE, or IgA (1, 123, 124). Additionally, somatic hypermutation introduces point mutations into the antigen-binding region of antibodies as T cells mature. This process refines and increases their affinity for specific antigens.

In addition to plasma cells, B cells also form long-lived plasma cells that continue to secrete low levels of antibodies after infection, as well as memory cells for a secondary response (63).

1.2.2.2 T Lymphocytes

T lymphocytes represent cell-mediated adaptive immunity. Their functions are diverse and range from direct induction of cell death in infected cells to supportive and immunomodulatory functions for other immune cells in controlling invading pathogens (1, 63).

The TCR identifies non-self peptides by specialized receptors known as major histocompatibility complexes (MHC) (63). There are two classes of MHC proteins, MHC class I and class II: MHC class I are expressed by all nucleated cells and continuously present peptides from the ubiquitin-dependent proteolysis of the cytosolic proteome (126). While peptides from endogenous proteins are ineffective against T cell activity, a T cell response is triggered upon detection of irregular peptides, such as viral proteins. MHC class II are expressed by APCs, especially dendritic cells, which consistently process extracellular proteins. After ingestion of the pathogen, its proteins are digested in lysosomal proteolysis, loaded onto MHC class II and presented to T cells in a local lymph node.

For effective T cell activation, various co-receptors and adhesion proteins complement the TCR binding strength and transmit co-stimulatory signals (1, 124, 127). The CD4 and CD8 co-receptors bind the invariant part of the MHC II and MHC I proteins, respectively, and thus not only stabilize TCR antigen binding, but also control the type of target cell with which the T cell engages. Lineage differentiation of $CD4^+$ and $CD8^+$ cells is a multi-step process in the thymus and depends on several influential factors such as cytokines, TCR signaling, transcription factors, CD4 and CD8 gene regulation, and even modulations in the periphery (128, 129). However, CD4 expression characterizes helper T cells, while CD8 expression characterizes cytotoxic T cells (63).

In addition to CD4 or CD8 co-receptors, the TCR associates with CD3 proteins, which provide the link between the cell surface activation signal and cytoplasmic signaling cascades (1, 124). Another essential T cell co-receptor is CD28, which binds to CD80 and CD86 on APCs and ensures effective T cell activation by induction of complementary downstream signaling (see 1.2.1).

$CD4^+$ T cells activate features of the adaptive immune response specifically tailored to the type of pathogen (63). They differentiate into T_H1, T_H2 or T_H17 cells depending on the individual cytokine environment which is generated in autocrine and paracrine manner upon activation (123, 129). While T_H1 cells mainly drive cell-mediated responses, T_H2 cells promote the humoral response and T_H17 cells support the neutrophil response (see 1.3.1). In contrast, some $CD4^+$ T cells remain in the lymph node to stimulate B cells. Cytotoxic $CD8^+$ T cells (Tc1 cells) directly target cells that express non-self-proteins, such as virus-infected cells or tumor cells. By

inserting perforins into the cell membrane, they infiltrate the targeted cell with granzymes that induce caspase activation and consequently DNA fragmentation and apoptosis (124).

To ensure tolerance to self-antigens and prevent autoimmunity, suppression of self-reactive lymphocytes is crucial (1, 63). To this end, those lymphocytes that have TCRs with high affinity for self-antigens are either targeted for negative selection and thus die by apoptosis, while some CD4+ differentiate into Treg cells during lymphocyte maturation. In addition, tolerance is maintained in mature lymphocytes outside the thymus in so-called peripheral tolerance. Peripheral tolerance is promoted by the induction of anergy (see 1.2.1) in the absence of costimulatory signals, the engagement of inhibitory receptors on APCs or other T cells, such as CTLA-4 or PD-1, or by Treg cells, which exert negative regulation by expressing the inhibitory receptor CTLA-4, secreting immunosuppressive cytokines, and absorbing IL-2.

1.2.2.3 Heterogeneous germline mutations in *CARD11* cause BENTA and CADINS diseases

CARD11, which is exclusively expressed in lymphoid and myeloid cells, is essential for scaffolding CBM complex formation upon TCR-stimulated canonical NF-κB activation (92, 94). Dysregulated NF-κB signaling is associated with diverse diseases ranging from inflammatory diseases to malignancies, autoimmunity and immunodeficiency diseases (130-133). In this line, somatic CARD11 mutations such as L251P have been associated with diffuse large B-cell lymphoma, angioimmunoblastic T-cell lymphoma, follicular helper T-cell-derived lymphoma, and adult T-cell leukemia/lymphoma, as they have been shown to promote increased NF-κB activity under basal and stimulated conditions (134-136). Similarly, inborn errors in any component of the CBM complex, classified as human inborn errors of immunity, also have severe consequences, and are associated with a variety of primary immunodeficiency diseases (137). Besides pure loss of function, an increasing number of germline point mutations in *CARD11* are associated with CARD11 gain of function (GOF), resulting in B cell expansion with NF-κB and T cell anergy (BENTA) disease, or loss of function (LOF), resulting in CARD11 associated atopy with dominant interference of NF-κB signaling (CADINS) disease.

Patients with heterozygous LOF germline mutations in *CARD11*, classified as CADINS disease, suffer from severe atopic disease and combined immunodeficiency leading to increased susceptibility to infections (138, 139). First, the missense mutations E57D, L194P and R975W

were discovered in affected patients with recurrent pulmonary infections causing respiratory symptoms and viral skin infections as a typical symptom (Figure 1-8) (139). Other patients with missense mutations such as R30W, R47H, R72G, R75Q, L92W, K143X, R187P and R974C presented with multi-organ atopy, autoimmunity and high susceptibility to infections (138, 140). Mechanistically, the mutant CARD11 interferes with functional wild type (WT) CARD11, presumably by disrupting CBM complex formation, and impairs NF-κB signaling (138-141). However, the mutations are distributed across different domains of CARD11, and mechanistic links between pathogenic *CARD11* mutations and the diverse phenotypes beyond NF-κB signaling in different patients remain elusive.

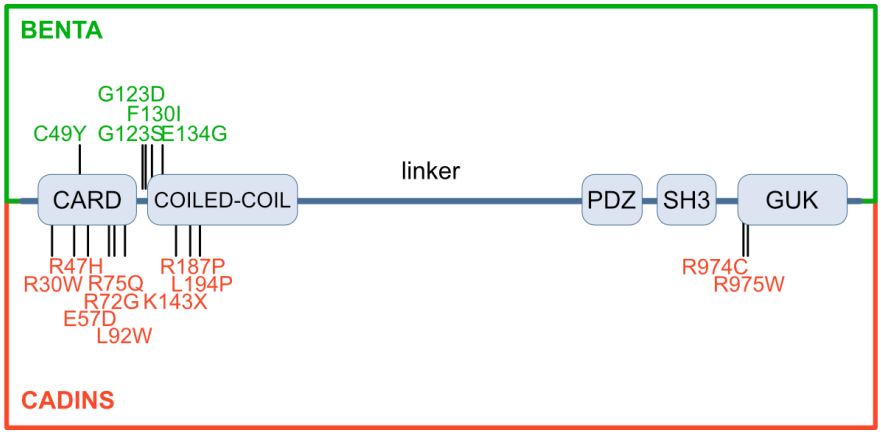

Figure 1-8: Schematic of heterozygous germline mutations in CARD11.
Mutations identified in patients diagnosed with BENTA disease are shown in the upper part (green) and mutations identified in patients diagnosed with CADINS disease are shown in the lower part (red).

In contrast, heterozygous GOF *CARD11* germline mutations cause a lymphoproliferative and immunodeficiency disorder classified as BENTA (142). In the first patients diagnosed with this disease, the missense mutation E134G was found, but more patients with other mutations such as C49Y, G123S, G123D, F130I were later identified (137, 142-144). Patients usually suffer from polyclonal B cell lymphocytosis associated with splenomegaly, lymphadenopathy, and accumulation of immature and naive B cells with poor capacity for humoral immune responses (142, 143, 145). This is associated with primary immunodeficiency leading to frequent sinus and ear infections and in some cases viral infections (142, 144). At the molecular level, CARD11 aggregates in both patient B and T cells, and the mutations appear to disrupt the autoinhibition of CARD11 by inducing constitutive CBM complex formation and consequently spontaneous constitutive activation of NF-κB (142, 146). Upon stimulation, patient T cells

resemble a state of anergy and are hyporesponsive, as reflected by their decreased activation of JNK, ERK, and NF-κB signaling, poor proliferation, and reduced interleukin secretion. Similarly, mouse experiments with constitutively active IKKβ revealed a B cell proliferation and T cell anergy phenotype, suggesting cell type-specific consequences of constitutive NF-κB induction (147, 148). Off note, some of the BENTA-associated germline mutations can also be found as somatic mutations in patients diagnosed with lymphoid malignancies (146). Oncogenic L251P CARD11, used as a positive control in our studies, induces elevated levels of constitutive and stimulated NF-κB activity similar to the BENTA-associated mutant CARD11 and exhibits a high proportion of spontaneously formed CARD11 aggregates (134). Nevertheless, the dichotomy in the functional consequences of spontaneous CBM complex activation in B and T cells cannot yet be explained mechanistically.

1.3 Transcriptional response upon SARS-CoV-2 infection

The human body is constantly challenged by the invasion of pathogens, which are countered by a robust immune system. Viruses are a major group of these pathogens that pose a persistent threat to human health. Our immune system is adept at detecting and neutralizing viral invasions, yet the recently emerged SARS-CoV-2 virus, a member of the human coronavirus family, caused millions of deaths in the recent pandemic (149). A critical aspect of SARS-CoV-2 pathogenicity, which results in severe forms of COVID-19 disease, is its ability to induce an exaggerated and sustained activation of NF-κB transcriptional activity (150, 151). This overactive response culminates in a dysregulated and detrimental immune response.

1.3.1 Human immune response against pathogens

1.3.1.1 The innate immune system

The innate immune system is highly conserved, although limited in specificity, and provides the first and immediate line of defense against pathogens (121, 124). The cellular compartment consists of cells for direct, cell-mediated cytotoxicity, such as natural killer cells, and phagocytes, such as macrophages and dendritic cells.

Phagocytes recognize pathogens with a group of germline-encoded receptors called pattern recognition receptors (PRR) (124, 127, 152). The PRR vary from secreted mannan-binding lectin to cell surface endocytic receptors to signaling pathway inducing receptors, such as toll-like

receptors (TLR), NOD-like receptors or RIG-like receptors, and trigger various immune responses. Their pathogen recognition is based on highly conserved, invariant structures found in most pathogens but not in human cells, summarized as pathogen-associated molecular patterns (PAMPs). Once a phagocyte binds a PAMP, it engulfs the pathogen, called phagocytosis, and digests it in the endosomal-lysosomal system. The pathogen-derived peptides resulting from the digestion are then presented on the surface of the phagocyte to promote the activation of the adaptive immune response (see 1.2.2).

The second major element of innate immunity is the complement system (124). It consists of at least 20 serum glycoproteins that are active in an amplification cascade of protein cleavage and increases the efficiency of pathogen ingestion by phagocytes. Primarily it is activated by antibodies binding to an antigen, but alternatively it can be activated by bacterial or yeast polysaccharides or via the mannan-binding lectin pathway. Either way, all triggers coincide with the activation of the central component C3, additional downstream cascade reactions and lead to the formation of transmembrane pores (membrane attack complex) in the surface of the pathogen, allowing osmotic lysis.

Once an invading pathogen has triggered an immune response, pro-inflammatory signals recruit leukocytes to the site of inflammation through a combination of adhesion molecules and chemokine gradients (124, 153). Adhesion molecules are located on the cell surface and modulate cytoskeletal organization, thus directly driving leukocyte migration. Chemokines are synthesized by innate immune cells and form a chemical gradient with chemotactic function to the site of inflammation to recruit more leukocytes and amplify the initial acute inflammatory response. Chemokines are a subgroup of cytokines and beyond chemoattraction, cytokines act as small messenger proteins in an autocrine, paracrine, or endocrine manner. Binding to their cell surface receptors initiates intracellular signaling and induces diverse effects such as cell activation, division, migration, or apoptosis. Furthermore, specific cytokine compositions ensure the interaction between innate and adaptive immune cells in the lymph node and control the priming of T cell subsets for an immune response appropriate to the type of infection.

1.3.1.2 Immune response to viral infection

Once a virus binds to the host cell surface, it enters the host cell by inducing endocytosis, membrane fusion, or receptor-mediated endocytosis and releases its genomic DNA or RNA into the cytosol (1, 63). There it exploits the host cell machinery, such as ribosomes and polymerases, and employs numerous strategies to alter host cell processes to focus all resources on its reproduction.

The released viral genomic material is a critical PAMP that is recognized by endosomal TLRs, RIG-like RNA sensor proteins, and DNA sensor proteins cGAS, IFI16, and STING (154). Upon binding, the antiviral immune response is initiated and aims to neutralize the infected host cell as well as protect adjacent uninfected cells. As a central element of the antiviral response, IRF transcription factors induce IFN gene expression and IFN type I and type III secretion. Stimulated interferon receptors activate the transcription factors STAT1, STAT2, and IRF9, whose IFN-stimulated gene products initiate an antiviral state, including expression of host cell restriction factors, accumulation of lymphocytes in lymph nodes, increase in cytotoxicity of NK and $CD8^+$ cells, skewing of T cell development toward the T_H1 subset, and upregulation of MHC class I expression (63). In addition, recognition of viral PAMPs activates the transcription factor NF-κB, which drives the expression of pro-inflammatory factors such as *CXCL8*, which is secreted to attract neutrophils, as well as CCL2-5 to bait other immune cells and IL-6 to stimulate acute phase virus clearance (154-157).

Moreover, $CD8^+$ lymphocytes recognize infected cells and induce their apoptosis, activate nucleases and secrete IFN-γ to stimulate phagocytes (63, 154). Virus-induced MHC class I depletion allows NK cells to recognize infected host cells and induce their cell death.

However, there is a complicated interplay between the antiviral immune response and the viral ability to evade the immune system (154). Viruses have a variety of immune escape mechanisms such as antigenic shift, interference with MHC class I antigen presentation, inducing T-cell exhaustion, hindering humoral, interferon and inflammatory responses, and affecting cytokines and apoptotic processes (154, 158, 159).

1.3.1.3 Diseases caused by human coronaviruses

Until 2019, there were six human coronaviruses (HCoVs), assigned to the genus of α-coronaviruses (HCoV-229E, HCoV-NL63) and β-coronaviruses (HCoV-OC43, HCoV-HKU1, MERS-CoV, SARS-CoV-1) (160). All of them probably spilled over from bats and infected humans via an individual intermediate host. While all HCoVs share a general genome organization and life cycle, they differ in detail such as the host receptors used for the virus entry as well as their accessory proteins. While HCoV-NL63 and SARS-CoV-1, bind with its spike protein to the ACE2 receptor of human cells to initiate virus internalization whereas the other HCoVs exploit different cell surface receptors. Generally, HCoVs cause respiratory tract infections of varying severity, but in interplay with comorbidities, weak immune responses and in elderly individuals, severe complications have been reported for all of them (160, 161).

The group of HCoV-NL63, HCoV-229E, HCoV-HKU1 and HCoV-OC43 are spread globally and cause mild or moderate seasonal respiratory infections (160). They have a short incubation time of 2-4 days and make up for 15-30% of common cold cases but usually, the infections are self-limiting. Although in some cases, particular and severe complications are connected to those viruses, they are no thread for the global health.

In contrast, SARS-CoV-1 and MERS-CoV caused epidemic outbreaks, emerging 2002 in China and 2012 in Saudi Arabia, respectively (162, 163). Patients infected with SARS-CoV-1 or MERS have fever and myalgia and show a broad spectrum of respiratory symptoms after an incubation time longer than known from the other human coronaviruses (163, 164). Over the course of infection, this can worsen to a pneumonia, respiratory failure, and acute respiratory distress syndrome (161). In addition, also other organs such as the liver, kidneys, gastrointestinal tract, and the nervous system are affected (160). Patients have markedly elevated levels of cytokines and chemokines that cause a strong inflammatory response in the respiratory tract and consequentially, severe damages in the lung tissue (165, 166). Overall, this leads to more severe cases and high mortality rates of 35% for MERS-CoV and 10% for SARS-CoV-1 infections (164, 167).

1.3.2 SARS-CoV-2 – the newly emerged human coronavirus

In December 2019, a new human infecting coronavirus has been discovered in the region of Wuhan in China. A cluster of patients showed symptoms of a respiratory infection and pneumonia and unbiased sequencing of their clinical samples revealed high sequence identity with a bat SARS-like CoV (168). The authorities designated the virus as SARS-CoV-2 and the caused disease coronavirus disease 19 (COVID-19) (169, 170). Upon rapid spread of the virus, it caused a global pandemic with more than 700 million confirmed cases and over 6.9 million deaths until April 2023 (149).

SARS-CoV-2 belongs to the coronaviridiae family and is classified as β-coronavirus (169). As such, it is the latest member of the coronavirus family that can infect humans (160, 161). Similar to HCoV-NL63 and SARS-CoV-1, SARS-CoV-2 attaches to the ACE2 receptor using its spike protein to infect human cells (171).

1.3.2.1 COVID-19 – the disease caused by SARS-CoV-2

The most common symptoms among COVID-19 patients are very comparable with SARS-CoV-1 and MERS infections, such as dry cough, shortness of breath, fever and fatigue but also additional symptoms occur, such as olfactory and gustatory dysfunctions (160, 161, 172). These symptoms can occur very mildly, presumably asymptomatic, as well as in very severe manifestation. Similarly, as with SARS-CoV-1 and MERS infections, patients further suffer from pathologic conditions in other organs, such as the gastrointestinal tract, liver, kidneys, nervous system, immune system and the cardiovascular system (172, 173). Overall, approximately 5% of COVID-19 patients need intensive care over the course of the disease. An estimation of the COVID-19 mortality is complicated by various impact factors, such as an unknown number of undiagnosed patients, the local protective measures, local availability, and quality of medical care as well as the outbreak stage. In Germany, the case fatality rate (CFR) peaked at approximately 5% but consistently dropped since then and now remains below 0.5%, whereas countries with insufficient medical care still have a CFR of up to 18% until today (174).

During the SARS-CoV-2 pandemic, numerous variants of the ancestral strain have evolved by acquiring point mutations across the viral genome (175). Especially mutations in the spike protein affect central features such as the infectivity, virulence, transmissibility, and immune

escape (176). This is reflected in the general evolution towards higher transmissibility and infectivity as well as more efficient immune escape across variants. In Germany, three different variants consecutively predominated the occurrence of infection (175). In January 2021, the α variant became prominent as it had significantly higher transmissibility as well as virulence compared to the ancestral strain (177, 178). This was followed from the δ variant in June 2021 with another increase of transmissibility, estimated to 60% compared to the α variant, and enhanced replication rate as well as immune escape (179, 180). The ο variant replaced the δ variant in December 2021 and keeps evolving new subvariants since then. It had adapted to a vaccinated population by improved immune escape, transmissibility and multiplication rate (181, 182). However, its virulence dropped and infected patients showed less severe symptoms and inflammatory responses.

1.3.2.2 Pathogenic inflammatory response in severe cases of COVID-19

Besides a majority of COVID-19 patients who recover from the viral infection without intensive medical treatment, some suffer from a more severe disease progression similar as known from SARS-CoV-1 and MERS infections and require hospitalization (160, 172). Comorbidities and risk factors such as high age, obesity, heart conditions, chronic kidney disease, asthma or diabetes significantly increase the risk to develop fatal symptoms, necessitating intensive care (183).

Generally, all organs that are affected by a SARS-CoV-2 infection can also take more severe damage, leading to a variety of complications (172). Besides liver and kidney pathologies, many hospitalized patients suffer from lymphopenia (173, 184). However, the major complication among hospitalized COVID-19 patients is pneumonia and acute respiratory distress syndrome. These can result in severe tissue damage in the lung and can progress to sepsis and acute respiratory failure (173) (185, 186).

Analysis of the immune response in patients with severe forms of COVID-19 revealed that SARS-CoV-2 affects both major aspects of the antiviral immune response (150, 151). On the one hand, the interferon response is significantly reduced, while on the other hand, the inflammatory cytokine response is significantly increased. This leads to another complication characteristic of severe cases of COVID-19, which is excessive levels of a variety of cytokines and chemokines such as TNF-α, IL-1β, IL-6, IL-8, IL-10 and IL-16 in the blood and

bronchoalveolar lavage fluid (BALF) of patients (150, 151, 184, 187-190). This disproportionate release leads to a dysregulated systemic hyperinflammation, classified as cytokine storm syndrome (185, 186, 191). Ultimately, the hypercytokinemia is accompanied by whole-body tissue damage, multiorgan failure and a driving cause for fatale outcome. A detailed analysis of patients' blood from COVID-19 patients with graded disease severity uncovered a direct correlation between the disease severity and the degree of inflammatory pathway induction and hypercytokinemia (150). Further, the magnitude of increase in cytokines is directly proportional to the patients´ viral load in the nasopharynges, BALF as well as in the blood (150, 187, 190). As result, elevated inflammatory markers are suggested as prognostic factors for severe disease progression (191, 192).

A central regulator of immune responses and inflammation is the transcription factor NF-κB (14). Correlating genes up-regulated in COVID-19 patients' blood with their disease severity grade revealed a gradual upregulation of the NF-κB pathway with increasing severity (150). Metatranscriptomic analyses of BALF samples confirmed the induction of NF-κB signaling and downstream chemokine signaling (190). Also, proteomic analyses of patient lung tissue displays this correlation, as it reveals a strong upregulation of upstream canonical and non-canonical NF-κB pathway proteins and downstream cytokines and chemokines (193). Finally, also *in vitro* experiments infecting human lung cell lines with SARS-CoV-2 virus reproduce the upregulation of cytokines and chemokines (151, 194, 195). Monitoring the transcriptional changes upon *in vitro* SARS-CoV-2 infections over time highlighted the upregulation of TNF-α signaling via the activation of NF-κB pathways as initial response starting 6 hours post infection already (196).

1.3.2.3 SARS-CoV-2 genome and proteome

Coronaviruses are large, enveloped viruses with a single-stranded, positive sense RNA genome and the basic genomic structure is comparable across all HCoVs (161). The genome has a size of 26-32 kilobases, which is exceptionally large, and is protected by a 5'-terminal cap and a 3'-poly-A tail. The upstream two-thirds of the genome encode ORF1a and ORF1b that encode all non-structural proteins, followed by the genes for the structural proteins spike (S), envelope (E), membrane (M) and nucleocapsid (N) (Figure 1-9). Additionally, this 3'-genomic stretch is

interspersed with ORFs encoding accessory viral proteins, which genomic location and number of genes strongly vary among the human coronaviruses (160, 161).

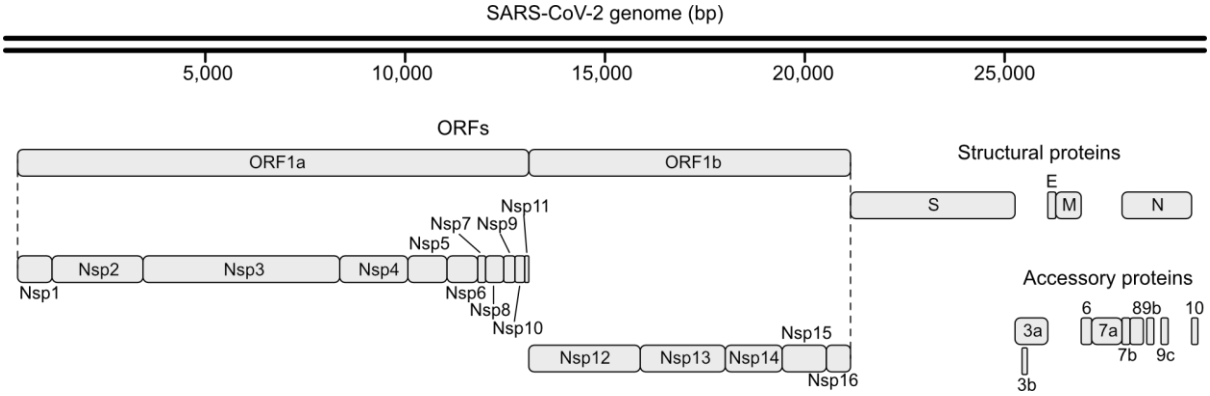

Figure 1-9: Schematic representation of the SARS-CoV-2 genome.
The SARS-CoV genome is approximately 30 kilobases in size. Two thirds of the genome encode ORF1a and ORF1b, which encode non-structural proteins (Nsp) 1-16, in addition to the structural proteins spike (S), envelope (E), membrane (M) and nucleocapsid (N). The 3' genomic region also contains nine ORFs encoding accessory viral proteins.

Interestingly, SARS-CoV-1 and SARS-CoV-2 have seven and eight accessory proteins, respectively, whereas the other HCoVs, that cause more mild diseases (see 1.3.1), have none or one (160). A comparison of the genomic sequences of SARS-CoV-1 and SARS-CoV-2 accessory proteins reveals only moderate sequence identity of 20 – 85%, whereas the non-structural proteins forming the viral replicase-transcriptase complex (RTC) mostly share > 95 % sequence identity (197). Overall, SARS-CoV-2 shares approximately 80 % sequence identity with SARS-CoV-1 (198) and therefore, functional similarities are expected and SARS-CoV-1 research findings are transferred to SARS-CoV-2 regarding essential viral features as the virus life cycle, replication and immune escape.

After entering the host cell, the coronaviral genomic RNA directly serves as mRNA for the synthesis of the viral replicase-transcriptase, which is encoded in ORF1 and ORF1b, upon exploitation of the host ribosomes (161). Both ORF1's are translated by ribosomal frameshifting and the resulting polyproteins pp1a and pp1b are cleaved by the two viral proteases papain-like protease (PLpro, contained in Nsp3) and main protease (Mpro, Nsp5) into the different non-structural proteins (199-201). These subsequently form the viral RTC. In SARS-CoV-2, the viral RNA-dependent RNA polymerase is represented by Nsp12 and binds to Nsp7 and Nsp8, which are the RNA primase (202-204). Together, these are scaffolded by the

membrane-anchored protein Nsp3 as well as attached to two helicases (Nsp13) and the complex of Nsp10, Nsp14 and Nsp16 (205, 206). In this complex, Nsp10 has a scaffolding and activity enhancing function for the mRNA cap methylation complex (207, 208). Nsp14 performs the viral proofreading with its exonuclease domain and forms the cap-0 with its N7-methyl transferase activity (see below) (207). This is further modified to a cap-1 by the 2'O-methylating activity of Nsp16 (209). The entire replication and transcription process take place in the confined space of double-membrane vesicles (DMV) which formation are promoted by Nsp4 and Nsp6 (210). Other non-structural proteins are suggested to have complementary functions, such as interference with the host protein expression through Nsp1 binding to the host ribosomes or contribution to immune evasion from the innate immune defense by Nsp15, as is acts as endoribonuclease and removes the PAMP 5'-polyuridines from the RNA (-) strand (211, 212).

After assembly of the viral RTC, it synthesizes a full-length RNA (-) strand to then, on the one hand, replicate full length RNA (+) strands for new virions and, on the other hand, transcribe sub-genomic mRNAs containing ORF's downstream from ORF1 (197). These sub-genomic RNAs are then utilized for the translation of the structural and accessory proteins. While the nucleocapsid protein N binds to viral genomic RNA and forms nucleoprotein complexes, the other structural proteins M, E and S form new virions in the host ER Golgi intermediate compartment (213-215). The accessory proteins contribute to SARS-CoV-2 replication and pathogenicity in various manners, as for example by promoting the virus release (ORF3a), inducing inflammatory processes (ORF3a) and counteracting IFN-1 signaling (ORF8, ORF9b), whereas the functions of other ORF proteins are still elusive (197, 216-219).

1.3.2.4 SARS-CoV-2 Nsp14

The nonstructural protein Nsp14 is highly conserved across the different human coronavirus species (220, 221). It is a bifunctional protein and can be structurally divided into an N-terminal exonuclease (ExoN) domain, a linker region, and a C-terminal N7-methyltransferase (N7-MTase) domain (Figure 1-10) (208). The exonuclease activity proofreads and excises wrongly inserted nucleotides during replication to ensure the genomic stability and is essential for SARS-CoV-2 replication (207, 221, 222). Crystal structures reveal that the ExoN domain is structurally related to the DEDD superfamily of exonucleases, with additional elements for

binding its cofactor Nsp10 (223, 224). The catalytic center of the ExoN domain is composed of four conserved acidic residues, D90, E92, E191, H268 and D273, and holds two metal ions, presumably Mg^{2+} or Mn^{2+} (207, 208). The binding of Nsp10 causes substantial conformational changes and allows for catalytic activity of the exonuclease. Furthermore, the protein stability of Nsp14 in complex with Nsp10 is strikingly increased (225).

The C-terminal N7-MTase domain catalyzes the methylation of the cap-guanine at position N7 to form the cap-0 structure, which is an intermediate step in the viral RNA capping process (207, 222). The capping of viral RNA contributes to viral survival and replication by protecting the RNA from host cell exonucleases, concealing it from recognition by the host antiviral response and allowing for viral RNA translation by the host machinery. Structural analysis of the MTase domain has revealed a unique fold, that is atypical of the traditional Rossman fold found in other RNA cap-MTase domains (208, 226). The active site brings the pre-capped RNA substrate and the methyl donor *S*-Adenosyl methionine (SAM) to proximity to facilitate a methyl group transfer. Mutational analysis of Nsp14 identified the residues W86, R310, D331, G333 and Y368 as the core SAM binding site and thus critical for MTase activity (207, 227). Binding of S-Adenosyl-homocysteine (SAH), which is the co-product of the MTase reaction, induces a conformational change in an SAM/SAH interacting loop and increases the Nsp14 protein stability, as described for Nsp10 binding the Nsp14 ExoN domain (208, 225). The hinge region connects the two Nsp14 domains and ensures a high level of mobility (228). It consists of a short loop (aa 286-300) between the domains but is complemented by three β-sheets that are inserted in the MTase domain fold (aa 406-430) (208, 228).

Besides these two main enzymatic activities, Nsp14 is also suggested to counteract the interferon response in various manners, promote recombination during replication and modulate host cell splicing(229-233) (234).

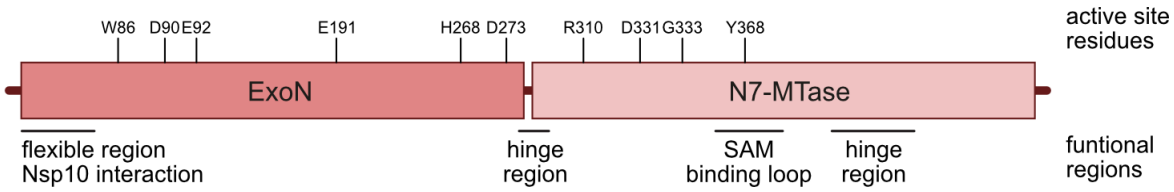

Figure 1-10: Schematic representation of Nsp14.

Nsp14 consists of an N-terminal ExoN domain and a C-terminal N7-MTase domain. Residues of the respective catalytic centers are highlighted, as well as protein regions with additional functions for structure, biological activity, and cofactor interactions.

1.3.2.5 SARS-CoV-2-human contactome maps viral protein-protein interactions with NF-κB signaling pathway

The systematic mapping of viral and human protein-protein interactions is a widespread approach to understand how SARS-CoV-2 is disturbing the human cell homeostasis. Many highly recognized studies used SARS-CoV-2 protein overexpression in Hek293(T) cells followed by AP-MS or Bio-ID coupled with MS to identify virus-host protein interactions (235-238). Others, such as May et al., applied the same Bio-ID and MS strategy in the human lung cell line A549 (239). The study of Stukalov et al. even complemented a virus-host interactome in A549 cells with additional determination of the host cell total proteome, transcriptome, ubiquitome and phosphoproteome after expression of SARS-CoV-2 proteins (240). Nevertheless, both techniques have a bias to display protein interactions in co-complexes, that are stable but may be indirect, and only coincide with each other to a limited extend (241, 242).

To address the discovery of direct, potentially transient, protein-protein interactions, a consortium of scientists performed a large-scale interactome mapping through a yeast two hybrid screen (242). The screen was performed with complementary assay versions and the results were quality-controlled and combined in a SARS-CoV-2-human contactome network. The comparison of the novel contactome with previously published SARS-CoV-2-human protein-protein interactions revealed overlapping results to a certain degree but also numerous so far undiscovered virus-host interactions as well as improved coverage of the individual tissue proteomes. The detailed analysis of the novel identified virus-host protein interactions revealed that targeted host proteins enriched in various pathways. One of these was the broad field of immune response. Specifically, Nsp9, Nsp14 and Nsp16 bound to NF-κB signaling pathways key components, such as TRAF2, IKBKG (NEMO) and REL (c-Rel) (Figure 1-11). Also, Nsp6 was found to interact with different immune receptors.

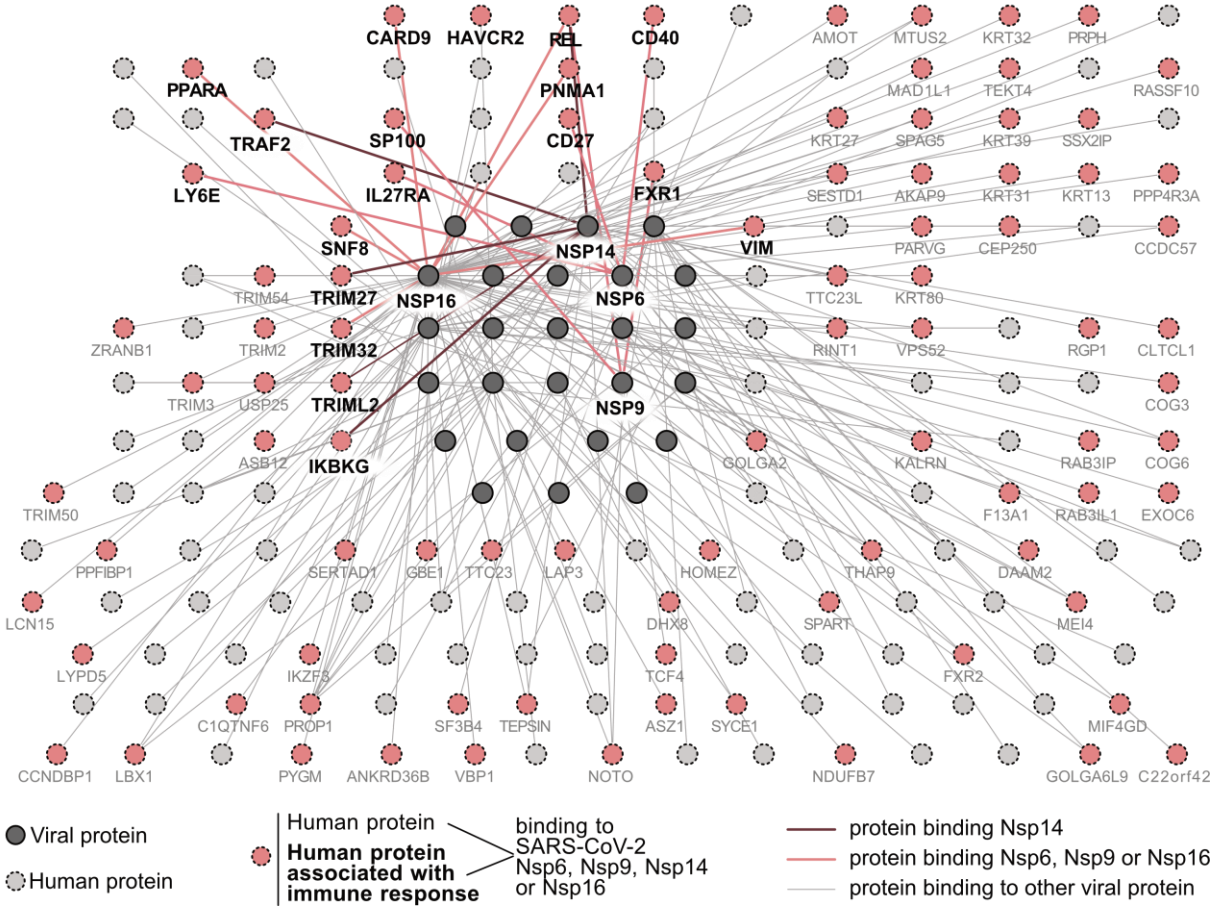

Figure 1-11: SARS-CoV-2 contactome with human interacting proteins.
SARS-CoV-2 human contactome network extracted from large-scale interactome mapping by a yeast two-hybrid screen. Human proteins that bind to viral Nsp6, Nsp9, Nsp14, and Nsp16 are labeled and highlighted in pink. Among these, factors involved in the human immune response, including key components of the NF-κB pathway, as well as viral proteins that bind them, are highlighted in bold. Figure adapted from (242).

2 Aims of the study

The coordinated activity of various transcription factors is critical for the modulation of gene transcription in response to external stimuli. In T lymphocytes, stimulation of the TCR activates a broad signaling network that ultimately converges on the induction of the key transcription factors NF-κB, AP-1, and NF-AT. Together, their activity drives a highly pathogen-specific immune response defined by an individualized composition of target gene expression.

To date, studies have focused on the activity of individual transcription factors without examining their crosstalk with each other. To address this gap, we developed a Jurkat T cell line that allows concurrent quantification of NF-κB, AP-1, and NF-AT activity using specific fluorescent proteins to comprehensively analyze T cell activation signaling relevant to immunological homeostasis. Using this tool, we investigated the impact of CARD11 gain- and loss-of-function mutations associated with immunological diseases on signaling pathways and their crosstalk, with the aim of elucidating the complex relationship between these mutations and the diverse patient symptoms.

Dysregulated NF-κB signaling is a hallmark of COVID-19 pathology, particularly in severe cases with an overactive immune response. Large-scale interactome mapping revealed that SARS-CoV-2 proteins interact with key components of the NF-κB pathway and host immune receptors. On this basis, the second part of the study aims to dissect how SARS-CoV-2 proteins mechanistically modulate host cell NF-κB signaling. We identified the central function of SARS CoV-2 Nsp14 in stimulating NF-κB. Therefore, we tested the role of its functional domains and enzymatic activities by comparing Nsp14 from different human coronaviruses and SARS-CoV-2 variants, and by studying the effects of Nsp14 mutations, cofactors, and pharmacological inhibitors. In addition, we probed the direct interactions between Nsp14 and human proteins implicated in the interactome data using binding assays and gene knock-out cell lines to define the essential human proteins required for Nsp14-mediated activation of NF-κB.

Overall, the goal of this study is to address the knowledge gap regarding transcription factor interactions in immune responses and the molecular mechanisms underlying NF-κB activation by SARS-CoV-2 proteins.

3 Results

3.1 Transcriptional activation in T cells

3.1.1 A novel reporter Jurkat T cell line to study NF-κB, AP1 and NF-AT crosstalk

Activation of T lymphocytes leads to transcriptional activation of the three major transcription factors NF-κB, AP-1 and NF-AT (2, 27, 38). The signaling pathways upstream of each transcription factor, as well as their target gene products, crosstalk with each other (43, 243). Thus, to gain a more comprehensive picture of T lymphocyte signaling and activation processes in homeostasis and pathogenic settings, we generated a Jurkat T cell line that expresses ECFP under the control of NF-κB, mCherry under the control of AP-1 and EGFP under the control of NF-AT. Upon activation of either transcription factor, it binds to the respective response element and initiates the expression of the fluorescent protein, which can be quantified in single cells by flow cytometric analysis.

3.1.1.1 Generation of a fluorescence-based triple transcriptional reporter Jurkat T cell line

For the generation of the triple transcriptional reporter (TTR) system, we obtained pSIRV NF-κB, AP-1 and NF-AT reporter plasmids generated by the Steinberger lab (244). Each reporter construct was amplified by PCR and ligated into our empty lentiviral pHAGE backbone (Figure 3-1).

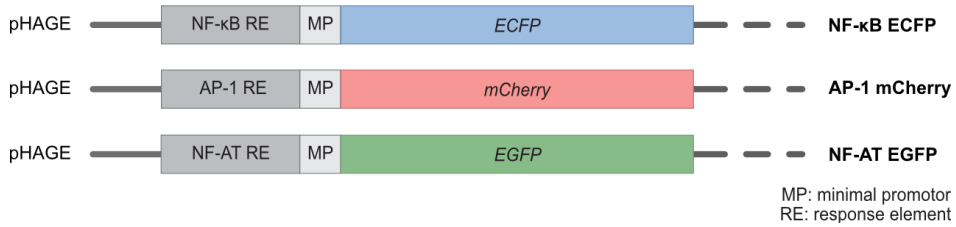

Figure 3-1: Scheme of NF-κB eCFP, AP-1 mCherry and NF-AT eGFP reporter constructs.
All three constructs were amplified from original retroviral pSIRV-constructs and ligated into a lentiviral pHAGE backbone.

We then generated lentiviruses for each reporter construct and performed lentiviral transduction of WT Jurkat T cells (TTR Jurkat T cells). To generate TTR Jurkat T cells with a maximal analytical range, we titrated the three viruses used for the transduction, stimulated the recovered cell lines, and determined the fluorescent signals by flow cytometry (data not

shown). We selected the final TTR WT Jurkat T cell line for minimal fluorescent background in the unstimulated state and maximal fluorescent signal from the largest population fraction upon stimulation (Figure 3-2).

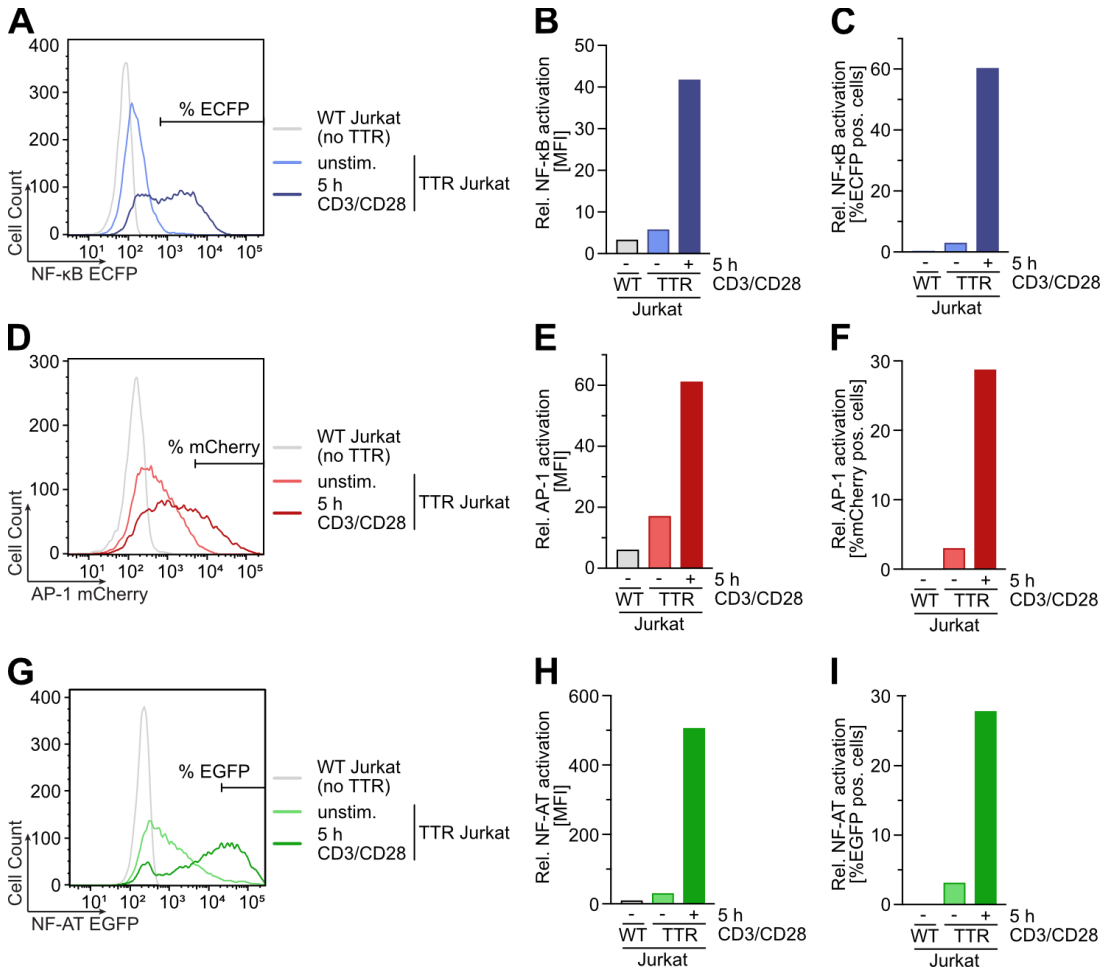

Figure 3-2: TTR Jurkat T cell line stimulated with anti-CD3/CD28.
Activation of (A-C) NF-κB, (D-F) AP-1 and (G-H) NF-AT was determined by flow cytometry of (A-C) ECFP, (D-F) mCherry and (G-I) EGFP positive cells. Cells were stimulated with anti-CD3/CD28 and secondary antibodies (anti-IgG's) for 5 hours prior to measurement. Quantification of stimulated cells was determined as (B) ECFP, (E) mCherry and (H) EGFP mean fluorescence intensity (MFI) and as (C) %ECFP, (F) %mCherry and (I) %EGFP positive cells by gating. The data represent an example experiment.

Flow cytometry measurement of fluorescent reporter cells is a single cell assay and therefore provides insight into the spectrum of transcription factor activation upon stimulation across an entire cell population. This means that small numbers of cells with both low and high levels of transcriptional activity are resolved, rather than going undetected in the averaged readout of a cell pool assay. In general, this assay allows the analysis of two different aspects: On the one hand, it is possible to use a gating strategy that selects for positive fluorescent signals to

quantify the population of cells with activated transcription factor (% fluorescence positive cells) (Figure 3-2B, E, H). On the other hand, fluorescence intensity reflects the level of transcription factor activity and can be quantified by calculating the median fluorescence intensity (MFI) of the populations (Figure 3-2C, F, I).

The AP-1 mCherry reporter was activated in most cells, resulting in a shift with a single peak and enabling the calculation of an MFI representing the intensity of AP-1 activity. In contrast, the NF-κB ECFP and NF-AT EGFP reporters were usually not activated in the entire cell population, but only in fractions, resulting in a flow cytometry shift with two peaks. Therefore, the calculated median of the entire shift does not represent the level of activation in stimulated cells only, but also counts in the unstimulated cells. Therefore, in such cases, the MFI may underestimate the activity level of the transcription factor. Instead, their activation has usually been quantified by determining the percentage of fluorescence-positive cells. The additional display of representative shifts allows the comparison of the activation intensity among fluorescence-positive cells and can be supported by the display of the MFI.

3.1.1.2 Specificity analysis of transcriptional reporters in the TTR Jurkat T cell line

To characterize the specificity of the triple reporter system and how crosstalk is reflected by the three different fluorescent signals, we used different inhibitors targeting the T cell activating pathways at different stages. Dasatinib was the most upstream inhibitor we used, as it inhibits the non-receptor tyrosine kinases of the Src family, including Fyn and Lck, and thus acts directly at the TCR receptor (Figure 3-3). We blocked NF-AT signaling with the calcineurin inhibitor FK506, which resulted in hyperphosphorylated NF-AT being retained inactively in the cytosol. To analyze the impact of NF-κB signaling, we first interfered with PKCθ using the pan-PKC inhibitor sotrastaurin and secondly targeted IKK-β in the IKK complex, which is further downstream in the signaling cascade, with MLN120B. Titrations of all inhibitors and anti-CD3/CD28 stimulation were added to the cells and transcriptional activation was measured after 24 hours.

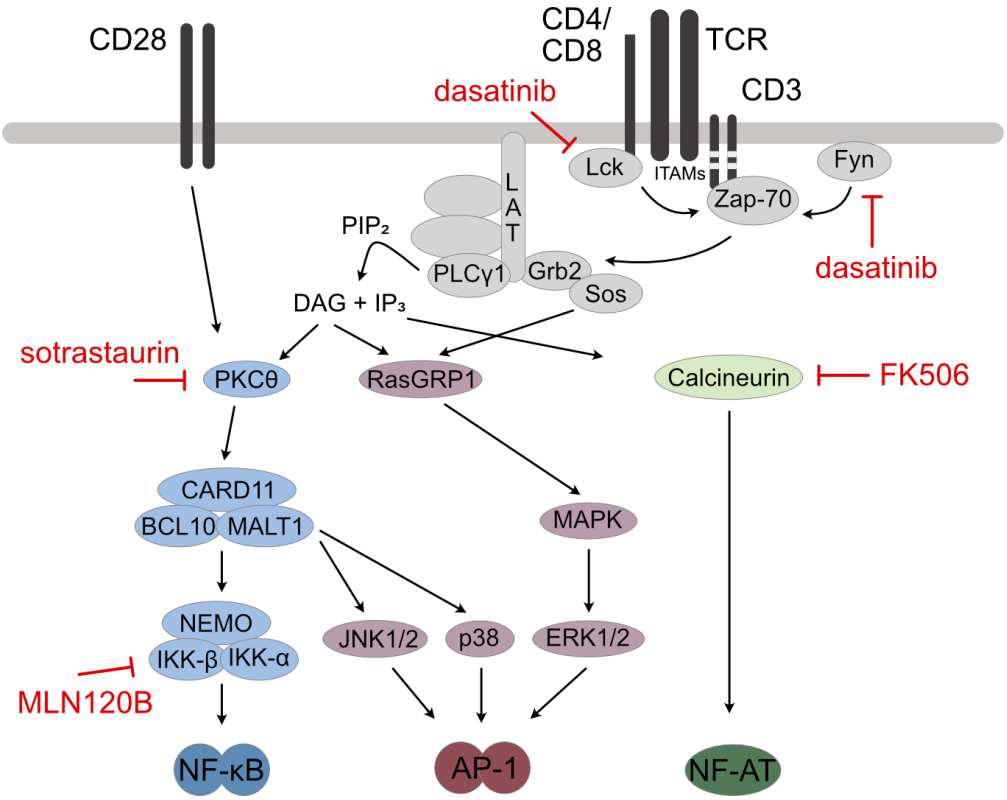

Figure 3-3: T cell signaling with inhibitors used for specificity analysis of the triple reporter system.
Upon antigen binding and TCR stimulation, the protein tyrosine kinases Lck and Fyn, inhibited by dasatinib, phosphorylate the immunoreceptor tyrosine-based activation motifs (ITAMs) within CD3 chains. Zap-70 binds to the phosphorylated CD3, recruiting LAT and a multiprotein complex is formed. Activated PLCγ1 catalyzes the formation of DAG and IP_3. DAG activates the CBM and IKK complexes, which induce NF-κB, via PKCθ. In this cascade, PKCθ is inhibited by sotrastaurin and IKKβ is inhibited by MLN120B. AP-1 is induced via RasGRP1 and the CBM complex, whereas IP_3 stimulates calcium efflux from the ER, thereby activating NF-AT via calcineurin (inhibited by FK506).

The activity of NF-κB (Figure 3-4A) and AP-1 (Figure 3-4B) was significantly reduced by 5.0 nM dasatinib. With increasing dose, their activation was further inhibited and the highest dose of 100 nM almost completely abolished NF-κB and AP-1 activity. NF-AT activation appeared to be even more sensitive to dasatinib, as increasing doses gradually suppressed NF-AT and an almost complete block of NF-AT activity was achieved with already 25 nM dasatinib (Figure 3-4C). Overall, the upstream tyrosine kinase inhibitor dasatinib efficiently inhibited the activation of all three transcription factors.

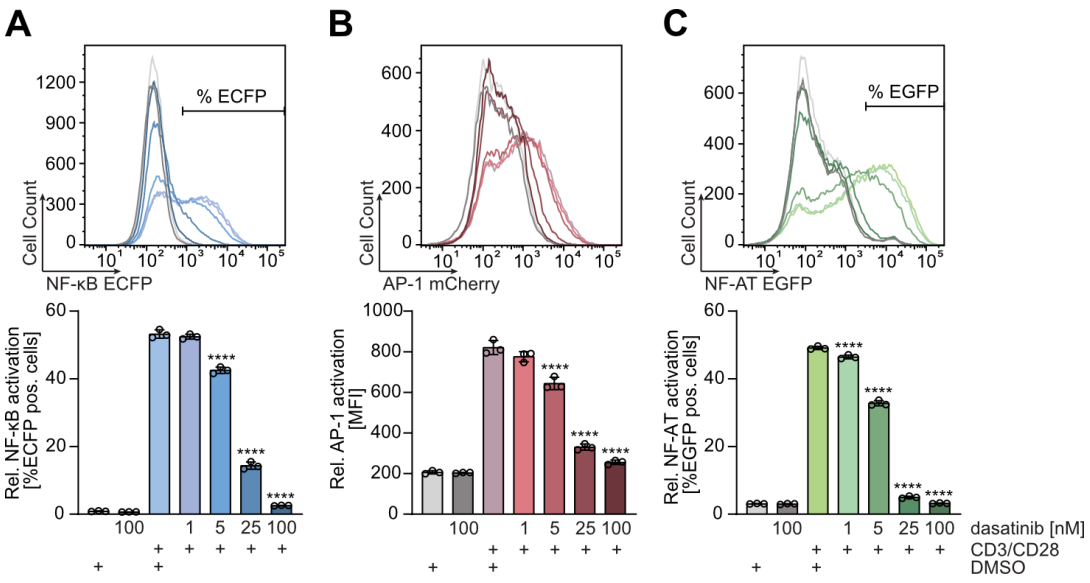

Figure 3-4: TTR Jurkat T cells treated with dasatinib and stimulated with anti-CD3/CD28.
Activation of (A) NF-κB, (B) AP-1 and (C) NF-AT was determined by flow cytometry of (A) ECFP, (B) mCherry and (C) EGFP positive cells. The cells were treated with 1.0 – 100 nM dasatinib for 30 minutes before they were stimulated with anti-CD3/CD28 and secondary antibodies (anti-IgG's) for 24 hours before measurement. The bars show quantification of (A) %ECFP positive cells, (B) mCherry MFI or (C) %EGFP positive cells as mean ± SD with n = 3 and representative shifts. Statistical significance was analyzed using one-way ANOVA followed by Tukey's test for multiple comparisons. Asterisks mark statistical significance compared to stimulated controls without inhibitor. ****P ≤ 0.0001.

Inhibition of NF-AT by FK506 was effective at a dose of 1.0 nM and directly resulted in a >2.5-fold reduction of NF-AT activity (Figure 3-5C). This was further suppressed by 10 nM FK506 to almost the level of unstimulated cells. However, FK506 also affected NF-κB at a dose of 1.0 nM to a significant but mild extent, which was enhanced to 50% interference by 10 nM FK506 (Figure 3-5A). In contrast, AP-1 did not appear to be affected by calcineurin inhibition (Figure 3-5B).

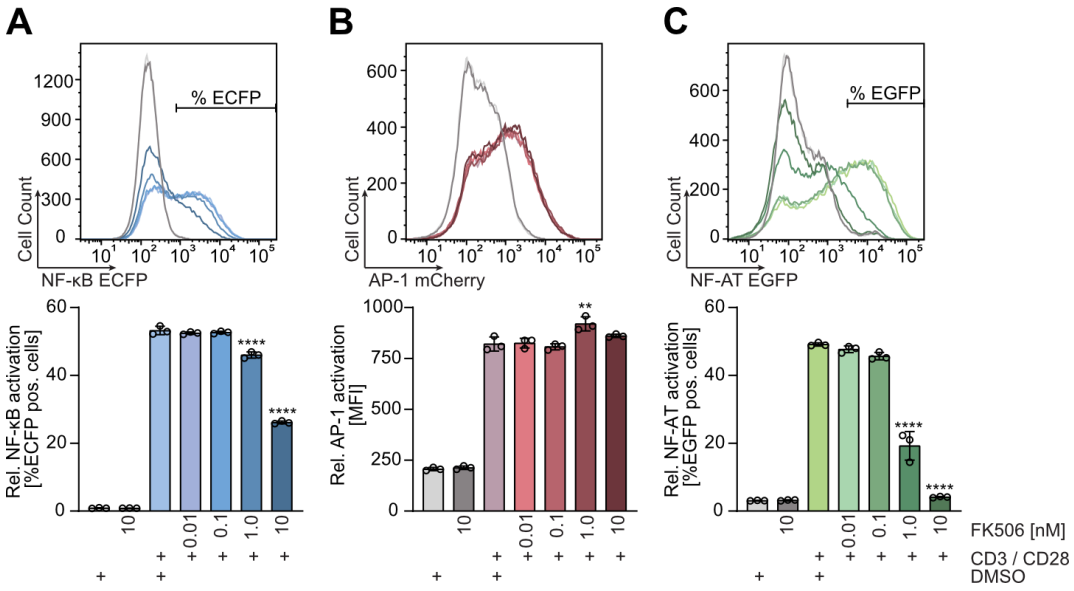

Figure 3-5: TTR Jurkat T cells treated with FK506 and stimulated with anti-CD3/CD28.
Activation of (A) NF-κB, (B) AP-1 and (C) NF-AT was determined by flow cytometry of (A) ECFP, (B) mCherry and (C) EGFP positive cells. The cells were treated with 0.01 - 10 nM FK506 for 30 minutes before they were stimulated with anti-CD3/CD28 and secondary antibodies (anti-IgG's) for 24 hours before measurement. The bars show quantification of (A) %ECFP positive cells, (B) mCherry MFI or (C) %EGFP positive cells as mean ± SD with n = 3 and representative shifts. Statistical significance was analyzed using one-way ANOVA followed by Tukey's test for multiple comparisons. Asterisks mark statistical significance compared to stimulated controls without inhibitor. **P ≤ 0.005, ****P ≤ 0.0001.

Sotrastaurin significantly hindered the NF-κB activity starting with a concentration of 10 nM, which was potentiated in dose escalation (Figure 3-6A). While 100 nM induced a 5-fold loss of NF-κB activity, 1000 nM Sotrastaurin completely inhibited the transcription factor. The activation of AP-1 mirrored the loss of NF-κB activity with increasing doses, but less pronounced. The AP-1 activity was significantly prevented by 100 nM and even more by 1000 nM Sotrastaurin, but there was still residual AP-1 signaling at the highest dose (Figure 3-6B). Similarly, low doses of Sotrastaurin had no remarkable effect on NF-AT signaling, whereas the highest dose of Sotrastaurin inhibited NF-AT by approximately 45% (Figure 3-6C). Taken together, inhibition of PKCθ mainly affected NF-κB and AP-1 signaling, whereas NF-AT was more independent of PKCθ activity.

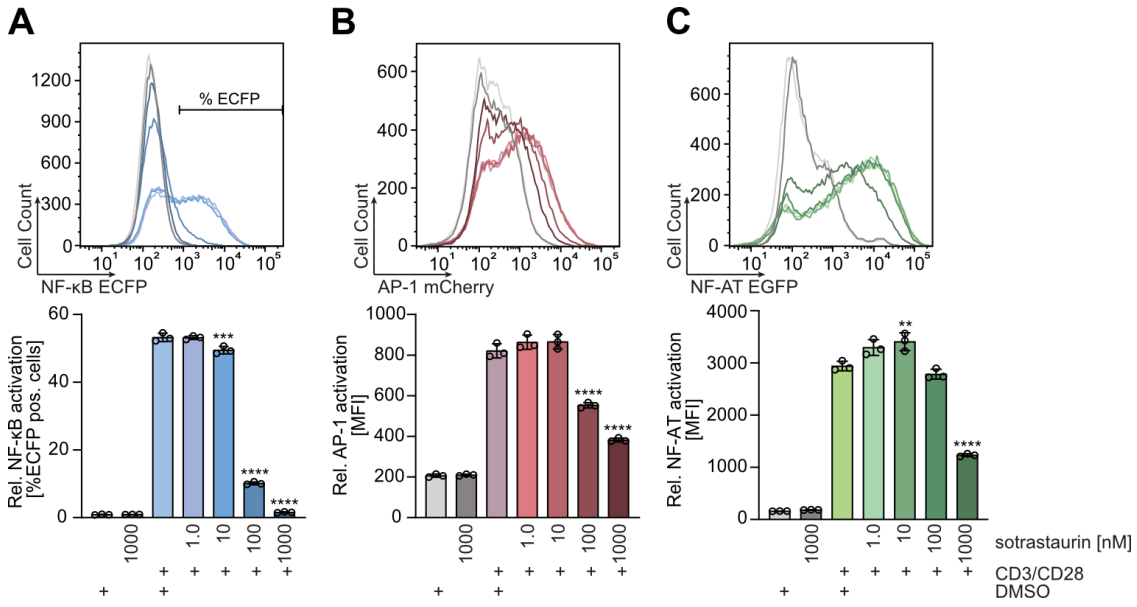

Figure 3-6: TTR Jurkat T cells treated with sotrastaurin and stimulated with anti-CD3/CD28.
Activation of (A) NF-κB, (B) AP-1 and (C) NF-AT was determined by flow cytometry of (A) ECFP, (B) mCherry and (C) EGFP positive cells. The cells were treated with 1.0 – 1000 nM sotrastaurin for 30 minutes before they were stimulated with anti-CD3/CD28 and secondary antibodies (anti-IgG's) for 24 hours before measurement. The bars show quantification of (A) %ECFP positive cells, (B) mCherry MFI or (C) EGFP MFI as mean ± SD with n = 3 and representative shifts. Statistical significance was analyzed using one-way ANOVA followed by Tukey's test for multiple comparisons. Asterisks mark statistical significance compared to stimulated controls without inhibitor. **P ≤ 0.005, ***P ≤ 0.001, ****P ≤ 0.0001.

The transcriptional activity of NF-κB was signaling gradually decreased with an increasing dose of MLN120B. While the effect with 1.0 nM MLN120B was significant but still weak, there was a >2-fold decline in NF-κB activity after treatment with the highest dose of 50 nM MLN120B (Figure 3-7A). Accordingly, the activation of AP-1 showed a comparable trend and was weakly inhibited by the highest dose of MLN120B (Figure 3-7B). The quantification of cells displaying NF-AT activity suggested no inhibition of NF-AT activation by MLN120B (Figure 3-7C). As a side note, the shifts of all samples treated with 50 nM MLN120B showed generally lower cell counts in all channels, suggesting fewer live cells in the gate and thus some toxicity of high doses of MLN120B. Overall, the effect of IKK-β inhibition was mainly limited to NF-κB signaling with AP-1 again reflecting NF-κB activity, whereas the activity of NF-AT was not affected.

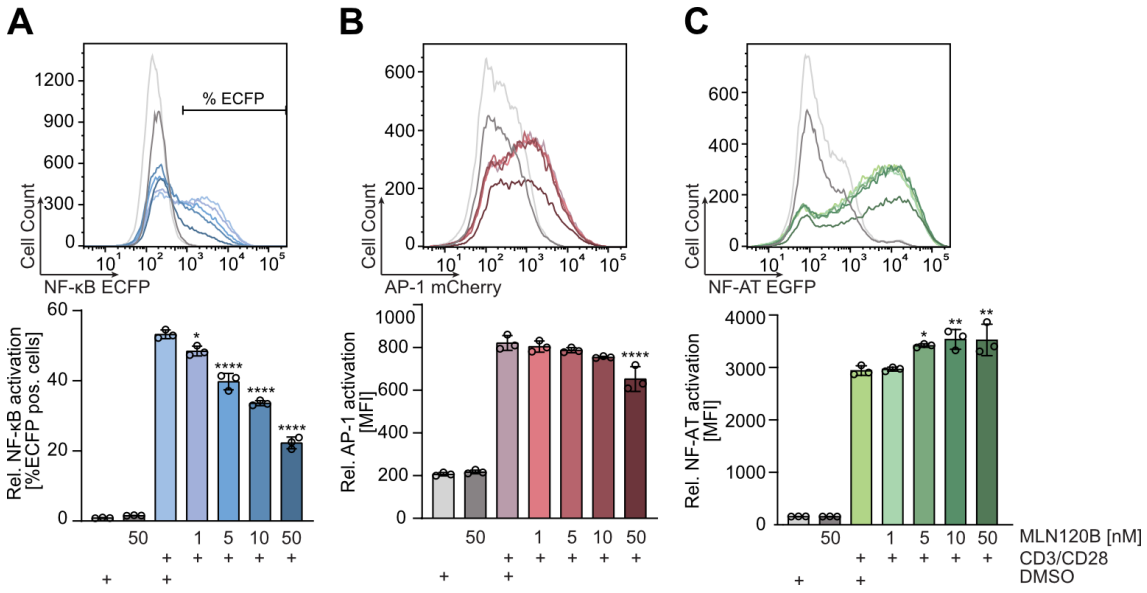

Figure 3-7: TTR Jurkat T cells treated with MLN120B and stimulated with anti-CD3/CD28.
Activation of (A) NF-κB, (B) AP-1 and (C) NF-AT was determined by flow cytometry of (A) ECFP, (B) mCherry and (C) EGFP positive cells. The cells were treated with 1.0 - 50 nM MLN120B for 30 minutes before they were stimulated with anti-CD3/CD28 and secondary antibodies (anti-IgG's) for 24 hours before measurement. The bars show quantification of (A) %ECFP positive cells, (B) mCherry MFI or (C) EGFP MFI as mean ± SD with n = 3 and representative shifts. Statistical significance was analyzed using one-way ANOVA followed by Tukey's test for multiple comparisons. Asterisks mark statistical significance compared to stimulated controls without inhibitor. *P ≤ 0.05, **P ≤ 0.005, ****P ≤ 0.0001.

Overall, the TTR Jurkat T cells have been successfully established as a new versatile tool for the quantification of transcriptional activity and crosstalk upon T cell stimulation. The fluorescence signals are specific for the activity of each transcription factor and accurately reflect inhibition of both upstream and downstream signaling, signaling crosstalk, and secondary effects.

3.1.1.3 Determination of optimal stimulation conditions in TTR Jurkat T cells

Next, we wanted to characterize the dynamics of transcription factor activation by different signals and over time. Therefore, we used three different stimuli that activate T lymphocytes in different ways and compared the activation levels of each transcription factor after 0, 5 or 24 h stimulation. Stimulation with anti-CD3 and anti-CD28 antibodies (CD3/CD28) most physiologically mimics T cell contact with an APC by stimulating the TCR subunit CD3 and the co-receptor CD28 (Figure 3-8). In contrast, PMA and ionomycin (P/I) act more downstream of TCR/CD28, activating PKCθ (PMA) and Ca^{2+} release from the endoplasmic reticulum (ionomycin). The third stimulus, TNF-α, binds the TNFR1 and activates the IKK complex via TRAF2/5 and TAK1/TAB1 and thus only the transcription factor NF-κB.

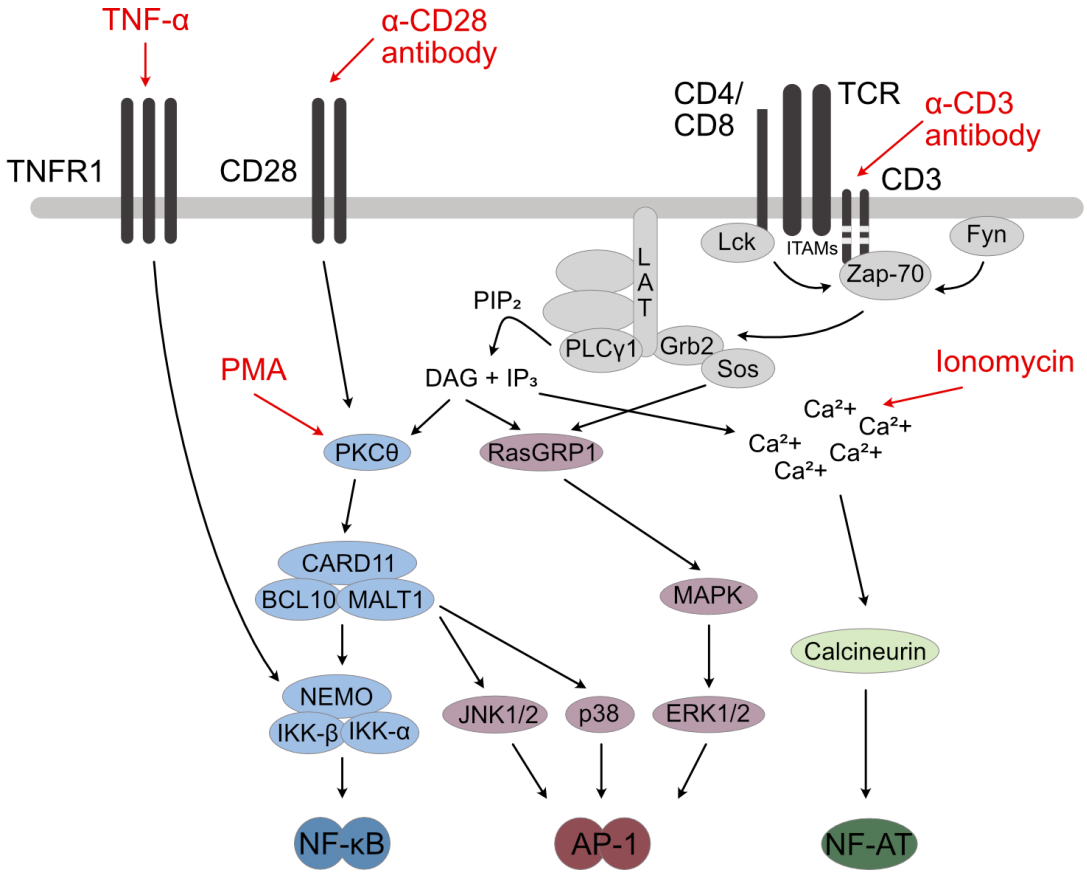

Figure 3-8: T cell signaling with stimuli used to characterize transcription factor activation dynamics.
Upon TCR stimulation with anti-CD3 antibodies, the protein tyrosine kinases Lck and Fyn phosphorylate the ITAMs within CD3 chains. Zap-70 binds to the phosphorylated CD3, recruiting LAT and forming a multiprotein complex. Activated PLCγ1 catalyzes the formation of DAG and IP_3. DAG promotes PKCθ activation, together with anti-CD28 antibody stimulated signaling or PMA stimulation, which induces CBM and IKK complex formation and NF-κB activation. Alternatively, the IKK complex is activated by TNF-α stimulation. In parallel, AP-1 is induced via RasGRP1 and the CBM complex. IP_3 stimulates calcium efflux from the ER as well as ionomycin stimulation, thereby activating NF-AT via calcineurin.

Both stimuli mimicking physiological T cell activation significantly activated NF-κB, resulting in a population with active NF-κB of about 30% by anti-CD3/CD28 and an approximately doubling of the NF-κB activity level by TNF-α after 5 h of treatment (Figure 3-9A). This population increased to approximately 55% ECFP-positive cells with anti-CD3/CD28 and nearly 8-fold with TNF-α after 24 h of stimulation. Conversely, P/I treatment promoted NF-κB activation in most of the population to an activity level that was 30 and 55 times higher after 5 and 24 h stimulation, respectively, compared to basal conditions.

AP-1 activity was significantly induced approximately 2-fold and 5-fold after 5 h of stimulation with anti-CD3/CD28 and P/I, which was strongly enhanced to >4-fold and >20-fold, respectively, after 24 h. In contrast, TNF-α did not activate AP-1 signaling after either 5 or 24 h of stimulation (Figure 3-9B).

Similarly, NF-AT was stimulated to a level of approximately 35% and 23% EGFP-positive cells, respectively, after 5 hours of treatment with both anti-CD3/CD28 and P/I (Figure 3-9C). This increased to >60% EGFP-positive cells for both after 24 h stimulation, whereas there was no induction of NF-AT after TNF-α stimulation.

Overall, 5 h of stimulation with a suitable stimulus is sufficient to induce measurable transcriptional activity, whereas prolonged stimulation over 24 h results in accumulation of fluorescent protein and thus stronger signals. These allow for a wider range of signal quantification and therefore a clearer determination of fine differences.

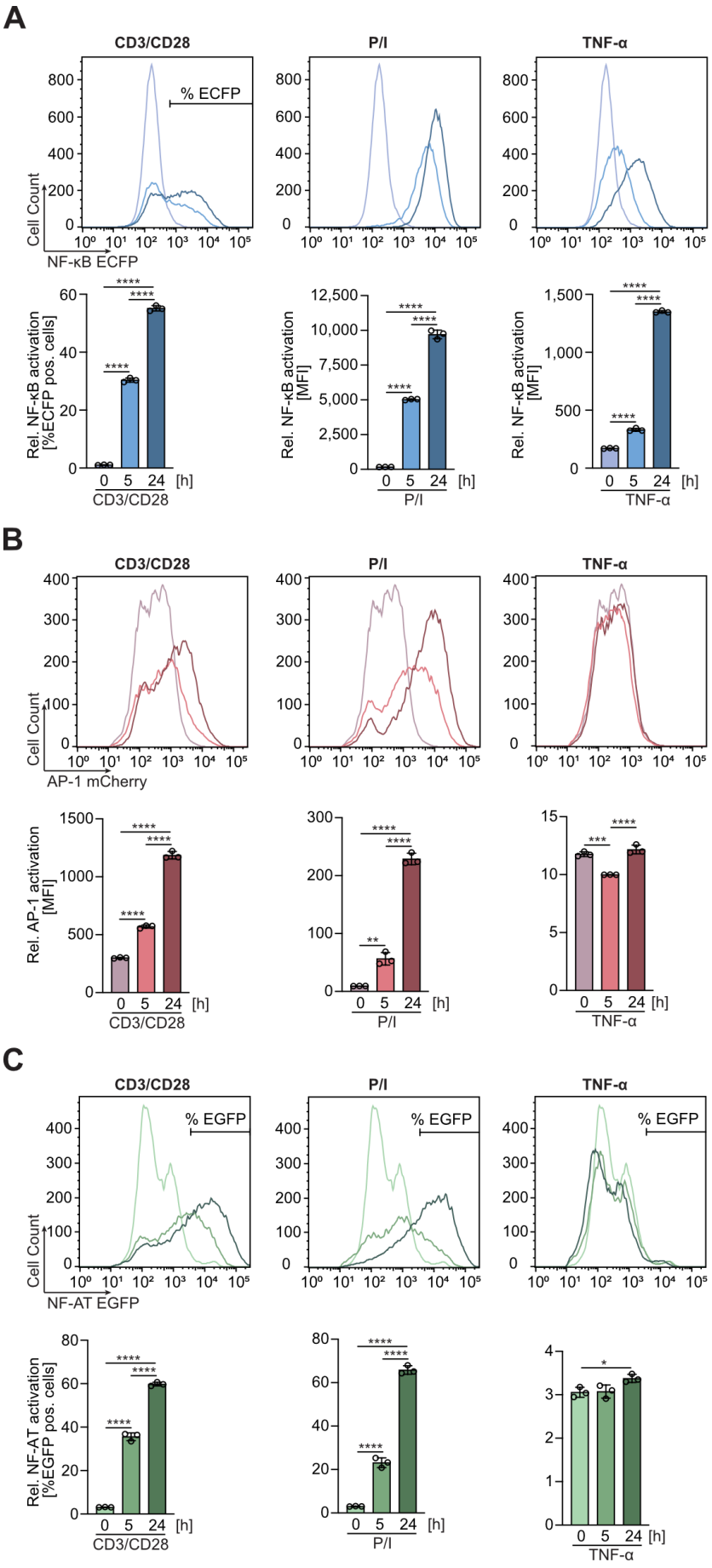
A
CD3/CD28
P/I
TNF-α
% ECFP
Cell Count
NF-κB ECFP
Rel. NF-κB activation [%ECFP pos. cells]
Rel. NF-κB activation [MFI]
0 5 24 [h]
CD3/CD28
P/I
TNF-α
B
AP-1 mCherry
Rel. AP-1 activation [MFI]
C
% EGFP
NF-AT EGFP
Rel. NF-AT activation [%EGFP pos. cells]

Figure 3-9: Anti-CD3/CD28, P/I and TNF-α stimulation of TTR Jurkat T cells for 0, 5 and 24 hours.
Activation of (A) NF-κB, (B) AP-1 and (C) NF-AT was determined by flow cytometry of (A) ECFP, (B) mCherry and (C) EGFP positive cells. The cells were stimulated with anti-CD3/CD28, P/I or TNF-α for 0, 5 and 24 hours before measurement. The bars show quantification of (A) %ECFP positive cells or ECFP MFI, (B) mCherry MFI or (C) %EGFP positive cells as mean ± SD with $n = 3$ and representative shifts. Statistical significance was analyzed using one-way ANOVA followed by Tukey's test for multiple comparisons. *P ≤ 0.05, **P ≤ 0.005, ***P ≤ 0.001, ****P ≤ 0.0001.

In addition to the stimulation dynamics over time, we determined the optimal conditions for the most efficient activation of all three transcription factors. To this end, we tested for the optimal concentration of anti-CD3 and anti-CD28 antibodies, as well as stimulus amplification by the addition of secondary anti-IgG antibodies, that crosslink the anti-CD3 and anti-CD28 antibodies. We first titrated 0 - 1000 ng/ml anti-CD3, either as a single stimulus or in combination with anti-CD28 or anti-CD28 + secondary antibodies, and quantified transcriptional activity by flow cytometry after 5 hours of stimulation.

Analysis of ECFP-positive cells revealed a similar pattern of NF-κB activation at different overall levels across all three anti-CD3 titrations with different supplements, always peaking at 100 ng/ml anti-CD3 (Figure 3-10A). Anti-CD3 alone activated NF-κB in at most 10% of the cells at very low intensity, as reflected by the shifts, but co-stimulation with anti-CD28 at each anti-CD3 concentration significantly enhanced NF-κB activity. NF-κB activation by low concentrations of anti-CD3 and anti-CD28 was further enhanced by supplementation with secondary crosslinking antibodies. The most efficient NF-κB stimulation was achieved with 100 ng/ml anti-CD3 and anti-CD28, inducing NF-κB activity in approximately 35% and 33% of cells without and with secondary crosslinking, respectively. However, the highest dose of 1000 ng/ml anti-CD3 resulted in a decrease of NF-κB activity to approximately 21% and 24% of ECFP-positive cells without and with secondary crosslinking, respectively, compared to stimulation with 100 ng/ml anti-CD3.

In contrast to NF-κB, both AP-1 and NF-AT were less sensitive to a gradual increase in anti-CD3 concentration and were induced in a more switch-like manner. While 1 ng/ml anti-CD3 had no effect, both AP-1 and NF-AT were significantly induced at 100 ng/ml as well as 1000 ng/ml, attaining an mCherry MFI of 309 and 22% NFAT EGFP positive cells, respectively (Figure 3-10B, C). This was only marginally increased by the addition of anti-CD28 or anti-CD28 + secondary antibodies. Stimulation with 10 ng/ml anti-CD3 increased the activation of AP-1

and NF-AT modestly with each additional stimulus, anti-CD28 or secondary crosslinking, but always at low levels.

Overall, AP-1 and NF-AT were efficiently activated by both high doses of anti-CD3, 100 ng/ml and 1000 ng/ml, with minor enhancement by the higher dose. In contrast, NF-κB was significantly most efficiently activated by 100 ng/ml anti-CD3. At this optimal dose of anti-CD3, the addition of cross-linking antibodies did not enhance NF-κB activity, whereas the NF-κB-inducing effects of lower doses of anti-CD3 are enhanced by antibody crosslinking.

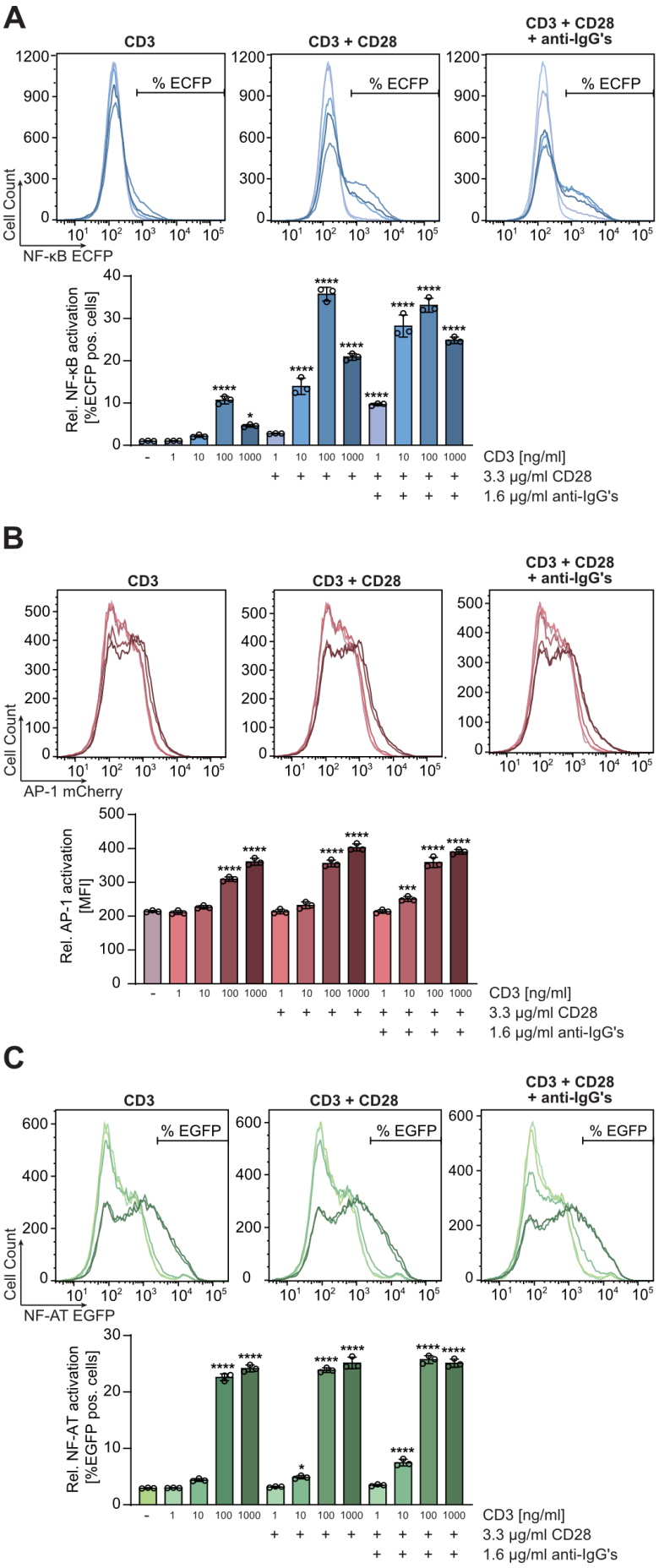
A
CD3
CD3 + CD28
CD3 + CD28 + anti-IgG's
% ECFP
Cell Count
NF-κB ECFP
Rel. NF-κB activation [%ECFP pos. cells]
CD3 [ng/ml]
3.3 µg/ml CD28
1.6 µg/ml anti-IgG's
B
CD3
CD3 + CD28
CD3 + CD28 + anti-IgG's
Cell Count
AP-1 mCherry
Rel. AP-1 activation [MFI]
CD3 [ng/ml]
3.3 µg/ml CD28
1.6 µg/ml anti-IgG's
C
CD3
CD3 + CD28
CD3 + CD28 + anti-IgG's
% EGFP
Cell Count
NF-AT EGFP
Rel. NF-AT activation [%EGFP pos. cells]
CD3 [ng/ml]
3.3 µg/ml CD28
1.6 µg/ml anti-IgG's

Figure 3-10: Titration of anti-CD3 for optimal stimulation of TTR Jurkat T cells.
Activation of (A) NF-κB, (B) AP-1 and (C) NF-AT was determined by flow cytometry of (A) ECFP, (B) mCherry and (C) EGFP positive cells. The cells were stimulated with titrations of anti-CD3, anti-CD3/CD28 or anti-CD3/CD28 + secondary antibodies (anti-IgG's) for 5 hours before measurement. The bars show quantification of (A) %ECFP positive cells, (B) mCherry MFI or (C) %EGFP positive cells as mean ± SD with n = 3 and representative shifts. Asterisks mark statistical significance compared to unstimulated controls. Statistical significance was analyzed using one-way ANOVA followed by Tukey's test for multiple comparisons. *P ≤ 0.05, ***P ≤ 0.001, ****P ≤ 0.0001.

Next, we continued to work with 100 ng/ml anti-CD3 and investigated the optimal dose of anti-CD28 stimulation. Therefore, we stimulated the cells with anti-CD3 and crosslinking antibodies, titrated different doses of anti-CD28 and analyzed the transcriptional activation by flow cytometry. Quantification of ECFP positive cells revealed that anti-CD28 alone already stimulated NF-κB mildly (Figure 3-11A). This was enhanced almost 3-fold by the addition of anti-CD3 stimulation. The reduction of anti-CD28 to 1.0 µg/ml did not affect the level of NF-κB activity, whereas 0.3 µg/ml showed a significant decrease of the stimulatory effect. In contrary, as expected, both AP-1 and NF-AT were, as expected, not activated by anti-CD28 alone but by combinatorial anti-CD3/CD28 stimulation (Figure 3-11B, C). Furthermore, there was no substantial effect of reducing the dose of anti-CD28 on the activation of either transcription factor.

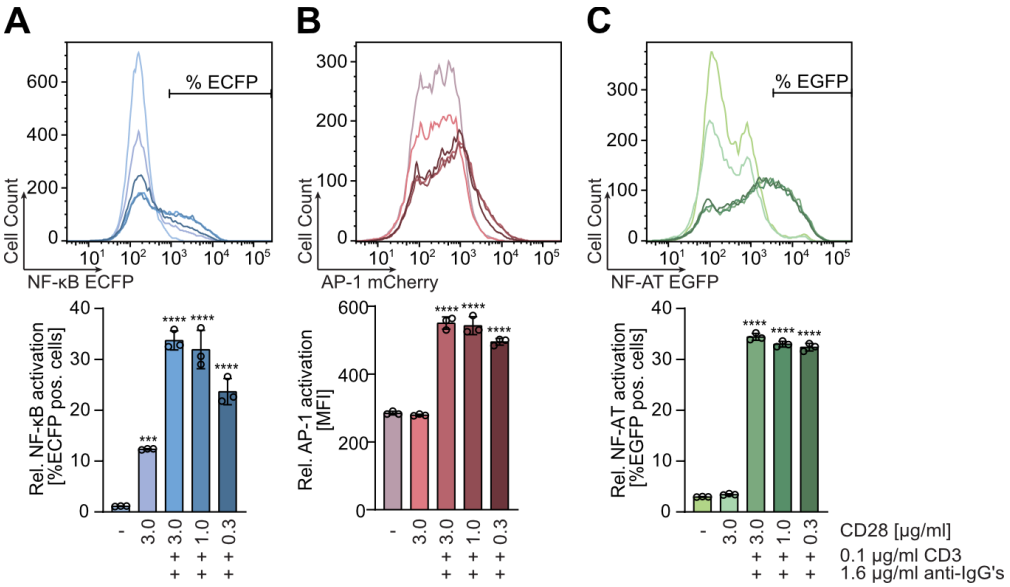

Figure 3-11: Titration of anti-CD28 for optimal stimulation of TTR Jurkat T cells.
Activation of (A) NF-κB, (B) AP-1 and (C) NF-AT was determined by flow cytometry of (A) ECFP, (B) mCherry and (C) EGFP positive cells. The cells were stimulated with titrations of anti-CD28, 0.1 µg/ml anti-CD3 and secondary antibodies (anti-IgG's) for 5 hours before measurement. The bars show quantification of (A) %ECFP positive cells, (B) mCherry MFI or (C) %EGFP positive cells as mean ± SD with n = 3 and representative shifts. Asterisks mark statistical significance compared to unstimulated controls. Statistical significance was analyzed using one-way ANOVA followed by Tukey's test for multiple comparisons. ***P ≤ 0.001, ****P ≤ 0.0001.

Thus, optimal stimulation of all three transcriptional reporters in the TTR Jurkat T cells was achieved with 100 ng/ml anti-CD3 and 1.0 µg/ml anti-CD28. Since this dose efficiently activated all transcription factors without secondary crosslinking antibodies, these were omitted in future experiments using the optimized stimulation conditions and only added for stimulations with lower concentrations of anti-CD3 and anti-CD28.

3.1.2 No transcriptional crosstalk induced by patient-derived CARD11 mutations

As scaffolding protein in the CBM complex, CARD11 has an essential role in the TCR/CD28 stimulated NF-κB signaling pathway (137). *CARD11* mutations, that trigger a loss or gain of the CARD11 function have detrimental consequences for the homeostasis of the immune system. Heterozygous germline mutations that cause a loss of function characterized by dampened activation of NF-κB signaling upon stimulation in patient lymphocytes, are classified as CADINS disease causing *CARD11* mutations. In contrast, another group of heterozygous germline *CARD11* mutations induces the BENTA disease, which is featured by strong B cell proliferation and anergic, hyporesponsive T cells.

The molecular mechanisms, how the respective *CARD11* mutations are leading to the patients' symptoms are still elusive for both, CADINS and BENTA disease. To understand, whether the symptoms are not solely caused by defective NF-κB signaling but also other central signaling pathways, such as AP-1 and NF-AT, we studied the consequences of patient-derived *CARD11* mutations in the TTR Jurkat T cells.

3.1.2.1 Overexpressing mutant CARD11 replicates heterozygous mutations in patients

To study potential transcriptional crosstalk induced by *CARD11* mutations, we selected R30W, E57D, L194P and R975W as examples for CADINS disease and C49Y as well as E134G as examples for BENTA disease. In addition, we compared the BENTA-associated mutations with L251P, which is a well-studied oncogenic *CARD11* mutation, and used it as a positive control. We generated CARD11 constructs with the respective point mutations and used a plasmid containing hΔCD2, a truncated (Δ) version of the gene for the surface marker hCD2, linked to the *CARD11* cDNA by a Thosea asigna virus sequence (T2A). The T2A oligopeptide sequence was first identified in picornaviruses (245). Its in-frame insertion between two protein coding sequences mediates a process called ribosome skipping at the end of the T2A sequence. There,

translation is terminated independently of a stop codon, the newly expressed polypeptide is released from the ribosome while the ribosome skips to the next codon and continues downstream translation. As a result, the two polypeptides separated by the T2A sequence are expressed equimolarly as individual proteins, expressed from a single open reading frame (245-247). Hence, this allows to quantitatively couple the protein expression of CARD11 with the expression of the surface marker protein hΔCD2. In addition, CARD11 was tagged with a strep-strep-flag to distinguish it from endogenous CARD11. To mimic the protein expression in patients with heterozygous mutant *CARD11*, we stably expressed WT and each mutant *CARD11* in TTR Jurkat T cells by lentiviral infection.

We first verified the equal CARD11 expression of the variants by quantifying hΔCD2 expression by flow cytometry. Compared to WT CARD11-expressing cells, all other CARD11-expressing cell lines exhibited the same level of hΔCD2 as shown by the FACS shifts, implying equal expression of all CADINS-associated CARD11 variants (Figure 3-12A). However, CARD11 protein detected by WB revealed different stabilities of the respective CARD11 variants (Figure 3-12B). While WT, R30W, and R975W are expressed at levels comparable to endogenous CARD11, L194P CARD11 appears to be less stable and thus reaches lower protein levels compared to endogenous CARD11. In contrast, E57D CARD11 appears to be more stable than other CARD11 variants.

The hΔCD2 expression coupled to the BENTA-associated CARD11 variants suggested slightly higher expression of E134G and C49Y compared to WT CARD11, while the expression of L251P CARD11 appeared to be at the same level as WT CARD11 (Figure 3-12C). However, protein quantification by WB revealed a significantly decreased protein stability of both the BENTA-associated and the oncogenic mutant CARD11 (Figure 3-12D). Therefore, mutant CARD11 protein levels were also lower compared to endogenous CARD11 levels.

Of note, WB with anti-Strep-tag staining revealed faint bands at the molecular weight of SSF-CARD11 for both parental WT Jurkat cells and mock-infected WT Jurkat cells (Figure 3-12 B and D). These are presumably non-specific bands at the same molecular weight as SSF-CARD11, as there is no corresponding band at the molecular weight of SSF-CARD11 (above endogenous CARD11) in anti-CARD11 staining of the same lysates. Finally, the irregular appearance of this non-specific band can be followed in another set of lysates from

the respective cell lines, prepared and analyzed early after infection, which showed no such band in one set of anti-Strep-tag stained WBs, but a mild non-specific signal in another anti-Strep-tag stained WB with the same lysates used for both experiments (data not shown).

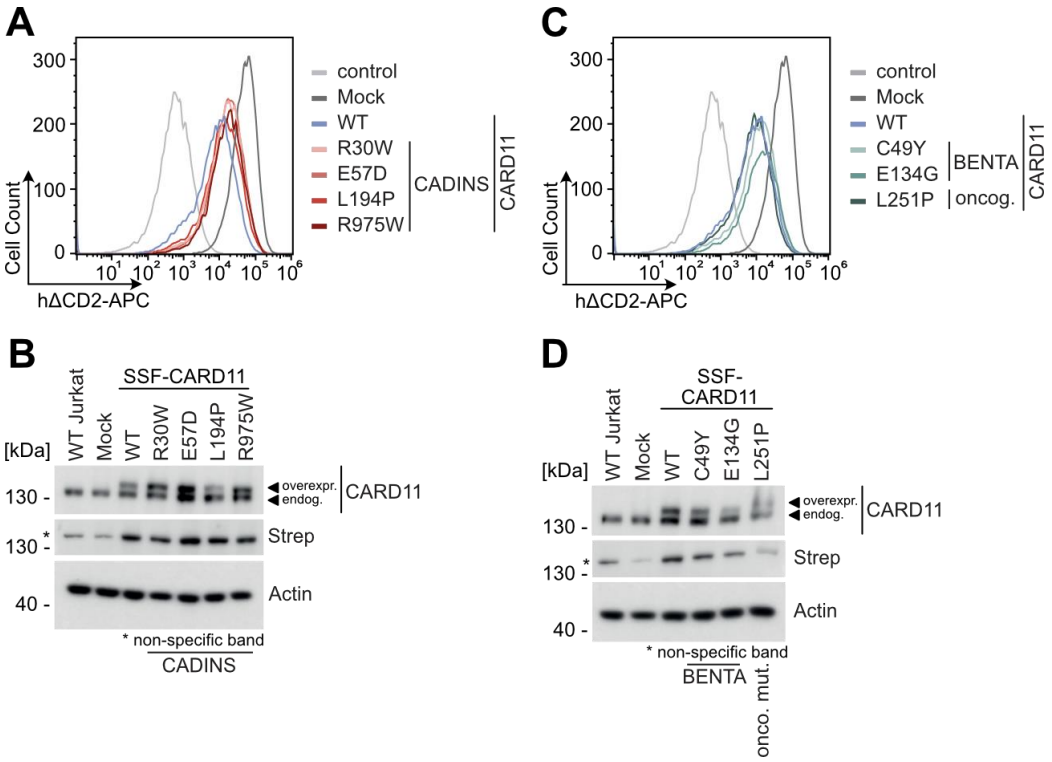

Figure 3-12: TTR Jurkat T cells overexpressing patient-derived CADINS and BENTA *CARD11* mutations.
(A, B) Determination of CARD11 carrying CADINS patient-derived mutations (A) via co-expressed cell surface marker protein hΔCD2 by flow cytometry and (B) via CARD11 protein levels determined by WB. (C, D) Determination of CARD11 carrying BENTA patient-derived mutations (C) via co-expressed cell surface marker protein hΔCD2 by flow cytometry and (D) via CARD11 protein levels determined by WB.

Overall, the lentiviral infections resulted in equivalent *CARD11* gene integrations of all infected constructs, but the inherent increased or decreased stability of some variants led to fluctuations in CARD11 protein levels between the different mutations. However, this is expected to be similar in patients and we have therefore continued our studies with these cell line sets.

Next, we examined the effect of the different patient-derived *CARD11* mutations on NF-κB activation in our TTR Jurkat T cells by flow cytometry. Under untreated conditions, the overexpression of WT *CARD11* mildly enhanced the basal NF-κB activity level, whereas mutated *CARD11* did not. However, the effect occurred in less than 1% ECFP-positive cells and was therefore negligible (Figure 3-13A). In contrast, upon additional T cell stimulation, there was a significant negative regulation of NF-κB signaling by CADINS-associated mutations.

Compared to cells overexpressing WT *CARD11*, the CD3/CD28-induced activity of NF-κB was significantly reduced in approximately 20% of the cell populations expressing R30W, E57D and L194P *CARD11* (Figure 3-13B). Only R975W *CARD11*-expressing cells show CD3/CD28-triggered NF-κB induction, which was only slightly reduced compared to WT *CARD11*-expressing cells. Stimulation with P/I revealed even more pronounced differences among the four CADINS-associated CARD11 variants regarding their effects on NF-κB activity. Similar to anti-CD3/CD28 stimulation, the R975W mutation again had the weakest effect, but reduced the level of NF-κB activity by one third (Figure 3-13C). The other CARD11 mutants again downregulated NF-κB significantly more strongly, also upon P/I stimulation, with an intermediate effect of 2.5-fold reduction by R30W CARD11 and the strongest negative regulation of 5-fold reduction by L194P CARD11.

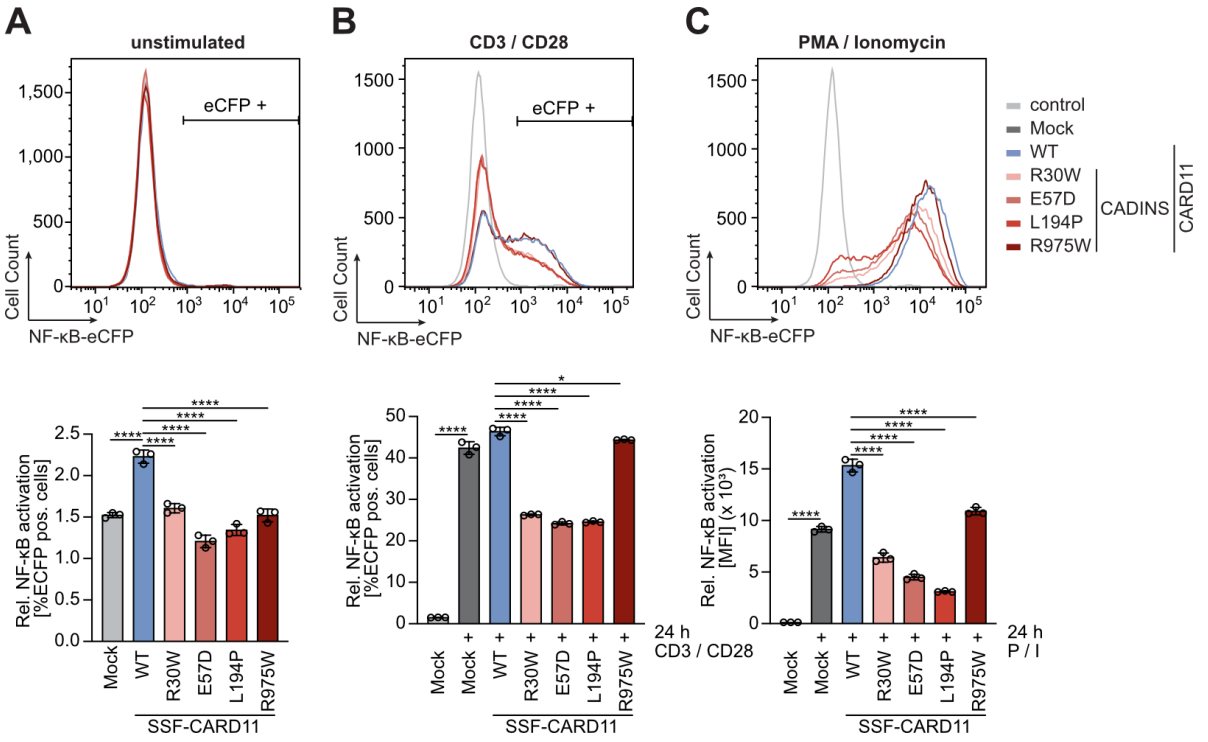

Figure 3-13: NF-κB activity in TTR Jurkat T cells overexpressing patient-derived CADINS *CARD11* mutations. Activation of NF-κB was determined by flow cytometry and the cells were (A) unstimulated or stimulated with (B) anti-CD3/CD28 or (C) P/I for 24 hours before measurement. The bars show quantification of %ECFP positive cells or EGFP MFI as mean ± SD with n = 3 and representative shifts. Statistical significance was analyzed using one-way ANOVA followed by Tukey's test for multiple comparisons. *P ≤ 0.05, ****P ≤ 0.0001.

Flow cytometric analysis of TTR Jurkat T cells overexpressing BENTA-associated and oncogenic CARD11 variants revealed a minor enhancement of basal NF-κB signaling (Figure 3-14A). The strongest effect was a tripling of cells with active NF-κB mediated by C49Y CARD11.

Stimulation with anti-CD3/CD28 or P/I revealed comparable effects of the disease-associated CARD11 variants: while there were no or only minor differences in stimulated NF-κB activity upon overexpression of WT, E134G, or L251P CARD11, *C49Y CARD11* again increased NF-κB signaling in approximately 30% of the cell population upon anti-CD3/CD28 stimulation (Figure 3-14B) and by approximately 45% MFI upon P/I stimulation (Figure 3-14C).

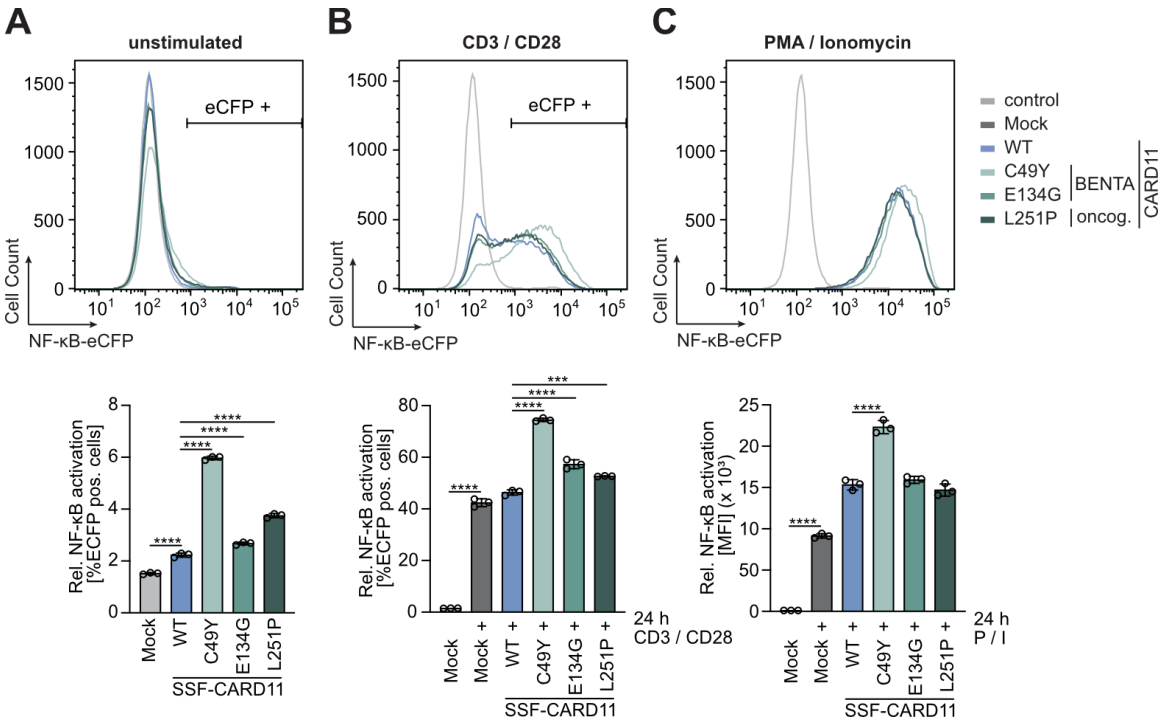

Figure 3-14: NF-κB activity in TTR Jurkat T cells overexpressing patient-derived BENTA *CARD11* mutations. Activation of NF-κB was determined by flow cytometry and the cells were (A) unstimulated or stimulated with (B) anti-CD3/CD28 or (C) P/I for 24 hours before measurement. The bars show quantification of %ECFP positive cells or EGFP MFI as mean ± SD with n = 3 and representative shifts. Statistical significance was analyzed using one-way ANOVA followed by Tukey's test for multiple comparisons. ***P ≤ 0.001, ****P ≤ 0.0001.

In conclusion, expression of CADINS-associated mutant *CARD11* resulted in robust CARD11 protein levels and decreased induction of NF-κB activity upon T cell stimulation. In contrast, BENTA-associated mutant CARD11 was only detectable at low protein levels, and only C49Y CARD11 had a mild enhancing effect on NF-κB signaling upon T cell stimulation.

3.1.2.2 CADINS- and BENTA-associated CARD11 mutations only mildly affect AP-1 and NF-AT activity

To further elucidate whether the disease-associated mutant *CARD11* also induces transcriptional crosstalk and affects the activation of AP-1 or NF-AT, we additionally analyzed their transcriptional activity in the flow cytometry measurements.

As with NF-κB, the CADINS-associated mutant CARD11 did not substantially affect the basal activity of AP-1 (Figure 3-15A). In contrast, CADINS-associated L194P and R975W CARD11 appeared to double the cell population with basal levels of NF-AT activity compared to WT CARD11 expressing cells (Figure 3-15D). Stimulation with anti-CD3/CD28 induced comparable levels of AP-1 (Figure 3-15B) and NF-AT activity (Figure 3-15E) in cells expressing both WT and each mutant CARD11, with only minor variations between the expressed *CARD11* variants. The induction of NF-AT by P/I stimulation also showed no substantial difference between any *CARD11* variants (Figure 3-15F), whereas R30W, E57D and L194P CARD11 inhibited the P/I stimulated transcriptional activity of AP-1 by more than 50% (Figure 3-15C). In contrary, as with NF-κB, R975W *CARD11* had only a weak negative effect on AP-1.

Analysis of AP-1 and NF-AT activity levels in cells overexpressing WT or BENTA-associated *CARD11* revealed no major effect of the disease-associated mutations. Most of the FACS shifts were well superimposed between the different cell lines, and the quantitative analysis also revealed only minor fluctuations for most cell lines and conditions (Figure 3-16A-F). Regarding AP-1 activation upon T-cell stimulation, only C49Y CARD11 very weakly increased the AP-1 transcriptional activity (Figure 3-16B, C). Similarly, C49Y and E134G CARD11 promoted NF-AT activation upon T-cell stimulation in only approximately 7% of the cell population more than WT CARD11 (Figure 3-16E, F). However, basal NF-AT activity was induced in up to 10% more cells upon expression of C49Y, E134G or L251P *CARD11* compared to cells expressing WT *CARD11* (Figure 3-16D).

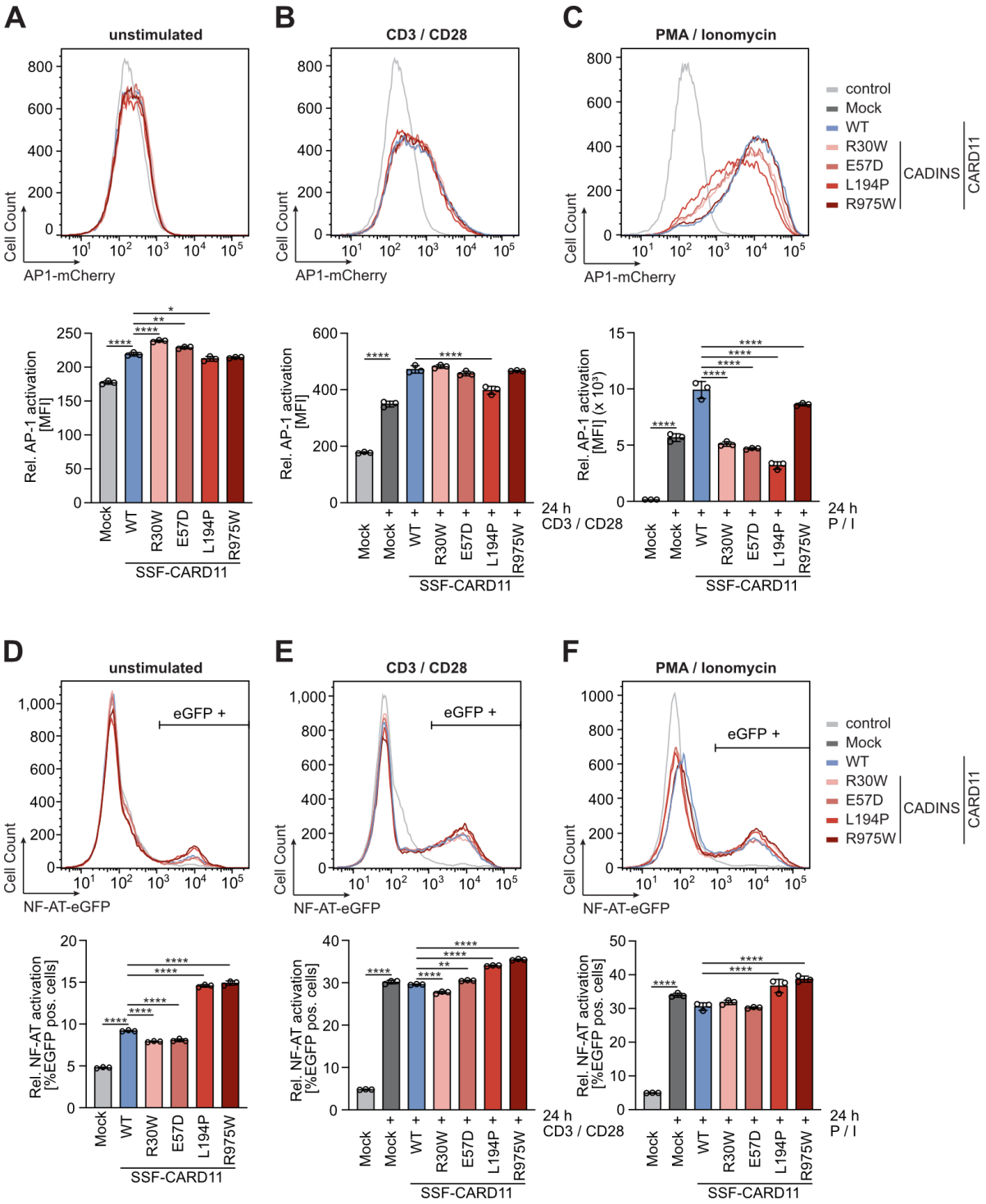

Figure 3-15: AP-1 and NF-AT activity in TTR Jurkat T cells overexpressing patient-derived CADINS *CARD11* mutations.

Activation of (A-C) AP-1 and (D-F) NF-AT was determined by flow cytometry and the cells were (A, D) unstimulated or stimulated with (B, E) anti-CD3/CD28 or (C, F) P/I for 24 hours before measurement. The bars show quantification of mCherry MFI, %EGFP positive cells or EGFP MFI as mean ± SD with n = 3 and representative shifts. Statistical significance was analyzed using one-way ANOVA followed by Tukey's test for multiple comparisons. *P ≤ 0.05, **P ≤ 0.005, ****P ≤ 0.0001.

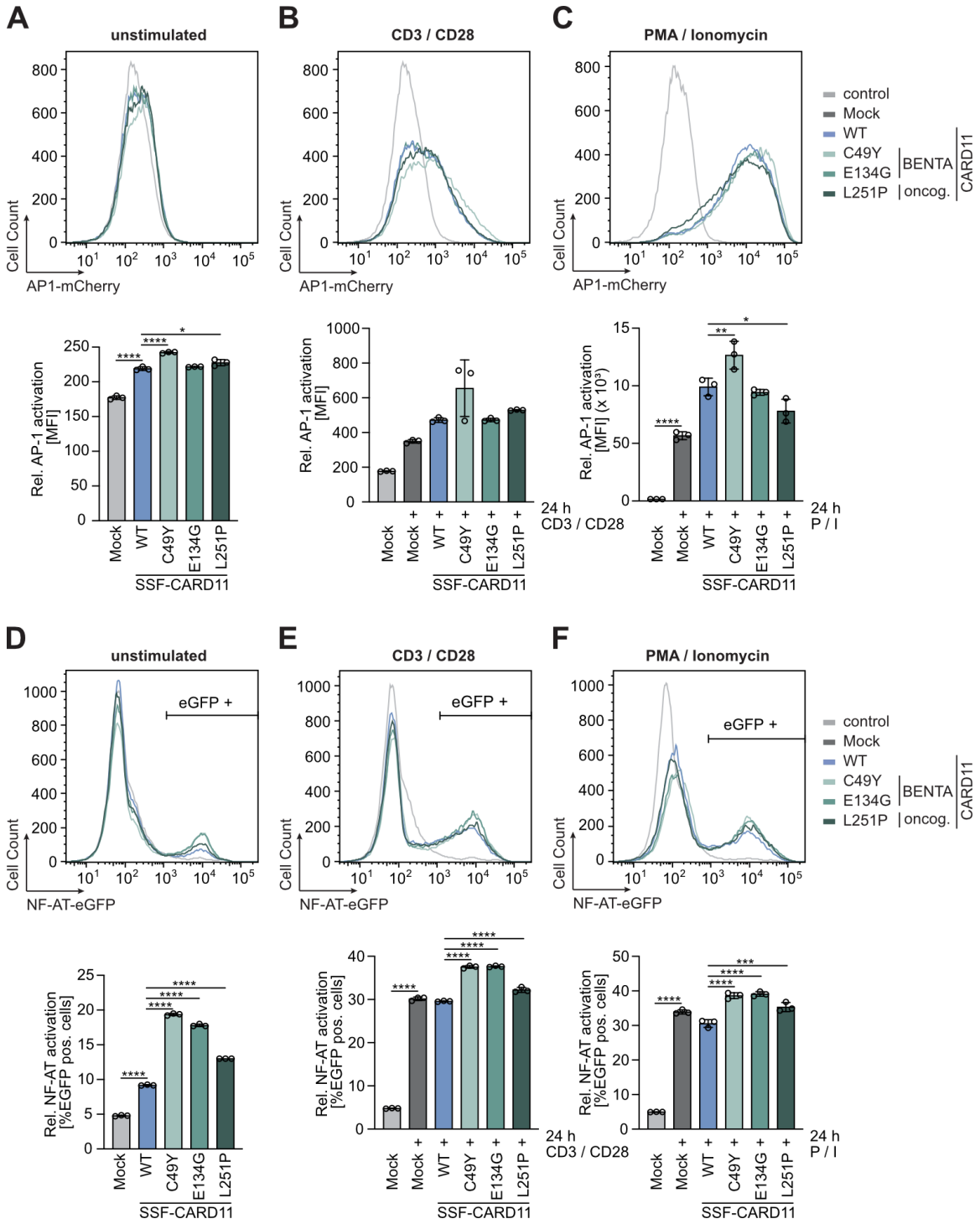

Figure 3-16: AP-1 and NF-AT activity in TTR Jurkat T cells overexpressing patient-derived BENTA *CARD11* mutations.

Activation of (A-C) AP-1 and (D-F) NF-AT was determined by flow cytometry and the cells were (A, D) unstimulated or stimulated with (B, E) anti-CD3/CD28 or (C, F) P/I for 24 hours before measurement. The bars show quantification of mCherry MFI or %EGFP positive cells as mean ± SD with n = 3 and representative shifts. Statistical significance was analyzed using one-way ANOVA followed by Tukey's test for multiple comparisons. *P ≤ 0.05, **P ≤ 0.005, ***P ≤ 0.001, ****P ≤ 0.0001.

Overall, there were only few and mild effects of the disease-associated *CARD11* mutations tested on the transcriptional activity of AP-1 or NF-AT. Upon strong stimulation by P/I treatment of CADINS-associated mutant *CARD11* expressing cells, AP-1 activity was diminished. In contrast, the BENTA-associated C49Y CARD11 mildly enhanced the activation of AP-1 and NF-AT upon stimulation. Besides, both CADINS- and BENTA-associated mutant *CARD11* expressing cells exhibited increased basal NF-AT activity in small proportions of the cell population.

To further analyze the enhanced basal activity of NF-AT upon mutant *CARD11* expression, we used the inhibitor FK506 to counteract this transcriptional activity (data not shown). However, the EGFP-positive cells appeared insensitive towards calcineurin inhibition. Additionally, we sorted the mutant *CARD11* expressing cells for low and high NF-AT transcriptional activity. We studied whether the level of NF-AT activity may affect NF-κB or AP-1 transcriptional activity via signaling crosstalk (data not shown). Also here, we could not identify significant differences, neither in basal conditions nor upon stimulation, between cells with low vs. high basal levels of NF-AT activity.

3.2 Transcriptional activation upon SARS-CoV-2 infection

3.2.1 SARS-CoV-2 Nsp14 activates the transcription factor NF-κB

When SARS-CoV-2 enters the human host cell, its homeostasis is disrupted as SARS-CoV-2 interferes with endogenous processes to ensure its replication whereas the host cell initiates various immune defense mechanisms. To gain insight into how exactly the virus perturbs host cell homeostasis, a systematic mapping of protein-protein interactions between SARS-CoV-2 and human cells was performed (242). The screen revealed 204 direct virus-host interactions with the immune response as a major targeted host cell function. These protein interactions are of particular interest given the detrimental consequences of dysregulated NF-κB activation that has been found in COVID-19 patients as well as upon *in vitro* SARS-CoV-2 infection.

3.2.1.1 Coronaviral Nsp14 is sufficient for NF-κB activation

Among the viral proteins associated with the human immune response, Nsp9, Nsp14 and Nsp16 were proposed to interact with proteins acting in the NF-κB signaling pathway, such as REL, TRAF2 or IKBKG, while Nsp6 was suggested to bind immune receptors, such as CD40 or

IL27RA (see 1.3.2, Figure 1-11). To validate these screening results and to identify the viral proteins that modulate host cell NF-κB activity, we overexpressed the candidate proteins in Hek293 cells and quantified the induced activation of NF-κB using a dual luciferase reporter assay. In addition to the putative effectors Nsp9, Nsp14, Nsp16 and Nsp6, we used the viral proteins E, N and Nsp7 as viral negative controls, since their contactome does not imply an immunoregulatory function, and IKK-β and A20 as human positive and negative controls. Comparing the NF-κB transcriptional activity 24 h after transfection, only IKK-β and Nsp14 significantly induced NF-κB activity (Figure 3-17A). In combination with TNF-α stimulation, only A20, but none of the tested viral proteins, functioned as negative regulator counteracting the NF-κB activity induced by TNF-α stimulation (Figure 3-17B). Instead, Nsp14 even enhanced TNF-α-induced stimulation of NF-κB. WB analysis of protein expression levels in the NF-κB reporter assay samples validated that all constructs were expressed, however protein levels varied widely despite transfection of equal amounts of plasmid (Figure 3-17C). Nsp14, as well as E, Nsp6 and Nsp7, was expressed at comparatively low levels. This implicates high efficiency of Nsp14 in its function as an activator of NF-κB signaling even at low protein levels.

To increase the Nsp14 protein level and to understand whether this affects the level of induced NF-κB activity, we continued with a titration of Nsp14, Nsp16 and Nsp9 (Figure 3-17D). The WB showed increases in protein expression for each construct, again with Nsp14 at lower levels compared to the others. Despites of this, Nsp14-induced NF-κB activation was dose-dependent and significantly enhanced with more Nsp14, while Nsp16 and Nsp9 still had no effect on NF-κB.

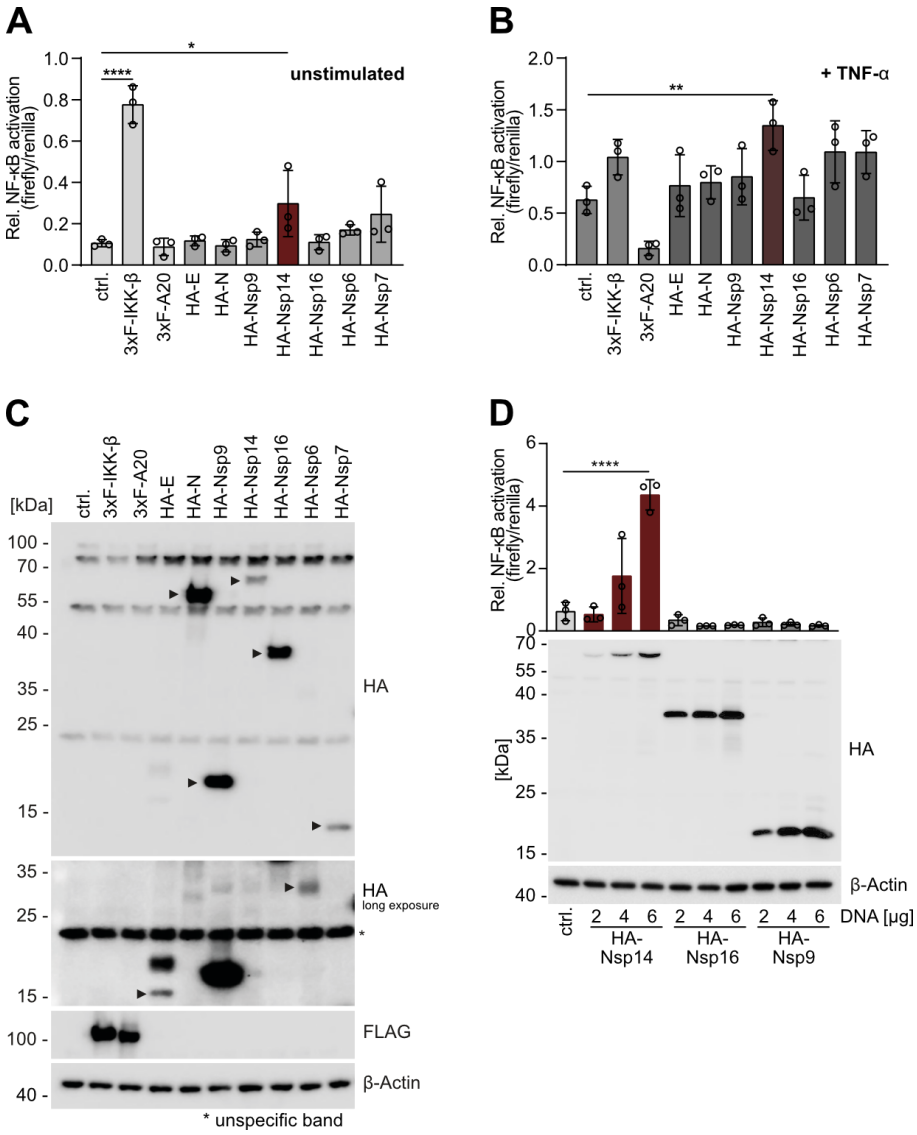

Figure 3-17: Nsp14 overexpression induces NF-κB activity in Hek293.
(A-B) Reporter assay quantifying NF-κB transcriptional activity after OE of IKK-β, A20 and SARS-CoV-2 proteins in (A) unstimulated or (B) TNF-α stimulated condition with (C) representative WB for determination of protein expression levels in Hek293. (D) NF-κB reporter assay in Hek293 after titrated OE of Nsp14, Nsp16 and Nsp9 with representative WB for determination of protein expression levels. Data are the mean ± SD with *n* = 3. Statistical significance was analyzed using one-way ANOVA followed by (A-B) Dunnett's and (D) Tukey's test for multiple comparisons. *P ≤ 0.05, **P ≤ 0.005, ****P ≤ 0.0001.

Over time, new SARS-CoV-2 variants have emerged and Nsp14 has been mutated in the δ and ο variants. To investigate whether these Nsp14 point mutations modulate the induction of NF-κB signaling, we generated the δ-variant Nsp14 with a point mutation in the MTase domain (A394V) and the ο-variant with a point mutation in the ExoN domain (I42V) (Figure 3-18A). Overexpression of WT and variant Nsp14 to equivalent protein levels for all variants revealed the same Nsp14-induced NF-κB activation as quantified by the NF-κB reporter assay (Figure 3-18B).

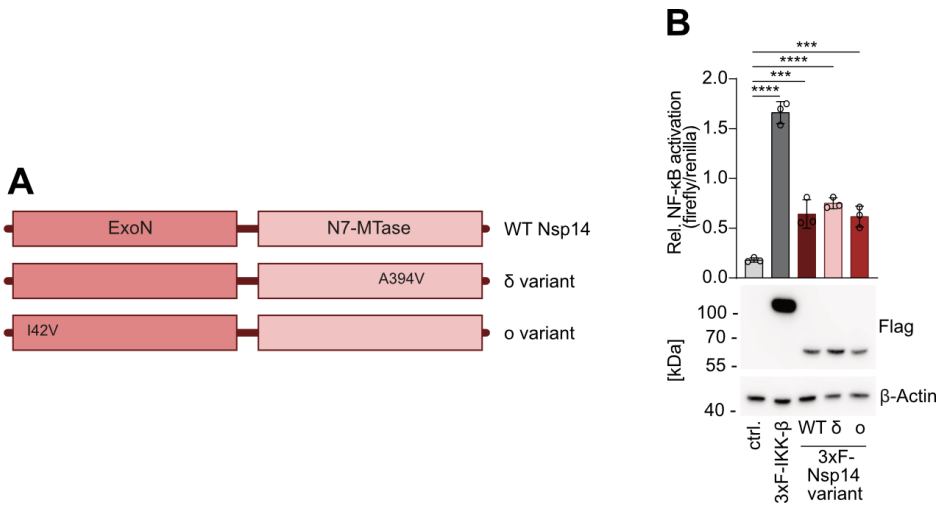

Figure 3-18: Nsp14 from SARS-CoV-2 variants.
(A) Schematic representation of WT, δ and ο variant Nsp14 with point mutations identified in respective SARS-CoV-2 variants. (B) NF-κB reporter assay after WT or variant Nsp14 OE with representative WB for determination of protein expression levels in Hek293. Data are the mean ± SD with *n* = 3. Statistical significance was analyzed using one-way ANOVA followed by Dunnett's test for multiple comparisons. ***P ≤ 0.001, ****P ≤ 0.0001.

Apart from their accessory proteins, human coronaviruses have a conserved genomic structure. Gene alignment analyses have highlighted the conservation of Nsp14 and especially its enzymatic cores across different human coronavirus strains (220, 221). To determine whether the activation of NF-κB signaling by Nsp14 alone is therefore also applicable to other coronaviruses or whether this is characteristic of SARS-CoV-2, we compared the effect of Nsp14 proteins derived from different coronaviruses. We used Nsp14 from MERS-CoV and SARS-CoV-1, which similarly trigger aberrant immune activation upon infection (248), as well as HCoV-OC43, HCoV-229E and HCoV-NL63, which cause mild respiratory symptoms (249), and compared their effect on NF-κB signaling. Most Nsp14 proteins promoted NF-κB activity to varying degrees, whereas HCoV-OC43 had no effect and HCoV-NL63 even decreased the basal transcriptional activity (Figure 3-19A). The WB revealed significant fluctuations in the

protein expression levels of the different Nsp14 proteins. A comparison of the Nsp14 protein levels and the corresponding intensity of NF-κB activation revealed a positive correlation for most coronaviruses. Only SARS-CoV-1 was an outlier and elicited significantly greater NF-κB stimulation compared to all other samples, while its Nsp14 expression was the lowest of all NF-κB-inducing Nsp14 constructs.

The two coronaviruses that did not induce Nsp-14-dependent NF-κB signaling, HCoV-OC43 and HCoV-NL63, typically cause mild symptoms, whereas the Nsp14 of the third coronavirus associated with mild symptoms, HCoV-229E, induced NF-κB activity. We wondered whether this lack of NF-κB induction by HCoV-OC43 and HCoV-NL63 Nsp14 was due to their low Nsp14 protein levels or whether their Nsp14 lacked the NF-κB activating function. Therefore, we titrated HCoV-OC43 and SARS-CoV-2 Nsp14 to increase the expression levels and monitored the transcriptional activation. With SARS-CoV-2, we reproduced our previous finding of a Nsp14 dose-dependent increase in NF-κB activation (Figure 3-19B). In contrast, HCoV-OC43 Nsp14 accumulated only mildly over the titration and did not activate NF-κB even at the highest dose.

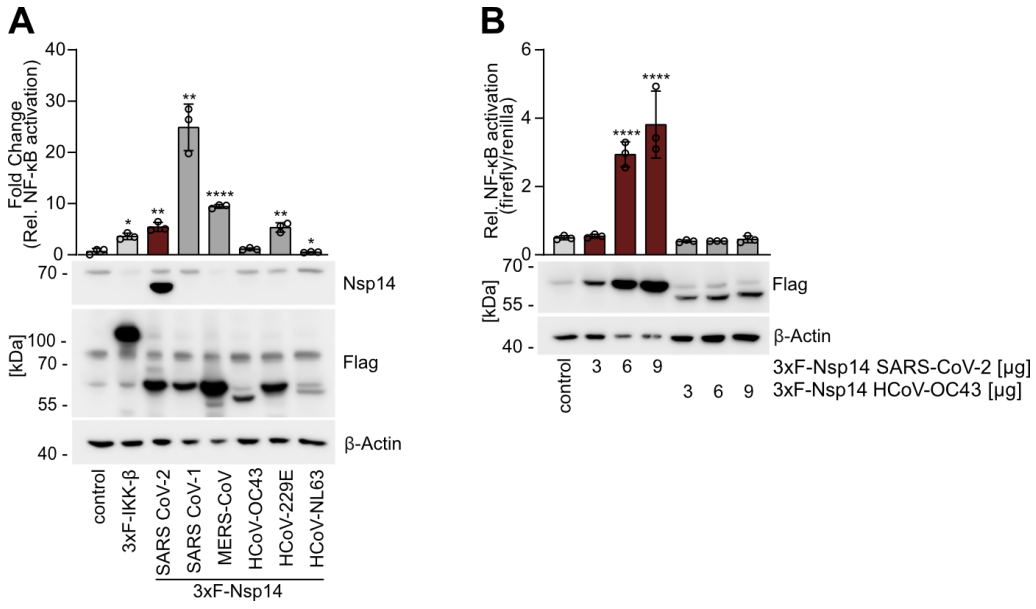

Figure 3-19: Nsp14 from various coronaviruses.
(A) NF-κB reporter assay after Nsp14 OE from various coronaviruses with representative WB for determination of protein expression levels in Hek293. Data are the mean of the fold change relative to the control ± SD with *n* = 3. (B) NF-κB reporter assay in Hek293 after titrated OE of SARS-CoV-2 and HCoV-OC43 Nsp14 with representative WB for determination of protein expression levels. Data are the mean ± SD with *n* = 3. Asterisk mark statistical significance compared to the control sample. Statistical significance was analyzed by A) one-sample t-test after

calculating log2 fold changes normalized to the control sample and B) one-way ANOVA followed by Dunnett's test for multiple comparisons. *P ≤ 0.05, **P ≤ 0.005, ****P ≤ 0.0001.

Taken together, these data suggest that primarily Nsp14 is responsible for the induction of NF-κB activity upon SARS-CoV-2 infection. This function is Nsp14 dose-dependent and not affected by point mutations that occur in SARS-CoV-2 variants. Also, this feature appears to be conserved in most other coronaviruses that infect humans.

3.2.1.2 Nsp14 is stabilized by Nsp10 and S-adenosylmethionine

Comparison of Nsp14 with other SARS-CoV-2 proteins and with Nsp14 from other coronaviruses upon ectopic over-expression of single viral proteins in human cells, consistently indicated markedly low levels of Nsp14 protein. Therefore, we continued to investigate the stabilizing role of its cofactors Nsp10 and SAM.

The SARS-CoV-2 protein Nsp10 is known to form a stable complex with the N-terminal domain of Nsp14, in which the stability of Nsp14 is significantly increased. To examine whether this complex formation also augments the stimulation of NF-κB, we compared the effect of Nsp14 and Nsp10 alone with co-expressed Nsp14 and Nsp10. While Nsp14 was again weakly expressed, it significantly accumulated upon co-expression with Nsp10 (Figure 3-20A). This increase in Nsp14 protein was reflected in enhanced activation of NF-κB. Nsp10 alone did not induce NF-κB, suggesting that the increased transcriptional activation upon co-expression of Nsp10 and Nsp14 is solely due to the stabilization of Nsp14. To identify factors that stabilize Nsp14 and thus allow enhanced activation of NF-κB.

The C-terminal MTase domain of Nsp14 uses SAM as a co-substrate and binding of S-adenosylhomocysteine, which is the product of the MTase reaction, also stabilizes Nsp14. Therefore, we supplemented the media of either IKK-β- or Nsp14-expressing cells with SAM and used TNF-α stimulation as a control. Indeed, SAM significantly stabilized Nsp14 but not IKK-β protein levels (Figure 3-20B). Furthermore, the induced NF-κB activity in Nsp14-expressing cells was significantly boosted by the addition of SAM, whereas the NF-κB activation induced by IKK-β was only slightly enhanced.

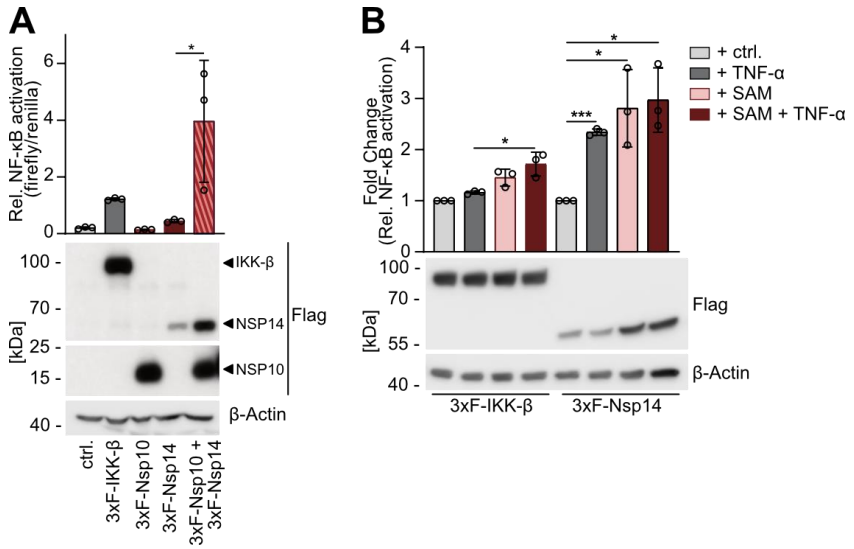

Figure 3-20: Nsp14 is stabilized by Nsp10 and SAM.
(A) NF-κB reporter assay after overexpression of Nsp10, Nsp14 and Nsp10+Nsp14 with representative WB for determination of protein expression levels in Hek293. (B) NF-κB reporter assay after Nsp14 OE combined with SAM supplementation and TNF-α stimulation with representative WB for determination of protein expression levels in Hek293. The OE and 1 mM SAM treatment were incubated for 72 h and 20 ng/ml TNF-α were added for the last 18 h. Values were normalized to untreated condition upon over-expression of each protein (Fold Change). Data are the mean ± SD with n = 3. Statistical significance was analyzed using (A) one-way ANOVA followed by Tukey's test for multiple comparisons and (B) one-sample t-test after calculating log2 fold changes normalized to the control treatment samples. *P ≤ 0.05, ***P ≤ 0.001

Hence, the addition of either cofactor stabilizes Nsp14, which consequently enhances the Nsp14 dose-dependent stimulation of NF-κB.

3.2.1.3 Nsp14 requires functional MTase domain for NF-κB activation

Next, we addressed the question of how Nsp14 mechanistically activates NF-κB. To this end, we generated Nsp14 mutants that were either truncated by a functional domain or lacked catalytic activity due to point mutations in the active site (Figure 3-21A). After overexpression of mutant Nsp14, we analyzed its ability to activate NF-κB using the NF-κB reporter assay.

The truncated forms of Nsp14 lacked either an entire enzymatic domain (ΔExoN and ΔN7-MTase) or the N-terminal stretch (ΔN-Term), which is the binding interface for the cofactor Nsp10 as well as an important structure for N7-MTase activity. The protein expression of the truncated Nsp14 mutants was significantly higher compared to WT Nsp14 as detected by WB (Figure 3-21B). Nevertheless, none of the truncation mutants was able to induce NF-κB activity. By testing Nsp14 mutants with genetically inactivated catalytic centers, we found that D90A E92A Nsp14, which lacks ExoN activity, still stimulated NF-κB signaling as efficiently as WT Nsp14 (Figure 3-21C). In contrast, D331A Nsp14, which lacks N7-MTase function, completely

lost its NF-κB-activating function despite higher expression levels. Combined disruption of both catalytic functions (D90A E92A D331A) had no additional effect compared to D331A Nsp14.

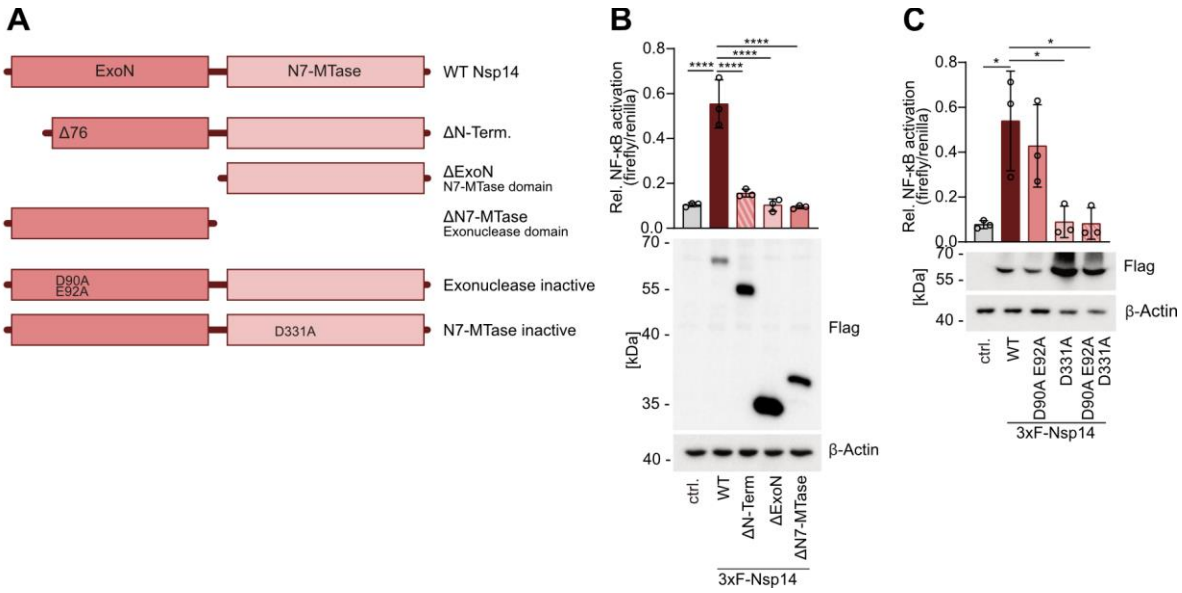

Figure 3-21: Nsp14 truncation and catalytically inactive mutants.
(A) Schematic representation of WT Nsp14 in comparison with truncation mutants and point mutants that lack either enzymatic activity. (B-C) NF-κB reporter assay after OE of (B) Nsp14 truncation mutants and (C) catalytically inactive Nsp14 point mutants with representative WB for determination of protein expression levels in Hek293. Data are the mean ± SD with *n* = 3. Statistical significance was analyzed using one-way ANOVA followed by Tukey's test for multiple comparisons. *P ≤ 0.05, ****P ≤ 0.0001.

To validate that the catalytic function of the methyltransferase causes the induction of NF-κB signaling, we used inhibitors of the MTase domain. Based on screens for specific Nsp14 MTase inhibitors (250-253), we selected two promising compounds: Nitazoxazide is an approved drug with antiviral activity against human coronaviruses (254, 255), which was also used in a clinical trial for the treatment of COVID-19 (NCT04341493). Although it was the most potent inhibitor of Nsp14-mediated RNA methylation based on in vitro experiments, its mode of action is not well understood (256). Its activity against a variety of pathogens is associated with many different proposed mechanisms, complemented by a proposed cap competition in SARS-CoV-2 (256, 257). The second putative inhibitor, pyridostatin, had the most potent and selective antiviral activity in an in vitro screen for Nsp14 MTase inhibitors, although the mode of action is not yet understood (252). It is known to stabilize specific DNA structures and has been suggested to target 5'-end RNA structures in a similar manner (252, 258). The general

methyltransferase inhibitor sinefungin was used as a positive control. Structurally, it is a SAM analog and has been used in the past against viral methyltransferases (259) and also for SARS-CoV-2, sinefungin has been used as an Nsp14 methyltransferase inhibitor in in vitro experiments (250, 252).

After overexpression of Nsp14, the inhibitors were added to the media for 16 h, before NF-κB activity was quantified with the reporter assay. None of the inhibitors attenuated the Nsp14-driven stimulation of NF-κB, but nitazoxanide even induced some mild NF-κB activity in the control (Figure 3-22). The WB also showed equal Nsp14 protein levels and no effect of the inhibitors on Nsp14.

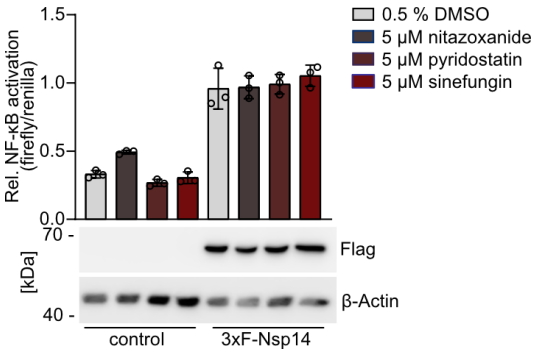

Figure 3-22: Nsp14 treated with MTase inhibitors.
NF-κB reporter assay after Nsp14 OE combined with MTase inhibitor treatment with representative WB for determination of protein expression levels in Hek293. The OE was incubated for 24 h, all inhibitors were added for the last 16 h at a concentration of 5 µM. Data are the mean ± SD with n = 3. Statistical significance was analyzed using two-way ANOVA followed by Tukey's test for multiple comparisons. There was no significant difference when comparing the post-treatment samples to the DMSO control treatment in each set of overexpression.

In all, full-length Nsp14 with the MTase domain intact is required, suggesting that Nsp14 employs its methyltransferase activity to stimulate NF-κB. The fact that none of the MTase inhibitors counteracted Nsp14-induced NF-κB signaling may either indicate a lack of activity in our cell-based assay or that the compounds' modes of action do not interfere with the NF-κB-inducing mechanism.

3.2.2 SARS-CoV-2 Nsp14 is inherently unstable

3.2.2.1 Nsp14 expression is downregulated upon stable integration in HEK293 cells

To further analyze how Nsp14 mechanistically affects NF-κB, we lentivirally transfected Hek293 cells to generate a cell pool in which all cells stably express Nsp14 at equivalent levels. Wegenerated hΔCD2-T2A-Nsp14 constructs to quantitatively couple the protein expression

of CARD11 with the expression of the surface marker protein hΔCD2 using the T2A sequence. Thus, Nsp14 expression levels were determined by WB and hΔCD2 surface expression was quantified by flow cytometry.

After allowing the cells to recover from lentiviral infection for 15 days, Nsp14 protein levels were analyzed by WB. To detect Nsp14 protein, a very high exposure was required, resulting in a strong non-specific band at ca. 50 kDa and a weak non-specific band at ca. 60 kDa. To ensure differentiation of the detected Nsp14 from the non-specific signal at 60 kDa, we confirmed the results with anti-Strep-tag staining (data not shown). The methyltransferase-inactive D331A Nsp14 was stably expressed as evidenced by WB (Figure 3-23A). In contrast, WT Nsp14 protein levels were significantly lower and barely detectable. This expression pattern of WT and D331A Nsp14 was reproduced in cells infected with both lower and higher virus concentrations (data not shown). Following culturing of the cells for an additional 15 days, D331A Nsp14 protein was significantly reduced to the detection limit, whereas WT Nsp14 was undetectable by WB.

In contrast to Nsp14 quantification by WB, hΔCD2 surface expression 15 days post infection indicated equivalent transcription and translation of both transduced constructs (Figure 3-23B-C). The diminished protein expression determined by WB 30 days post infection was similarly reflected in hΔCD2 surface expression: While the hΔCD2 shift of WT Nsp14 expressing cells was significantly attenuated, D331A Nsp14 expressing cells still showed a greater shift than WT Nsp14 expressing cells, but also significantly reduced compared to the control (Figure 3-23D-E).

This suggests that the stable expression of Nsp14 is first downregulated at the protein level and then at the level of Nsp14 gene expression. In this process, both WT and mutant Nsp14 are inhibited, with a significant emphasis on reducing MTase active rather than inactive Nsp14 (see section 4.2.2).

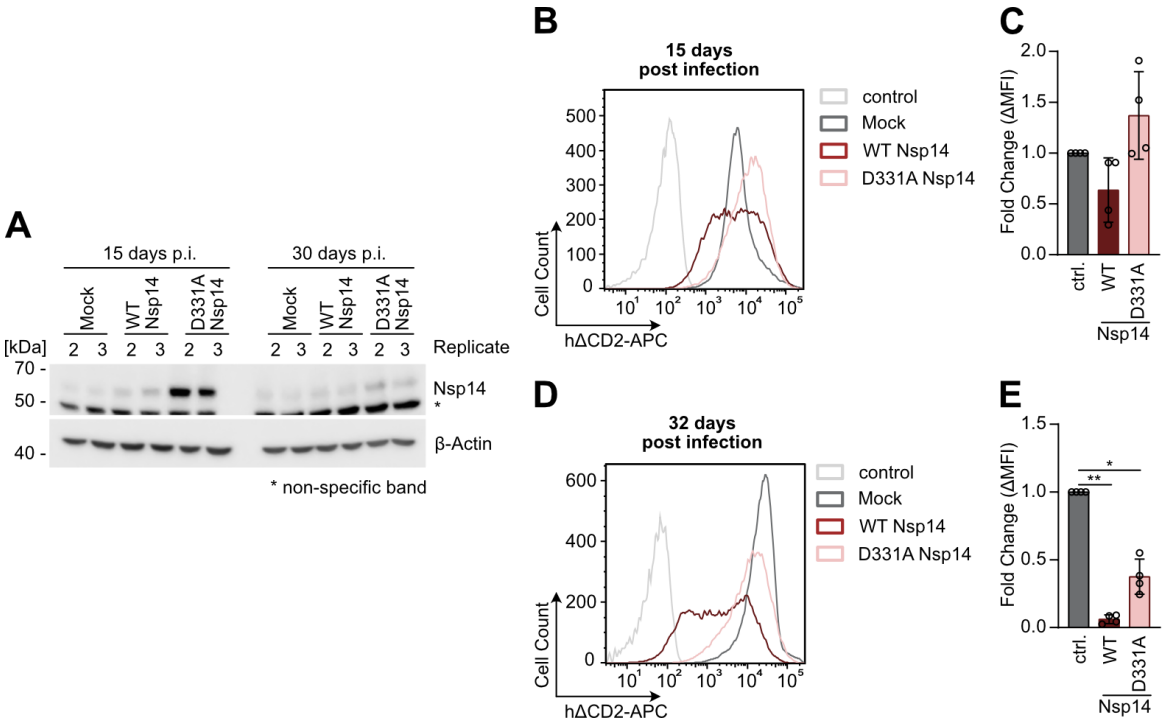

Figure 3-23: Hek293 stably expressing Nsp14.
(A) Protein levels of Nsp14 determined 15 and 30 days after lentiviral transduction of Hek293 in two representative biological replicates, analyzed by WB. (B-E) Quantification of Nsp14 expression via co-expressed cell surface marker protein hΔCD2 by flow cytometry (B-C) 15 days after infection. (D-E) 30 days after infection. (B, D) Shifts are representative, determined in biological replicate 2. (C, E) Fold Change of ΔMFI (Delta Median Fluorescence Intensity; ratio of measured MFI [sample] and MFI [control cells]) normalized to mock-infected cells, values are mean ± SD, n = 4. Statistical significance was analyzed by one-sample t-test after calculating log2 fold changes normalized to the Mock sample. *P ≤ 0.05, **P ≤ 0.005

3.2.2.2 Inducible Nsp14 expression reveals post-translational instability of Nsp14

The low levels of Nsp14 and the additional loss of expression over time after stable integration suggest some mechanisms downregulating Nsp14 expression and/or stability at the transcriptional or post-translational level. Therefore, we generated Hek293 and HCT116 cells expressing WT or D331A Nsp14 under the control of a tetracycline responsive element. This DOX-inducible expression allows us to monitor the dynamics of Nsp14 expression and associated regulatory mechanisms over time. After transducing the Nsp14 constructs, we treated the cells with puromycin to select for a cell pool where all cells expressed Nsp14. We then investigated the optimal dose of doxycycline to induce maximal expression of Nsp14. After treatment with titrated doses of doxycycline for 4 days, Nsp14 protein levels were analyzed by WB. In both cell lines, Hek293 (Figure 3-24A) and HCT116 (Figure 3-24B), doxycycline treatment induced D331A Nsp14 protein expression, albeit at low levels requiring

high exposure for detection, whereas WT Nsp14 was again barely detectable. Neither WT nor D331A Nsp14 expression could be enhanced by increasing the dose of doxycycline.

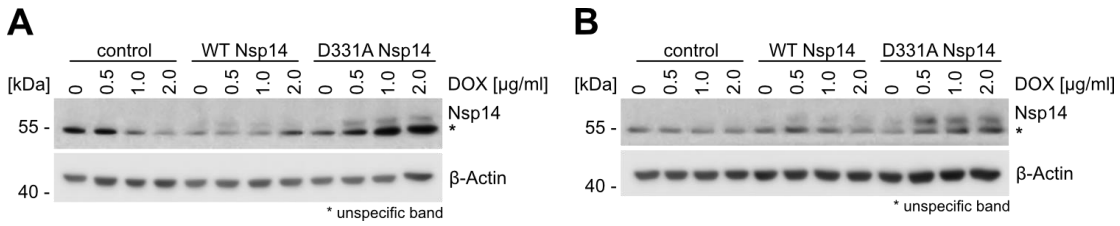

Figure 3-24: Hek293 and HCT116 with inducible Nsp14 expression.
(A) Hek293 and (B) HCT116 with tet-on regulated Nsp14 expression. Expression of WT or D331A Nsp14 was induced with titration of doxycycline for 4 days and Nsp14 expression was determined by WB.

We continued to use the DOX-inducible Nsp14 expression to investigate whether the Nsp14 expression in general and the significant difference between WT and D331A Nsp14 specifically is regulated at the transcriptional or translational level. Therefore, we harvested mRNA after doxycycline treatment and quantified *Nsp14* transcripts by RT-PCR. In contrast to the different protein levels measured after gene induction with the same DOX dose, WT and D331A *Nsp14* transcripts were at equivalent levels in Hek293 (Figure 3-25A) and HCT116 (Figure 3-25B) cells, suggesting equal transcription. Next, we added the proteasome inhibitor MG-132 to analyze whether proteasomal degradation controls Nsp14 at the post-translational level. Again, the overall low protein levels required high exposure for detection, which increased the appearance of non-specific bands and prevented clear analysis. However, WT Nsp14 to accumulate in Hek293 (Figure 3-25C) and presumably also in HCT116 (Figure 3-25D) upon MG-132 treatment, although only to a minor extent. In contrast, D331A Nsp14 did not appear to be affected by the proteasome.

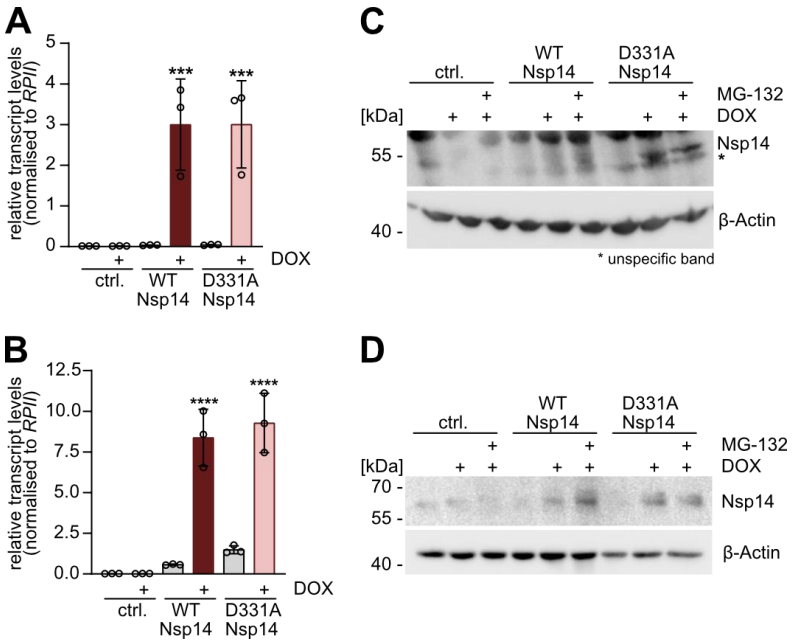

Figure 3-25: WT Nsp14 protein is instable in Hek293 and HCT116 cells.
Doxycycline-induced expression of Nsp14 in (A, C) Hek293 and (B, D) HCT116 cells. (A-B) Nsp14 transcript levels after induction of Nsp14 expression with 0.5 µg/ml DOX for 4 days in (A) Hek293 and (B) HCT116 cells analyzed by RT-PCR. Values measured for Nsp14 were normalized to RPII transcript levels (mean ± SD, n = 3). Statistical significance was analyzed using one-way ANOVA followed by Tukey's test for multiple comparisons. ***P ≤ 0.001, ****P ≤ 0.0001. (C, D) Stabilization of WT Nsp14 by addition of 25 µM MG-132 for 6 hours in addition to induction of Nsp14 expression with 0.5 µg/ml DOX for 4 days in (C) Hek293 and (D) HCT116 cells. Lysates were analyzed for Nsp14 protein levels by WB.

In summary, Nsp14, especially methyltransferase-active Nsp14, was consistently expressed at very low levels, even at stable or inducible expression. hΔCD2 analysis and mRNA quantification suggested equivalent transcription of both methyltransferase-active and inactive Nsp14 that was impaired after prolonged expression. The accumulation of WT Nsp14 upon proteasomal inhibition indicates inherent instability as well as degradation of active Nsp14.

3.2.3 Overexpressed Nsp14 is not sufficient to induce endogenous NF-κB signaling

3.2.3.1 Nsp14 does not activate the endogenous NF-κB signaling pathway

To explore at what point in the NF-κB pathway Nsp14 interferes to mediate its activating stimulus, we overexpressed WT and D331A Nsp14, with IKK-β as a positive control, and examined total protein levels as well as activating protein modifications throughout the canonical and non-canonical NF-κB pathway.

Overexpression of IKK-β significantly activated the canonical pathway as evidenced by phosphorylation of TAK1, IKKα/β and p65, as well as mild cleavage of p105 and degradation of IκB-α (Figure 3-26A). Although IKK-β is not directly active in the non-canonical pathway, its overexpression even caused a mild expression of cIAP2, presumably via some crosstalk, and some enrichment of RelB, which is a target gene of NF-κB (Figure 3-26B). The expression of Nsp14 was clearly weaker compared to IKK-β, and as noted above, WT Nsp14 is less expressed than the D331A Nsp14 mutant (Figure 3-26A, B). In addition, the total protein concentration in the sample derived from WT Nsp14 overexpressing cells was lower compared to the other samples, as reflected by reduced β-actin. Nevertheless, there was no evidence of altered protein levels, such as accumulation of NIK or RelB. Surprisingly, analysis of both canonical and non-canonical NF-κB signaling also revealed no evidence of active signaling by protein phosphorylation upon expression of Nsp14.

To verify that overexpressed Nsp14 is not sufficient to induce endogenous NF-κB signaling, we increased Nsp14 protein levels by titration. Nevertheless, Nsp14 remained weaker expressed than IKK-β (Figure 3-26C). While IKK-β activated the pathway as evidenced by phosphorylation of IKKα/β, IκB-α, and p65 and degradation of IκB-α, Nsp14 was ineffective with respect to the endogenous signaling cascade.

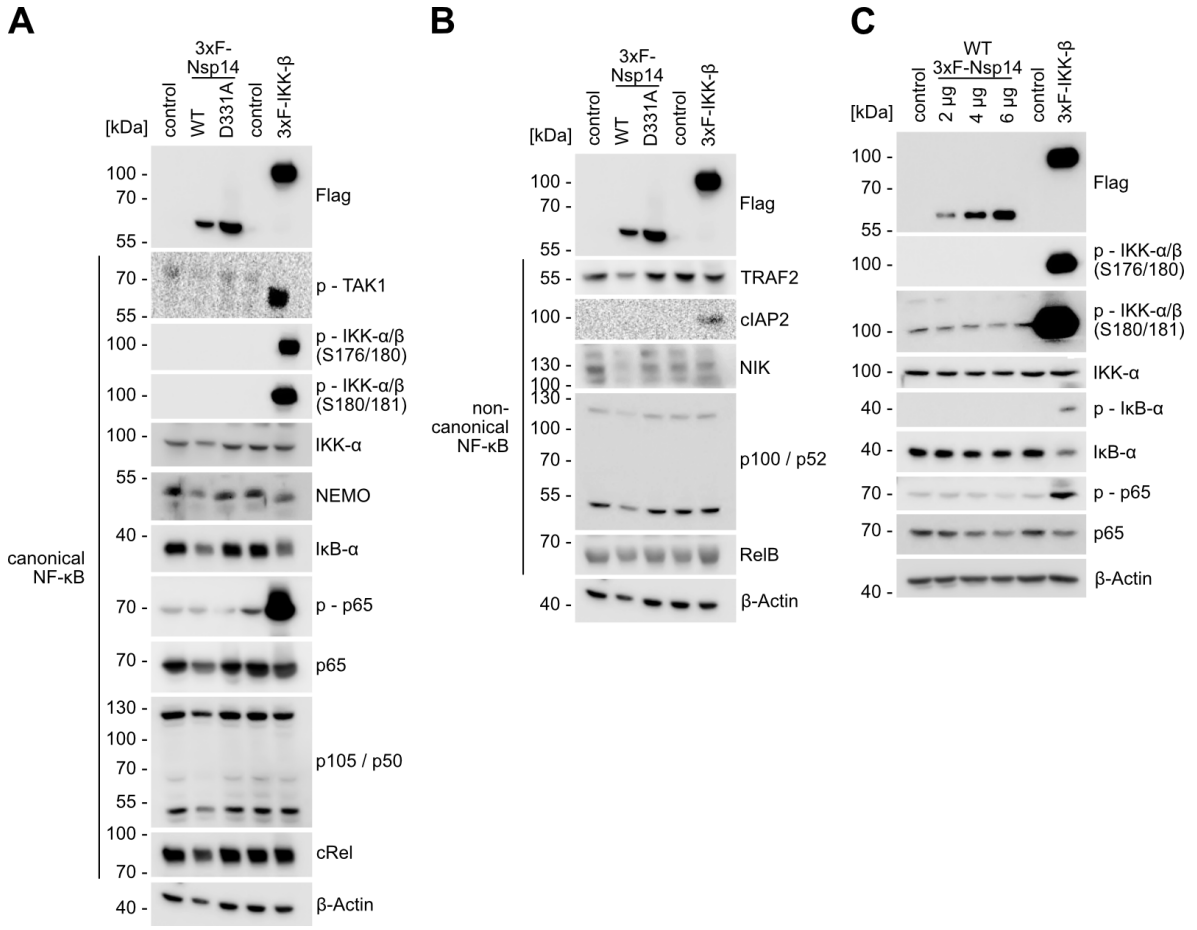

Figure 3-26: The endogenous NF-κB signaling pathway is not activated by Nsp14 overexpression.
(A-B) WT and D331A Nsp14, along with IKK-β, were overexpressed in Hek293 cells and lysates were analyzed by WB for activation of the (A) canonical and (B) non-canonical NF-κB signaling pathway. Western blots displayed in (A) and (B) were performed with the same lysates, the same Flag and Actin stains are shown in both figures. (C) WT Nsp14 OE was titrated, and lysates were analyzed by WB for activation of the canonical NF-κB signaling pathway.

In summary, there were no protein modifications reflecting activation of the endogenous NF-κB signaling pathway upon Nsp14 overexpression, which contrasts with our results with the NF-κB reporter assay.

3.2.3.2 Nsp14 does not efficiently induce transcription of endogenous NF-κB target gene loci

To follow up on these conflicting findings in reporter assays and WB analysis, we examined whether Nsp14 can induce transcription of endogenous NF-κB target gene loci. We overexpressed WT and D331A Nsp14 as well as IKK-β in Hek293 cells and prepared lysates for protein and gene expression analysis. WB analysis showed that all constructs were expressed, but at different levels as described above (Figure 3-27A). We started with the quantification of *CXCL8* transcripts, as *CXCL8* is consistently upregulated in COVID-19 patients. Indeed, IKK-β and WT Nsp14, but not the methyltransferase-defective D331A Nsp14, significantly induced *CXCL8* transcription (Figure 3-27B-C). However, the effect of WT Nsp14 was very mild, as demonstrated by the fact that *CXCL8* transcript levels were approximately 60-fold higher in IKK-β expressing cells compared to WT Nsp14 expressing cells. Transcripts of other well-known NF-κB target genes, specifically *NFKBIA*, *TNFAIP3,* and *ICAM1*, were also markedly enriched upon IKK-β expression (Figure 3-27D, F, H), but not WT or D331A Nsp14 expression (Figure 3-27E, H, I).

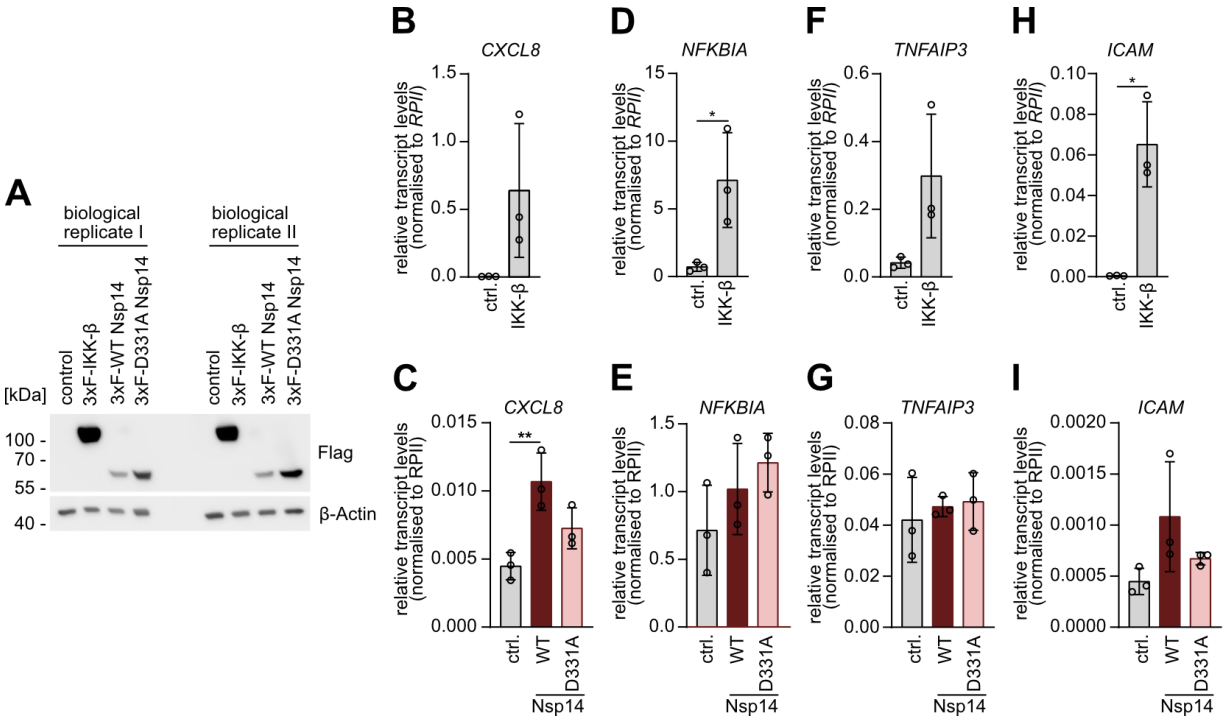

Figure 3-27: Expression of NF-κB target genes upon Nsp14 overexpression.
(A) Protein levels of transfected Nsp14 and IKK-β in two representative biological replicates analyzed by WB. (B - I) Expression of NF-κB target genes (B, C) *CXCL8* (D, E) *NFKBIA* (F, G) *TNFAIP3* (H, I) *ICAM1* in Hek293 cells overexpressing (B, D, F, H) IKK-β and (C, E, G, I) WT or D331A Nsp14, quantified in RT-PCR. Values measured for

target genes were normalized to RPII transcript levels (mean ± SD, n = 3). Statistical significance was analyzed using (B, D, F, H) unpaired Students´ t-test and (C, E, G, I) one-way ANOVA followed by Tukey's test for multiple comparisons.

Since Nsp14 could stimulate NF-κB-dependent transcription of the plasmids used in the reporter assay, but not of most of the endogenous NF-κB target genes tested, we wondered whether Nsp14 might not be sufficient to remodel and open endogenous NF-κB target gene promoters. We addressed this by combining TNF-α stimulation with Nsp14 overexpression to add a stimulus that induces chromatin remodeling and opening of NF-κB binding sites. After verifying the expression of Nsp14 by WB (Figure 3-28A), we quantified the transcript levels of *CXCL8*, *NFKBIA* and *TNFAIP3*. We detected a mild upregulation of *CXCL8* and *TNFAIP3* upon Nsp14 expression, although not statistically significant, which was enhanced by co-stimulation with TNF-α (Figure 3-28B, D). *NFKBIA* transcription was induced by TNF-α stimulation alone or in combination with Nsp14 but not by Nsp14 alone (Figure 3-28C). Nevertheless, the combinatorial effects of TNF-α and Nsp14 were just as strong as the effect of TNF-α alone for all target genes analyzed, indicating that Nsp14 did not contribute substantially.

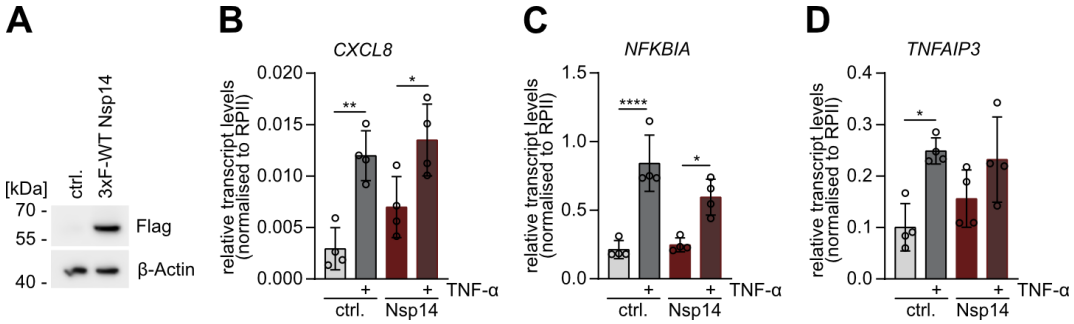

Figure 3-28: Expression of NF-κB target genes upon Nsp14 overexpression and TNF-α stimulation.
(A) Protein levels of transfected Nsp14 in one representative biological replicate analyzed by WB. (B - D) Expression of NF-κB target genes (B) *CXCL8* (C) *NFKBIA* (D) *TNFAIP3* in Hek293 cells upon Nsp14 OE and TNF-α stimulation, quantified in RT-PCR. Values measured for target genes were normalized to RPII transcript levels (mean ± SD, n = 4). Statistical significance was analyzed using one-way ANOVA followed by Tukey's test for multiple comparisons. *P ≤ 0.05, **P ≤ 0.005, ****P ≤ 0.0001.

Given the inherent instability of Nsp14, which could be counteracted by the addition of the cofactors Nsp10 or SAM, we next examined whether this influences Nsp14-mediated transcriptional activity of NF-κB at endogenous loci. Therefore, we overexpressed Nsp10, Nsp14 or both together and confirmed the stabilization of Nsp14 by Nsp10 as shown by WB (Figure 3-29A). Subsequent gene expression analysis by RT-PCR revealed a very mild upregulation of *ICAM1*, although not statistically significant (Figure 3-29C, D), but no effect on *CXCL8*, *NFKBIA* and *TNFAIP3* gene expression (Figure 3-29B, D) upon overexpression of Nsp14.

In contrast, Nsp14 stabilized by Nsp10 significantly, although still very weakly, induced the transcription of *CXCL8*, *ICAM1* and *NFKIBA*, but not *TNFAIP* (Figure 3-29B-E).

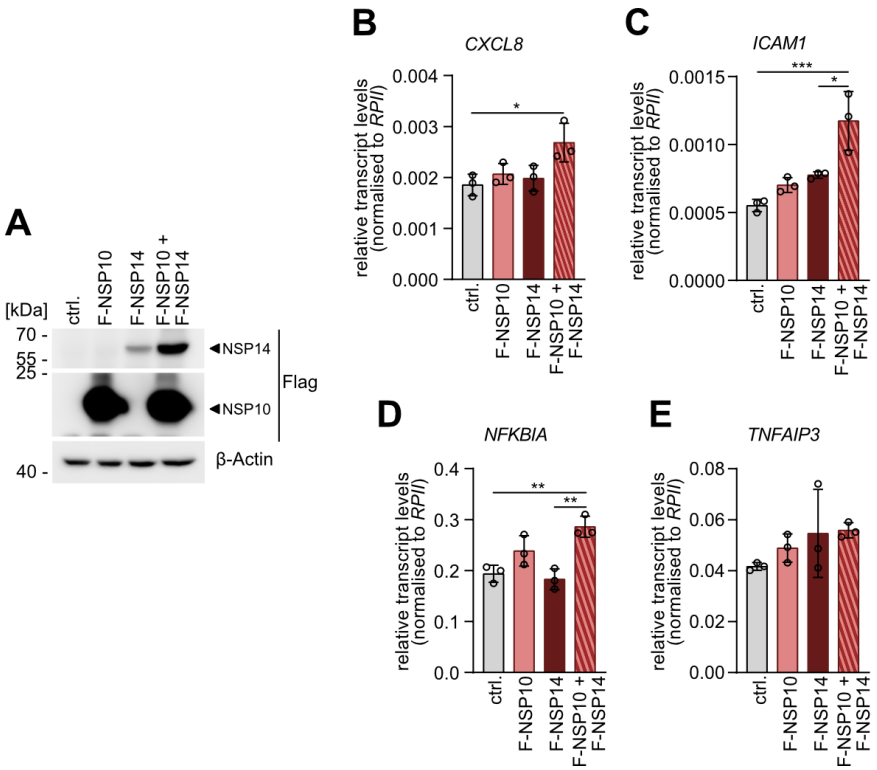

Figure 3-29: Expression of NF-κB target genes upon Nsp14 overexpression and Nsp10 co-expression.
(A) Protein levels of transfected Nsp14 and Nsp10 in one representative biological replicate analyzed by WB. (B - E) Expression of NF-κB target genes (B) *CXCL8* (C) *ICAM1* (D) *NFKBIA* (E) *TNFAIP3* in Hek293 cells upon Nsp14 OE and Nsp10 co-expression, quantified in RT-PCR. Values measured for target genes were normalized to RPII transcript levels (mean ± SD, n = 3). Statistical significance was analyzed using one-way ANOVA followed by Tukey's test for multiple comparisons. *P ≤ 0.05, **P ≤ 0.005, ***P ≤ 0.001

Supplementation of cells with SAM also stabilized Nsp14 in a similar manner as previously shown and verified by WB (Figure 3-30A). However, again no strong transcription of NF-κB target genes was detectable. Similar to the previous experiment, Nsp14 overexpression led to a slight increase in *CXCL8* transcripts, but this was not statistically significant (Figure 3-30B). Stabilization by SAM supplementation could slightly increase Nsp14-induced gene transcription of *ICAM1* and *TNFAIP3*, but this was statistically significant only for *ICAM1* (Figure 3-30C, E).

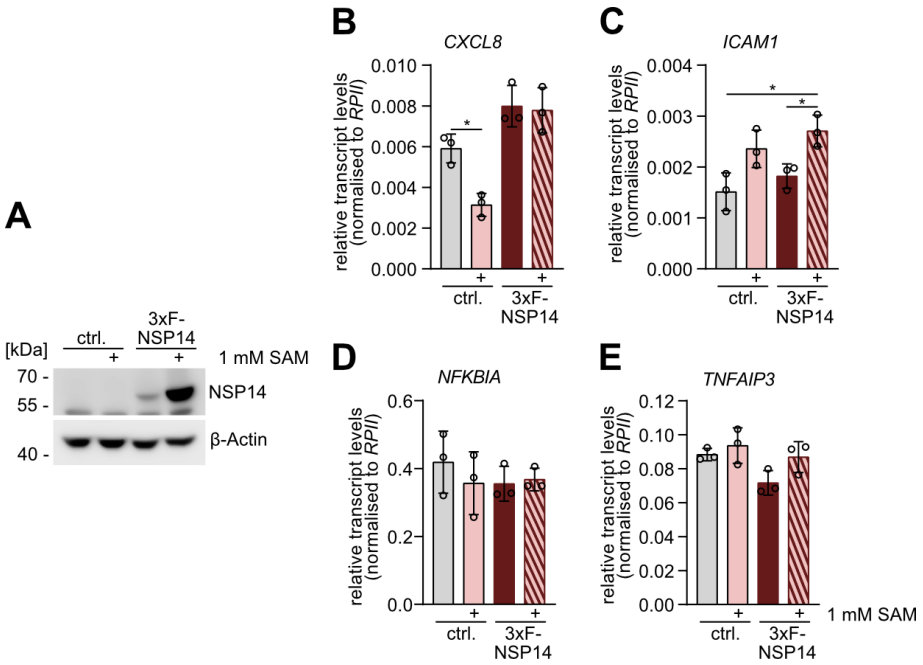

Figure 3-30: Expression of NF-κB target genes upon Nsp14 overexpression and SAM treatment.
(A) Protein levels of transfected Nsp14 in one representative biological replicate analyzed by WB. (B - E) Expression of NF-κB target genes (B) *CXCL8* (C) *ICAM1* (D) *NFKBIA* (E) *TNFAIP3* in Hek293 cells upon Nsp14 OE and SAM treatment, quantified in RT-PCR. Values measured for target genes were normalized to RPII transcript levels (mean ± SD, n = 3). Statistical significance was analyzed using one-way ANOVA followed by Tukey's test for multiple comparisons. *P ≤ 0.05.

Overall, these results suggest that transient overexpression of Nsp14 was sufficient to induce NF-κB transcriptional activity on a co-transfected reporter plasmid whereas it could not induce robust transcription of endogenous NF-κB target gene loci modeled by chromatin.

3.2.4 Nsp14-induced canonical NF-κB signaling relies on NEMO/IKKγ and NF-κB p65

3.2.4.1 Nsp14 does not form stable complexes with putative human binding partners

The systematic mapping of SARS-CoV-2 protein interactions with the human host cell proteome revealed that Nsp14 binds to 27 human proteins (242). Among those were NEMO/*IKBKG*, c-Rel and TRAF2, which are all part of the canonical and/or non-canonical NF-κB signaling pathways (Figure 3-31).

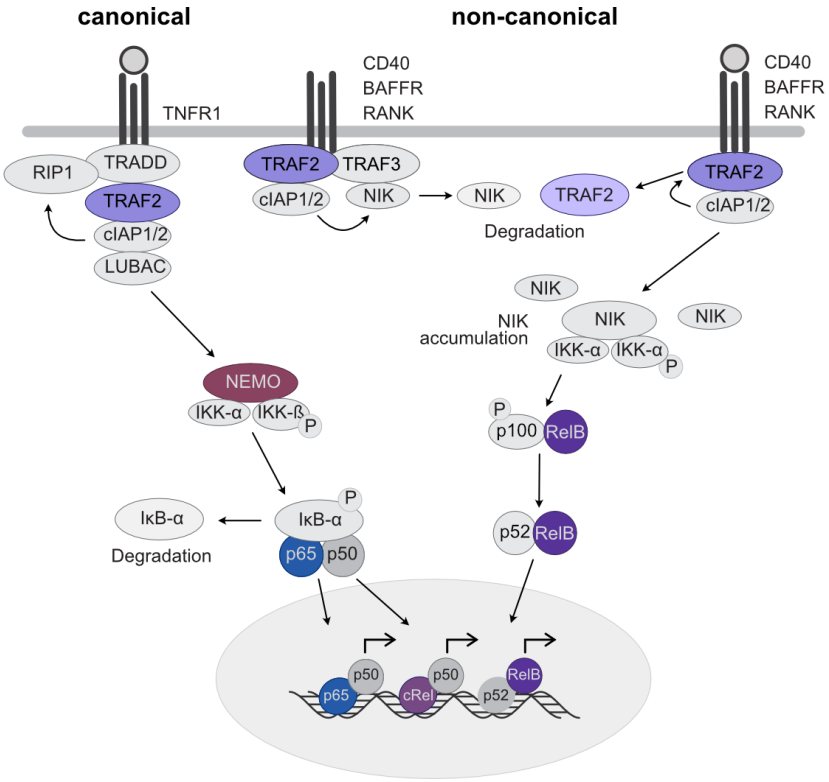

Figure 3-31: Schematic of the canonical and non-canonical NF-κB signaling pathways with putative Nsp14 interactors highlighted.
TRAF2 acts as a positive regulator in the TNFR1 receptor complex, inducing canonical NF-κB signaling, whereas it has a negative regulatory function in TNF superfamily receptor complexes, that activate non-canonical NF-κB signaling. While NEMO and p65 function exclusively in canonical NF-κB signaling, RelB is active only in non-canonical NF-κB activity. Proteins identified in the Nsp14 contactome are highlighted in color.

To understand how MTase-active Nsp14 regulates the stimulation of NF-κB mechanistically, we examined complex formation of Nsp14 with the putative human binding partners. Therefore, we co-expressed eGFP-Nsp14 with cytosolic Flag-NEMO or Flag-TRAF2 and nuclear Flag-c-Rel or Flag-p65 and controlled the experiment with co-expression of eGFP-Nsp14 with Flag-Nsp10 as well as IKK-β-eGFP with Flag-NEMO. After performing GFP-Trap pulldowns we tested for proteins associated with Nsp14 by Western blot. In both experiments we found stable complex formation of eGFP-Nsp14 with Flag-Nsp10 and eGFP-IKK-β with Flag-NEMO, as expected (Figure 3-32A). In contrast, we could neither detect any binding of Nsp14 to the cytosolic Flag-NEMO or Flag-TRAF2 (Figure 3-32B) nor to the nuclear Flag-cRel or Flag-p65.

This implies that Nsp14 does not form stable complexes with either of the putative human interactors in NF-κB signaling pathways but may instead modulate NF-κB signaling independent from direct binding.

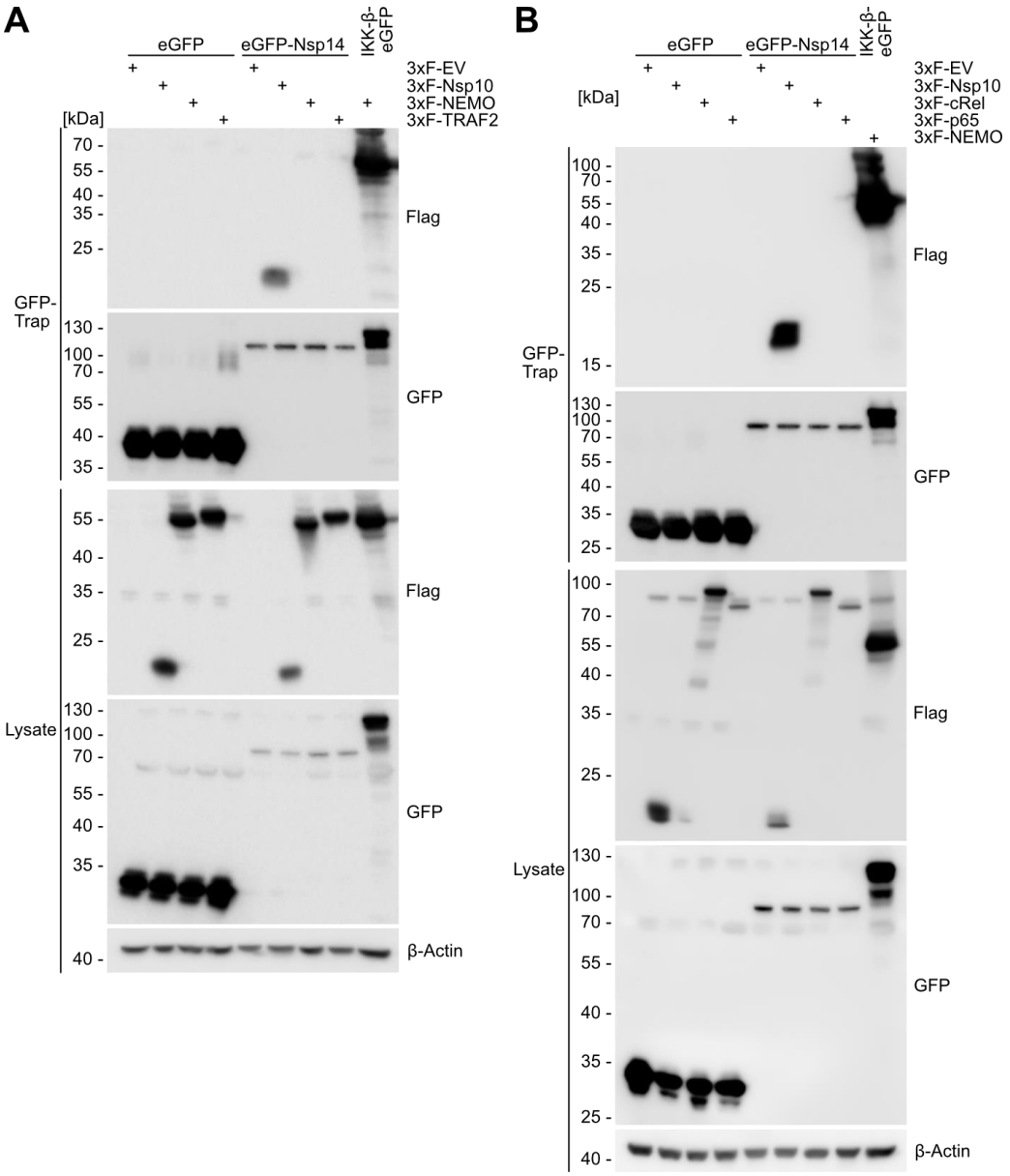

Figure 3-32: Nsp14 does not stably bind putative human binding partners.
(A-B) eGFP-Nsp14 was co-expressed with (A) flag-tagged NEMO and TRAF2 or (B) flag-tagged cRel and p65. Co-expression of eGFP-Nsp14 with flag-tagged Nsp10 and IKK-β-eGFP with flag-tagged NEMO were used as positive controls. Association of Nsp14 with putative human interacting proteins was analyzed by Nsp14 pull down via GFP-Traps and Western blot.

3.2.4.2 Nsp14 induces canonical NF-κB signaling via NEMO and p65, but not c-Rel

The next step was to dissect whether Nsp14-induced NF-κB activation relies on the canonical or non-canonical pathway. To this end, we continued to analyze NF-κB activation in the absence of the human candidate proteins, as they may still be involved despite failing to form stable complexes with Nsp14.

We generated knockout (KO) Hek293 cells using CRISPR/Cas9 technology and performed either cell dilution to expand single cell clones or puromycin selection to grow KO cell pools.

We started with NEMO, which is the non-catalytic subunit of the IKK complex and a central hub of the canonical NF-κB signaling pathway (Figure 3-31). We used single guide RNAs (sgRNAs) targeting either exon 3 (sgRNA #1) or exon 2 (sgRNA #2) of *IKBKG* (Figure 3-33A), transfected the guides and Cas9, and expanded single cell KO clones. The clones were tested for NEMO protein expression by Western blot analysis, which revealed absence of NEMO in all clones (Figure 3-33B). In addition, genomic DNA was isolated from these clones, the sgRNA target site was amplified by PCR, and the KO was confirmed by sequencing the amplified fragment (data not shown). For further experiments, we selected two clones (#3 and #18) generated with sgRNA #1 and one clone (#36) generated with sgRNA #2. We transfected WT and *IKBKG* KO cells with Nsp14 or stimulated the cells with TNF-α and quantified the NF-κB activity using the reporter assay. As expected, TNF-α did not stimulate NF-κB activity but also the basal level of NF-κB signaling is reduced in *IKBKG* KO cells (Figure 3-33C). Similarly, Nsp14-driven induction of NF-κB was significantly impaired, but not completely abolished, in *IKBKG* KO cells. Western blot analysis of the lysates verified equivalent Nsp14 expression levels in all cell lines, thus excluding variance in Nsp14 protein levels as a determinant for NF-κB stimulation (Figure 3-33D).

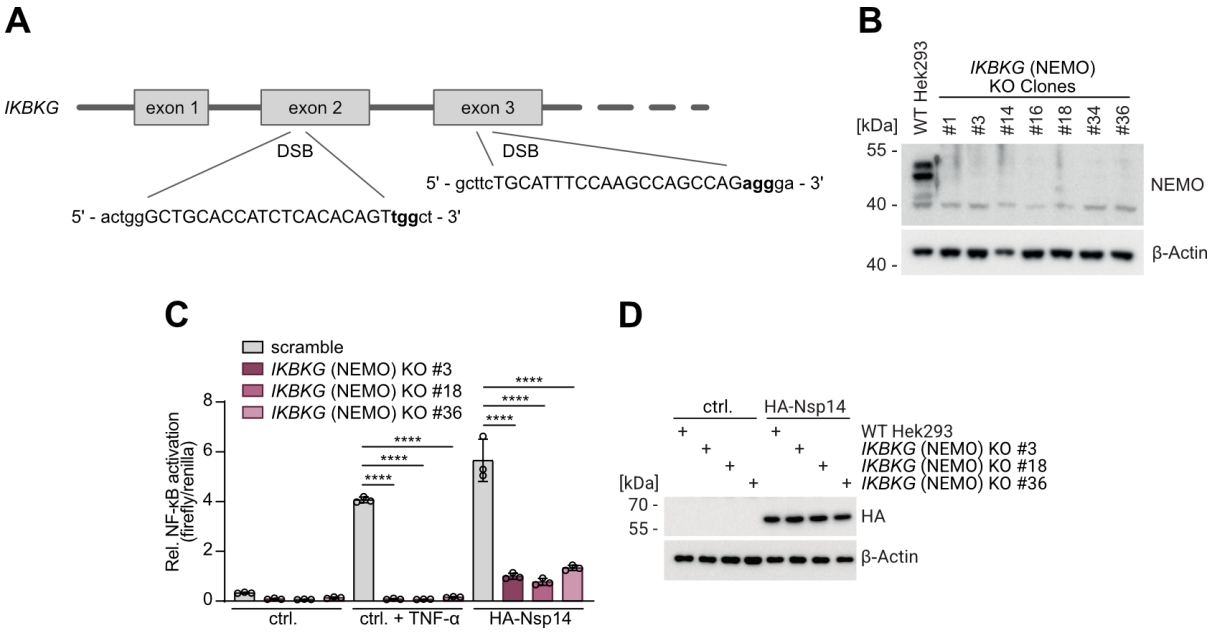

Figure 3-33: Nsp14-induced NF-κB signaling is significantly impaired in *IKBKG* (NEMO) KO Hek293.
(A) Scheme of the *IKBKG* exons targeted by Cas9 with sgRNA #1 (exon 3) or sgRNA #2 (exon 2). (B) Absence of NEMO protein in *IKBKG* KO Hek293 cell clones analyzed by Western blot. (C) NF-κB reporter assay after TNF-α stimulation or Nsp14 OE in WT and *IKBKG* KO Hek293 with (D) representative WB for determination of protein expression levels. Data are the mean ± SD with n = 3. Statistical significance was analyzed using two-way ANOVA followed by Tukey's test for multiple comparisons. ****P ≤ 0.0001.

The NF-κB family member c-Rel acts as a transcription factor downstream of NEMO by forming homo- and heterodimers with p50 and p65 (260) (Figure 3-31). It was also identified in the Nsp14 contactome, suggesting a role in Nsp14-stimulated activation of NF-κB. To determine whether Nsp14 regulates NF-κB activity via c-Rel, we performed lentiviral infections with the LentiCRISPRv2 system. We used three different sgRNAs targeting exon 2 (sgRNA #2), exon 3 (sgRNA #3) and exon 5 (sgRNA #1) (Figure 3-34A) together with a scramble control containing only Cas9 without sgRNA and puromycin selection after Cas9 and sgRNA transduction to generate three different *REL* KO Hek293 cell pools. Western blot analysis showed a complete absence of c-Rel in all *REL* KO cell pools (Figure 3-34B). Next, we overexpressed Nsp14 in parallel with TNF-α stimulation and quantified NF-κB activity with the reporter assay. With both treatments, we observed robust activation of NF-κB without deficiency in *REL* KO cells (Figure 3-34C), despite equivalent Nsp14 expression as verified by Western blot analysis (Figure 3-34D).

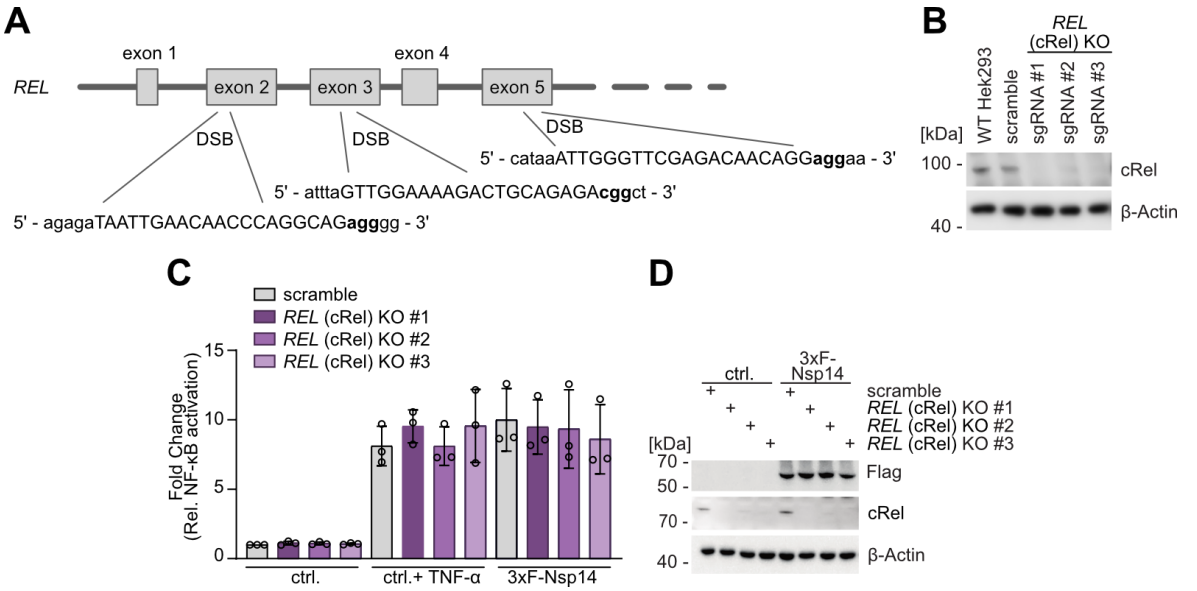

Figure 3-34: cRel is not essential for NF-κB activation induced by Nsp14.
(A) Scheme of the *REL* exons targeted by Cas9 with sgRNA #1 (exon 5), sgRNA #2 (exon 2) or sgRNA #3 (exon 3). (B) Absence of c-Rel protein in *REL* KO Hek293 cell pools analyzed by Western blot. (C) NF-κB reporter assay after TNF-α stimulation or Nsp14 OE in control and *REL* KO Hek293 with (D) representative WB for determination of protein expression levels. All values were normalized to untreated control cells (Fold Change). Data are the mean ± SD with n = 3. Statistical significance was analyzed by one-sample t-test after calculating log2 fold changes normalized to the control treatment sample. There was no significant difference when comparing the KO cell line samples with the scramble cell line sample in each treatment set.

Another NF-κB subunit is p65, which forms homo- and heterodimers with p50 and c-Rel to exert its transcriptional transactivation function (260) (Figure 3-31). Therefore, we asked whether p65 is involved in Nsp14-stimulated NF-κB activity, either alone or in complex with c-Rel. Using the lentiCRISPRv2 system, we generated pools of *RELA* KO Hek293 cells with three different sgRNAs targeting exon 3 (sgRNA #1 (5'-end) and #2 (3'-end)) or exon 4 (sgRNA #3) and combined sgRNA #1 and #2 with *REL* sgRNA #1 to generate *REL*/*RELA* double knockout (DKO) Hek293 (Figure 3-35A). The depletion of p65 and c-Rel was verified by Western blot analysis (Figure 3-35B). We started to analyze the cell pools lacking p65 by equivalent overexpression of IKK-β or Nsp14 as displayed in the Western blot analysis (Figure 3-35C). The reporter assay revealed a significant loss of NF-κB activation stimulated by either IKK-β or Nsp14 in *REL* KO cells. This was true even in cells transduced with *RELA* sgRNA #1, although re-evaluation of p65 ablation in Western blot analysis suggested residual p65 expression. Comparison of Nsp-14-driven NF-κB induction with basal activity levels in *REL* KO cells suggested some residual Nsp14-induced NF-κB activity, although not statistically significant. Using the *REL*/*RELA* DKO, we tested whether c-Rel contributes to the residual NF-κB activity in

REL KO cells. However, after equivalent overexpression of IKK-β and Nsp14, we demonstrated that the activation of NF-κB by either stimulus was not further reduced by additional c-Rel depletion in *RELA* KO cells (Figure 3-35D).

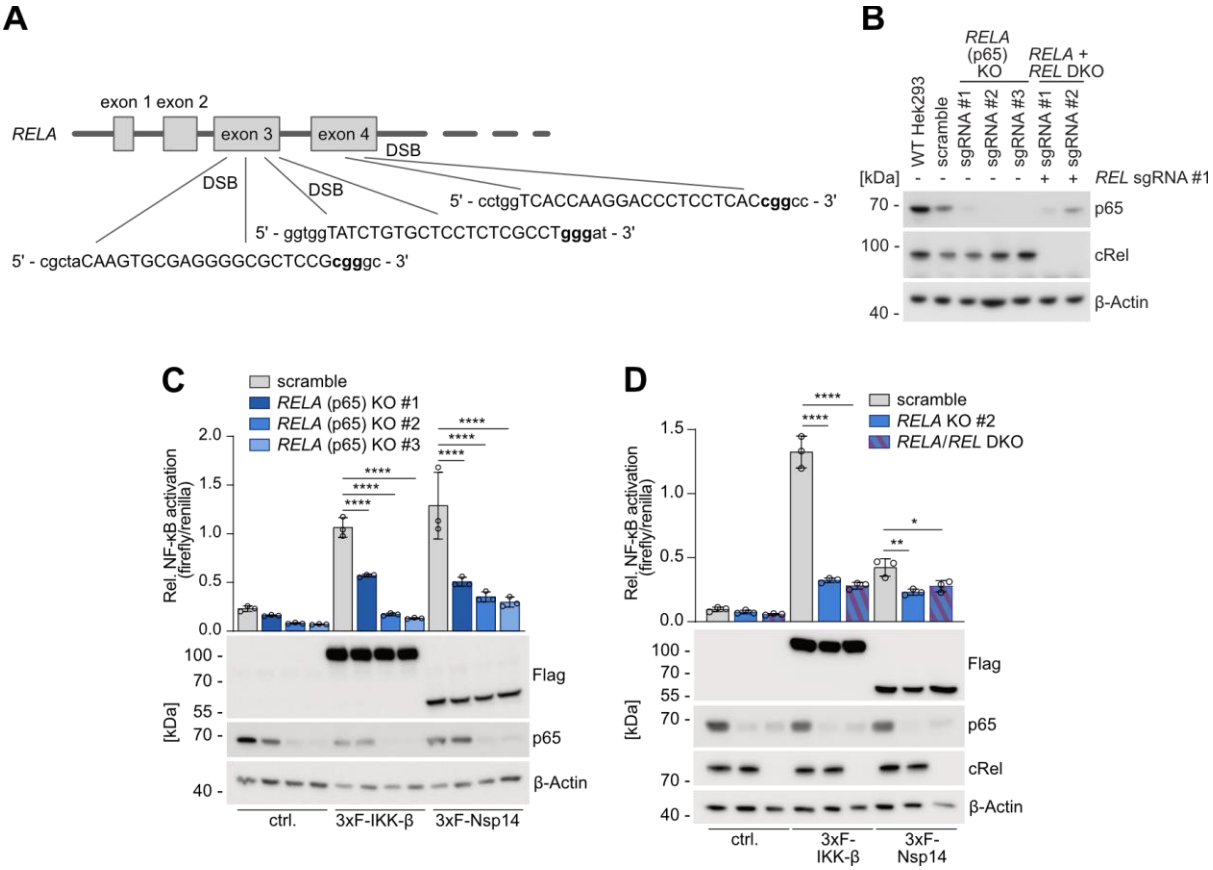

Figure 3-35: Nsp14-induced NF-κB activity is mainly based on p65.
(A) Scheme of the *RELA* exons targeted by Cas9 with sgRNA #1 (exon 3, 5'-end), sgRNA #2 (exon 3, 3'-end) or sgRNA #3 (exon 4) (B) Absence of p65 and c-Rel protein in *RELA* KO and *REL*/*RELA* DKO Hek293 cell pools analyzed by Western blot. (C-D) NF-κB reporter assay after IKK-β or Nsp14 OE in control and (C) *RELA* KO Hek293 or (D) *REL*/*RELA* DKO Hek293 with representative WB for determination of protein expression levels. Data are the mean ± SD with n = 3. Statistical significance was analyzed using two-way ANOVA followed by Tukey's test for multiple comparisons. *P ≤ 0.05, **P ≤ 0.005, ****P ≤ 0.0001.

In summary, Nsp14-induced stimulation activates canonical NF-κB signaling mediated by NEMO/IKK. Further, the Nsp14-stimulated NF-κB relies on p65 but not c-Rel as crucial component of the transcription factor.

3.2.4.3 Non-canonical NF-κB signaling is not essential for Nsp14-driven NF-κB activity

The last human candidate protein identified in the Nsp14-contactome, that is part of NF-κB signaling pathways, is TRAF2. In fact, TRAF2 assembles into complexes at various receptors and has a dual role in NF-κB signaling. In the canonical NF-κB pathway induced by a stimulated TNFR1 complex, it assembles in a complex with TRADD, cIAP1/2, LUBAC and RIP1 and plays

an activating role in the recruitment and activation of the IKK complex (Figure 3-31) (261). In contrast, under basal conditions TRAF2 binds to receptors that promote non-canonical NF-κB signaling and mediates the inhibitory degradation of NIK, thus acting as a negative regulator (16). Upon ligation of such receptors, degradation of TRAF2 is part of the activating mechanism.

To determine whether TRAF2 mediates Nsp14-dependent activation of NF-κB via either pathway, canonical or non-canonical, we generated *TRAF2* KO clones. After transfection with two sgRNAs both targeting exon 2 (Figure 3-36A) and Cas9, we expanded single cell clones and tested them for TRAF2 expression by Western blot. None of the *TRAF2* KO clones showed TRAF2 expression (Figure 3-36B), so we selected clone #7 and #19 for further analysis. After TNF-α stimulation or overexpression of Nsp14, we quantified the activation of NF-κB using the reporter assay. In unstimulated conditions, *TRAF2* KO cells showed enhanced basal NF-κB activation, presumably because of missing suppression of non-canonical signaling (Figure 3-36C). However, there was no significant loss of NF-κB activation by TNF-α or equivalent Nsp14 expression, as verified by Western blot analysis (Figure 3-36D). Instead, clone #19 even displayed mildly enhanced NF-κB signaling upon Nsp14 overexpression, which may be driven by elevated basal NF-κB activity and slightly higher expression of Nsp14.

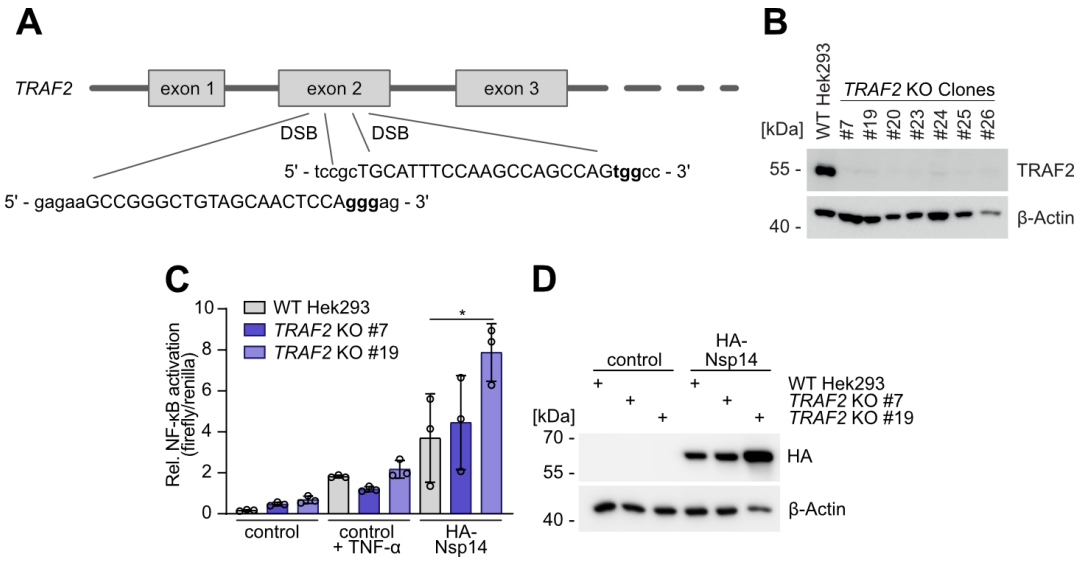

Figure 3-36: TRAF2 is not required for Nsp14-driven activation of NF-κB.
(A) Scheme of the *TRAF2* exons targeted by Cas9 with sgRNA #1 (exon 2, 5'-end) and sgRNA #2 (exon 2, 3'-end). (B) Absence of TRAF2 protein in *TRAF2* KO Hek293 cell clones analyzed by Western blot. (C) NF-κB reporter assay after TNF-α stimulation or Nsp14 OE in WT and *TRAF2* KO Hek293 with (D) representative WB for determination of

protein expression levels. Data are the mean ± SD with n = 3. Statistical significance was analyzed using two-way ANOVA followed by Tukey's test for multiple comparisons. *P ≤ 0.05.

Since we could already rule out interference with upstream non-canonical NF-κB signaling using the *TRAF2* KO cells, we also investigated whether Nsp14 affects downstream non-canonical NF-κB signaling. RelB is the third NF-κB subunit with a transactivation domain and heterodimerizes with p52 for non-canonical NF-κB activity (260) (Figure 3-31). We generated *RELB* KO and *RELB*/*RELA* DKO cells using the LentiCRISPRv2 system and three different sgRNAs targeting RELB exon 2 (sgRNA #2) or exon 4 (sgRNA #1 (5'-end) and #3 (3'-end)) (Figure 3-37A). Western blot analysis after puromycin selection showed successful ablation of RelB with sgRNA #1 and #3, but not with sgRNA #2, and in DKO cells additionally a significant reduction of p65 protein levels (Figure 3-37B). Therefore, cells generated with *RELB* sgRNA #2 were excluded from further experiments. However, RelB ablation did not affect Nsp14-induced NF-κB activation, as reflected by the reporter assay (Figure 3-37C). Similarly, we again detected a strong inhibition of Nsp14-driven NF-κB activity with p65 depletion, whereas there was no further reduction in transcriptional activity in *RELB*/*RELA* DKO cells (Figure 3-37D).

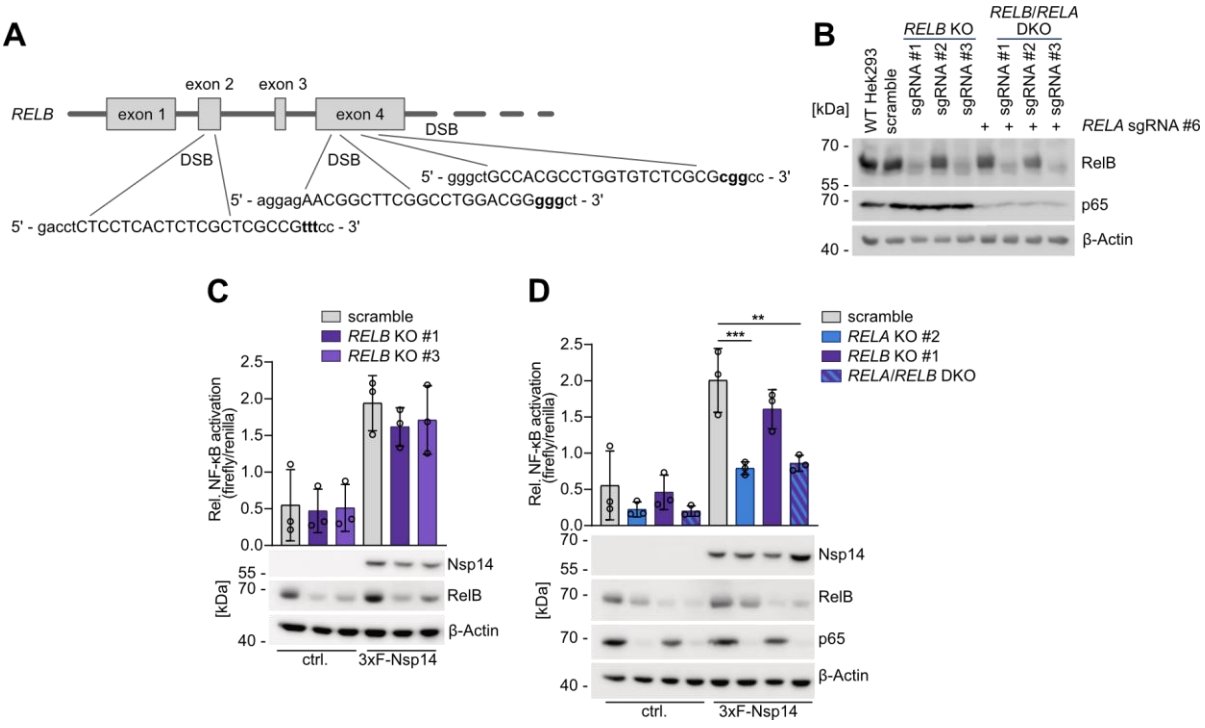

Figure 3-37: Nsp14 does not trigger RelB-dependent non-canonical NF-κB signaling.
(A) Scheme of the *RELB* exons targeted by Cas9 with sgRNA #1 (exon 4, 5'-end), sgRNA #2 (exon 2) or sgRNA #3 (exon 4, 3'-end) (B) Absence of RelB and p65 protein in *RELB* KO and *RELB*/*RELA* DKO Hek293 cell pools analyzed by Western blot. (C-D) NF-κB reporter assay after Nsp14 OE in control and (C) *RELB* KO Hek293 or (D) *RELB*/*RELA* DKO Hek293 with representative WB for determination of protein expression levels. Data are the mean ± SD with

n = 3. Statistical significance was analyzed using two-way ANOVA followed by Tukey's test for multiple comparisons. **P ≤ 0.005, ***P ≤ 0.001.

Taken together, this suggests that Nsp14 does not interact with non-canonical NF-κB signaling, but mainly stimulates NEMO/IKK and NF-κB p65 activity.

4 Discussion

Transcription factors are central to the regulation of gene expression, coordinating a wide range of essential cellular functions from developmental fate determination to specific cellular responses to extrinsic signals. Within the immune system, NF-κB plays a central role in orchestrating a tailored inflammatory response to pathogens, a role that is both complemented and modulated by crosstalk with other transcription factors such as NF-AT and AP-1.

4.1 Generation and application of a TTR Jurkat T cell line

Upon antigen recognition, T cell receptor engagement triggers a complex interplay of intracellular signaling cascades culminating in the activation of the key transcription factors NF-κB, AP-1, and NF-AT. These cascades and their associated gene products control T lymphocyte differentiation, proliferation, survival, and cytokine production. To elucidate these processes, we have developed a Jurkat T cell reporter line using ECFP, mCherry, and EGFP as fluorescent indicators of NF-κB, AP-1, and NF-AT activity, respectively. This tool allows an integrated analysis of signaling dynamics and functional responses in T lymphocytes.

CADINS and BENTA are two diseases caused by heterozygous loss-of-function and gain-of-function germline mutations, respectively, in *CARD11*. So far, they have been described to affect NF-κB activity, but this is not sufficient to mechanistically explain the patients' symptoms. We investigated whether mutant CARD11 may also modulate the crosstalk with AP-1 and NF-AT and used our new TTR Jurkat T cells to comprehensively study the effects of CADINS- and BENTA-associated *CARD11* mutations on T cell activation. Although we could not detect any modulation of AP-1 or NF-AT activity, this study demonstrates the advantages of the new reporter cell line.

4.1.1 The TTR system displays the activation of major T cell transcription factors

The new TTR Jurkat T cell line is a powerful tool for comprehensive and simultaneous analysis of the activity of the major T cell transcription factors NF-κB, AP-1 and NF-AT. Furthermore, single cell analysis by flow cytometry allows a qualitative analysis by analyzing in how many

cells there is transcriptional activity (% fluorescence pos. cells) and a quantitative analysis by measuring the intensity of transcriptional analysis (MFI).

Until now, the analysis of T cell activation was mainly limited to cell pool analysis methods or single signaling pathways. Assays that analyze entire pools of cells, such as electromobility shift assay, dual luciferase assay, or Western blot, allowed the estimation of transcription factor activity as an average of all analyzed cells (262-264). However, this neglected the insight into each individual cell and therefore the understanding of whether all cells were activated to a similar extent or whether only a few cells were strongly activated while another subgroup was unresponsive. Furthermore, the quantification of transcriptional activity could only be estimated with limited accuracy based on EMSA or WB, while the use of dual luciferase assays based on transient reporter expression limits the time period monitored and also does not reflect transcriptional activity at chromatin modeled gene loci in the nucleus (262-264). In contrast, the use of single fluorescent transcription reporters stably integrated into the genome of cells allowed the analysis of a single cell over variable time periods and the precise quantification of transcriptional activity, but only for one transcription factor per cell line (265). Therefore, the novel TTR Jurkat T cell line offers a more precise analysis of T cell activation and represents a broader spectrum of signaling pathways that regulate T cell activation processes.

Reporter plasmid constructs were obtained from Jutz et al. (244), but our methodology differed by using a polyclonal reporter cell pool rather than a monoclonal cell line. While flow cytometric analysis of cell pools inherently produces broader shifts than that of clonal populations, this approach mitigates the risk of clonal bias. Clonal variance is a major concern because site-specific integration of reporter constructs can bias responses to stimuli, potentially yielding artifactual data (266). In contrast, our polyclonal system provides a more representative view of T cell activation by averaging the bias of individual cell responses. This method ensures a more reliable interpretation of activation signals, despite the trade-off in signal resolution that comes with using a heterogeneous cell population.

Subsequent validation of the new TTR Jurkat T cell line using various inhibitors and stimuli confirmed the specificity of the system in detecting transcription factor activation and in reflecting crosstalk in upstream signaling pathways as well as among transcription factors (Figure 4-1). The effects of inhibitors targeting different arms of the T cell signaling network

emphasized the relative independence of Ca^{2+}-regulated NF-AT activity and the close interrelationship between NF-κB and AP-1 activating pathways. As a general pattern, downregulation of NF-κB was associated with a reduction of AP-1 activity, reflecting the regulation of AP-1 subunits by NF-κB (114, 115). However, PKCθ inhibition with sotrastaurin not only affected NF-κB and AP-1, but even slightly reduced the induction of NF-AT. This could be caused by PKCθ, which affects NF-AT by altering IP_3 generation and Ca^{2+} mobilization, or it could be a consequence of NF-AT requiring cooperation with AP-1 for efficient transcriptional activity (43, 267). In contrast, interference with calcineurin activity revealed crosstalk with the NF-κB activating pathway, for example through dephosphorylation of BCL-10 by calcineurin (268).

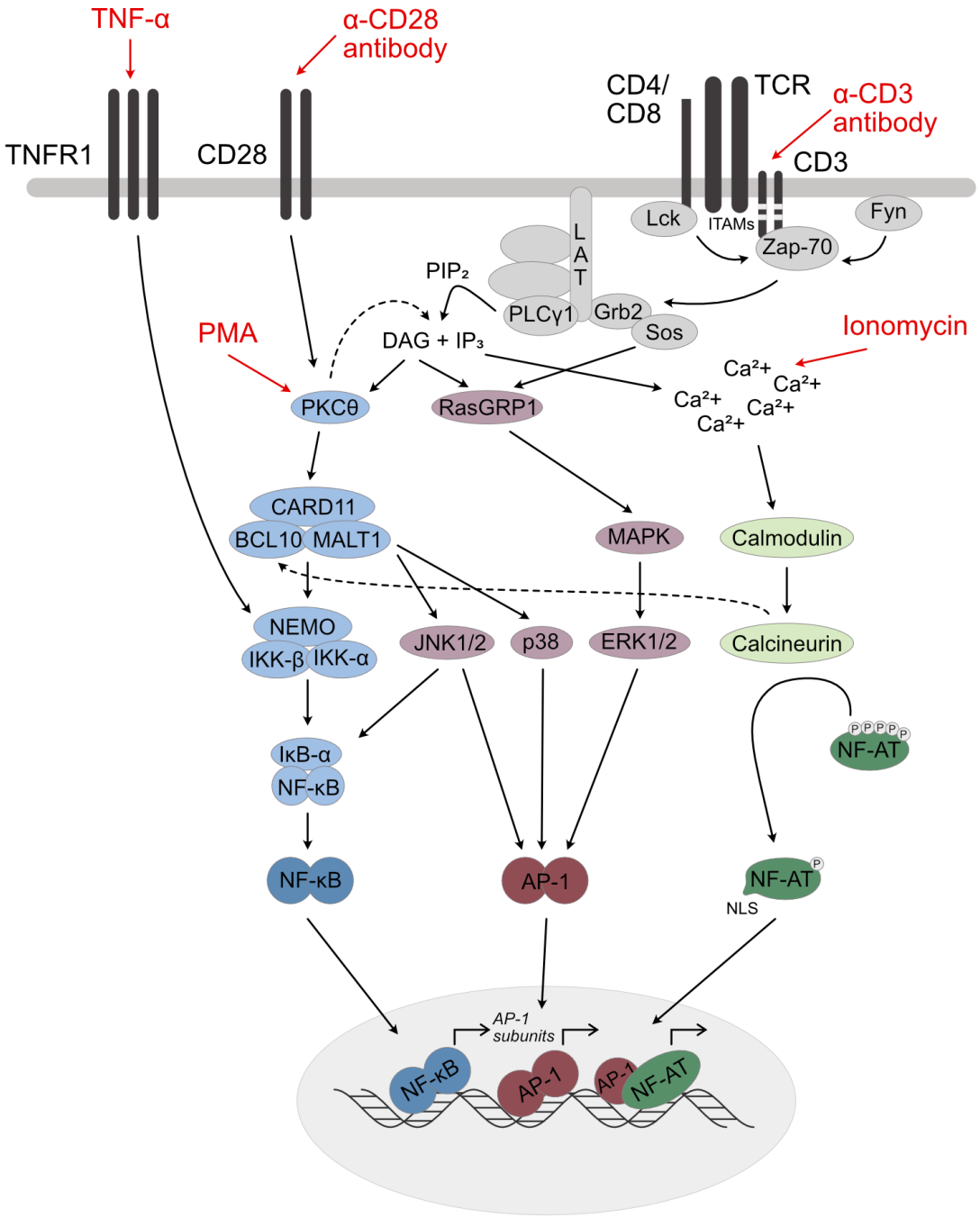

Figure 4-1: T cell signaling with crosstalk between NF-κB, AP-1 and NF-AT signaling pathways.
Upon T cell stimulation with anti-CD3, the multiprotein complex is formed at the membrane and activated PLCγ1 catalyzes the formation of DAG and IP_3. DAG activates, together with anti-CD28 antibody stimulated signaling or PMA stimulation, the NF-κB pathway via PKCθ and the AP-1 pathway via RasGRP1 and the CBM complex. Alternatively, the IKK complex formation in induced by TNF-α stimulation. IP_3, as well as ionomycin stimulation, stimulates calcium efflux from the ER, thereby activating NF-AT via calcineurin. Downstream of the signaling cascades, NF-κB drives de novo synthesis of AP-1 subunits, while AP-1 and NF-AT cooperate for a T cell-activating transcriptional program. Dashed lines indicate additional signaling crosstalk detected in this study.

The TTR Jurkat T cell line facilitates monitoring of activation dynamics for all three transcription factors. However, the inherent delay of the system in accumulating fluorescent proteins to

detectable levels makes it unfavorable for detecting very early, rapid, or small differences in signaling. Nevertheless, comparative measurements after five and 24 hours of stimulation clearly showed differential activation kinetics in our assays. NF-κB activation was rapidly detected because its preformed, cytosolic active components are rapidly released upon stimulation (2). NF-AT also responds immediately to stimulation, and the enhanced eGFP signal after sustained stimulation underscores its requirement for sustained elevation of intracellular Ca^{2+} levels (49). In contrast, the mCherry signal indicative of AP-1 activation is delayed, reflecting the need for de novo synthesis of its active components (3). Thus, despite the temporal resolution limitations, the TTR system effectively reflects the signaling dynamics and interplay between these transcription factors.

Treatment with different stimuli in a range of concentrations not only enabled the determination of an optimal stimulation, but also validated the sensitivity of the TTR system to such variations. Concerning the activation of NF-κB, the synergy of a main and a co-stimulus is clear and measurable, since both anti-CD3 and anti-CD28 alone induced a low level of eCFP expression, but only together they induced full eCFP expression and thus, NF-κB activity. Also, the fluctuation of NF-κB-induced eCFP expression upon titration of both, CD3 and CD28, reflects the subtle interplay of both signaling pathways as described previously (79). In contrast, both AP-1 and NF-AT are largely independent of CD28 signaling and depend predominantly on LAT complex formation and PLCγ activation.

As an aside, in previous work we have shown that stimulation with CD3 titration can facilitate detailed examination of specific response parameters, including stimulation thresholds and the intensity of transcriptional responses (111). In a separate application, the TTR system has been used to examine individual aspects of T cell signaling more comprehensively (269). Putting these aspects together, the new reporter opens a wide range of possibilities to study T cell signaling both comprehensively and in depth.

Taken together, the novel TTR Jurkat T cell line represents an important tool to precisely examine endogenous regulatory mechanisms and downstream responses. This innovative tool allows in-depth and comprehensive analyses of T cell activation processes, with broad applications for research in diverse biological contexts.

4.1.2 CADINS- and BENTA-causing *CARD11* mutations are not inducing transcriptional crosstalk in T cells

CARD11, which serves as a scaffolding protein within the CBM complex, plays a central role in the NF-κB signaling pathway that is activated by TCR/CD28 stimulation. Therefore, mutations in *CARD11* can adversely affect the balance of the immune system and lead to various diseases. CADINS and BENTA disease are both caused by heterozygous germline mutations of *CARD11*, with CADINS associated with LOF and BENTA associated with GOF function mutations. However, the spectrum of symptoms cannot be explained by dysregulated NF-κB signaling alone. We have used the new TTR Jurkat T cell line to investigate a possible crosstalk with AP-1 or NF-AT signaling, which may alter the overall T cell activation. Although we could not demonstrate a crosstalk to AP-1 or NF-AT contributing to CADINS or BENTA disease, this study demonstrates that the TTR Jurkat T cells are a versatile and powerful new tool to comprehensively study T cell activation signaling at the single cell level.

The growing group of CADINS-associated *CARD11* mutations are not focused on a specific CARD11 domain. Instead, many mutations occur in the CARD domain, but also the coiled-coil and MAGUK domains can contain such disease-causing mutations. In our study, stable overexpression of R30W, E57D, and L194P CARD11 with mutations in the CARD or coiled-coil domain counteracted NF-κB activation upon stimulation, which is consistent with the results of previous studies using transient expression of these mutant *CARD11* (138-140). However, Ma et al. also described a mild but significant impairment of NF-κB stimulation after transient expression of the R975W CARD11 variant mutated in the MAGUK domain, whereas we could not replicate this negative regulatory effect on NF-κB (139). In addition to the impairment of NF-κB activation, the R30W mutation was also associated with reduced phosphorylation of JNK in a heterozygous mouse model, suggesting crosstalk of negative regulation with AP-1 (141). However, in our TTR Jurkat T cells the AP-1 activity was only slightly decreased by the strong P/I stimulation and not by the more natural anti-CD3/CD28 stimulation. Thus, R30W may interfere with JNK phosphorylation, but does not have a significant downstream effect on AP-1 activation and is therefore unlikely to be critical for patient symptoms. Finally, there was no modulation of NF-AT activity by either of the CADINS-associated CARD11 mutants.

These results suggest that the respective *CARD11* mutations affect only NF-κB downstream signaling, without significant crosstalk with AP-1 or NF-AT. It has been previously shown that R30W, E57D and L194P CARD11 are defective in the formation of the CBM complex (138, 139). Therefore, it can be speculated that mutations in the CARD, coiled-coil or MAGUK domain affect binding to BCL10, aggregation of CARD11 or recruitment to the plasma membrane. Depending on the severity and nature of the mutation, CBM complex formation and downstream NF-κB and JNK signaling may be partially or completely affected, resulting in different symptoms in different patients.

In BENTA patients, a single heterozygous mutation in *CARD11* can have GOF features, reflected in B cell proliferation and constitutive NF-κB activity in B and T cells, and at the same time LOF features, associated with T cell anergy upon stimulation. To date, this has been attributed to a consequential failure of CARD11 autoinhibition leading to constitutive formation of the CBM complex and IκB-α degradation, thereby activating NF-κB (142, 146). However, the origin of the anergic phenotype has not been identified, yet. Here, we detected some very mild enhancement of NF-κB by C49Y CARD11 in basal and stimulated condition but we could not reproduce this clear constitutive NF-κB activity upon overexpression of C49Y and E134G *CARD11* described previously (142, 146). Based on the activating signal from the CBM complex without co-receptor stimulation, we speculated that this single signal could provoke NF-AT driving anergy. In addition, patient T cells exhibited a lack of JNK phosphorylation, which could result in decreased AP-1 activity and thus, promote expression of anergy-associated NF-AT target genes. (142). However, we did not find any modulation of NF-AT activity by mutant CARD11 and there was only slightly enhanced AP-1 activity by expression of C49Y but not E134G CARD11 upon anti-CD3/CD28 stimulation.

Comparing the mutant CARD11 protein levels, the C49Y and E134G CARD11 protein levels were comparatively low. This was true not only in our study but also in the stable overexpression by Chan et al. and the transient co-expression by Snow et al. (142, 146). This could indicate, for example, inherent instability of mutant CARD11, endogenous counter-regulation leading to degradation of mutant CARD11, or severe deleterious effects leading to premature cell death upon exceeding a critical level of mutant CARD11. These processes may be regulated differently in B and T cells, leading to the dichotomy observed in BENTA patients:

While B cells can cope with mutant CARD11 and the resulting amplification of NF-κB signaling, T cells may have evolved mechanisms to counteract, including the induction of an anergic state independent of NF-AT activation.

Regardless of their LOF or GOF classification, certain overexpressed mutant CARD11 variants resulted in persistent NF-AT activity in a subset of cells. Follow-up experiments to elucidate this phenomenon were inconclusive, as the NF-AT activity did not respond to calcineurin regulation, nor did it appear to affect the NF-κB or AP-1 pathways. Therefore, we hypothesize that the observed persistent eGFP signal may not be directly attributable to NF-AT induction but may instead result from aberrant epigenetic activation or the positional effect of reporter gene integration within a highly transcriptionally active genomic region in these cells.

A close analysis of previous studies on CADINS- and BENTA-associated *CARD11* mutations revealed that some mechanistic *in vitro* studies were performed in *CARD11*-deficient Jurkat T cells overexpressing mutant *CARD11* homozygously. In this setting, C49Y and E134G CARD11 indeed significantly induced constitutive activation of NF-κB (142, 144). In contrast, upon ectopic, transient overexpression of mutant *CARD11* in WT T cells, aberrant T cell activation is much weaker, especially compared to WT *CARD11* overexpressing cells (142, 270). On the other hand, stable overexpression of C49Y *CARD11* in WT Jurkat T cells clearly induces constitutive NF-κB activity as detected by EMSA (146). Similar differences based on the choice of expression system occurred for the CADINS-associated R975W *CARD11*. While homozygous transient expression of E57D, L194P, and R975W *CARD11* significantly impeded NF-κB activation, this effect was substantially reduced by heterozygous transient expression of R975W *CARD11* compared to the other mutants (139). Taken together, these results suggest that the protein level of mutant CARD11 on the one hand and the ratio of additional WT CARD11 on the other hand are critical factors that regulate the severity of perturbations by mutant CARD11. Furthermore, this is modulated differently by transient and stable mutant *CARD11* expression and varies between individual mutations. Indeed, in our experiments, the protein levels of C49Y and E134G CARD11 were significantly lower than endogenous WT CARD11, which may explain the weak effects on downstream signaling and is a limitation of the study.

However, our experimental approach using stable overexpression of mutant *CARD11* closely approximates the cellular conditions observed in patient lymphocytes. Given the moderate effects reported in previous studies using heterozygous mutant *CARD11* expression, we are confident that our experimental design provides a close representation of the signaling dynamics present in patient-derived lymphocytes (139, 142, 270).

The observation that the effect of mutant CARD11 on signaling is more subtle than expected supports the notion that patient phenotypes may arise from more than impaired NF-κB activity. It suggests that the perturbations in CBM complex formation and function may extend their influence to other signaling axes, potentially beyond the scope of AP-1 and NF-AT. This interplay of multiple, nuanced alterations within the cellular signaling network may culminate in the diverse clinical manifestations associated with the diseases.

4.2 The SARS-CoV-2 Nsp14 stimulates host cell NF-κB activity

When SARS-CoV-2 infects human cells, it disrupts cellular homeostasis and triggers immune responses. Systematic mapping of the SARS-CoV-2 human contactome revealed protein-protein interactions associated with the human immune response. Considering the severely dysregulated NF-κB activity leading to hyperinflammation in COVID-19 patients, we used these results as a starting point to investigate the molecular mechanism of how SARS-CoV-2 induces NF-κB signaling in host cells.

4.2.1 Full length Nsp14 with active MTase domain stimulates NF-κB

Based on the results of the systematic virus-host cell interactome, we tested all viral proteins associated with immune response proteins for their ability to activate NF-κB. We identified Nsp14 as the SARS-CoV-2 protein that induces NF-κB activity in a dose-dependent manner. By testing Nsp14 variants derived from SARS-CoV-2 virus variants as well as from other human coronaviruses, we found that this is a more general property of Nsp14.

The Nsp14 protein level of the different human coronaviruses and the level of induced NF-κB activity were positively correlated, as SARS-CoV-1 and MERS-CoV Nsp14 were well expressed and both induced NF-κB even more than SARS-CoV-2 Nsp14. Both diseases are also characterized by a strong inflammatory response with increased levels of cytokines and

chemokines, suggesting comparable activation mechanisms (165, 166). In contrast, Nsp14 derived from other human coronaviruses was expressed rather weakly and no activation of NF-κB was detected, which probably contributes to the mild symptoms caused (160). In particular, the protein stability of HCoV-OC43-derived Nsp14 appears to be tightly regulated, as shown in the titration experiment. Taken together, these observations indicate that the stability of the Nsp14 protein varies among human coronaviruses. The observed association between reduced levels of Nsp14 and decreased NF-κB activation suggests that therapeutic targeting of Nsp14 may reduce the severity of the symptoms it induces. However, the consequences of NF-κB induction by Nsp14 appear to be additionally individually regulated among the different human coronaviruses. This is suggested by the expression of Nsp14 derived from HCoV-229E, which resulted in protein and NF-κB activity levels comparable to those of Nsp14 derived from SARS-CoV-2. However, infection with HCoV-22E is associated with only mild cold-like symptoms, suggesting an additional regulation controlling the NF-κB-induced inflammatory response (160).

To elucidate the molecular mechanisms driving Nsp14-induced host cell NF-κB signaling, we performed a systematic evaluation of Nsp14 domains and enzymatic functions. Notably, the two domains of Nsp14 are structurally interdependent, although they exhibit independent enzymatic activities and this is reflected in their ability to induce NF-κB (207, 271). Removal or truncation of either domain resulted in complete prevention of NF-κB activation, a finding consistent with the results reported by Li et al. (272). Interestingly, mutation of the ExoN catalytic center had no effect on NF-κB induction. Instead, genetic inactivation of the MTase catalytic center led to a complete inhibition of Nsp14-triggered NF-κB activation, which is corroborated by findings from another study (234). The Nsp14 MTase domain acts without recognition of sequences that mark viral RNA and can substitute for homologous enzymes in other organisms (271). Thus, even in the absence of assistance from other viral proteins, Nsp14 may be able to affect the capping of host cell RNAs. This could disrupt host cell mRNA homeostasis and consequently the levels of endogenous proteins. Changes in the expression levels of either direct regulators of the NF-κB pathway, such as A20 or IκB-α, or modulating enzymes, such as kinases or ubiquitin ligases, which modify the signaling pathway that activates NF-κB through their enzymatic activities, could then culminate in NF-κB activation.

As a second approach to verify the importance of the MTase enzymatic activity, we used different inhibitors targeting the Nsp14 MTase domain: Both nitazoxanide and pyridostatin have been identified as inhibitors of Nsp14 MTase activity in *in vitro* screens and reduced virus replication in cell-based assays (252, 255, 256). As positive controls, we used the standard MTase inhibitor and SAM analog sinefungin. However, none of the inhibitors affected the Nsp14-induced activation of NF-κB. This may indicate that the modes of action of these compounds, which remain undefined for SARS-CoV-2 Nsp14, may not target the molecular mechanism of Nsp14 to activate NF-κB. In addition, the concentrations of inhibitors may not have been sufficient to affect the overexpressed Nsp14 in our model, especially considering that the levels of active enzyme may be lower during natural viral infection or in the context of antiviral assays and recombinant protein studies. Moreover, several cellular factors may contribute to the reduced efficacy of these compounds in our assays. Cellular mechanisms may limit the intracellular accumulation of inhibitors, either by restricting their uptake, accelerating their metabolism, or actively exporting them, thus reducing their effective concentrations and consequently their inhibitory potential on Nsp14. Furthermore, the binding affinity of the inhibitors to the MTase domain of Nsp14 may be too weak to compete with the enzyme's natural substrate, SAM, in the cellular milieu. Besides, endogenous MTase enzymes within the cell may have higher affinities for these inhibitors, thus reducing their inhibitory effects on Nsp14. Nevertheless, there is a growing number of studies with *in silico* and *in vitro* screens, proposing a variety of Nsp14 MTase inhibitors which efficacy and ability to cross plasma membranes remain to be verified *in vivo* (250-253).

In addition to the critical role of the MTase domain, our study demonstrated that the cofactors of both Nsp14 domains, SAM and Nsp10, contribute to increased Nsp14 protein levels as well as NF-κB induction. This finding is consistent with previous research highlighting the stabilization of Nsp14 upon co-expression with Nsp10, as well as the addition of SAH, which is a by-product of the MTase reaction (207, 225). While there is a crystal structure resolving how Nsp10 stabilizes Nsp14, there is currently no structural analysis of Nsp14 in complex with SAH (224). However, we propose that the binding of SAM strengthens the conformation of the flexible SAM binding region, similar to the Nsp10-induced stabilization (208). Considering the dose-dependent relationship between Nsp14 and NF-κB activation, which mirrors the

correlation observed between the viral load in patients and the extent of their inflammatory responses, we suggest that the enhanced NF-κB activity is directly linked to the accumulation of Nsp14 protein (150, 190). However, the presence of the co-substrate may also enhance the enzymatic activity of Nsp14 MTase, which is essential for NF-κB induction. In addition, SAM supplementation may affect NF-κB through several other pathways, as evidenced by the mild NF-κB induction in IKK-β overexpressing controls and presented in the existing literature (273-276). Nevertheless, SAM does not stabilize IKK-β protein levels, suggesting a separate mode of action with Nsp14.

In conclusion, we have shown that the expression of Nsp14 alone is sufficient to induce NF-κB in the host cell. This Nsp14 function requires the full-length protein with the enzymatically active N7-MTase domain. Furthermore, this NF-κB inducing activity of Nsp14 is present in all SARS-CoV-2 variants as well as other human coronaviruses.

4.2.2 Nsp14 is instable without viral accessory proteins

As a next step, we wanted to understand how Nsp14 interacts with host cell signaling pathways leading to NF-κB activation. Therefore, we generated cells with stable or inducible Nsp14 expression as a valuable tool and found that WT Nsp14 and, to a lesser extent, D331A Nsp14 are inherently unstable.

Both approaches, lentiviral infection allowing for stable expression and doxycycline-inducible expression of Nsp14, resulted in substantially low protein levels, with significantly less WT Nsp14 compared to D331A Nsp14. This could not be reversed by increasing the dose of doxycycline in the inducible Nsp14 expressing cells. The strong and equivalent expression of CD2 in the stably Nsp14-expressing cells as well as equal transcript levels of WT and D331A Nsp14 detected in both cell lines inducibly expressing Nsp14 suggest that the Nsp14 genes are transcribed equally. Inhibition of proteasomal degradation showed that especially active Nsp14 was stabilized, suggesting that the Nsp14 protein is unstable and degraded. This implies that host cells tightly control the expression, stability, and activity of Nsp14 due to its potential negative impact on cellular functions. The use of proteasomal degradation as a defense mechanism against viral proteins has been extensively studied for other viruses, such as HIV-1 (277, 278). Therefore, we speculate that the cells recognize Nsp14 as non-self and its

N7-MTase activity as potentially harmful and thus initiate its removal. In addition, cells stably expressing Nsp14 appeared to downregulate Nsp14 gene transcription in the long term, as indicated by significant loss of hΔCD2 expression. Silencing of integrated transgenes is also a well-known defense mechanism of infected host cells and appears to be applied in cells with genomic integration of Nsp14 (279).

Our previous finding, that Nsp14-Nsp10 interaction stabilizes Nsp14 and enhances its ability to induce NF-κB activation implicates a strong cooperativity between viral factors in influencing human immune and inflammatory responses. On this basis, we anticipate that working with *in vitro* SARS-CoV-2 infections would provide the full spectrum of viral accessory factors that contribute to Nsp14 stabilization and counteraction of host cell defense mechanisms. Moreover, such studies could reveal the physiological levels of Nsp14 present in cells from infected patients, thus avoiding the potential artifact of overexpression inherent in our current assays. It is important to acknowledge that the forced overexpression of Nsp14 protein levels in our study may be a limitation, as it may induce cellular stress responses and activate innate defense mechanisms. As a result, dissecting the nuances of host defenses upon artificial induction of high levels of Nsp14 may not accurately and exclusively reflect the immune response elicited during natural viral infection.

Overall, active Nsp14 protein levels are consistently maintained at a low equilibrium within the host cell, reflecting robust cellular regulatory mechanisms. This underscores the effective response of the host cell, which employs defense mechanisms to mitigate the potential damage resulting from Nsp14 enzymatic activity.

4.2.3 Nsp14 induces NF-κB activity via the canonical signaling pathway

To address the unresolved question of how Nsp14 interferes with host cell signaling pathways culminating in NF-κB activation, we continued to work with transient overexpression of Nsp14 and analyzed the NF-κB-inducing upstream signaling pathways as well as NF-κB target gene expression. We found that there was very little NF-κB target gene expression from endogenous loci but could specify that Nsp14 acts on NF-κB via NEMO and p65.

Based on the hypothesis that Nsp14 N7-MTase activity may modify host cell mRNA and thus either protein levels of direct NF-κB pathway proteins or modulating enzymes, leading to

variations in modifications such as phosphorylation, we analyzed the canonical and non-canonical signaling pathway by WB. However, in contrast to overexpressed IKK-β, there was no detectable activation of either pathway upon expression of Nsp14. Therefore, we focused on downstream effects and analyzed the transcriptional activity of NF-κB towards endogenous gene loci. Overexpression of active Nsp14, but not D331A Nsp14, induced transcription of the NF-κB target gene *CXCL8*, consistent with *in vitro* studies by Zaffagni et al. and Li et al. as well as consistently elevated levels of IL-8 in the blood and lungs of patients (151, 184, 188, 189, 234, 272). As an aside, previous studies have proposed that IL-8 counteracts the interferon response to viral infection and facilitates viral replication (280, 281). Also in the context of SARS-CoV-2 infection, this property of IL-8 may contribute to the overall deficiency in the interferon response and may account for its prominent upregulation in COVID-19 patients.

Except for *CXCL8*, which induction was extremely mild compared to the overexpression of IKK-β, there was no transcription of other classical NF-κB target genes such as *NFKBIA*, *TNFAIP3* or *ICAM1* induced by Nsp14. Surprisingly, the addition of TNF-α stimulation, Nsp10 co-expression or SAM supplementation did not increase target gene expression, even though Nsp14 protein was stabilized by Nsp10 and SAM. This is in stark contrast to the strong enhancement of NF-κB activity we detected with ectopically expressed reporter plasmids. Although similar studies reported increases in *IL6* and *NFKBIA* transcripts in addition to *CXCL8* under analogous experimental conditions, they also failed to show elevated transcript levels of a broader panel of NF-κB target genes (234, 272). Our attempts to replicate these findings were unsuccessful, as our reanalysis of the RNA sequencing data from Zaffagni et al. did not confirm a significant increase in *NFKBIA* levels, or in any other NF-κB target gene, nor was *IL6* induction evident in our samples (data not shown). In addition, our findings contradict results from *in vitro* SARS-CoV-2 infection of A549 cells, which stimulated the transcription of numerous NF-κB target genes (196). Comparing the studies, we suggest that different experimental setups and cellular environments provide different insights into the underlying mechanism. First, the firefly reporter plasmid is transiently expressed outside the genomic environment and is therefore readily accessible to NF-κB. Conversely, NF-κB binding sites within the promoter regions of endogenous loci may be inaccessible within chromatin structures and require remodeling for efficient target gene transcription. Second, the use of

different cell lines provides variant protein levels across the proteome, which is an additional factor that may influence the efficiency of Nsp14 in modulating NF-κB signaling. And third, as discussed above, Nsp14 is not stable and therefore protein levels are difficult to control when overexpressed in cells, whereas *in vitro* SARS-CoV-2 infections provide the full viral environment. Thus, Nsp14 alone can promote NF-κB activity, but full induction of target genes from endogenous loci requires the involvement of additional viral or host elements, possibly involving mechanisms for chromatin decondensation.

Knowing that Nsp14 does not directly modify the canonical or non-canonical NF-κB pathway, we followed up on the findings from the virus-host interactome. According to the yeast two-hybrid screen results, Nsp14 binds to the NF-κB pathway proteins TRAF2, NEMO and c-Rel. Despite of this, we could not detect stable protein-protein interactions between Nsp14 and any of the putative human binding partners. However, a transient or unstable interaction may not be detectable by our assay.

Besides, a proteomic screen identified inosine 5'-monophosphate dehydrogenase 2 (IMPDH2) as a potential binding partner of Nsp14, with pull-down assays confirming this interaction (235, 272). This Nsp14-IMPDH2 complex is postulated to enhance the enzymatic activity of IMPDH2, which has been implicated as a critical factor in Nsp14-driven NF-κB activation (234, 272). However, the primary role of IMPDH2 is known to be in *de novo* GTP biosynthesis, regulating nucleotide metabolism, a pathway of particular interest in oncology (282, 283). Consequently, the direct link between IMPDH2 activity and NF-κB signaling remains tenuous, with studies reporting conflicting results regarding its effect on NF-κB as well as other pathways such as p38, JNK1/2, ERK1/2, and AKT (284-286). The exact molecular mechanisms remain elusive, suggesting that IMPDH2 may exert a more general modulation of cellular signaling networks. Furthermore, the specific mechanistic details of how the Nsp14-IMPDH2 interaction influences NF-κB signaling during SARS-CoV-2 infection have not been elucidated (234, 272). Zaffagni et al. hypothesized that Nsp14-induced IMPDH2 activity increases intracellular GTP levels, which in turn are required for capping, and thus may promote Nsp14 MTase activity. However, this hypothesis does not directly explain how Nsp14 MTase activity leads to increased levels of NF-κB activity.

In contrast, our series of gene KO experiments revealed that Nsp14 induces NF-κB via the canonical signaling pathway requiring NEMO and p65, whereas the putative binding partners TRAF2 and c-Rel as well as RelB are not required for Nsp14-induced NF-κB activity. The KO of *IKBKG* completely abolished NF-κB activation upon stimulation with TNF-α and significantly prevented Nsp14-induced NF-κB activation, suggesting the functional involvement of NEMO in Nsp14-driven NF-κB activation. Nevertheless, the residual level of NF-κB activity observed after Nsp14 expression in the *IKBKG* KO cells suggests that Nsp14 still elicits some NF-κB transcriptional response, presumably through a NEMO-independent mechanism. Furthermore, Nsp14 relies on p65, a protein not initially identified in our Nsp14 contactome, instead of c-Rel to initiate NF-κB signaling. This observation is consistent with previous research demonstrating p65 phosphorylation and translocation following SARS-CoV-2 infection and *in vitro* Nsp14 expression (196, 272). This observed discrepancy between the contactome results, and our functional data could be attributed to the structural similarity of c-Rel and p65, as both proteins have identical functional domains, overlapping activation triggers and target genes (260). This functional redundancy may also extend to Nsp14-mediated NF-κB activation, where they may compensate for each other depending on their expression levels in different cell types. Notably, NF-κB signaling induced by SARS-CoV-2 plays a dual role, contributing both to the cytokine storm during infection and facilitating viral replication. *In vitro* experiments using A549 lung cells have demonstrated the essential role of NEMO, c-Rel and p65 in SARS-CoV-2 replication (196, 242). This supports the hypothesis that c-Rel and p65 may act in a compensatory manner. Further studies are needed to determine whether Nsp14-triggered NF-κB activation is responsible for driving SARS-CoV-2 replication and to explore whether variations in the requirement for c-Rel and p65 are associated with specific cell types. In conclusion, Nsp14 triggers NF-κB transcriptional activity through the canonical signaling pathway, relying on NEMO and p65, with *CXCL8* as a key target gene. Notably, there is no involvement of the non-canonical RelB in NF-κB transcriptional activation.

Our results lead us to hypothesize that the MTase enzymatic activity of Nsp14 is critical, potentially modifying viral or host mRNAs to modulate NF-κB transcriptional activity. This action is likely to result in the primary enhancement of the transcriptional activity of canonical NF-κB complexes, including p65, as opposed to serving as an initial activator of NF-κB. This

proposed model suggests that Nsp14 does not directly trigger upstream NF-κB signaling, but rather amplifies the basal NF-κB activity inherent in cells, as demonstrated by the residual activity in *IKBKG* KO cells. A similar phenomenon has been observed with respiratory syncytial virus and a comparable mechanism is conceivable (287).

Also, the stimulation of NF-κB may result from the orchestrated action of several different stimuli in addition to Nsp14 MTase activity. On the one hand, several studies have implicated other SARS-CoV-1 proteins, such as E, N, S, 3a and 7a, in the stimulation of NF-κB, which may also apply to their analogues in SARS-CoV-2 (288-291). On the other hand, virus-induced innate immune signaling such as TLR, RIG-I or MDA5 downstream signaling as well as ER stress may also contribute to the stimulation of NF-κB (157, 161, 292). The synergy of these concurrent SARS-CoV-2-induced inflammatory triggers including Nsp14 may culminate in a modest activation of NF-κB, sufficient to initiate cytokine and chemokine release. As the infection progresses, positive feedback loops may amplify this response, generating a stronger wave of NF-κB activation, resulting in the release of even more cytokines and the start of a vicious cycle of inflammation.

4.3 Conclusion and perspectives

The engagement of T cell receptors initiates a complex signaling network that ultimately converges on the induction of three key transcription factors, specifically NF-κB, AP-1, and NF-AT. Together, they orchestrate a highly pathogen-specific immune response characterized by a distinct profile of target gene expression.

We have generated a Jurkat T cell line containing the NF-κB, AP-1 and NF-AT response elements linked to the expression of the fluorescent proteins eCFP, mCherry and eGFP and demonstrated their advantages for comprehensive quantification of transcriptional activities by flow cytometry. A future application is a CRISPR-Cas9 KO screen that, when coupled with various T cell treatments - ranging from different types of stimulation and inhibitors to the incorporation of disease-related mutations - can facilitate an in-depth dissection of TCR signaling pathways. Such an approach would elucidate the roles of specific proteins within the TCR signaling complex, delineate the contributions of co-receptor pathways to various downstream signaling events, and unravel the intricate signaling networks that link receptor

activation to transcription factor responses. In addition, the use of cell sorting techniques to enrich populations based on changes in transcriptional activity, with subsequent mass spectrometry or RNA sequencing analysis of these populations, may reveal previously unrecognized regulators in T cell signaling pathways.

In this study, we used the new TTR Jurkat T cell line to decipher potential transcriptional crosstalk upon expression of patient-derived CADINS and BENTA-associated *CARD11* mutations. However, we could not identify any significant aberrant activity of AP-1 or NF-AT induced by mutant CARD11. In both diseases, the *CARD11* mutations are mainly located in the CARD and coiled-coil domain, which facilitate the CARD11 autoinhibition. Previous studies have shown that some mutations promote CBM complex formation, while others disrupt it (138, 141, 146). It would be interesting to model these different mutations in a CARD11 structure to understand whether there is a mechanistic pattern of how single point mutations can efficiently modulate the autoinhibition. Furthermore, this could provide insights into what other protein interactions between the CBM complex and signaling molecules might be affected and consequently contribute to the different symptoms of the patients. Besides, the generation of *CARD11* KO TTR Jurkat T cells and reconstitution with mutant CARD11 only would allow for generally stronger phenotypes and potentially reveal mild effects on AP-1 and NF-AT. Finally, cells with highly aberrant NF-κB, AP-1 or NF-AT could be enriched by cell sorting and subsequently analyzed by mass spectrometry for modulated protein levels or post-translational modifications involved in T cell signaling. By incorporating these approaches, knowledge gained from the study of oncogenic CARD11 mutations should be integrated into the analysis. Such studies have already contributed to a comprehensive understanding of the role of CARD11 in CBM complex assembly and the perturbations caused by disease-associated mutations (293-295). The use of this knowledge will be of great value in our exploration of the molecular basis of CARD11-associated pathologies.

In the second part of this study, we focused on elucidating the process that allows for disproportionate stimulation of NF-κB during SARS-CoV-2 infection of human host cells. The NF-κB-induced cytokine storm syndrome in COVID-19 patients is characterized by excessive levels of cytokines and chemokines and is one of the major causes of severe disease progression (185, 186, 191). Therefore, elucidation of the molecular mechanisms underlying

this potent NF-κB activation is the necessary basis for the development of targeted treatment options. Mechanistically, we have shown that full-length Nsp14 with N7-MTase catalytic activity is central to the stimulation of canonical NF-κB activity. The necessity of the catalytically active methylase domain implies that Nsp14 may also modify endogenous host mRNA. However, it is still unclear how this would be spatially regulated, as Nsp14 localizes to viral double-membrane vesicles in the cytosol to modify viral RNA but would need to translocate to the nucleus to target host mRNA. Various imaging studies have localized Nsp14 primarily to the cytosol but could not rule out nuclear Nsp14 (248, 296-299). It would be interesting to determine whether the virus provides a transport mechanism with its own proteins or whether it can hijack a host cell machinery for this Nsp14 translocation. In addition, it will be of particular interest to determine which host mRNAs are affected, whether Nsp14 follows a selective or non-selective pattern, and to elucidate the underlying mechanisms culminating in the activation of NF-κB.

Overall, the results of this study provide an important element in the understanding of how SARS-CoV-2 infection leads to NF-κB hyperactivation in COVID-19 patients. Together with the wealth of other SARS-CoV-2 studies, this lays the foundation for the development of targeted anti-inflammatory treatments that either specifically target the SARS-CoV-2 Nsp14 MTase domain or interfere with the Nsp14-dependent activation of NF-κB further downstream in the mechanism.

5 Materials

5.1 Instruments and equipment

Agarose gel chambers	NeoLab, Heidelberg
Attune Acoustic Focusing Cytometer	Thermo Fisher Scientific, Waltham, USA
Autoclave – VX-95	Systec, Linden
Bacterial culture flasks/tubes	Schott, Zwiesel; BD, Heidelberg
Cell culture centrifuge, 5804	Eppendorf, Hamburg
Cell culture flasks	BD, Heidelberg
Cell culture flasks/plates	BD, Heidelberg; Nunc, Wiesbaden
Cell culture plates	BD, Heidelberg; Nunc, Rochester, USA
Cell scraper	Sarstedt, Newton, USA
Cell strainer (100 µM)	NeoLab, Heidelberg
Cell viability analyzer - ViCell-XR	Beckman Coulter, Krefeld
Cell-counting chamber Neubauer	NeoLab, Heidelberg
Centrifuge Beckman Avanti J-26 XP	Beckman Coulter, Krefeld
Centrifuges - 5810R, 5417R, 5471C, 5804	Eppendorf, Hamburg
CO_2 incubators	Binder, Tuttlingen
Cooling cell culture centrifuge, 5810R	Eppendorf, Hamburg
Cooling table centrifuge, 5417R	Eppendorf, Hamburg
Cryo tubes	Greiner Bio-One, Frickenhausen
Electroporation cuvettes, Gene Pulser	Bio-Rad, München
Electroporator - Gene Pulser Xcell System	Bio-Rad, München
Eppendorf tubes	Eppendorf, Hamburg
FACS tubes	BD, Heidelberg; Wagner & Munz, München
Falcon tubes	BD, Heidelberg
Filter pipette tips - TipOne	StarLab, Hamburg
Freezers and Fridges	Liebherr, Ochsenhausen
Gel Documentation System - Intas Gel iX Imager	Intas, Göttingen
Heatblock	Techne, Staffordshire, UK
Ice machine – Scotsman AF20	Scotsman Ice Systems, Vernon Hills, USA
Incubator shaker – I 26	New Brunswick Scientific, Hamburg
Incubators	Sartorius, Göttingen; Heraeus, Hanau
LightCycler plates 96 well	4titude, Berlin
LightCycler480	Roche, Mannheim
Magnetic stirrer	NeoLab, Heidelberg
Micro scales, scale	Kern & Sohn, Balingen

Microscopes	Leica, Wetzlar
Microwave	SHARP, Hamburg
Nanodrop 2000	Thermo Fisher Scientific, Waltham, USA
Petri dishes	Greiner Bio-One, Frickenhausen
pH meter - inoLab pH7110	WTW, Weilheim
Pipette tips	Eppendorf, Hamburg
Pipettes - Reference	Eppendorf, Hamburg
Pipetting aid - accu-jet pro	Brand, Wertheim
Plastic filter tips TipOne (RNase free)	StarLab, Hamburg
Plastic pipettes	Greiner Bio-One, Frickenhausen
Plastic tips	Eppendorf, Hamburg
Power supplies - EV202, EV243	Consort, Turnhout, Belgium
Precision scale – New Classic MS	Mettler Toledo, Gießen
PVDF membrane	Merck Millipore, Darmstadt
Rotator – Intelli-Mixer	NeoLab, Heidelberg
SDS-PAGE chamber	Roth, Karlsruhe
Semi-dry blotter	PHASE, Lübeck; Peqlab, Erlangen
Serological pipettes - Cellstar	Greiner Bio-One, Frickenhausen
Shaker - Polymax 1040	Heidolph Instruments, Schwabach
Syringes	Braun, Melsungen
Table centrifuge, 5471C	Eppendorf, Hamburg
Thermocycler	Eppendorf, Hamburg
Thermocycler – Mastercycler gradient	Eppendorf, Hamburg
Tissue Culture Hoods Safeflow 1.2	Nunc, Wiesbaden
Ultra-pure water system - Milli-Q Plus	Merck Millipore, Darmstadt
ViCell-XR cell viability analyzer	Beckman Coulter, Krefeld
Vortexer	Heidolph Instruments, Schwabach
Western blotting transfer – PVDF-membrane, 0.45 µm	Merck Millipore, Darmstadt
Western blotting transfer – Whatman paper	Roth, Karlsruhe
Whatman paper	Roth, Karlsruhe
Berthold Centro LB960 microplate reader	Berthold, Bad Wildbad
INTAS ECL Chemostar	INTAS Science Imaging Instruments, Göttingen
BD LSRFortessa™ Cell Analyzer	BD, Heidelberg

5.2 Chemicals

5.2.1 General chemicals

Acrylamide/Bisacrylamide	Roth, Karlsruhe
Agarose	Biozym, Hessisch Oldendorf
Ammonium persulfate (APS)	Bio-Rad, München
Ampicillin	Roth, Karlsruhe
Bovine serum albumin (BSA)	Sigma-Aldrich, Taufkirchen
Calcium chloride ($CaCl_2$)	Roth, Karlsruhe
cOmplete – Protease Inhibitor Cocktail	Roche, Mannheim
Dimethyl sulfoxide (DMSO)	Roth, Karlsruhe
Dithiothreitol (DTT)	Sigma-Aldrich, Taufkirchen
DNA 1kb plus ladder	Thermo Fisher Scientific, Waltham, USA
dNTP-Mix	Thermo Fisher Scientific, Waltham, USA
DPBS (w/o $MgCl_2$ and $CaCl_2$)	Thermo Fisher Scientific, Waltham, USA
Ethanol (EtOH, p. a.)	Merck, Darmstadt
Ethidium bromide (EtBr)	Roth, Karlsruhe
Ethylenediaminetetraacetic acid (EDTA)	Roth, Karlsruhe
Gel Loading Dye, Purple (6x)	NEB, Frankfurt
GFP-Trap	Chromotek, Martinsried
Glycerol	Roth, Karlsruhe
Glycine	Roth, Karlsruhe
HEPES	Roth, Karlsruhe
Isopropyl alcohol (p.a.)	Merck, Darmstadt
Kanamycin	Roth, Karlsruhe
LB-Agar (Luria/Miller)	Roth, Karlsruhe
LB-Medium (Luria/Miller)	Roth, Karlsruhe
Magnesium chloride	Roth, Freiburg
Methanol (MeOH, p.a.)	Merck, Darmstadt
Milk powder	Roth, Karlsruhe
Monopotassium phosphate (KH_2PO_4)	Roth, Karlsruhe
Nonidet P40 substitute (NP-40)	Sigma-Aldrich, Taufkirchen
PageRuler Prestained Protein Ladder	Thermo Fisher Scientific, Waltham, USA
Polybrene	Sigma-Aldrich, Taufkirchen
Potassium chloride (KCl)	Roth, Karlsruhe
Roti-Load 1 - 4x SDS sample buffer	Roth, Karlsruhe
S.O.C. Medium	Thermo Fisher Scientific, Waltham, USA
Sodium acetate	Roth, Karlsruhe

Sodium chloride (NaCl)	Roth, Karlsruhe
Sodium dodecyl sulfate (SDS)	Roth, Karlsruhe
Sodium fluoride	Sigma-Aldrich, Taufkirchen
Sodium hydrogen phosphate (Na_2HPO_4)	Roth, Karlsruhe
Sodium vanadate	Roth, Karlsruhe
TAE buffer (50x)	Omnilab, Bremen
Tetramethylethylenediamine (TEMED)	Roth, Karlsruhe
Tris(hydroxymethyl)-aminomethan (Tris)	Roth, Karlsruhe
TritonX-100	Roth, Karlsruhe
Trizol	Thermo Fisher Scientific, Waltham, USA
Tween-20	Roth, Karlsruhe
Western blotting detection (ECL substrate) 20x LumiGlo and 20x Peroxide	Cell Signaling Technology, Frankfurt
X-tremeGENE HP Transfection Reagent	Roche, Mannheim
β-Glycerophosphate	Sigma-Aldrich, Taufkirchen

5.2.2 Cell culture

DMEM (Dulbecco's modified eagle medium)	Thermo Fisher Scientific, Waltham, USA
Fetal calf serum (FCS)	Thermo Fisher Scientific, Waltham, USA
Penicillin-Streptomycin (10,000 U/ml) (P/S)	Thermo Fisher Scientific, Waltham, USA
RPMI (Roswell Park Memorial Institute) 1640	Thermo Fisher Scientific, Waltham, USA
Trypsin (0.05%)/EDTA	Thermo Fisher Scientific, Waltham, USA
Optimem	Thermo Fisher Scientific, Waltham, USA
DMSO	Roth, Freiburg

5.2.3 Stimulants and inhibitors

Dasatinib	Biomol, Hamburg
doxycycline (DOX)	Sigma Aldrich, Taufkirchen
FK506	Santa Cruz, Heidelberg
Ionomycin	Calbiochem, Schwalbach
MG-132	Merck Millipore, Darmstadt
MLN120B	Biozol, Eching
nitazoxanide	Biomol, Hamburg
Phorbol 12-myristate 13-acetate (PMA)	Merck Millipore, Darmstadt
pyridostatin	Biomol, Hamburg
S-adenosylmethionine (SAM)	Sigma Aldrich, Taufkirchen
sinefungin	Biomol, Hamburg
Sotrastaurin	Biozol, Eching
Tumor necrosis factor alpha (TNFα)	Biomol, Hamburg

5.3 Buffers and solutions

2x HBS (HEPES buffered saline)	50 mM HEPES (pH 7), 280 mM NaCl, 1.5 mM Na_2HPO_4
4x Stacking gel buffer	0.5 M Tris (pH 6.8)
5x Separation gel buffer	1.88 M Tris (pH 8.8)
Annealing buffer	50 mM Tris-HCl (pH 8.0), 70 mM NaCl
Blocking solution (WB)	5% (w/v) milk powder in PBS-T
Blotting buffer	25 mM Tris (pH 8.3), 192 mM Glycine, 20% (v/v) MeOH
Co-IP buffer	150 mM NaCl, 25 mM HEPES (pH 7.5), 0.2% (v/v) NP-40, 1 mM glycerol, 1 mM DTT, cOmplete protease inhibitors, 10 mM NaF, 8 mM β-glycerophosphate, 300 µM sodium vanadate
High salt buffer	20 mM HEPES (pH 7.9), 350 mM NaCl, 20% (v/v) glycerol, 1 mM $MgCl_2$, 0.5 mM EDTA, 0.1 mM EGTA, 1% (v/v) NP-40, 1 mM DTT, cOmplete protease inhibitors, 10 mM NaF, 8 mM β-glycerophosphate, 300 µM sodium vanadate
Agar plates	LB (20 g/l), Agar (15 g/l)
LB medium	25 g/l
PBS (phosphate buffered saline)	137 mM NaCl, 2.7 mM KCl, 10 mM Na_2HPO_4, 1.7 mM KH_2PO_4
PBS-T	0.1% (v/v) Tween-20 in PBS
SDS Electrophoresis buffer	25 mM Tris (pH 8.8), 192 mM Glycine, 0.1% (w/v) SDS
Separation gel	375 mM Tris (pH 8.8), 7.5-15% (v/v) Acrylamide, 0.1% (w/v) SDS, 0.1% (w/v) APS, 0.1% (v/v) TEMED
Stacking gel	125 mM Tris (pH 6.8), 3% (v/v) Acrylamide, 0.1% (w/v) SDS, 0.1% (w/v) APS, 0.1% (v/v) TEMED
TBE buffer	Tris (50 mM), Boric acid (50 mM), EDTA (1 mM), pH 8.3

5.4 Kits and enzymes

Herculase II DNA Polymerase	Agilent Technologies, Waldbronn
NucleoSpin Gel and PCR Clean-up Kit	Macherey-Nagel, Düren
NucleoSpin Plasmid Mini Kit	Macherey-Nagel, Düren
Plasmid Maxi Kit	Macherey-Nagel, Düren
Proteinase K	NEB, Frankfurt
QIAshredder	Qiagen, Hilden
Restriction enzymes	Qiagen, Hilden
Restriction buffers	Qiagen, Hilden
RNeasy RNA isolation Kit	Qiagen, Hilden
T4 DNA ligase	NEB, Frankfurt
Takyon™ No ROX SYBR 2X MasterMix blue dTTP	Eurogentec, Seraing, Belgium
Verso cDNA Synthesis Kit	Thermo Fisher Scientific, Waltham, USA
Dual Luciferase System 1000 Assays	Promega, Madison, USA

5.5 Plasmids and Oligonucleotides

5.5.1 Vectors

Table 5-1: List of general vectors.

General vector	Information
pHAGE-PGK-L1-hΔCD2-T2A-Flag-Strep-Strep (pHAGE-SSF; mock)	Lentiviral vector. Obtained from Dr. Marc Schmidt-Supprian. Flag-Strep-Strep-Tag was cloned into pHAGE-PGK-L1-hΔCD2-T2A by *SalI*/*BamHI*.
pEF-3x FLAG (3xF)	Basis vector pEF4HIS-C (Invitrogen). His sequence was replaced by three repeating Flag sequences (*HindIII*/*KpnI*, D. Krappmann).
pEF-HA	Basis vector pEF4HIS-C (Invitrogen). His sequence was replaced by HA sequences (*HindIII*/*BamHI*, A. Eitelhuber)
pX458	Cas9 from S. pyogenes with 2A-EGFP, and cloning backbone for sgRNA (addgene #52961; gifted by F. Zhang)
LentiCRISPR v2	Cas9 from S. pyogenes in lentiviral vector with puromycin selection marker, cloning backbone for sgRNA (addgene #48138; gifted by F. Zhang)
pMD2.G	Lentiviral envelope plasmid (addgene #12259; gifted by D. Trono)
psPAX2	Lentiviral packaging plasmid (addgene #12260; gifted by D. Trono)
pLV-tTRKRAB-red	cDNA of RFP was transferred into pLV-tTRKRAB empty plasmid (S. Pfeiffer, addgene #12249; gifted by D. Trono)
pEGFP-C1	Mammalian expression vector for N-terminal eGFP-tagged protein expression (Clontech)
pEF-3xF-A20	cDNA of A20 was transferred into pEF-3xF empty plasmid (*EcoRI*/*NotI*; H. Yin)
pHAGE-SSF-L251P CARD11	cDNA of CARD11 mutant 2 N-terminally tagged with StrepTagII was transferred into pHAGE empty plasmid (M. Bognar)
pcDNA-3xF-cRel	cDNA of cRel was transferred into pcDNA empty plasmid (addgene #27253; gifted by T. Gilmore)
pRK5-3xF-IKKβ	cDNA of IKKβ was transferred into pRK5 empty plasmid (D. Krappmann)
IKKβ-eGFP	cDNA of IKKβ was transferred into pEGFP-N1 empty plasmid (D. Krappmann)
pcDNA3-3xF-NEMO	cDNA of NEMO was transferred into pcDNA3 empty plasmid (D. Krappmann)

pMH-F-HA-SARS-CoV-2 POI POI: E, N, Nsp9, Nsp14, Nsp16, Nsp6, Nsp7	Viral gene sequences were synthesized based on SARS-CoV-2 Wuhan-Hu-1, NCBI reference NC_045512.2, start and stop codons were added by site-directed mutagenesis and transferred into pMH-Flag-HA empty plasmid (addgene #101766, B. Weller)
pEF-3xF-TRAF2	cDNA of TRAF2 was transferred into pEF-3xF empty plasmid (T. Gehring)

Table 5-2: List of vectors generated for this study.

Additional vectors	**Information**
pHAGE-NF-κB-eCFP	NF-κB response element coupled to cDNA of eCFP was transferred into pHAGE empty vector (*SalI/XbaI*)
pHAGE-AP-1-mCherry	AP-1 response element coupled to cDNA of mCherry was transferred into pHAGE empty vector (*SalI/BamHI*)
pHAGE-NF-AT-eGFP	NF-AT response element coupled to cDNA of eGFP was transferred into pHAGE empty vector (*SalI/BamHI*)
pHAGE-SSF-CARD11 variants: WT, R30W, C49Y, E57D, E134G, L194P, R975W	cDNA of CARD11 variants were transferred into pHAGE-SSF empty plasmid (*NotI/BamHI;* templates were gifted from A. Snow)
pEF-3xF-Nsp14 variants: WT, A394V (δ), I42V (ο)	cDNA of Nsp14 variants were transferred into pEF-3xF empty plasmid (*NotI/BamHI;* templates were gifted from P. Falter-Braun)
pEF-3xF-Nsp14 origins: SARS-CoV-2, SARS-CoV-1, MERS-CoV, HCoV-OC43, HCoV-229E, HCoV-NL63	cDNA of Nsp14 variants from different viral origins were transferred into pEF-3xF empty plasmid (*NotI/BamHI;* templates were gifted from P. Falter-Braun)
pEF-3xF-Nsp14 variants: ΔN-Term, ΔExoN, ΔN7-MTase, D90A E92A, D331A, D90A E92A D331A	Mutations were introduced by site-directed mutagenesis. cDNA of Nsp14 was transferred into pEF-3xF empty plasmid (*NotI/BamHI)*
pHAGE-SSF-Nsp14 variants: WT, D331A	cDNA of Nsp14 variants were transferred into pHAGE-SSF empty plasmid (*XbaI/SalI*)
pLVTHM-Nsp14 variants: WT, D331A	cDNA of Nsp14 variants were transferred into pLVTHM empty plasmid (NEBuilder)
eGFP-Nsp14	cDNA of Nsp14 variants were transferred into pEGFP-C1 empty plasmid (*Xho1 / BamHI*)
pEF-3xF-Nsp10	cDNA of Nsp10 was transferred into pEF-3xF empty plasmid (NotI/BamHI; template was gifted from P. Falter-Braun, sequence

	based on SARS-CoV-2 Wuhan-Hu-1, NCBI reference NC_045512.2)
pEF-3xF-p65	cDNA of p65 was transferred into pEF-3xF empty plasmid (*Not I / BamHI;* addgene #21966)

5.5.2 Sequences of used sgRNA

Table 5-3: List of sgRNAs used and vectors into which they were ligated.

Name	Sequence (5'– 3')	Targeted exon	vector
TRAF2 sgRNA #1	GCCGGGCTGTAGCAACTCCA	Exon 2	pX458
TRAF2 sgRNA #2	AGGCCCTTCCAGGCGCAGTG	Exon 2	
IKBKG sgRNA #1	TGCATTTCCAAGCCAGCCAG	Exon 3	pX458
IKBKG sgRNA #2	GCTGCACCATCTCACACAGT	Exon 2	
RELA sgRNA #1	CAAGTGCGAGGGCGCTCCG	Exon 3	LentiCRISPR v2
RELA sgRNA #2	TATCTGTGCTCCTCGCCT	Exon 3	
RELA sgRNA #3	TCACCAAGGACCCTCCTCAC	Exon 4	
REL sgRNA #1	ATTGGGTTCGAGACAACAGG	Exon 5	LentiCRISPR v2
REL sgRNA #2	TAATTGAACAACCCAGGCAG	Exon 2	
REL sgRNA #3	GTTGGAAAAGACTGCAGAGA	Exon 3	
RELB sgRNA #1	AACGGCTTCGGCCTGGACGG	Exon 4	LentiCRISPR v2
RELB sgRNA #2	CTCCTCACTCTCGCTCGCCG	Exon 2	
RELB sgRNA #3	GCCACGCCTGGTGTCTCGCG	Exon 4	

5.5.3 Primer for RT-PCR

Table 5-4: Human RT-PCR primer sequences.

Target gene	Sequence (5'– 3')	T_m
RPII fw	GCACCACGTCCAATGACA	64 °C
RPII rev	GTGCGGCTGCTTCCATAA	
CXCL8 fw (272)	CTTGGCAGCCTTCCTGATTT	60 °C
CXCL8 rev	GGGTGGAAAGGTTGGAGTATG	
ICAM fw	GGCTGGAGCTGTTGAGAAC	64 °C
ICAM rev	ACTGTGGGTTCAACCTCTG	
NFKBIA fw	AGGACGGGGACTCGTTCCTG	64 °C
NFKBIA rev	CAAGTGGAGTGGAGTCTGCTG	
TNFAIP3 fw	CTGAAAACGAACGGTGACGG	64 °C
TNFAIP3 rev	CGTGTGTCTGTTCCTTGAGCG	
Nsp14 fw	CGGAAACCCAAAGGCTATCA	60 °C
Nsp14 rev	TGTGGGTAGCGTAAGAGTAGAA	

5.6 *Escherichia coli* (*E. coli*) strains

TOP10	F⁻*mcr*A Δ(*mrr-hsd*RMS-*mcr*BC) φ80*lac*ZΔM15 Δ*lac*X74 *rec*A1 *ara*D139 Δ(*ara-leu*)*7697 gal*U *gal*K *rps*L(Str^R) *end*A1 *nup*G
STBL3	F⁻*mcr*B *mrr hsd*S20(rB⁻, mB⁻) *rec*A13 *sup*E44 *ara*⁻14 *gal*K2 *lac*Y1 *pro*A2 *rps*L20(Str^R) *xyl*-5 λ⁻ *leu mtl*-1

5.7 Eukaryotic cell lines

Jurkat T cells	human T cell line, derived from acute T cell leukemia patient
Hek293 cells	human embryonic kidney cell line containing Adenovirus 5 DNA
Hek293T cells	HEK293 cells containing SV40 large T-antigen
TTR Jurkat T cells	human T cell line, generated by lentiviral infection
TRAF2$^{-/-}$ Hek293 cells	human embryonic kidney cell line, generated by CRISPR/Cas9
IKBKG$^{-/-}$ Hek293 cells	human embryonic kidney cell line, generated by CRISPR/Cas9
RELA$^{-/-}$ Hek293 cells	human embryonic kidney cell line, generated by CRISPR/Cas9
REL$^{-/-}$ Hek293 cells	human embryonic kidney cell line, generated by CRISPR/Cas9
RELB$^{-/-}$ Hek293 cells	human embryonic kidney cell line, generated by CRISPR/Cas9
scramble Hek293 cells	human embryonic kidney cell line, generated by CRISPR/Cas9

5.8 Antibodies

5.8.1 Primary antibodies

Table 5-5: List of used primary antibodies.

Antibody	Dilution	Source	Identifier
Mouse monoclonal β-Actin (C4)	1:5000	Santa Cruz, Heidelberg	Cat#sc-47778; RRID: AB_626632
Rabbit monoclonal CARD11 (1D12)	1:1,000	Cell Signaling Technology, Frankfurt	Cat #4435; RRID: AB_2070359
Mouse monoclonal cIAP2 (F30-2285)	1:1,000	BD, Heidelberg	Cat#552782; RRID: AB_394463
Rabbit polyclonal cRel	1:1,000	Santa Cruz, Heidelberg	Cat#sc-70, RRID: AB_2178727
Rabbit polyclonal anti-GFP	1:1,000	Cell Signaling Technology, Frankfurt	Cat#2555; RRID: AB_390710
Mouse monoclonal IκBα (L35A5)	1:1,000	Cell Signaling Technology, Frankfurt	Cat#4814. RRID: AB_390781
Mouse monoclonal IKKα (14A231)	1:1,000	Merck Millipore, Darmstadt	Cat#05-536; RRID: AB_11213043
Mouse monoclonal anti-FLAG M2	1:10,000	Sigma-Aldrich, Taufkirchen	Cat#F3165; RRID: AB_259529

Mouse monoclonal anti-HA [12CA5]	1:1,000	Sigma-Aldrich, Taufkirchen	Cat#11583816001, RRID: AB_514505
Mouse monoclonal IKKγ/NEMO (1.T.26)	1:1,000	Santa Cruz, Heidelberg	Cat#sc-71331; RRID: AB_1124812
Rabbit polyclonal NIK	1:1,000	Cell Signaling Technology, Frankfurt	Cat#4994; RRID: AB_2297422
Rabbit polyclonal Nsp14	1:1,000	Cell Signaling Technology, Frankfurt	Cat#99098
Rabbit polyclonal NF-κB2 p100/p52	1:1,000	Cell Signaling Technology, Frankfurt	Cat#4882; RRID: AB_10695537
Rabbit monoclonal NF-κB p105/p50 (E381)	1:1,000	Abcam, Cambridge, UK	Cat# ab32360; RRID: AB_776748
Rabbit polyclonal NF-κB p65 (C-20)	1:1,000	Santa Cruz, Heidelberg	Cat#sc-372; RRID: AB_632037
Mouse monoclonal p-IκBα (S32/36) (5A5)	1:1,000	Cell Signaling Technology, Frankfurt	Cat#9246; RRID: AB_2151442
Rabbit monoclonal p-IKKα/β (S176/180) (16A6)	1:1,000	Cell Signaling Technology, Frankfurt	Cat#2697; RRID: AB_2079382
Rabbit polyclonal p-IKKα (S180)/IKKβ (S181)	1:1,000	Cell Signaling Technology, Frankfurt	Cat#2681; RRID: AB_331624
Rabbit monoclonal NF-κB p-p65 (S536)	1:1,000	Cell Signaling Technology, Frankfurt	Cat#3033; RRID: AB_331284
Rabbit monoclonal p-TAK1 (Thr184/187) (90C7)	1:1,000	Cell Signaling Technology, Frankfurt	Cat# 4508
Rabbit monoclonal RelB (C1E4)	1:1,000	Cell Signaling Technology, Frankfurt	Cat#4922, RRID: AB_2179173
HRP conjugated mouse monoclonal Strep	1:1,000	IBA, Göttingen	Cat#2-1509-001
Rabbit polyclonal TRAF2	1:1,000	Cell Signaling Technology, Frankfurt	Cat#4712, RRID: AB_2209848

5.8.2 Secondary antibodies

Table 5-6: List of secondary antibodies.

Antibody	Dilution	Source	Identifier
Donkey polyclonal anti-mouse IgG	1:10,000	Jackson ImmunoResearch, Cambridgeshire, UK	Cat#715-035-150; RRID: AB_2340770
Donkey polyclonal anti-rabbit IgG	1:10,000	Jackson ImmunoResearch, Cambridgeshire, UK	Cat#711-035-152; RRID: AB_10015282

5.8.3 Stimulatory antibodies

Table 5-7: List of stimulatory antibodies.

Antibody	Source	Identifier
Mouse monoclonal anti-human CD28 [CD28.2]	BD Biosciences, Franklin Lakes, USA	Cat#555725; RRID: AB_396068
Mouse monoclonal anti-human CD3 [HIT3a]	BD Biosciences, Franklin Lakes, USA	Cat# 555336; RRID: AB_395742
Rat monoclonal anti-mouse IgG1 [A85-1]	BD Biosciences, Franklin Lakes, USA	Cat#553440; RRID: AB_394860
Rat monoclonal anti-mouse IgG2a [R19-15]]	BD Biosciences, Franklin Lakes, USA	Cat#553387; RRID: AB_394825

5.8.4 FACS antibodies

Table 5-8: List of FACS antibodies.

Antibody	Source	Identifier
Mouse monoclonal anti-CD2-APC [RPA-2.10]	Thermo Fisher Scientific, Waltham, USA	Cat# 17-0029-41; RRID: AB_10806970

5.9 Software

Adobe Illustrator CS6 (version 16)	Adobe Systems, San José, USA
Adobe Photoshop CS6 (version 16)	Adobe Systems, San José, USA
CLC Main Workbench (version 7.0.3)	Qiagen, Hilden
Endnote 21	Clarivate Analytics, Philadelphia, USA
FlowJo (version 10)	FlowJo LLC, Ashland, USA
GraphPad Prism (version 8.0.2)	GraphPad, San Diego, USA
Microsoft Office 2010	Microsoft Corp., Redmond, USA
Affinity Photo (Version 1.10.5)	Serif, Nottingham, UK
Affinity Designer (Version 1.10.5)	Serif, Nottingham, UK
ChemoStar software (Chemo Star Imager Version 0.3.18)	INTAS Science Imaging, Göttingen
MikroWin 2010	Labsis, Neunkirchen-Seelscheid

6 Methods

6.1 Molecular biology methods

6.1.1 Polymerase chain reaction

For DNA amplification, polymerase chain reaction (PCR) was performed according to the standard protocol with adjusted times and cycle numbers.

Table 6-1: PCR standard protocol.

Component	Amount
Template DNA	30 ng
5’ primer (10 µM)	1.25 µl
3’ primer (10 µM)	1.25 µl
dNTP (25 mM)	0.5 µl
Herculase buffer (10x)	10 µl
DNA polymerase (Herculase)	1.0 µl
	Add to 50 µl H_2O

Table 6-2: PCR standard program.

Step	Temperature	Time	
Melting	98 °C	2 min	
Melting	98 °C	30 s	30 – 40 cycles
Annealing	Tm primer -5°C	20 s	
Extension	72 °C	1 min / 1 kb	
Extension	72 °C	2 min	

After amplification, the correct product size was confirmed on an agarose gel, and the PCR products were purified using a NucleoSpin Gel and PCR Clean-up Mini kit (Macherey-Nagel) according to the manufacturer's instructions. Megaprimer PCR was used for site-directed mutagenesis to generate enzymatically inactive Nsp14 mutants. In the first step, the megaprimer was amplified using a primer containing the desired mutation and a primer covering the closer end of the coding sequence. In the second step, the purified megaprimer fragment was used in a second PCR to amplify the full-length gene. The PCR product was then cloned into the target vector using restriction enzymes. pLVTHM constructs were cloned using

the NEBuilder HiFi DNA assembly cloning kit according to the manufacturer's instructions (NEB).

6.1.2 DNA restriction digestion, agarose gel electrophoresis and DNA extraction

PCR products were digested with restriction enzymes in appropriate buffers supplied by NEB. Agarose gels were prepared by dissolving agarose in TBE buffer with the addition of ethidium bromide. After enzymatic digestion, the products were mixed with 6x DNA loading buffer and separated by gel electrophoresis in TBE buffer at 90 V. For product size determination, 5 µl of 1 kb plus DNA ladder was loaded on the side. DNA fragment bands were visualized with UV light and excised from the gel. For gel extraction of DNA, the NucleoSpin Gel and PCR Clean-up Mini kit (Macherey-Nagel) was used according to the manufacturer's instructions.

6.1.3 DNA ligation and transformation of *E.coli*

The digested DNA fragments and plasmid backbones were ligated using the T4 DNA Ligation Kit (NEB) according to the manufacturer's instructions. Depending on the size ratio of the insert fragment to the backbone, a molar ratio of 1:3 to 1:5 was used for ligation. The ligation mixture was added to competent *Escherichia coli* (*E. coli*) TOP10 or STBL3 cells. After 10 minutes of incubation on ice, a heat shock at 42°C for 45 seconds was performed. The cells were cooled again on ice, 500 µl of S.O.C. medium was added, and the cells were incubated at 37°C for 60 minutes on a shaker. The grown cells were plated on LB agar plates with appropriate antibiotic and incubated overnight at 37°C.

6.1.4 Cultivation of *E.coli* and plasmid preparation

To isolate plasmid DNA, transformed E. coli were grown in LB medium supplemented with the appropriate antibiotic overnight on a shaker (180 rpm) at 37°C. For analysis, 3 ml of LB medium was inoculated with a single colony picked from an LB agar plate, and DNA was isolated using the NucleoSpin Plasmid Mini Kit (Macherey-Nagel) according to the manufacturer's instructions. To prepare larger amounts of plasmid DNA, competent E. coli were re-transformed with 100-400 ng of the purified plasmid and grown overnight on a shaker (180 rpm) at 37°C in 200-400 ml LB medium supplemented with the appropriate antibiotic. Plasmid

isolation was performed using the NucleoBond Xtra Maxi Kit (Macherey-Nagel) according to the manufacturer's instructions.

6.1.5 DNA sequencing

Purified DNA and appropriate primers were sent to Eurofins Genomics (Ebersberg, Germany) for sequencing.

6.1.6 Genomic DNA extraction

For the extraction of genomic DNA from eukaryotic cells, 1 x 106 cells were washed once with ice-cold PBS and resuspended in 100 µl RNAse-free H2O. The cells were lysed by incubation at 95°C for 5 min and 20 mg/ml proteinase K was added. The mixture was incubated at 52 °C for 3 h and then the proteinase K was inactivated by a heat shock at 95 °C for 5 min. The mixture was cleared by centrifugation at 6000 x g for 2 min and the supernatant was diluted with H2O to the desired concentration.

6.1.7 RNA extraction

For RNA extraction from cells overexpressing WT or D331A Nsp14, 2x 10^6 cells were washed once with ice-cold PBS, 5 volumes of Trizol were added and incubated for 5 min at RT. After adding 1 volume of chloroform, the sample was shaken vigorously, incubated for 3 min, and centrifuged at 20,000 x g for 5 min at 4 °C. The colorless aqueous phase was then isolated, homogenized on QIAshredder columns (Qiagen), and used for RNA isolation using the RNeasy Kit (Qiagen) according to the manufacturer's instructions. For the other experiments, RNA was harvested from 2x10^6 cells and isolated using the RNeasy Kit (Qiagen) according to the manufacturer's instructions. The concentration of RNA was then measured using NanoDrop and the RNA was stored at -80°C.

6.1.8 Reverse transcription into cDNA

The RNA was transcribed to cDNA using the Verso cDNA synthesis kit (Thermo Fisher Scientific according to the manufacturer's instructions. Doing so, random hexamers served as primers for the Reverse Transcriptase and generated cDNA samples were stored at -20 °C.

6.1.9 Real-time PCR

To quantify RNA levels of specific genes, quantitative real-time PCR (RT-PCR) was performed using the Takyon™ No ROX SYBR 2X MasterMix blue dTTP (Eurogentec). This mix contains the fluorescent dye SYBR Green, which binds to double-stranded DNA. Therefore, the fluorescent signal increased with each amplification cycle and was detected using a LightCycler 480 (LC-480, Roche). The following standard protocol was used for RT-PCR:

Table 6-3: RT-PCR standard protocol.

Component	Amount
Template cDNA	2.5 µl (25 ng)
5′ primer (20 µM)	0.5 ul
3′ primer (20 µM)	0.5 ul
Takyon™ No ROX SYBR 2X MasterMix blue dTTP	5 µl
H_2O	1.5 µl

Table 6-4: RT-PCR standard program.

Step	Temperature	Time	
Melting	95 °C	10 min	
Melting	95 °C	10 s	40-45 cycles
Annealing	60 °C / 64 °C	10 s	
Extension	72 °C	10 s	
Melting curve	60 °C – 95 °C	2 min	

Human RNA polymerase II (RP2) was used as an internal control for quantification of target gene expression. Calculation of relative expression levels was performed using the ΔΔCp method (300).

6.2 Cell culture methods

6.2.1 Storage of cell lines

For storage of suspension and adherent cells, a pellet of 0.5-1x10^7 cells was resuspended in 1 ml of freezing medium (DMEM/RPMI, 20% FCS, 15% DMSO). The samples were then transferred to cryotubes and placed in a freezing chamber containing isopropanol at -80°C overnight. For long-term storage, cells were stored in liquid nitrogen.

6.2.2 Cultivation of cell lines

Hek293, Hek293T and HCT116 cells were grown in DMEM medium containing 10% FCS and 100 U/ml P/S at 37°C and 5% CO2 in a humidified atmosphere. When the cells reached 80% confluence, they were split. To detach the cells from the culture dishes, they were rinsed with PBS and incubated with 1-3 ml of 0.05% trypsin/EDTA solution for approximately 5 minutes. The trypsin reaction was stopped by adding fresh DMEM medium. The cells were then either diluted in flasks or seeded in appropriate dishes for subsequent experiments.

Jurkat T cells were maintained in RPMI medium containing 10% FCS and 100 U/ml P/S at a density of 0.2 - 1.5 x 10^6 cells/ml. One day before an experiment, the cells were supplemented with fresh media and adjusted to a density of 0.8 x 106 cells/ml.

6.2.3 Lentiviral transduction of Jurkat T cells and Hek293 cells

For lentivirus production, 2.5x10^6 Hek293T cells were seeded in a 10 cm dish the day before. Cells were transfected with 1 µg pMD2.G (Addgene #12259, gifted by D. Trono), 1.5 µg psPAX2 (Addgene #12260, gifted by D. Trono) and 2 µg plasmid of interest using X-tremeGENE HP DNA Transfection Reagent (Roche) according to the manufacturer's protocol. After a 3-day incubation period for virus production, the virus-containing supernatant was filtered through a 0.45 µm pore size filter and viral transduction was performed after addition of 8 µg/ml polybrene. The cells were incubated with the virus for an appropriate time, then washed three times with PBS and kept in fresh medium for recovery.

For the generation of TTR Jurkat T cells, single virus productions were performed for each reporter construct. Subsequently, 0.5x10^6 Jurkat T cells were infected with either 2000 µl virus transducing pHAGE-NF-κB-*eCFP*, 500 µl virus transducing pHAGE-AP-1-*mCherry* or 2000 µl virus transducing pHAGE-NF-AT-*eGFP* for single reporter Jurkat T cells used as controls or 1500 µl virus transducing pHAGE-NF-κB-*eCFP*, 500 µl virus transducing pHAGE-AP-1-*mCherry*, and 3000 µl virus transducing pHAGE-NF-AT-*eGFP* together for TTR Jurkat T cells. After 24 hours of incubation, the virus was removed from the cells and the cells were allowed to recover for two weeks before analysis.

To generate stable CARD11- or Nsp14-expressing cell lines, cells were lentivirally transduced with different pHAGE-*hΔCD2*-T2A-*CARD11* and pHAGE-*hΔCD2*-T2A-*Nsp14* constructs. With

the T2A element, both a truncated human surface marker, *hΔCD2*, and *CARD11 / Nsp14* are translated from the same mRNA using a mechanism known as ribosomal skipping (301). After translation termination at the 2A C-terminus and release of the nascent polypeptide from the ribosome, the downstream sequence is translated by the same ribosome, resulting in the production of two different proteins. For stable overexpression of CARD11, $0.5x10^6$ Jurkat T cells were infected with 1500 µl of virus, whereas for stable overexpression of Nsp14, 200,000 Hek293 cells were infected with 50 µl of virus. After 24 hours of incubation, the virus was removed from the cells and the cells were allowed to recover for two weeks before analysis.

6.2.4 Generation of knock out cell lines

To generate Hek293 cells with knockout (KO) of *TRAF2* and *IKBKG*, cells were transfected with pX458 plasmids (Addgene #48138, gifted by F. Zhang) containing Cas9 and sgRNAs using the calcium phosphate protocol as described in 6.2.6. After 24 hours of incubation, GFP-positive cells were isolated by FACS sorting. The sorted cells were then seeded into 96-well plates at various densities (0.5, 2, and 5 cells/well) using serial dilution. These plates were then incubated for approximately 10 days to allow time for cell clones to grow, which were then harvested, expanded, and analyzed by PCR and Western blot.

HEK293 cells with knockouts of *REL*, *RELA*, and *RELB* were generated by lentiviral transduction of LentiCRISPR v2 constructs carrying Cas9 and sgRNAs targeting these genes, while control cell lines (referred to as "scramble") were generated with constructs lacking any sgRNA. Lentivirus production and cell transduction procedures were performed according to the protocols described in 6.2.3. Transduction was performed with 1 ml virus (for *REL* KO) or 3 ml virus (for *RELA* and *RELB* KO) together with 8 µg/ml polybrene added to 350,000 HEK293 cells. For double knockouts (DKO), the volume of virus and polybrene was doubled. Transduced cells were subjected to puromycin selection at a concentration of 1.0 µg/ml for 48 hours and then maintained at the same puromycin concentration. The successful knock our was confirmed by WB.

6.2.5 Generation of HCT116 and Hek293 cells with tet-on regulated Nsp14 expression

A two-step viral transduction process was used to generate Hek293 and HCT116 cells with DOX-inducible Nsp14 expression. In the first step, the TetR-KRAB cassette was integrated

using pLV-tTRKRAB-red, and in the second step, the tetracycline response element-regulated Nsp14 expression constructs (pLVTHM- empty as control, pLVTHM-WT Nsp14, and pLVTHM-D331A Nsp14) were introduced. Both viral transductions were performed using 2 ml virus-containing supernatant and 8 µg/ml polybrene in 480,000 HEK293 or HCT116 cells. After three days of incubation, the transduced cells were washed twice with PBS and successful infection, resulting in >90% HEK293 KRAB and HCT116 KRAB cells, was verified by fluorescence microscopy. After the second transduction, freshly washed cells were treated with 1.0 µg/ml DOX for three days and then selected with puromycin by combining 1.0 µg/ml DOX with 1.0 µg/ml puromycin for 48 hours. Cells were then maintained under standard conditions and individual Nsp14 expression was induced by the addition of DOX.

6.2.6 Overexpressing proteins in Hek293 cells

For protein overexpression and subsequent NF-κB assay, $1x10^6$ Hek293 cells were transfected using the calcium phosphate method. Cells were seeded on a 60 mm dish one day before transfection. For transfection, different total amounts of DNA between samples were equalized by adding empty vector DNA. DNA was diluted in 200 µl of 250 mM $CaCl_2$ solution and mixed by vortexing. The DNA mixture was then added dropwise to 200 µl of 2x HBS solution while gently vortexing. The transfection mixture was incubated for 15 min at RT and then added dropwise to the cells. After 6 hours of incubation, the transfection medium was replaced with fresh medium and cells were analyzed or treated 24 hours after transfection.

For the preparation of protein lysates used for GFP Traps or direct analysis by Western blot, $2.5x10^6$ cells were seeded and the amount of DNA as well as the calcium phosphate transfection protocol were adjusted by a factor of 2.5.

6.2.7 Stimulation and inhibitor treatment of Jurkat T cells

One day before stimulation, cells were diluted to a density of $0.8x10^6$ cells/ml. For stimulation, cells were seeded at a density of $0.8x10^6$ cells/ml in a 24-well plate and the stimulants were added. All stimulations were incubated for 5 hours unless otherwise stated.

PMA / ionomycin stimulation was performed at a concentration of 200 ng/ml PMA and 747 ng/ml ionomycin. Unless otherwise indicated, anti-CD3/CD28 stimulation was performed with

100 ng/ml murine anti-human anti-CD3 antibody (IgG1) and 1.0 µg/ml murine anti-human anti-CD28 antibody (IgG2a). For cross-linking of stimulating antibodies, 1.6 µg/ml anti-mouse IgG1 and 1.6 µg/ml anti-mouse IgG2a were used. For TNFα stimulation, 20 ng/ml TNFα was used. Inhibitors were added at concentrations of 1.0-100 nM dasatinib, 0.01-10 nM FK506, 1.0-1000 nM sotrastaurin, and 1.0-50 nM MLN120B 30 minutes prior to cell stimulation.

6.2.8 Stimulation and compound treatment of Hek293 cells

TNFα stimulation was performed with 20 ng/ml TNFα for 4 hours. SAM supplementation was performed at a concentration of 1 mM SAM for 72 hours. When SAM supplementation was combined with TNFα stimulation, TNFα was added 18 hours before the end of the SAM incubation period. To inhibit Nsp14 MTase activity, the inhibitors nitazoxanide, pyridostatin, and sinefungin were added at a concentration of 5 µM for 6 hours. MG-132 treatment was performed at a concentration of 25 µM for 6 hours.

6.3 Flow cytometry

6.3.1 Staining of surface molecules

To measure the surface expression of hΔCD2 on infected cells, a sample of 0.1x 106 cells was washed and resuspended in PBS. For staining, the anti-CD2-APC antibody was added at a 1:400 dilution and incubated for 15 min at 4°C in the dark. After washing and resuspension in PBS, the cells were analyzed in an Attune Acoustic Focusing Cytometer.

6.3.2 Flow cytometry and cell sorting

Sorting of GFP-positive cells during KO cell line generation (7.2.4) was performed on a Cytomation MoFlow coupled to a SortMaster DropletControl (Cytomation) using a 100 µm nozzle.

The TTR Jurkat T cells were washed and resuspended in PBS after stimulation and analyzed on a Fortessa. Jurkat T cells expressing only one transcriptional reporter were used as control cells to allow for compensation.

6.4 Biochemical and immunological methods

6.4.1 Preparation of whole cell lysates

For analysis of protein expression levels and downstream pathway activation, $1x10^6$ to $3x10^6$ Jurkat T cells were collected by centrifugation at 350 x g for 5 minutes at 4 °C, washed with PBS, and then lysed in 50-100 µl of high salt buffer. In the case of Hek293 cells used for the same analysis, $1.0\text{-}2.5x10^6$ cells on 6 cm or 10 cm dishes were washed with PBS and 350 or 500 µl of high salt buffer was added. The cells were then scraped from the dishes and the resulting lysates were transferred to tubes. These lysates were vortexed for 20 minutes at 4°C and then centrifuged (20,000 x g, 10 minutes, 4°C) to remove insoluble cellular debris. For Western blot analysis, 4x SDS loading buffer (Rotiload, Roth) was added to the samples and boiled at 95°C for 4 minutes.

6.4.2 Protein-protein interaction studies

To study protein interactions, 2.5 x 10^6 Hek293 cells were seeded in 10 cm dishes and transfected the next day with 7.5 µg pEGFP-C1 and 5 µg 3xFlag-pEF4 constructs (6.2.6). After 24 h incubation, the cells were washed with PBS, 500 µl of co-IP buffer was added, and the cells were scraped from the plates. The transferred lysates were incubated in tubes for 20 min at 4°C with shaking. After clearing the lysates by centrifugation (20,000 x g, 10 min), a sample of 30 µl lysates was taken, mixed with 4x SDS loading buffer (Rotiload, Roth) and boiled at 95°C for 4 min (lysate control). The remaining cell extracts were mixed with GFP Trap beads (Chromotek), previously equilibrated in co-IP buffer, and incubated for 1 h at 4°C with rotation. The beads were then washed six times in co-IP buffer (2500 x g, 2 min, 4 °C centrifugation) and resuspended in 25 µl 4x SDS loading buffer (Rotiload, Roth) and boiled at 95°C for 7 min. Both lysate and pull-down fraction were analyzed by WB and antibody detection.

6.4.3 SDS polyacrylamide gel electrophoresis

Cellular protein extracts were subjected to SDS polyacrylamide gel electrophoresis (SDS-PAGE) under reducing conditions. Acrylamide concentrations ranging from 7% to 12.5% and the polymerization starters APS and TEMED were used to generate separation gels with different pore sizes. After complete polymerization of the separating gel, a 5% polyacrylamide stacking

gel with sample wells was overlaid. After complete polymerization, protein lysates were loaded, and a pre-stained protein ladder (Thermo Fisher Scientific) was included for estimation of protein molecular weights. Electrophoresis was performed in SDS electrophoresis buffer at 120 V for 60 to 90 min.

6.4.4 Western Blot

To detect proteins separated by SDS-PAGE, a semi-dry Western blot (WB) transfer system was used to transfer proteins electrophoretically to PVDF membranes. The PVDF was first activated in methanol and then equilibrated in blotting buffer. The membrane and SDS gel were sandwiched between Whatman filter papers soaked in blotting buffer and placed in the blotting device. The transfer was performed for 110 min at a current of 90 mA per gel. After the transfer, the membranes were incubated in PBS-T with 5% milk at RT with shaking to prevent non-specific antibody binding. Specific primary antibodies were diluted in PBS-T with 2.5% milk and incubated with the membrane overnight at 4°C with shaking. The next day, the membranes were washed three times in PBS-T and horseradish peroxidase (HRP)-coupled secondary antibodies (in PBS-T containing 1.25% milk) were added for 1 hour at RT, shaking. Detection was by enhanced chemiluminescence catalyzed by HRP upon addition of LumiGlo reagent (CST). The light emission resulting from the enzymatic reaction was detected using an ECL Chemocam imager (INTAS) and ChemoStar software (INTAS).

6.4.5 NF-κB reporter assay

For the NF-κB reporter assay, 1×10^6 Hek293 cells were seeded in a 60-mm dish and transfected the next day using the calcium phosphate protocol (6.2.6). The transfection mixture contained 10 ng NF-κB reporter plasmid (6 × NF-κB firefly luciferase pGL2), 50 ng pTK reporter (Renilla luciferase), and 2-12 µg protein expression vectors. After 24 h incubation, cells were either treated or analyzed directly. Luciferase activity was quantified using a dual luciferase reporter kit (Promega) according to the manufacturer's instructions. For confirmation of target protein expression, 30 µl lysate samples were supplemented with 4x SDS loading buffer (Rotiload, Roth) and boiled at 95°C for 4 min for analysis by WB. Luminescence of both firefly and renilla luciferases was measured using a luminometer (Berthold Centro LB960 microplate reader, MikroWin 2010 software) and reported in relative light units (RLU). NF-κB induction was

expressed as the ratio of firefly luminescence (RLU) to Renilla luminescence (RLU) (Relative NF-κB activation).

6.5 Statistical analysis

For NF-κB reporter assays and RT-PCR, we used a sample size of either three or four (n = 3 or n = 4), and results are expressed as mean ± standard deviation (SD). The unpaired Student's t-test was used to determine statistical significance between two independent groups. When comparing multiple groups with a single variable, we used one-way ANOVA with post hoc analysis using either Tukey's or Dunnett's multiple comparison test. For data sets with multiple groups and two variables, two-way ANOVA followed by Tukey's multiple comparison test was used. Fold change data were normalized to control samples as described in the figure legends, and statistical significance for these data was determined by calculating log2 fold changes relative to the normalizations and assessed using a one-sample t-test. Significance levels are indicated by asterisks: * for $P \leq 0.05$, ** for $P \leq 0.005$, *** for $P \leq 0.001$, and **** for $P \leq 0.0001$.

7 Abbreviations

°C	degree Celsius
aa	amino acid
alpha / α	anti
ANOVA	Analysis of Variance
AP-1	activator protein-1
APC	antigen-presenting cells
APS	ammonium persulfate
ATF	activating transcription factor
BAFFR	B-cell activating factor receptor
BALF	bronchoalveolar lavage fluid
BCL10	B-cell CLL/lymphoma 10
BCR	B cell receptor
BENTA	B cell expansion with NF-κB and T cell anergy
bp	base pairs
BSA	Bovine serum albumin
bZIP	basic region-leucine zipper
Ca^{2+}	calcium
$CaCl_2$	Calcium chloride
CADINS	CARD11 associated atopy with dominant interference of NF-κB signaling
CaM	calmodulin
CARD	caspase recruitment domain
CARD11	Caspase recruitment domain-containing protein 11
CARMA1	CARD-containing MAGUK 1 (also known as CARD11)
Cas9	CRISPR-associated protein-9
CBM	CARD11-BCL10-MALT1
CD	cluster of differentiation
CD3/CD28	anti-CD3 and anti-CD28 antibodies
cDNA	complementary DNA
CFR	case fatality rate
cIAP1/2	cellular inhibitor of apoptosis 1 and 2
CO_2	carbon dioxide
COVID-19	coronavirus disease 19
CRAC	Ca2+-release-activated Ca2+
CRISPR	Clustered Regularly Interspaced Short Palindromic Repeats
C-Terminus	Carboxyl-terminus
ctrl.	control
d	delta
DAG	diacylglycerol
DD	death domain
DKO	double knockouts
DMEM	Dulbecco's modified eagle medium

ΔMFI	delta median fluorescence intensity
DMSO	Dimethyl sulfoxide
DMV	double-membrane vesicles
DNA	deoxyribonucleic acid
DOX	doxycycline
DSB	double-strand break
DTT	Dithiothreitol
E	envelope
E.coli	*Escherichia coli*
ECL	enhanced chemiluminescence
EDTA	Ethylenediaminetetraacetic acid
endog.	endogenous
ER	endoplasmic reticulum
ERK	extracellular-signal-regulated kinase
EtBr	Ethidium bromide
EtOH	Ethanol
EV	empty vector (used as control)
ExoN	exonuclease
FACS	fluorescence-activated cell sorting
FC	Fold Change
FCS	Fetal calf serum
g	gram
g	gravity
GADS	GRB2-related adaptor downstream of Shc
GFP	green fluorescent protein
GOF	gain of function
GPCR	G protein-coupled receptors
Grb2	growth factor receptor-bound protein 2
GRR	glycine-rich region
GUK	Guanylate kinase
h	hour
h	human
HBS	HEPES buffered saline
HCoV	human coronavirus
Hek	human embryonic kidney
HRP	horseradish peroxidase
I	Ionomycin
IB	inhibitor of NF-B alpha
IFNγ	interferon gamma
Ig	immunoglobulin-like
IKK	IκB kinase
IL	interleukin
IL-1R	interleukin-1 receptor
IMPDH2	inosine 5'-monophosphate dehydrogenase 2
IP3	inositol 1,4,5-trisphosphate

ITAM	immunoreceptor tyrosine activation motif
IκB	inhibitor of κB
JNK	c-Jun N-terminal kinases
KCl	Potassium chloride
kDa	kilo Dalton
KH_2PO4	Monopotassium phosphate
KO	knockout
l	liter
LAT	linker for activation of T cells
LB	Luria/Miller
LC	LightCycler
LOF	loss of function
LTβR	lymphotoxin-β receptor
LZ	leucine zipper
M	molar concentration
MAGUK	Membrane-associated guanylate kinase
MALT1	mucosa-associated lymphoid tissue protein 1
MAPK	mitogen-activated protein kinase
MeOH	Methanol
MERS	Middle East Respiratory Syndrome
MFI	median fluorescence intensity
MHC	major histocompatibility complexes
min	minute
ml	milliliter
mM	millimolar
MP	minimal promoter
Mpro	main protease
mRNA	messenger RNA
MTase	methyltransferase
N	nucleocapsid
Na_2HPO4	Sodium hydrogen phosphate
NaCl	Sodium chloride
NEMO	NF-B essential modulator
NF-AT	nuclear factor of activated T-cells
NF-κB	nuclear factor κ-light-chain-enhancer of activated B-cells
ng	nanogram
NIK	NF-κB-inducing kinase
NLR	NOD-like receptor
NLS	nuclear localization signal
nM	nanomolar
NP-40	Nonidet P40 substitute
Nsp	non-structural proteins
N-terminus	amino-terminus
O_2	oxygen
OE	overexpression

oncog.	oncogenic
ORF	open reading frame
P	phosphorylation
p.i.	post infection
P/I	PMA and ionomycin
P/S	Penicillin-Streptomycin
PAMP	pathogen-associated molecular pattern
Para	paracaspase
PBS	phosphate buffered saline
PBS-T	PBS-Tween 20
PCR	Polymerase chain reaction
PD	pull-down
PDK1	phosphatidylinositol-dependent kinase 1
PDZ	post-synaptic density 95/discs large/zonula occludens
PH	pleckstrin homology
PI3K	phosphoinositide 3 kinase
PIP_2	phosphatidyl inositol 4,5-bisphosphate
PIP_3	phosphatidyl inositol 3,4,5-trisphosphate
PKC	protein kinase C
PLCγ	phospholipase C gamma
PLpro	proteases papain-like protease
PMA	Phorbol 12-myristate 13-acetate
PRR	pattern recognition receptors
RANK	receptor activator of NF-κB
RasGRP1	RAS guanyl releasing protein 1
RE	response element
Rel.	relative
RHD	Rel homology domain
RLR	RIG-I-like receptors
RLU	relative light units
RNA	ribonucleic acid
RP2	RNA polymerase II
RPMI	Roswell Park Memorial Institute
RT	room temperature
RTC	replicase-transcriptase complex
RT-PCR	Real-time PCR
S	spike
SAH	S-Adenosyl-homocystein
SAM	S-Adenosyl methionine
SARS	severe acute respiratory syndrome
SD	standard deviation
SDS	Sodium dodecyl sulfate
SDS-PAGE	SDS polyacrylamide gel electrophoresis
sgRNA	single guide RNA
SH3	SRC Homology 3

SLP76	lymphocyte cytosolic protein 2
SSF	2xStrep-tag II-Flag
TAD	transcriptional activation domain
TCR	T cell receptor
TEMED	Tetramethylethylenediamine
TLR	toll-like receptors
Tm	melting temperature
TNFα	Tumor necrosis factor alpha
TRAF	TNF receptor associated factor
Treg	regulatory T cell
Tris	Tris(hydroxymethyl)-aminomethan
TTR	triple transcriptional reporter
µg	microgram
unstim.	unstimulated
v/v	volume per volume
w/v	weight per volume
WB	Western Blot
WT	wild type
ZAP70	zeta-chain-associated protein kinase 70

8 References

1. Bruce Alberts AJ, Julian Lewis, David Morgan, Martin Raff, Keith Roberts, Peter Walter, . Molecular Biology of the cell2008.

2. Hayden MS, Ghosh S. Signaling to NF-kappaB. Genes Dev. 2004;18(18):2195-224.

3. Shaulian E, Karin M. AP-1 as a regulator of cell life and death. Nat Cell Biol. 2002;4(5):E131-6.

4. Hogan PG, Chen L, Nardone J, Rao A. Transcriptional regulation by calcium, calcineurin, and NFAT. Genes Dev. 2003;17(18):2205-32.

5. Oeckinghaus A, Ghosh S. The NF-kappaB family of transcription factors and its regulation. Cold Spring Harb Perspect Biol. 2009;1(4):a000034.

6. Chen CC, Manning AM. Transcriptional regulation of endothelial cell adhesion molecules: a dominant role for NF-kappa B. Agents Actions Suppl. 1995;47:135-41.

7. Karin M. Nuclear factor-κB in cancer development and progression. Nature. 2006;441(7092):431-6.

8. Bonizzi G, Karin M. The two NF-kappaB activation pathways and their role in innate and adaptive immunity. Trends Immunol. 2004;25(6):280-8.

9. Baldwin AS, Jr. The NF-kappa B and I kappa B proteins: new discoveries and insights. Annu Rev Immunol. 1996;14:649-83.

10. Ghosh S, May MJ, Kopp EB. NF-kappa B and Rel proteins: evolutionarily conserved mediators of immune responses. Annu Rev Immunol. 1998;16:225-60.

11. Siggers T, Chang AB, Teixeira A, Wong D, Williams KJ, Ahmed B, et al. Principles of dimer-specific gene regulation revealed by a comprehensive characterization of NF-κB family DNA binding. Nat Immunol. 2011;13(1):95-102.

12. Smale ST. Dimer-specific regulatory mechanisms within the NF-κB family of transcription factors. Immunol Rev. 2012;246(1):193-204.

13. Biology BU. NF-kB Target Genes: Boston University Biology; [

14. Hinz M, Scheidereit C. The IκB kinase complex in NF-κB regulation and beyond. EMBO Rep. 2014;15(1):46-61.

15. Zandi E, Chen Y, Karin M. Direct Phosphorylation of IκB by IKKα and IKKβ: Discrimination Between Free and NF-κB-Bound Substrate. Science. 1998;281(5381):1360-3.

16. Sun S-C. The non-canonical NF-κB pathway in immunity and inflammation. Nature Reviews Immunology. 2017;17(9):545-58.

17. Dejardin E, Droin NM, Delhase M, Haas E, Cao Y, Makris C, et al. The lymphotoxin-beta receptor induces different patterns of gene expression via two NF-kappaB pathways. Immunity. 2002;17(4):525-35.

18. Claudio E, Brown K, Park S, Wang H, Siebenlist U. BAFF-induced NEMO-independent processing of NF-kappa B2 in maturing B cells. Nat Immunol. 2002;3(10):958-65.

19. Coope HJ, Atkinson PG, Huhse B, Belich M, Janzen J, Holman MJ, et al. CD40 regulates the processing of NF-kappaB2 p100 to p52. Embo j. 2002;21(20):5375-85.

20. Kayagaki N, Yan M, Seshasayee D, Wang H, Lee W, French DM, et al. BAFF/BLyS receptor 3 binds the B cell survival factor BAFF ligand through a discrete surface loop and promotes processing of NF-kappaB2. Immunity. 2002;17(4):515-24.

21. Novack DV, Yin L, Hagen-Stapleton A, Schreiber RD, Goeddel DV, Ross FP, Teitelbaum SL. The IkappaB function of NF-kappaB2 p100 controls stimulated osteoclastogenesis. J Exp Med. 2003;198(5):771-81.

22. Liao G, Zhang M, Harhaj EW, Sun SC. Regulation of the NF-kappaB-inducing kinase by tumor necrosis factor receptor-associated factor 3-induced degradation. J Biol Chem. 2004;279(25):26243-50.

23. Vallabhapurapu S, Matsuzawa A, Zhang W, Tseng PH, Keats JJ, Wang H, et al. Nonredundant and complementary functions of TRAF2 and TRAF3 in a ubiquitination cascade that activates NIK-dependent alternative NF-kappaB signaling. Nat Immunol. 2008;9(12):1364-70.

24. Xiao G, Harhaj EW, Sun SC. NF-kappaB-inducing kinase regulates the processing of NF-kappaB2 p100. Mol Cell. 2001;7(2):401-9.

25. Senftleben U, Cao Y, Xiao G, Greten FR, Krähn G, Bonizzi G, et al. Activation by IKKalpha of a second, evolutionary conserved, NF-kappa B signaling pathway. Science. 2001;293(5534):1495-9.

26. Xiao G, Fong A, Sun SC. Induction of p100 processing by NF-kappaB-inducing kinase involves docking IkappaB kinase alpha (IKKalpha) to p100 and IKKalpha-mediated phosphorylation. J Biol Chem. 2004;279(29):30099-105.

27. Foletta VC, Segal DH, Cohen DR. Transcriptional regulation in the immune system: all roads lead to AP-1. Journal of Leukocyte Biology. 1998;63(2):139-52.

28. Chinenov Y, Kerppola TK. Close encounters of many kinds: Fos-Jun interactions that mediate transcription regulatory specificity. Oncogene. 2001;20(19):2438-52.

29. Fonseca GJ, Tao J, Westin EM, Duttke SH, Spann NJ, Strid T, et al. Diverse motif ensembles specify non-redundant DNA binding activities of AP-1 family members in macrophages. Nature Communications. 2019;10(1):414.

30. Chang L, Karin M. Mammalian MAP kinase signalling cascades. Nature. 2001;410(6824):37-40.

31. Karin M. The regulation of AP-1 activity by mitogen-activated protein kinases. J Biol Chem. 1995;270(28):16483-6.

32. Cavigelli M, Dolfi F, Claret FX, Karin M. Induction of c-fos expression through JNK-mediated TCF/Elk-1 phosphorylation. Embo j. 1995;14(23):5957-64.

33. Gupta S, Campbell D, Dérijard B, Davis RJ. Transcription factor ATF2 regulation by the JNK signal transduction pathway. Science. 1995;267(5196):389-93.

34. Hibi M, Lin A, Smeal T, Minden A, Karin M. Identification of an oncoprotein- and UV-responsive protein kinase that binds and potentiates the c-Jun activation domain. Genes Dev. 1993;7(11):2135-48.

35. Han J, Jiang Y, Li Z, Kravchenko VV, Ulevitch RJ. Activation of the transcription factor MEF2C by the MAP kinase p38 in inflammation. Nature. 1997;386(6622):296-9.

36. Mancini M, Toker A. NFAT proteins: emerging roles in cancer progression. Nat Rev Cancer. 2009;9(11):810-20.

37. Macián F, García-Cózar F, Im SH, Horton HF, Byrne MC, Rao A. Transcriptional mechanisms underlying lymphocyte tolerance. Cell. 2002;109(6):719-31.

38. Macian F. NFAT proteins: key regulators of T-cell development and function. Nat Rev Immunol. 2005;5(6):472-84.

39. Vaeth M, Maus M, Klein-Hessling S, Freinkman E, Yang J, Eckstein M, et al. Store-Operated Ca(2+) Entry Controls Clonal Expansion of T Cells through Metabolic Reprogramming. Immunity. 2017;47(4):664-79.e6.

40. Hermann-Kleiter N, Baier G. NFAT pulls the strings during CD4+ T helper cell effector functions. Blood. 2010;115(15):2989-97.

41. Mognol GP, Carneiro FR, Robbs BK, Faget DV, Viola JP. Cell cycle and apoptosis regulation by NFAT transcription factors: new roles for an old player. Cell Death Dis. 2016;7(4):e2199.

42. Fathman CG, Lineberry NB. Molecular mechanisms of CD4+ T-cell anergy. Nature Reviews Immunology. 2007;7(8):599-609.

43. Rao A, Luo C, Hogan PG. Transcription factors of the NFAT family: regulation and function. Annual review of immunology. 1997;15:707-47.

44. Lopez-Rodríguez C, Aramburu J, Rakeman AS, Rao A. NFAT5, a constitutively nuclear NFAT protein that does not cooperate with Fos and Jun. Proc Natl Acad Sci U S A. 1999;96(13):7214-9.

45. Neuhofer W. Role of NFAT5 in inflammatory disorders associated with osmotic stress. Curr Genomics. 2010;11(8):584-90.

46. Okamura H, Aramburu J, García-Rodríguez C, Viola JP, Raghavan A, Tahiliani M, et al. Concerted dephosphorylation of the transcription factor NFAT1 induces a conformational switch that regulates transcriptional activity. Mol Cell. 2000;6(3):539-50.

47. Berridge MJ. Inositol trisphosphate and calcium signalling mechanisms. Biochim Biophys Acta. 2009;1793(6):933-40.

48. Zhang SL, Yu Y, Roos J, Kozak JA, Deerinck TJ, Ellisman MH, et al. STIM1 is a Ca2+ sensor that activates CRAC channels and migrates from the Ca2+ store to the plasma membrane. Nature. 2005;437(7060):902-5.

49. Prakriya M, Feske S, Gwack Y, Srikanth S, Rao A, Hogan PG. Orai1 is an essential pore subunit of the CRAC channel. Nature. 2006;443(7108):230-3.

50. James P, Vorherr T, Carafoli E. Calmodulin-binding domains: just two faced or multi-faceted? Trends Biochem Sci. 1995;20(1):38-42.

51. Kissinger CR, Parge HE, Knighton DR, Lewis CT, Pelletier LA, Tempczyk A, et al. Crystal structures of human calcineurin and the human FKBP12-FK506-calcineurin complex. Nature. 1995;378(6557):641-4.

52. Shaw KT, Ho AM, Raghavan A, Kim J, Jain J, Park J, et al. Immunosuppressive drugs prevent a rapid dephosphorylation of transcription factor NFAT1 in stimulated immune cells. Proc Natl Acad Sci U S A. 1995;92(24):11205-9.

53. Wesselborg S, Fruman DA, Sagoo JK, Bierer BE, Burakoff SJ. Identification of a physical interaction between calcineurin and nuclear factor of activated T cells (NFATp). J Biol Chem. 1996;271(3):1274-7.

54. Luo C, Shaw KT, Raghavan A, Aramburu J, Garcia-Cozar F, Perrino BA, et al. Interaction of calcineurin with a domain of the transcription factor NFAT1 that controls nuclear import. Proc Natl Acad Sci U S A. 1996;93(17):8907-12.

55. Loh C, Carew JA, Kim J, Hogan PG, Rao A. T-cell receptor stimulation elicits an early phase of activation and a later phase of deactivation of the transcription factor NFAT1. Mol Cell Biol. 1996;16(7):3945-54.

56. Beals CR, Sheridan CM, Turck CW, Gardner P, Crabtree GR. Nuclear export of NF-ATc enhanced by glycogen synthase kinase-3. Science. 1997;275(5308):1930-4.

57. Okamura H, Garcia-Rodriguez C, Martinson H, Qin J, Virshup DM, Rao A. A conserved docking motif for CK1 binding controls the nuclear localization of NFAT1. Mol Cell Biol. 2004;24(10):4184-95.

58. Zhu J, Shibasaki F, Price R, Guillemot JC, Yano T, Dötsch V, et al. Intramolecular masking of nuclear import signal on NF-AT4 by casein kinase I and MEKK1. Cell. 1998;93(5):851-61.

59. Kar P, Mirams GR, Christian HC, Parekh AB. Control of NFAT Isoform Activation and NFAT-Dependent Gene Expression through Two Coincident and Spatially Segregated Intracellular Ca(2+) Signals. Mol Cell. 2016;64(4):746-59.

60. Nayak A, Glöckner-Pagel J, Vaeth M, Schumann JE, Buttmann M, Bopp T, et al. Sumoylation of the transcription factor NFATc1 leads to its subnuclear relocalization and interleukin-2 repression by histone deacetylase. J Biol Chem. 2009;284(16):10935-46.

61. Kim JH, Kim K, Youn BU, Jin HM, Kim JY, Moon JB, et al. RANKL induces NFATc1 acetylation and stability via histone acetyltransferases during osteoclast differentiation. Biochem J. 2011;436(2):253-62.

62. Terui Y, Saad N, Jia S, McKeon F, Yuan J. Dual role of sumoylation in the nuclear localization and transcriptional activation of NFAT1. J Biol Chem. 2004;279(27):28257-65.

63. Abul K. Abbas AHL, Shiv Pillai. Cellular and Molecular Immunology. 10 ed: Elsevier; 2018.

64. Hwang J-R, Byeon Y, Kim D, Park S-G. Recent insights of T cell receptor-mediated signaling pathways for T cell activation and development. Experimental & Molecular Medicine. 2020;52(5):750-61.

65. Irving BA, Chan AC, Weiss A. Functional characterization of a signal transducing motif present in the T cell antigen receptor zeta chain. J Exp Med. 1993;177(4):1093-103.

66. van Oers NS, Killeen N, Weiss A. Lck regulates the tyrosine phosphorylation of the T cell receptor subunits and ZAP-70 in murine thymocytes. J Exp Med. 1996;183(3):1053-62.

67. Chan AC, Iwashima M, Turck CW, Weiss A. ZAP-70: a 70 kd protein-tyrosine kinase that associates with the TCR zeta chain. Cell. 1992;71(4):649-62.

68. Zhang W, Sloan-Lancaster J, Kitchen J, Trible RP, Samelson LE. LAT: the ZAP-70 tyrosine kinase substrate that links T cell receptor to cellular activation. Cell. 1998;92(1):83-92.

69. Bubeck Wardenburg J, Fu C, Jackman JK, Flotow H, Wilkinson SE, Williams DH, et al. Phosphorylation of SLP-76 by the ZAP-70 protein-tyrosine kinase is required for T-cell receptor function. J Biol Chem. 1996;271(33):19641-4.

70. Shah NH, Wang Q, Yan Q, Karandur D, Kadlecek TA, Fallahee IR, et al. An electrostatic selection mechanism controls sequential kinase signaling downstream of the T cell receptor. Elife. 2016;5.

71. Liu SK, Fang N, Koretzky GA, McGlade CJ. The hematopoietic-specific adaptor protein gads functions in T-cell signaling via interactions with the SLP-76 and LAT adaptors. Curr Biol. 1999;9(2):67-75.

72. Rhee SG. Regulation of phosphoinositide-specific phospholipase C. Annu Rev Biochem. 2001;70:281-312.

73. Fu G, Chen Y, Yu M, Podd A, Schuman J, He Y, et al. Phospholipase C{gamma}1 is essential for T cell development, activation, and tolerance. J Exp Med. 2010;207(2):309-18.

74. Prasad KV, Cai YC, Raab M, Duckworth B, Cantley L, Shoelson SE, Rudd CE. T-cell antigen CD28 interacts with the lipid kinase phosphatidylinositol 3-kinase by a cytoplasmic Tyr(P)-Met-Xaa-Met motif. Proc Natl Acad Sci U S A. 1994;91(7):2834-8.

75. Koyasu S. The role of PI3K in immune cells. Nature Immunology. 2003;4(4):313-9.

76. Lemmon MA. Pleckstrin Homology Domains: Two Halves Make a Hole? Cell. 2005;120(5):574-6.

77. Villalba M, Bi K, Hu J, Altman Y, Bushway P, Reits E, et al. Translocation of PKC[theta] in T cells is mediated by a nonconventional, PI3-K- and Vav-dependent pathway, but does not absolutely require phospholipase C. J Cell Biol. 2002;157(2):253-63.

78. Lee KY, D'Acquisto F, Hayden MS, Shim JH, Ghosh S. PDK1 nucleates T cell receptor-induced signaling complex for NF-kappaB activation. Science. 2005;308(5718):114-8.

79. Schmitz ML, Krappmann D. Controlling NF-κB activation in T cells by costimulatory receptors. Cell Death & Differentiation. 2006;13(5):834-42.

80. Díaz-Flores E, Siliceo M, Martínez AC, Mérida I. Membrane translocation of protein kinase Ctheta during T lymphocyte activation requires phospholipase C-gamma-generated diacylglycerol. J Biol Chem. 2003;278(31):29208-15.

81. Hara H, Bakal C, Wada T, Bouchard D, Rottapel R, Saito T, Penninger JM. The molecular adapter Carma1 controls entry of IkappaB kinase into the central immune synapse. J Exp Med. 2004;200(9):1167-77.

82. Wang D, Matsumoto R, You Y, Che T, Lin XY, Gaffen SL, Lin X. CD3/CD28 costimulation-induced NF-kappaB activation is mediated by recruitment of protein kinase C-theta, Bcl10, and IkappaB kinase beta to the immunological synapse through CARMA1. Mol Cell Biol. 2004;24(1):164-71.

83. Oeckinghaus A, Wegener E, Welteke V, Ferch U, Arslan SC, Ruland J, et al. Malt1 ubiquitination triggers NF-kappaB signaling upon T-cell activation. Embo j. 2007;26(22):4634-45.

84. Wu CJ, Ashwell JD. NEMO recognition of ubiquitinated Bcl10 is required for T cell receptor-mediated NF-kappaB activation. Proc Natl Acad Sci U S A. 2008;105(8):3023-8.

85. Ebinu JO, Stang SL, Teixeira C, Bottorff DA, Hooton J, Blumberg PM, et al. RasGRP links T-cell receptor signaling to Ras. Blood. 2000;95(10):3199-203.

86. Kortum RL, Rouquette-Jazdanian AK, Samelson LE. Ras and extracellular signal-regulated kinase signaling in thymocytes and T cells. Trends Immunol. 2013;34(6):259-68.

87. Blonska M, Lin X. CARMA1-mediated NF-kappaB and JNK activation in lymphocytes. Immunol Rev. 2009;228(1):199-211.

88. Ruland J, Duncan GS, Wakeham A, Mak TW. Differential requirement for Malt1 in T and B cell antigen receptor signaling. Immunity. 2003;19(5):749-58.

89. Beinke S, Robinson MJ, Hugunin M, Ley SC. Lipopolysaccharide activation of the TPL-2/MEK/extracellular signal-regulated kinase mitogen-activated protein kinase cascade is regulated by IkappaB kinase-induced proteolysis of NF-kappaB1 p105. Mol Cell Biol. 2004;24(21):9658-67.

90. Koga K, Takaesu G, Yoshida R, Nakaya M, Kobayashi T, Kinjyo I, Yoshimura A. Cyclic adenosine monophosphate suppresses the transcription of proinflammatory cytokines via the phosphorylated c-Fos protein. Immunity. 2009;30(3):372-83.

91. Diehn M, Alizadeh AA, Rando OJ, Liu CL, Stankunas K, Botstein D, et al. Genomic expression programs and the integration of the CD28 costimulatory signal in T cell activation. Proc Natl Acad Sci U S A. 2002;99(18):11796-801.

92. Meininger I, Krappmann D. Lymphocyte signaling and activation by the CARMA1-BCL10-MALT1 signalosome. Biol Chem. 2016;397(12):1315-33.

93. Gehring T, Seeholzer T, Krappmann D. BCL10 - Bridging CARDs to Immune Activation. Front Immunol. 2018;9:1539.

94. Roche MI, Ramadas RA, Medoff BD. The role of CARMA1 in T cells. Crit Rev Immunol. 2013;33(3):219-43.

95. Hara H, Yokosuka T, Hirakawa H, Ishihara C, Yasukawa S, Yamazaki M, et al. Clustering of CARMA1 through SH3–GUK domain interactions is required for its activation of NF-κB signalling. Nature Communications. 2015;6(1):5555.

96. Bertin J, Wang L, Guo Y, Jacobson MD, Poyet JL, Srinivasula SM, et al. CARD11 and CARD14 are novel caspase recruitment domain (CARD)/membrane-associated guanylate kinase (MAGUK) family members that interact with BCL10 and activate NF-kappa B. J Biol Chem. 2001;276(15):11877-82.

97. Tanner MJ, Hanel W, Gaffen SL, Lin X. CARMA1 coiled-coil domain is involved in the oligomerization and subcellular localization of CARMA1 and is required for T cell receptor-induced NF-kappaB activation. J Biol Chem. 2007;282(23):17141-7.

98. Schlauderer F, Seeholzer T, Desfosses A, Gehring T, Strauss M, Hopfner KP, et al. Molecular architecture and regulation of BCL10-MALT1 filaments. Nat Commun. 2018;9(1):4041.

99. Langel FD, Jain NA, Rossman JS, Kingeter LM, Kashyap AK, Schaefer BC. Multiple protein domains mediate interaction between Bcl10 and MALT1. J Biol Chem. 2008;283(47):32419-31.

100. Lucas PC, Yonezumi M, Inohara N, McAllister-Lucas LM, Abazeed ME, Chen FF, et al. Bcl10 and MALT1, independent targets of chromosomal translocation in malt lymphoma, cooperate in a novel NF-kappa B signaling pathway. J Biol Chem. 2001;276(22):19012-9.

101. Matsumoto R, Wang D, Blonska M, Li H, Kobayashi M, Pappu B, et al. Phosphorylation of CARMA1 plays a critical role in T Cell receptor-mediated NF-kappaB activation. Immunity. 2005;23(6):575-85.

102. Sommer K, Guo B, Pomerantz JL, Bandaranayake AD, Moreno-García ME, Ovechkina YL, Rawlings DJ. Phosphorylation of the CARMA1 linker controls NF-kappaB activation. Immunity. 2005;23(6):561-74.

103. Qiao Q, Yang C, Zheng C, Fontán L, David L, Yu X, et al. Structural architecture of the CARMA1/Bcl10/MALT1 signalosome: nucleation-induced filamentous assembly. Mol Cell. 2013;51(6):766-79.

104. McCully RR, Pomerantz JL. The protein kinase C-responsive inhibitory domain of CARD11 functions in NF-kappaB activation to regulate the association of multiple signaling cofactors that differentially depend on Bcl10 and MALT1 for association. Mol Cell Biol. 2008;28(18):5668-86.

105. Jattani RP, Tritapoe JM, Pomerantz JL. Intramolecular Interactions and Regulation of Cofactor Binding by the Four Repressive Elements in the Caspase Recruitment Domain-containing Protein 11 (CARD11) Inhibitory Domain. J Biol Chem. 2016;291(16):8338-48.

106. Ishiguro K, Green T, Rapley J, Wachtel H, Giallourakis C, Landry A, et al. Ca2+/calmodulin-dependent protein kinase II is a modulator of CARMA1-mediated NF-kappaB activation. Mol Cell Biol. 2006;26(14):5497-508.

107. Brenner D, Brechmann M, Röhling S, Tapernoux M, Mock T, Winter D, et al. Phosphorylation of CARMA1 by HPK1 is critical for NF-κB activation in T cells. Proceedings of the National Academy of Sciences. 2009;106(34):14508-13.

108. Shinohara H, Maeda S, Watarai H, Kurosaki T. IkappaB kinase beta-induced phosphorylation of CARMA1 contributes to CARMA1 Bcl10 MALT1 complex formation in B cells. J Exp Med. 2007;204(13):3285-93.

109. Bidère N, Ngo VN, Lee J, Collins C, Zheng L, Wan F, et al. Casein kinase 1alpha governs antigen-receptor-induced NF-kappaB activation and human lymphoma cell survival. Nature. 2009;458(7234):92-6.

110. Moreno-García ME, Sommer K, Haftmann C, Sontheimer C, Andrews SF, Rawlings DJ. Serine 649 phosphorylation within the protein kinase C-regulated domain down-regulates CARMA1 activity in lymphocytes. J Immunol. 2009;183(11):7362-70.

111. Kutzner K, Woods S, Karayel O, Gehring T, Yin H, Flatley A, et al. Phosphorylation of serine-893 in CARD11 suppresses the formation and activity of the CARD11-BCL10-MALT1 complex in T and B cells. Sci Signal. 2022;15(723):eabk3083.

112. Eitelhuber AC, Warth S, Schimmack G, Düwel M, Hadian K, Demski K, et al. Dephosphorylation of Carma1 by PP2A negatively regulates T-cell activation. Embo j. 2011;30(3):594-605.

113. Moreno-García ME, Sommer K, Shinohara H, Bandaranayake AD, Kurosaki T, Rawlings DJ. MAGUK-controlled ubiquitination of CARMA1 modulates lymphocyte NF-kappaB activity. Mol Cell Biol. 2010;30(4):922-34.

114. Fujioka S, Niu J, Schmidt C, Sclabas GM, Peng B, Uwagawa T, et al. NF-kappaB and AP-1 connection: mechanism of NF-kappaB-dependent regulation of AP-1 activity. Mol Cell Biol. 2004;24(17):7806-19.

115. Krappmann D, Wegener E, Sunami Y, Esen M, Thiel A, Mordmuller B, Scheidereit C. The IkappaB kinase complex and NF-kappaB act as master regulators of lipopolysaccharide-induced gene expression and control subordinate activation of AP-1. Mol Cell Biol. 2004;24(14):6488-500.

116. Stein B, Baldwin AS, Jr., Ballard DW, Greene WC, Angel P, Herrlich P. Cross-coupling of the NF-kappa B p65 and Fos/Jun transcription factors produces potentiated biological function. Embo j. 1993;12(10):3879-91.

117. Chen L, Glover JN, Hogan PG, Rao A, Harrison SC. Structure of the DNA-binding domains from NFAT, Fos and Jun bound specifically to DNA. Nature. 1998;392(6671):42-8.

118. Fields PE, Gajewski TF, Fitch FW. Blocked Ras Activation in Anergic CD4⁺ T Cells. Science. 1996;271(5253):1276-8.

119. Healy JI, Dolmetsch RE, Timmerman LA, Cyster JG, Thomas ML, Crabtree GR, et al. Different Nuclear Signals Are Activated by the B Cell Receptor during Positive Versus Negative Signaling. Immunity. 1997;6(4):419-28.

120. Martinez GJ, Pereira RM, Äijö T, Kim EY, Marangoni F, Pipkin ME, et al. The transcription factor NFAT promotes exhaustion of activated $CD8^+$ T cells. Immunity. 2015;42(2):265-78.

121. Janeway CA. How the immune system protects the host from infection. Microbes and Infection. 2001;3(13):1167-71.

122. Warrington R, Watson W, Kim HL, Antonetti FR. An introduction to immunology and immunopathology. Allergy Asthma Clin Immunol. 2011;7 Suppl 1(Suppl 1):S1.

123. Chaplin DD. Overview of the immune response. J Allergy Clin Immunol. 2010;125(2 Suppl 2):S3-23.

124. Parkin J, Cohen B. An overview of the immune system. Lancet. 2001;357(9270):1777-89.

125. Kumar BV, Connors TJ, Farber DL. Human T Cell Development, Localization, and Function throughout Life. Immunity. 2018;48(2):202-13.

126. Pishesha N, Harmand TJ, Ploegh HL. A guide to antigen processing and presentation. Nat Rev Immunol. 2022;22(12):751-64.

127. Medzhitov R, Janeway C, Jr. Innate immunity. N Engl J Med. 2000;343(5):338-44.

128. Taniuchi I. CD4 Helper and CD8 Cytotoxic T Cell Differentiation. Annu Rev Immunol. 2018;36:579-601.

129. Pennock ND, White JT, Cross EW, Cheney EE, Tamburini BA, Kedl RM. T cell responses: naive to memory and everything in between. Adv Physiol Educ. 2013;37(4):273-83.

130. Liu T, Zhang L, Joo D, Sun S-C. NF-κB signaling in inflammation. Signal Transduction and Targeted Therapy. 2017;2(1):17023.

131. Karin M. NF-kappaB as a critical link between inflammation and cancer. Cold Spring Harb Perspect Biol. 2009;1(5):a000141.

132. Sun SC, Chang JH, Jin J. Regulation of nuclear factor-κB in autoimmunity. Trends Immunol. 2013;34(6):282-9.

133. Zhang Q, Lenardo MJ, Baltimore D. 30 Years of NF-κB: A Blossoming of Relevance to Human Pathobiology. Cell. 2017;168(1-2):37-57.

134. Lenz G, Davis RE, Ngo VN, Lam L, George TC, Wright GW, et al. Oncogenic CARD11 mutations in human diffuse large B cell lymphoma. Science. 2008;319(5870):1676-9.

135. Vallois D, Dobay MPD, Morin RD, Lemonnier F, Missiaglia E, Juilland M, et al. Activating mutations in genes related to TCR signaling in angioimmunoblastic and other follicular helper T-cell–derived lymphomas. Blood. 2016;128(11):1490-502.

136. Kataoka K, Nagata Y, Kitanaka A, Shiraishi Y, Shimamura T, Yasunaga J-i, et al. Integrated molecular analysis of adult T cell leukemia/lymphoma. Nature Genetics. 2015;47(11):1304-15.

137. Lu HY, Bauman BM, Arjunaraja S, Dorjbal B, Milner JD, Snow AL, Turvey SE. The CBM-opathies-A Rapidly Expanding Spectrum of Human Inborn Errors of Immunity Caused by Mutations in the CARD11-BCL10-MALT1 Complex. Front Immunol. 2018;9:2078.

138. Dadi H, Jones TA, Merico D, Sharfe N, Ovadia A, Schejter Y, et al. Combined immunodeficiency and atopy caused by a dominant negative mutation in caspase activation and recruitment domain family member 11 (CARD11). J Allergy Clin Immunol. 2018;141(5):1818-30.e2.

139. Ma CA, Stinson JR, Zhang Y, Abbott JK, Weinreich MA, Hauk PJ, et al. Germline hypomorphic CARD11 mutations in severe atopic disease. Nat Genet. 2017;49(8):1192-201.

140. Dorjbal B, Stinson JR, Ma CA, Weinreich MA, Miraghazadeh B, Hartberger JM, et al. Hypomorphic caspase activation and recruitment domain 11 (CARD11) mutations associated with diverse immunologic phenotypes with or without atopic disease. J Allergy Clin Immunol. 2019;143(4):1482-95.

141. Hutcherson SM, Bedsaul JR, Pomerantz JL. Pathway-Specific Defects in T, B, and NK Cells and Age-Dependent Development of High IgE in Mice Heterozygous for a CADINS-Associated Dominant Negative CARD11 Allele. J Immunol. 2021;207(4):1150-64.

142. Snow AL, Xiao W, Stinson JR, Lu W, Chaigne-Delalande B, Zheng L, et al. Congenital B cell lymphocytosis explained by novel germline CARD11 mutations. J Exp Med. 2012;209(12):2247-61.

143. Gupta M, Aluri J, Desai M, Lokeshwar M, Taur P, Lenardo M, et al. Clinical, Immunological, and Molecular Findings in Four Cases of B Cell Expansion With NF-κB and T Cell Anergy Disease for the First Time From India. Front Immunol. 2018;9(1049).

144. Buchbinder D, Stinson JR, Nugent DJ, Heurtier L, Suarez F, Sukumar G, et al. Mild B-cell lymphocytosis in patients with a CARD11 C49Y mutation. J Allergy Clin Immunol. 2015;136(3):819-21.e1.

145. Arjunaraja S, Nosé BD, Sukumar G, Lott NM, Dalgard CL, Snow AL. Intrinsic Plasma Cell Differentiation Defects in B Cell Expansion with NF-κB and T Cell Anergy Patient B Cells. Front Immunol. 2017;8:913.

146. Chan W, Schaffer TB, Pomerantz JL. A quantitative signaling screen identifies CARD11 mutations in the CARD and LATCH domains that induce Bcl10 ubiquitination and human lymphoma cell survival. Mol Cell Biol. 2013;33(2):429-43.

147. Sasaki Y, Derudder E, Hobeika E, Pelanda R, Reth M, Rajewsky K, Schmidt-Supprian M. Canonical NF-kappaB activity, dispensable for B cell development, replaces BAFF-receptor signals and promotes B cell proliferation upon activation. Immunity. 2006;24(6):729-39.

148. Krishna S, Xie D, Gorentla B, Shin J, Gao J, Zhong XP. Chronic activation of the kinase IKKβ impairs T cell function and survival. J Immunol. 2012;189(3):1209-19.

149. COVID-19 Weekly Epidemiological Update [press release]. 06 April 2023 2023.

150. Hadjadj J, Yatim N, Barnabei L, Corneau A, Boussier J, Smith N, et al. Impaired type I interferon activity and inflammatory responses in severe COVID-19 patients. Science. 2020;369(6504):718.

151. Blanco-Melo D, Nilsson-Payant BE, Liu W-C, Uhl S, Hoagland D, Møller R, et al. Imbalanced Host Response to SARS-CoV-2 Drives Development of COVID-19. Cell. 2020;181(5):1036-45.e9.

152. Akira S, Uematsu S, Takeuchi O. Pathogen recognition and innate immunity. Cell. 2006;124(4):783-801.

153. Sokol CL, Luster AD. The chemokine system in innate immunity. Cold Spring Harb Perspect Biol. 2015;7(5).

154. Maarouf M, Rai KR, Goraya MU, Chen J. Immune Ecosystem of Virus-Infected Host Tissues. International Journal of Molecular Sciences. 2018;19.

155. Hoffmann E, Dittrich-Breiholz O, Holtmann H, Kracht M. Multiple control of interleukin-8 gene expression. Journal of Leukocyte Biology. 2002;72(5):847-55.

156. Bezzerri V, Borgatti M, Finotti A, Tamanini A, Gambari R, Cabrini G. Mapping the Transcriptional Machinery of the IL-8 Gene in Human Bronchial Epithelial Cells. The Journal of Immunology. 2011;187(11):6069-81.

157. Santoro MG, Rossi A, Amici C. NF-κB and virus infection: who controls whom. The EMBO Journal. 2003;22(11):2552-60.

158. Alcami A, Koszinowski UH. Viral mechanisms of immune evasion. Immunology Today. 2000;21(9):447-55.

159. Deng L, Zeng Q, Wang M, Cheng A, Jia R, Chen S, et al. Suppression of NF-κB Activity: A Viral Immune Evasion Mechanism. Viruses. 2018;10(8):409.

160. Kesheh MM, Hosseini P, Soltani S, Zandi M. An overview on the seven pathogenic human coronaviruses. Reviews in Medical Virology. 2022;32(2):e2282.

161. Lim YX, Ng YL, Tam JP, Liu DX. Human Coronaviruses: A Review of Virus-Host Interactions. Diseases. 2016;4(3).

162. Control ECfDPa. MERS-CoV worldwide overview 2023 [Available from: https://www.ecdc.europa.eu/en/middle-east-respiratory-syndrome-coronavirus-mers-cov-situation-update.

163. Organization WH. Severe Acute Respiratory Syndrome (SARS) 2023 [Available from: https://www.who.int/health-topics/severe-acute-respiratory-syndrome#tab=tab_1.

164. Organization WH. Middle East respiratory syndrome coronavirus (MERS-CoV) 2022 [Available from: https://www.who.int/en/news-room/fact-sheets/detail/middle-east-respiratory-syndrome-coronavirus-(mers-cov).

165. Wong CK, Lam CW, Wu AK, Ip WK, Lee NL, Chan IH, et al. Plasma inflammatory cytokines and chemokines in severe acute respiratory syndrome. Clin Exp Immunol. 2004;136(1):95-103.

166. Zhou J, Chu H, Li C, Wong BH, Cheng ZS, Poon VK, et al. Active replication of Middle East respiratory syndrome coronavirus and aberrant induction of inflammatory cytokines and chemokines in human macrophages: implications for pathogenesis. J Infect Dis. 2014;209(9):1331-42.

167. Organization WH. Summary of probable SARS cases with onset of illness from 1 November 2002 to 31 July 2003 2015 [Available from: https://www.who.int/publications/m/item/summary-of-probable-sars-cases-with-onset-of-illness-from-1-november-2002-to-31-july-2003.

168. Zhu N, Zhang D, Wang W, Li X, Yang B, Song J, et al. A Novel Coronavirus from Patients with Pneumonia in China, 2019. N Engl J Med. 2020;382(8):727-33.

169. Gorbalenya AE, Baker SC, Baric RS, de Groot RJ, Drosten C, Gulyaeva AA, et al. The species Severe acute respiratory syndrome-related coronavirus: classifying 2019-nCoV and naming it SARS-CoV-2. Nature Microbiology. 2020;5(4):536-44.

170. Organization WH. Novel Coronavirus (2019-nCoV) Situation Report – 22: World Health Organization; 2020 [Available from: https://www.who.int/docs/default-source/coronaviruse/situation-reports/20200211-sitrep-22-ncov.pdf.

171. Othman H, Bouslama Z, Brandenburg JT, da Rocha J, Hamdi Y, Ghedira K, et al. Interaction of the spike protein RBD from SARS-CoV-2 with ACE2: Similarity with SARS-CoV, hot-spot analysis and effect of the receptor polymorphism. Biochem Biophys Res Commun. 2020;527(3):702-8.

172. Wiersinga WJ, Rhodes A, Cheng AC, Peacock SJ, Prescott HC. Pathophysiology, Transmission, Diagnosis, and Treatment of Coronavirus Disease 2019 (COVID-19): A Review. JAMA. 2020;324(8):782-93.

173. Huang C, Wang Y, Li X, Ren L, Zhao J, Hu Y, et al. Clinical features of patients infected with 2019 novel coronavirus in Wuhan, China. The Lancet. 2020;395(10223):497-506.

174. Edouard Mathieu HR, Lucas Rodés-Guirao, Cameron Appel, Charlie Giattino, Joe Hasell, Bobbie Macdonald, Saloni Dattani, Diana Beltekian, Esteban Ortiz-Ospina and Max Roser. Coronavirus Pandemic (COVID-19) 2020 [Available from: https://ourworldindata.org/coronavirus.

175. Hadfield J, Megill C, Bell SM, Huddleston J, Potter B, Callender C, et al. Nextstrain: real-time tracking of pathogen evolution. Bioinformatics. 2018;34(23):4121-3.

176. Firouzabadi N, Ghasemiyeh P, Moradishooli F, Mohammadi-Samani S. Update on the effectiveness of COVID-19 vaccines on different variants of SARS-CoV-2. Int Immunopharmacol. 2023;117:109968.

177. Giles B, Meredith P, Robson S, Smith G, Chauhan A. The SARS-CoV-2 B.1.1.7 variant and increased clinical severity—the jury is out. The Lancet Infectious Diseases. 2021;21(9):1213-4.

178. Volz E, Mishra S, Chand M, Barrett JC, Johnson R, Geidelberg L, et al. Assessing transmissibility of SARS-CoV-2 lineage B.1.1.7 in England. Nature. 2021;593(7858):266-9.

179. del Rio C, Malani PN, Omer SB. Confronting the Delta Variant of SARS-CoV-2, Summer 2021. JAMA. 2021;326(11):1001-2.

180. Mlcochova P, Kemp SA, Dhar MS, Papa G, Meng B, Ferreira IATM, et al. SARS-CoV-2 B.1.617.2 Delta variant replication and immune evasion. Nature. 2021;599(7883):114-9.

181. Bouzid D, Visseaux B, Kassasseya C, Daoud A, Fémy F, Hermand C, et al. Comparison of Patients Infected With Delta Versus Omicron COVID-19 Variants Presenting to Paris Emergency Departments. Annals of Internal Medicine. 2022;175(6):831-7.

182. Ma K, Chen J. Omicron XE emerges as SARS-CoV-2 keeps evolving. The Innovation. 2022;3(3):100248.

183. Prevention CfDCa. Underlying Medical Conditions Associated with Higher Risk for Severe COVID-19: Information for Healthcare Professionals 2023 [updated Feb. 9, 2023. Available from: https://www.cdc.gov/coronavirus/2019-ncov/hcp/clinical-care/underlyingconditions.html.

184. Qin C, Zhou L, Hu Z, Zhang S, Yang S, Tao Y, et al. Dysregulation of Immune Response in Patients With Coronavirus 2019 (COVID-19) in Wuhan, China. Clinical Infectious Diseases. 2020;71(15):762-8.

185. Mehta P, McAuley DF, Brown M, Sanchez E, Tattersall RS, Manson JJ. COVID-19: consider cytokine storm syndromes and immunosuppression. Lancet. 2020;395(10229):1033-4.

186. Henderson LA, Canna SW, Schulert GS, Volpi S, Lee PY, Kernan KF, et al. On the Alert for Cytokine Storm: Immunopathology in COVID-19. Arthritis Rheumatol. 2020;72(7):1059-63.

187. Lucas C, Wong P, Klein J, Castro TBR, Silva J, Sundaram M, et al. Longitudinal analyses reveal immunological misfiring in severe COVID-19. Nature. 2020;584(7821):463-9.

188. Liao M, Liu Y, Yuan J, Wen Y, Xu G, Zhao J, et al. Single-cell landscape of bronchoalveolar immune cells in patients with COVID-19. Nature Medicine. 2020;26(6):842-4.

189. Xiong Y, Liu Y, Cao L, Wang D, Guo M, Jiang A, et al. Transcriptomic characteristics of bronchoalveolar lavage fluid and peripheral blood mononuclear cells in COVID-19 patients. Emerg Microbes Infect. 2020;9(1):761-70.

190. Zhou Z, Ren L, Zhang L, Zhong J, Xiao Y, Jia Z, et al. Heightened Innate Immune Responses in the Respiratory Tract of COVID-19 Patients. Cell Host Microbe. 2020;27(6):883-90.e2.

191. Ruan Q, Yang K, Wang W, Jiang L, Song J. Clinical predictors of mortality due to COVID-19 based on an analysis of data of 150 patients from Wuhan, China. Intensive Care Med. 2020;46(5):846-8.

192. Herold T, Jurinovic V, Arnreich C, Lipworth BJ, Hellmuth JC, von Bergwelt-Baildon M, et al. Elevated levels of IL-6 and CRP predict the need for mechanical ventilation in COVID-19. J Allergy Clin Immunol. 2020;146(1):128-36.e4.

193. Leng L, Cao R, Ma J, Mou D, Zhu Y, Li W, et al. Pathological features of COVID-19-associated lung injury: a preliminary proteomics report based on clinical samples. Signal Transduct Target Ther. 2020;5(1):240.

194. Ravindra NG, Alfajaro MM, Gasque V, Huston NC, Wan H, Szigeti-Buck K, et al. Single-cell longitudinal analysis of SARS-CoV-2 infection in human airway epithelium identifies target cells, alterations in gene expression, and cell state changes. PLoS Biol. 2021;19(3):e3001143.

195. Fiege JK, Thiede JM, Nanda HA, Matchett WE, Moore PJ, Montanari NR, et al. Single cell resolution of SARS-CoV-2 tropism, antiviral responses, and susceptibility to therapies in primary human airway epithelium. PLOS Pathogens. 2021;17(1):e1009292.

196. Nilsson-Payant BE, Uhl S, Grimont A, Doane AS, Cohen P, Patel RS, et al. The NF-κB Transcriptional Footprint Is Essential for SARS-CoV-2 Replication. Journal of Virology. 2021;95(23):e01257-21.

197. Arya R, Kumari S, Pandey B, Mistry H, Bihani SC, Das A, et al. Structural insights into SARS-CoV-2 proteins. J Mol Biol. 2021;433(2):166725.

198. Zhou P, Yang X-L, Wang X-G, Hu B, Zhang L, Zhang W, et al. A pneumonia outbreak associated with a new coronavirus of probable bat origin. Nature. 2020;579(7798):270-3.

199. Harcourt BH, Jukneliene D, Kanjanahaluethai A, Bechill J, Severson KM, Smith CM, et al. Identification of Severe Acute Respiratory Syndrome Coronavirus Replicase Products and Characterization of Papain-Like Protease Activity. Journal of Virology. 2004;78(24):13600-12.

200. Rut W, Lv Z, Zmudzinski M, Patchett S, Nayak D, Snipas SJ, et al. Activity profiling and crystal structures of inhibitor-bound SARS-CoV-2 papain-like protease: A framework for anti–COVID-19 drug design. Science Advances. 2020;6(42):eabd4596.

201. Ziebuhr J, Snijder EJ, Gorbalenya AE. Virus-encoded proteinases and proteolytic processing in the Nidovirales. Journal of General Virology. 2000;81(4):853-79.

202. Gao Y, Yan L, Huang Y, Liu F, Zhao Y, Cao L, et al. Structure of the RNA-dependent RNA polymerase from COVID-19 virus. Science. 2020;368(6492):779-82.

203. Kirchdoerfer RN, Ward AB. Structure of the SARS-CoV nsp12 polymerase bound to nsp7 and nsp8 co-factors. Nature Communications. 2019;10(1):2342.

204. te Velthuis AJW, van den Worm SHE, Snijder EJ. The SARS-coronavirus nsp7+nsp8 complex is a unique multimeric RNA polymerase capable of both de novo initiation and primer extension. Nucleic Acids Research. 2011;40(4):1737-47.

205. Imbert I, Snijder EJ, Dimitrova M, Guillemot J-C, Lécine P, Canard B. The SARS-Coronavirus PLnc domain of nsp3 as a replication/transcription scaffolding protein. Virus Research. 2008;133(2):136-48.

206. Ivanov KA, Thiel V, Dobbe JC, Meer Yvd, Snijder EJ, Ziebuhr J. Multiple Enzymatic Activities Associated with Severe Acute Respiratory Syndrome Coronavirus Helicase. Journal of Virology. 2004;78(11):5619-32.

207. Saramago M, Bárria C, Costa VG, Souza CS, Viegas SC, Domingues S, et al. New targets for drug design: importance of nsp14/nsp10 complex formation for the 3'-5' exoribonucleolytic activity on SARS-CoV-2. FEBS J. 2021;288(17):5130-47.

208. Imprachim N, Yosaatmadja Y, Newman JA. Crystal structures and fragment screening of SARS-CoV-2 NSP14 reveal details of exoribonuclease activation and mRNA capping and provide starting points for antiviral drug development. Nucleic Acids Res. 2022.

209. Bouvet M, Debarnot C, Imbert I, Selisko B, Snijder EJ, Canard B, Decroly E. In Vitro Reconstitution of SARS-Coronavirus mRNA Cap Methylation. PLOS Pathogens. 2010;6(4):e1000863.

210. Angelini MM, Akhlaghpour M, Neuman BW, Buchmeier MJ. Severe Acute Respiratory Syndrome Coronavirus Nonstructural Proteins 3, 4, and 6 Induce Double-Membrane Vesicles. mBio. 2013;4(4):10.1128/mbio.00524-13.

211. Thoms M, Buschauer R, Ameismeier M, Koepke L, Denk T, Hirschenberger M, et al. Structural basis for translational shutdown and immune evasion by the Nsp1 protein of SARS-CoV-2. Science. 2020;369(6508):1249-55.

212. Hackbart M, Deng X, Baker SC. Coronavirus endoribonuclease targets viral polyuridine sequences to evade activating host sensors. Proceedings of the National Academy of Sciences. 2020;117(14):8094-103.

213. Chang C-k, Chen C-MM, Chiang M-h, Hsu Y-l, Huang T-h. Transient Oligomerization of the SARS-CoV N Protein – Implication for Virus Ribonucleoprotein Packaging. PLOS ONE. 2013;8(5):e65045.

214. Ujike M, Taguchi F. Incorporation of Spike and Membrane Glycoproteins into Coronavirus Virions. Viruses. 2015;7(4):1700-25.

215. Satarker S, Nampoothiri M. Structural Proteins in Severe Acute Respiratory Syndrome Coronavirus-2. Archives of Medical Research. 2020;51(6):482-91.

216. Lu W, Zheng B-J, Xu K, Schwarz W, Du L, Wong CKL, et al. Severe acute respiratory syndrome-associated coronavirus 3a protein forms an ion channel and modulates virus release. Proceedings of the National Academy of Sciences. 2006;103(33):12540-5.

217. Siu K-L, Yuen K-S, Castano-Rodriguez C, Ye Z-W, Yeung M-L, Fung S-Y, et al. Severe acute respiratory syndrome Coronavirus ORF3a protein activates the NLRP3 inflammasome by promoting TRAF3-dependent ubiquitination of ASC. The FASEB Journal. 2019;33(8):8865-77.

218. Li J-Y, Liao C-H, Wang Q, Tan Y-J, Luo R, Qiu Y, Ge X-Y. The ORF6, ORF8 and nucleocapsid proteins of SARS-CoV-2 inhibit type I interferon signaling pathway. Virus Research. 2020;286:198074.

219. Jiang H-w, Zhang H-n, Meng Q-f, Xie J, Li Y, Chen H, et al. SARS-CoV-2 Orf9b suppresses type I interferon responses by targeting TOM70. Cellular & Molecular Immunology. 2020;17(9):998-1000.

220. Nencka R, Silhan J, Klima M, Otava T, Kocek H, Krafcikova P, Boura E. Coronaviral RNA-methyltransferases: function, structure and inhibition. Nucleic Acids Research. 2022;50(2):635-50.

221. Ogando NS, Zevenhoven-Dobbe JC, Meer Yvd, Bredenbeek PJ, Posthuma CC, Snijder EJ, Gallagher T. The Enzymatic Activity of the nsp14 Exoribonuclease Is Critical for Replication of MERS-CoV and SARS-CoV-2. Journal of Virology. 2020;94(23):e01246-20.

222. Robson F, Khan KS, Le TK, Paris C, Demirbag S, Barfuss P, et al. Coronavirus RNA Proofreading: Molecular Basis and Therapeutic Targeting. Mol Cell. 2020;79(5):710-27.

223. Ma Y, Wu L, Shaw N, Gao Y, Wang J, Sun Y, et al. Structural basis and functional analysis of the SARS coronavirus nsp14–nsp10 complex. Proceedings of the National Academy of Sciences. 2015;112(30):9436-41.

224. Lin S, Chen H, Chen Z, Yang F, Ye F, Zheng Y, et al. Crystal structure of SARS-CoV-2 nsp10 bound to nsp14-ExoN domain reveals an exoribonuclease with both structural and functional integrity. Nucleic Acids Research. 2021;49(9):5382-92.

225. Riccio AA, Sullivan ED, Copeland WC. Activation of the SARS-CoV-2 NSP14 3′–5′ exoribonuclease by NSP10 and response to antiviral inhibitors. Journal of Biological Chemistry. 2022;298(1).

226. Byszewska M, Śmietański M, Purta E, Bujnicki JM. RNA methyltransferases involved in 5' cap biosynthesis. RNA Biol. 2014;11(12):1597-607.

227. Chen Y, Tao J, Sun Y, Wu A, Su C, Gao G, et al. Structure-function analysis of severe acute respiratory syndrome coronavirus RNA cap guanine-N7-methyltransferase. J Virol. 2013;87(11):6296-305.

228. Ferron F, Subissi L, Silveira De Morais AT, Le NTT, Sevajol M, Gluais L, et al. Structural and molecular basis of mismatch correction and ribavirin excision from coronavirus RNA. Proc Natl Acad Sci U S A. 2018;115(2):E162-e71.

229. Hayn M, Hirschenberger M, Koepke L, Nchioua R, Straub JH, Klute S, et al. Systematic functional analysis of SARS-CoV-2 proteins uncovers viral innate immune antagonists and remaining vulnerabilities. Cell Rep. 2021;35(7):109126.

230. Lei X, Dong X, Ma R, Wang W, Xiao X, Tian Z, et al. Activation and evasion of type I interferon responses by SARS-CoV-2. Nat Commun. 2020;11(1):3810.

231. Pan R, Kindler E, Cao L, Zhou Y, Zhang Z, Liu Q, et al. N7-Methylation of the Coronavirus RNA Cap Is Required for Maximal Virulence by Preventing Innate Immune Recognition. mBio. 2022;13(1):e0366221.

232. Yuen CK, Lam JY, Wong WM, Mak LF, Wang X, Chu H, et al. SARS-CoV-2 nsp13, nsp14, nsp15 and orf6 function as potent interferon antagonists. Emerg Microbes Infect. 2020;9(1):1418-28.

233. Gribble J, Stevens LJ, Agostini ML, Anderson-Daniels J, Chappell JD, Lu X, et al. The coronavirus proofreading exoribonuclease mediates extensive viral recombination. PLoS Pathog. 2021;17(1):e1009226.

234. Zaffagni M, Harris JM, Patop IL, Pamudurti NR, Nguyen S, Kadener S. SARS-CoV-2 Nsp14 mediates the effects of viral infection on the host cell transcriptome. Elife. 2022;11.

235. Gordon DE, Jang GM, Bouhaddou M, Xu J, Obernier K, White KM, et al. A SARS-CoV-2 protein interaction map reveals targets for drug repurposing. Nature. 2020;583(7816):459-68.

236. Nabeel-Shah S, Lee H, Ahmed N, Burke GL, Farhangmehr S, Ashraf K, et al. SARS-CoV-2 nucleocapsid protein binds host mRNAs and attenuates stress granules to impair host stress response. iScience. 2022;25(1):103562.

237. Chen Z, Wang C, Feng X, Nie L, Tang M, Zhang H, et al. Interactomes of SARS-CoV-2 and human coronaviruses reveal host factors potentially affecting pathogenesis. The EMBO Journal. 2021;40(17):e107776.

238. Li J, Guo M, Tian X, Wang X, Yang X, Wu P, et al. Virus-Host Interactome and Proteomic Survey Reveal Potential Virulence Factors Influencing SARS-CoV-2 Pathogenesis. Med. 2021;2(1):99-112.e7.

239. May DG, Martin-Sancho L, Anschau V, Liu S, Chrisopulos RJ, Scott KL, et al. A BioID-Derived Proximity Interactome for SARS-CoV-2 Proteins. Viruses. 2022;14(3):611.

240. Stukalov A, Girault V, Grass V, Karayel O, Bergant V, Urban C, et al. Multilevel proteomics reveals host perturbations by SARS-CoV-2 and SARS-CoV. Nature. 2021;594(7862):246-52.

241. Yu H, Braun P, Yildirim MA, Lemmens I, Venkatesan K, Sahalie J, et al. High-quality binary protein interaction map of the yeast interactome network. Science. 2008;322(5898):104-10.

242. Kim D-K, Weller B, Lin C-W, Sheykhkarimli D, Knapp JJ, Dugied G, et al. A proteome-scale map of the SARS-CoV-2–human contactome. Nature Biotechnology. 2023;41(1):140-9.

243. Oeckinghaus A, Hayden MS, Ghosh S. Crosstalk in NF-κB signaling pathways. Nature Immunology. 2011;12(8):695-708.

244. Jutz S, Leitner J, Schmetterer K, Doel-Perez I, Majdic O, Grabmeier-Pfistershammer K, et al. Assessment of costimulation and coinhibition in a triple parameter T cell reporter line: Simultaneous measurement of NF-κB, NFAT and AP-1. Journal of Immunological Methods. 2016;430:10-20.

245. Luke GA, de Felipe P, Lukashev A, Kallioinen SE, Bruno EA, Ryan MD. Occurrence, function and evolutionary origins of '2A-like' sequences in virus genomes. J Gen Virol. 2008;89(Pt 4):1036-42.

246. Donnelly MLL, Luke G, Mehrotra A, Li X, Hughes LE, Gani D, Ryan MD. Analysis of the aphthovirus 2A/2B polyprotein 'cleavage' mechanism indicates not a proteolytic reaction, but a novel translational effect: a putative ribosomal 'skip'. Journal of General Virology. 2001;82(5):1013-25.

247. Sharma P, Yan F, Doronina VA, Escuin-Ordinas H, Ryan MD, Brown JD. 2A peptides provide distinct solutions to driving stop-carry on translational recoding. Nucleic Acids Research. 2011;40(7):3143-51.

248. Zhang J, Cruz-Cosme R, Zhuang MW, Liu D, Liu Y, Teng S, et al. A systemic and molecular study of subcellular localization of SARS-CoV-2 proteins. Signal Transduct Target Ther. 2020;5(1):269.

249. Rabaan AA, Al-Ahmed SH, Haque S, Sah R, Tiwari R, Malik YS, et al. SARS-CoV-2, SARS-CoV, and MERS-COV: A comparative overview. Infez Med. 2020;28(2):174-84.

250. Basu S, Mak T, Ulferts R, Wu M, Deegan T, Fujisawa R, et al. Identifying SARS-CoV-2 antiviral compounds by screening for small molecule inhibitors of Nsp14 RNA cap methyltransferase. Biochemical Journal. 2021;478(13):2481-97.

251. Devkota K, Schapira M, Perveen S, Khalili Yazdi A, Li F, Chau I, et al. Probing the SAM Binding Site of SARS-CoV-2 Nsp14 In Vitro Using SAM Competitive Inhibitors Guides Developing Selective Bisubstrate Inhibitors. SLAS Discov. 2021:24725552211026261.

252. Kasprzyk R, Spiewla TJ, Smietanski M, Golojuch S, Vangeel L, De Jonghe S, et al. Identification and evaluation of potential SARS-CoV-2 antiviral agents targeting mRNA cap guanine N7-Methyltransferase. Antiviral Res. 2021;193:105142.

253. Samrat SK, Bashir Q, Zhang R, Huang Y, Liu Y, Wu X, et al. A universal fluorescence polarization high throughput screening assay to target the SAM-binding sites of SARS-CoV-2 and other viral methyltransferases. Emerg Microbes Infect. 2023;12(1):2204164.

254. Cao J, Forrest JC, Zhang X. A screen of the NIH Clinical Collection small molecule library identifies potential anti-coronavirus drugs. Antiviral Res. 2015;114:1-10.

255. Wang M, Cao R, Zhang L, Yang X, Liu J, Xu M, et al. Remdesivir and chloroquine effectively inhibit the recently emerged novel coronavirus (2019-nCoV) in vitro. Cell Res. 2020;30(3):269-71.

256. Pearson LA, Green CJ, Lin D, Petit AP, Gray DW, Cowling VH, Fordyce EAF. Development of a High-Throughput Screening Assay to Identify Inhibitors of the SARS-CoV-2 Guanine-N7-Methyltransferase Using RapidFire Mass Spectrometry. SLAS Discov. 2021;26(6):749-56.

257. Shakya A, Bhat HR, Ghosh SK. Update on Nitazoxanide: A Multifunctional Chemotherapeutic Agent. Curr Drug Discov Technol. 2018;15(3):201-13.

258. Zhao C, Qin G, Niu J, Wang Z, Wang C, Ren J, Qu X. Targeting RNA G-Quadruplex in SARS-CoV-2: A Promising Therapeutic Target for COVID-19? Angew Chem Int Ed Engl. 2021;60(1):432-8.

259. Pugh CS, Borchardt RT, Stone HO. Sinefungin, a potent inhibitor of virion mRNA(guanine-7-)-methyltransferase, mRNA(nucleoside-2'-)-methyltransferase, and viral multiplication. J Biol Chem. 1978;253(12):4075-7.

260. Hayden MS, Ghosh S. NF-κB, the first quarter-century: remarkable progress and outstanding questions. Genes Dev. 2012;26(3):203-34.

261. Shi J-H, Sun S-C. Tumor Necrosis Factor Receptor-Associated Factor Regulation of Nuclear Factor κB and Mitogen-Activated Protein Kinase Pathways. Front Immunol. 2018;9.

262. Hellman LM, Fried MG. Electrophoretic mobility shift assay (EMSA) for detecting protein-nucleic acid interactions. Nat Protoc. 2007;2(8):1849-61.

263. Kopish KR, editor LUCIFERASE REPORTER ASSAYS: POWERFUL, ADAPTABLE TOOLS FOR CELL BIOLOGY RESEARCH2008.

264. Pillai-Kastoori L, Schutz-Geschwender AR, Harford JA. A systematic approach to quantitative Western blot analysis. Analytical Biochemistry. 2020;593:113608.

265. Gewies A, Graß C, Krappmann D. Methods to Study CARD11-BCL10-MALT1 Dependent Canonical NF-κB Activation in Jurkat T Cells. Methods Mol Biol. 2021;2366:125-43.

266. El-Guendy N, Sinai AP. Potential problems inherent in cell-based stable NF-kappaB-GFP reporter systems. Mol Cell Biochem. 2008;312(1-2):147-55.

267. Pfeifhofer C, Kofler K, Gruber T, Tabrizi NG, Lutz C, Maly K, et al. Protein kinase C theta affects Ca2+ mobilization and NFAT cell activation in primary mouse T cells. J Exp Med. 2003;197(11):1525-35.

268. Frischbutter S, Gabriel C, Bendfeldt H, Radbruch A, Baumgrass R. Dephosphorylation of Bcl-10 by calcineurin is essential for canonical NF-kappaB activation in Th cells. European journal of immunology. 2011;41(8):2349-57.

269. O'Neill TJ, Seeholzer T, Gewies A, Gehring T, Giesert F, Hamp I, et al. TRAF6 prevents fatal inflammation by homeostatic suppression of MALT1 protease. Sci Immunol. 2021;6(65):eabh2095.

270. Shields AM, Bauman BM, Hargreaves CE, Pollard AJ, Snow AL, Patel SY. A Novel, Heterozygous Three Base-Pair Deletion in CARD11 Results in B Cell Expansion with NF-κB and T Cell Anergy Disease. J Clin Immunol. 2020;40(2):406-11.

271. Chen Y, Cai H, Pan Ja, Xiang N, Tien P, Ahola T, Guo D. Functional screen reveals SARS coronavirus nonstructural protein nsp14 as a novel cap N7 methyltransferase. Proceedings of the National Academy of Sciences. 2009;106(9):3484-9.

272. Li T-W, Kenney AD, Park J-G, Fiches GN, Liu H, Zhou D, et al. SARS-CoV-2 Nsp14 protein associates with IMPDH2 and activates NF-κB signaling. Front Immunol. 2022;13.

273. Barroso M, Kao D, Blom HJ, Tavares de Almeida I, Castro R, Loscalzo J, Handy DE. S-adenosylhomocysteine induces inflammation through NFkB: A possible role for EZH2 in endothelial cell activation. Biochim Biophys Acta. 2016;1862(1):82-92.

274. García-Román R, Salazar-González D, Rosas S, Arellanes-Robledo J, Beltrán-Ramírez O, Fattel-Fazenda S, Villa-Treviño S. The differential NF-kB modulation by S-adenosyl-L-methionine, N-acetylcysteine and quercetin on the promotion stage of chemical hepatocarcinogenesis. Free Radical Research. 2008;42(4):331-43.

275. Li TWH, Yang H, Peng H, Xia M, Mato JM, Lu SC. Effects of S-adenosylmethionine and methylthioadenosine on inflammation-induced colon cancer in mice. Carcinogenesis. 2012;33(2):427-35.

276. Moon MK, Kim M, Chung SS, Lee HJ, Koh SH, Svovoda P, et al. S-Adenosyl-L-methionine ameliorates TNFα-induced insulin resistance in 3T3-L1 adipocytes. Experimental & Molecular Medicine. 2010;42(5):345-52.

277. Proulx J, Borgmann K, Park I-W. Post-translational modifications inducing proteasomal degradation to counter HIV-1 infection. Virus Research. 2020;289:198142.

278. Schwartz O, Maréchal V, Friguet B, Arenzana-Seisdedos F, Heard J-M. Antiviral Activity of the Proteasome on Incoming Human Immunodeficiency Virus Type 1. Journal of Virology. 1998;72(5):3845-50.

279. Doerfler W. Patterns of DNA methylation--evolutionary vestiges of foreign DNA inactivation as a host defense mechanism. A proposal. Biol Chem Hoppe Seyler. 1991;372(8):557-64.

280. Khabar KS, Al-Zoghaibi F, Al-Ahdal MN, Murayama T, Dhalla M, Mukaida N, et al. The alpha chemokine, interleukin 8, inhibits the antiviral action of interferon alpha. J Exp Med. 1997;186(7):1077-85.

281. Polyak SJ, Khabar KSA, Rezeiq M, Gretch DR. Elevated Levels of Interleukin-8 in Serum Are Associated with Hepatitis C Virus Infection and Resistance to Interferon Therapy. Journal of Virology. 2001;75(13):6209-11.

282. Kofuji S, Sasaki AT. GTP metabolic reprogramming by IMPDH2: unlocking cancer cells' fuelling mechanism. J Biochem. 2020;168(4):319-28.

283. Hedstrom L. IMP Dehydrogenase: Structure, Mechanism, and Inhibition. Chemical Reviews. 2009;109(7):2903-28.

284. Liao LX, Song XM, Wang LC, Lv HN, Chen JF, Liu D, et al. Highly selective inhibition of IMPDH2 provides the basis of antineuroinflammation therapy. Proc Natl Acad Sci U S A. 2017;114(29):E5986-e94.

285. Andreucci M, Faga T, Lucisano G, Uccello F, Pisani A, Memoli B, et al. Mycophenolic acid inhibits the phosphorylation of NF-kappaB and JNKs and causes a decrease in IL-8 release in H2O2-treated human renal proximal tubular cells. Chem Biol Interact. 2010;185(3):253-62.

286. Toubiana J, Rossi AL, Grimaldi D, Belaidouni N, Chafey P, Clary G, et al. IMPDHII protein inhibits Toll-like receptor 2-mediated activation of NF-kappaB. J Biol Chem. 2011;286(26):23319-33.

287. Fiedler MA, Wernke-Dollries K. Incomplete regulation of NF-kappaB by IkappaBalpha during respiratory syncytial virus infection in A549 cells. J Virol. 1999;73(5):4502-7.

288. DeDiego ML, Nieto-Torres JL, Regla-Nava JA, Jimenez-Guardeño JM, Fernandez-Delgado R, Fett C, et al. Inhibition of NF-κB-mediated inflammation in severe acute respiratory syndrome coronavirus-infected mice increases survival. J Virol. 2014;88(2):913-24.

289. Liao Q-J, Ye L-B, Timani KA, Zeng Y-C, She Y-L, Ye L, Wu Z-H. Activation of NF-κB by the Full-length Nucleocapsid Protein of the SARS Coronavirus. Acta Biochimica et Biophysica Sinica. 2005;37(9):607-12.

290. Kanzawa N, Nishigaki K, Hayashi T, Ishii Y, Furukawa S, Niiro A, et al. Augmentation of chemokine production by severe acute respiratory syndrome coronavirus 3a/X1 and 7a/X4 proteins through NF-kappaB activation. FEBS Lett. 2006;580(30):6807-12.

291. Dosch SF, Mahajan SD, Collins AR. SARS coronavirus spike protein-induced innate immune response occurs via activation of the NF-kappaB pathway in human monocyte macrophages in vitro. Virus Res. 2009;142(1-2):19-27.

292. Hiscott J, Kwon H, Génin P. Hostile takeovers: viral appropriation of the NF-kB pathway. The Journal of Clinical Investigation. 2001;107(2):143-51.

293. Lamason RL, McCully RR, Lew SM, Pomerantz JL. Oncogenic CARD11 mutations induce hyperactive signaling by disrupting autoinhibition by the PKC-responsive inhibitory domain. Biochemistry. 2010;49(38):8240-50.

294. Jattani RP, Tritapoe JM, Pomerantz JL. Cooperative Control of Caspase Recruitment Domain-containing Protein 11 (CARD11) Signaling by an Unusual Array of Redundant Repressive Elements. J Biol Chem. 2016;291(16):8324-36.

295. Jones TA, Hutcherson SM, Bedsaul JR, Pomerantz JL. Dysregulated CARD11 signaling in the development of diffuse large B cell lymphoma. LymphoSign Journal. 2020;7(3):90-103.

296. Liu X, Huuskonen S, Laitinen T, Redchuk T, Bogacheva M, Salokas K, et al. SARS-CoV-2–host proteome interactions for antiviral drug discovery. Molecular Systems Biology. 2021;17(11):e10396.

297. Walter M, Chen IP, Vallejo-Gracia A, Kim IJ, Bielska O, Lam VL, et al. SIRT5 is a proviral factor that interacts with SARS-CoV-2 Nsp14 protein. bioRxiv. 2022.

298. Shi F-S, Yu Y, Li Y-L, Cui L, Zhao Z, Wang M, et al. Expression Profile and Localization of SARS-CoV-2 Nonstructural Replicase Proteins in Infected Cells. Microbiology Spectrum. 2022;10(4):e00744-22.

299. Meyers JM, Ramanathan M, Shanderson RL, Donohue L, Ferguson I, Guo MG, et al. The proximal proteome of 17 SARS-CoV-2 proteins links to disrupted antiviral signaling and host translation. bioRxiv. 2021.

300. Pfaffl MW. A new mathematical model for relative quantification in real-time RT-PCR. Nucleic Acids Res. 2001;29(9):e45.

301. Szymczak AL, Workman CJ, Wang Y, Vignali KM, Dilioglou S, Vanin EF, Vignali DA. Correction of multi-gene deficiency in vivo using a single 'self-cleaving' 2A peptide-based retroviral vector. Nat Biotechnol. 2004;22(5):589-94.

Appendix

Publications

Results of this thesis are part of:

Tofaute, M. J., Weller, B., Graß, C., Halder, H., Dohai, B., Falter-Braun, P., and Krappmann, D. SARS-CoV-2 NSP14 MTase activity is critical for inducing canonical NF-κB activation., Bioscience Report, 44(1).

Kim,D.-K., Weller, B., Lin, C.-W., Sheykhkarimli, D., Knapp, J. J., Dugied, G., Zanzoni, A., Pons, C., **Tofaute, M. J.**, Maseko, S. B., Spirohn, K., Laval, F., Lambourne, L., Kishore, N., Rayhan, A., Sauer, M., Young, V., Halder, H., Marín-de la Rosa, N., Pogoutse, O., Strobel, A., Schwehn, P., Li, R., Rothballer, S. T., Altmann, M., Cassonnet, P., Coté, A. G., Vergara, L. E. Hazelwood, I., Liu, B. B., Nguyen, M., Pandiarajan, R., Dohai, B., Rodriguez Coloma, P. A., Poirson, J., Giuliana, P., Willems, L., Taipale, M., Jacob, Y., Hao, T., Hill, D. E., Brun, C., Twizere, J.-C., Krappmann, D., Heinig, M., Falter, C., Aloy, P., Demeret, C., Vidal, M., Calderwood, M. A., Roth, F. P. and Falter-Braun, P. (2022). A proteome-scale map of the SARS-CoV-2 human contactome. Nat. Biotechnol., 41 (1), 140-149.

O'Neill, T. J., Seeholzer, T., Gewies, A., Gehring, T., Giesert, F., Hamp, I., Graß, C., Schmidt, H., Kriegsmann, K., **Tofaute, M. J.**, Demski, K., Poth, T., Rosenbaum, M., Schnalzger, T., Ruland, J., Göttlicher, M., Kriegsmann, M., Naumann, R., Heissmeyer, V., Plettenburg, O., Wurst, W., Krappmann, D. (2021). TRAF6 prevents fatal inflammation by homeostatic suppression of MALT1 protease. Science immunology, 6(65), eabh2095.

Research articles:

Young, V., Dohai, B., Hitch, T., Hyden, P., Weller, B., Heusden, N., Saha, D., Macgregor, J., Maseko, S., Lin, C.-W., Boujeant, M., Choteau, S., Ober, F., Schwehn, P., Rothballer, S., Altmann, M., Altmann, S., Strobel, A., Rothballer, M., **Tofaute, M.**, Heinig, M., Clavel, T., Twizere, J.-C., Vincentelli, R., Boes, M., Krappmann, D., Falter, C., Rattei, T., Brun, C., Zanzoni, A. and Falter-Braun, P. A gut meta-interactome map reveals modulation of human immunity by microbiome effectors, submitted.

Kutzner, K., Woods, S., Karayel, O., Gehring, T., Yin, H., Flatley, A., Graß, C., Wimberger, N., **Tofaute, M. J.**, Seeholzer, T., Feederle, R., Mann, M., Krappmann, D. (2022). Phosphorylation of serine-893 in CARD11 suppresses the formation and activity of the CARD11-BCL10-MALT1 complex in T and B cells. Sci Signal., 15 (723)

Lawrence, R. E., Cho, K. F., Rappold, R., Thrun, A., **Tofaute, M.**, Kim, D. J., Moldavski, O., Hurley, J. H. and Zoncu, R. (2018). A nutrient-induced affinity switch controls mTORC1 activation by its Rag GTPase-Ragulator lysosomal scaffold. Nat Cell Biol., 20 (9), 1052-1063.

Review:

O´Neill, T. J., **Tofaute, M. J.** and Krappmann, D. (2023). Function and targeting of MALT1 paracaspase in cancer. Cancer Treatment Reviews, 117 (2023), 102568.

Eidesstattliche Erklärung

Ich versichere hiermit an Eides statt, dass die vorgelegte Dissertation von mir selbständig und ohne unerlaubte Hilfe angefertigt ist.

München, den 01.12.2023 _____Marie J. Tofaute_____

(Unterschrift)

Erklärung

Hiermit erkläre ich,

- ✓ dass die Dissertation nicht ganz oder in wesentlichen Teilen einer anderen Prüfungskommission vorgelegt worden ist.
- ✓ dass ich mich anderweitig einer Doktorprüfung ohne Erfolg nicht unterzogen habe.

München, den 01.12.2023 _____Marie J. Tofaute_____

(Unterschrift)